Università degli Studi di Cagliari
Università degli Studi di Sassari

DOTTORATO DI RICERCA
In Scienze e Tecnologie Chimiche

Ciclo XXXV

Development of New Synthesis Methods of Proteins/Enzymes-Metal Organic Frameworks (MOFs) Hybrid Composite Materials for Biomedical Applications

Settore scientifico disciplinare di afferenza

CHIM/03

Presentata da:	Giada Mannias
Coordinatori Dottorato:	Prof.ssa Carla Cannas Prof. Stefano Enzo
Tutor:	Prof. Guido Ennas

Anno accademico 2021 – 2022

To my beloved family and friends

who have always believed in me

The present Ph.D. thesis is based on my three-year research at the Ph.D. School (Chemical Science and Technology Ph.D. Course, XXXV cycle) of the University of Sassari (Italy), in collaboration with the University of Cagliari (Italy). It is submitted as a requirement for obtaining the Ph.D. degree with the further certificate of Doctor Europaeus. The whole research has been financed by the University of Cagliari with the Sardinia Regional Government fundings (P.O.R. Sardegna F.S.E. Operational Programme of the Autonomous Region of Sardinia, European Social Fund 2014-2020 – Asse III "Istruzione e Formazione" – Obiettivo Tematico 10 "Investire nell'istruzione, nella formazione e nella formazione professionale per le competenze e l'apprendimento permanente" per le aree di specializzazione D.G.R. n. 43/12 del 01/09/2015: ICT, Reti intelligenti per la gestione efficiente dell'energia, Biomedicina, Turismo e beni culturali e ambientali).

Giada Mannias

Table of Contents

Summary

This three-year Ph.D. research project is the result of the collaboration among the research group of Prof. Guido Ennas from University of Cagliari (Italy), expert in innovative and green synthesis approaches of micro- and nanomaterials, including mechanochemistry and sonochemistry, and the research group of Dr. Sarah Hudson from University of Limerick (Ireland), expert in biocatalysts and drug-delivery systems.

The research focuses on the development of innovative synthesis routes for the preparation of proteins/enzymes – Metal Organic Frameworks (MOFs) hybrid composite materials for biomedical applications. In particular, alternative sonochemical and mechanochemical methods have been explored for the one-pot synthesis of glucose oxidase – iron(III) trimesate composites under eco- and bio-compatible conditions. Conventional harsh synthesis conditions have been overcome in order to minimise enzyme denaturation and activity loss, while retaining structural and textural features of the MOF. Beside their biocompatibility and low cost, one of the advantages of using iron(III) trimesate materials to immobilise biomolecules is their peroxidase-mimic behaviour. Indeed, such MOFs do not act as passive supports for the immobilisation of glucose oxidase, but also perform as enzyme-mimics, avoiding the immobilisation of additional peroxidase enzymes. Hybrid glucose oxidase – iron(III) trimesate composites prepared via mechanochemical and sonochemical approaches under mild conditions were applied as sensitive biosensors for glucose colorimetric detection.

Chapter 1 first gives a general overview on Metal-Organic Frameworks' chemistry, design and classification, focusing on structures built up from iron(III) and 1,3,5-benzentricarboxylate, also known as iron(III) trimesate materials. Chemical, physical features and main applications fields of these MOFs are extensively reported. A discussion on the most common synthesis methods is then proposed, focusing mainly on mechanochemical and sonochemical alternative approaches and their advantages compared to conventional methods. Finally, *ex vivo* applications of biomolecules and the strategies employed for their immobilisation on solid supports are introduced, illustrating the potential advantages of using alternative methods under mild conditions to preserve biomolecules functionality.

Experimental section is divided in four chapters: Chapter 2 deals with the synthesis and characterisation of an iron(III) trimesate material under mild biomolecule-friendly conditions via mechanochemical approach. Moreover, mechanochemically-prepared iron(III) trimesate MOFs have been employed for hydrogen peroxide biosensing and preliminary studies on their usage as drug-delivery systems are described. In Chapter 3 mechanosynthesis for the *in situ* immobilisation of Glucose Oxidase (GOx) during iron(III) trimesate MOF building-up is illustrated. Physicochemical characterisation of samples, biocatalytic studies, and the application of the obtained enzyme-MOF hybrid composites for glucose biosensing are further discussed. Chapter 4 describes the sonochemical synthesis and characterisation of an iron(III) trimesate material under green, biomolecule-friendly conditions. In Chapter 5 one-pot immobilisation of GOx on iron(III) trimesate MOF using sonochemical approach is described, followed by characterisation of the obtained composites and their usage for glucose detection.

All samples were characterised by Fourier transform infrared spectroscopy (FT-IR), X-ray powder diffraction (XRPD), thermal analysis, scanning electron microscopy (SEM), and nitrogen physisorption at -196 °C.

Finally, Chapter 6 is dedicated to the conclusions and future perspectives of this research work.

Chapter 1:

Introduction

1. Introduction

1.1. Metal-organic frameworks (MOFs)

Metal-organic frameworks, abbreviated to MOFs, are a subclass of coordination polymers (CPs) composed of metal centres, called nodes, joined by organic ligands via coordination bonds to constitute highly porous architectures.[1]

The term MOF was used for the first time in 1995 by Omar Yaghi et al. to describe a porous 3D network consisting of slightly distorted trigonal planar copper(I) centres linked by rod-like 4,4'-bipyridine ligands.[2] MOFs have rapidly attracted the attention in the last decades because of their zeolite-like features: stability and microporosity of the framework, high specific surface areas, host-guest interactions, and selective catalytic activity. Because of these properties, MOFs have been applied in several fields, including catalysis, gas storage and separation, sensing, drug delivery and electrochemical charge storage.[3] Unlike zeolites, which are aluminosilicate inorganic frameworks with highly ordered microporous structure,[4] a wide variety of organic ligands and metal ions can be combined, giving rise to a potentially infinite range of topologies and structures. Moreover, MOF pore size and shape can be easily tuned, even from the micropore to the mesopore scale, by simply changing the length and/or the nature of the ligands.[5]

1.1.1. IUPAC definition and terminology

MOFs and CPs constitute prolific research areas involving interdisciplinary fields, such as inorganic and coordination chemistry and crystal engineering. A variety of different terminologies were in use among research groups, eventually causing confusion in literature searches and unnecessary misunderstandings within the scientific community. Therefore, considering the growing interest in MOFs, also at the industrial level, in 2009 the International Union of Pure and Applied Chemistry (IUPAC) started a project to define terminology and nomenclature guidelines on coordination polymers and metal–organic frameworks, to be added to the previously offered definitions of coordination compound, coordination entity, polymer and macromolecule. A coordination compound is “any compound that contains a coordination entity”, which in turn is “an ion or neutral molecule that is composed of a central atom, usually

that of a metal, to which is attached a surrounding array of atoms or groups of atoms, each of which is called ligands".[6] A polymer is any "substance composed of macromolecules".[7] Macromolecules are molecules "of high relative molecular mass, the structure of which essentially comprises the multiple repetition of units derived, actually or conceptually, from molecules of low relative molecular mass".[7]

According to the current IUPAC recommendations, a hierarchical terminology in which the most general term is coordination polymer is strongly recommended. Coordination networks represents a subclass of coordination polymers and MOFs are a further subclass of coordination networks (Figure 1.1).

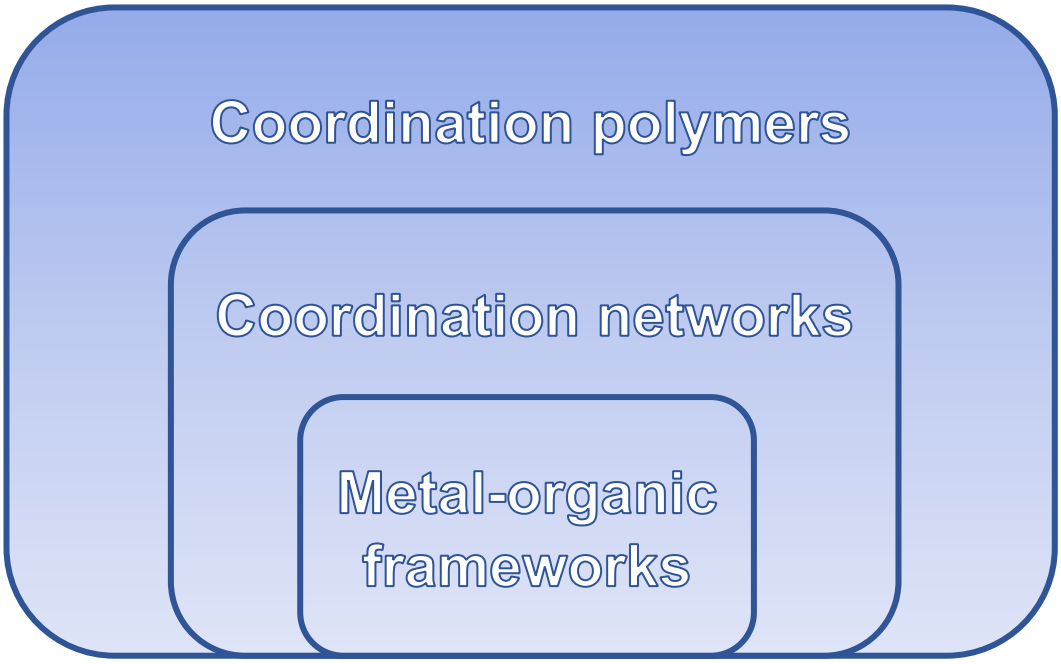

Figure 1.1. Hierarchical classification of coordination polymers, coordination networks and metal-organic frameworks according to IUPAC recommendations.[8]

The current terminology guidelines are as follows:[8]

- **Coordination polymers**

A coordination polymer is "a coordination compound with repeating coordination entities extending in 1, 2, or 3 dimensions".[8]

Crystallinity does not constitute a requirement for coordination polymers. Consequently, the use of the terms "1-periodic, 2-periodic, and 3-periodic", used for crystalline states is discouraged. Conversely, the prefixes "1D-, 2D-, and 3D-" are acceptable to indicate the degree

of extension of the coordination polymer. An example of coordination polymer is given in Figure 1.2.

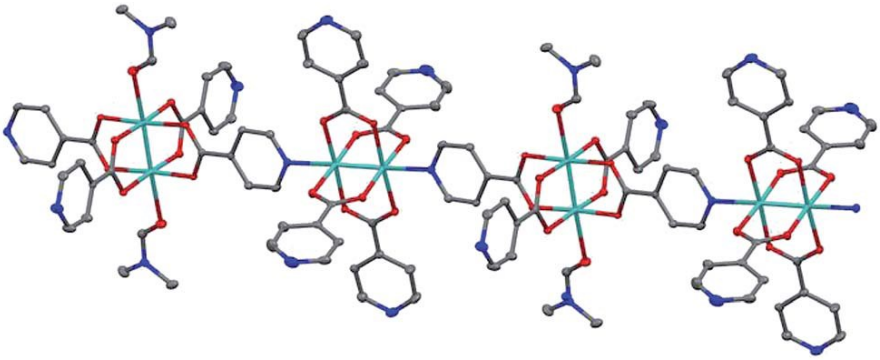

Figure 1.2. An example of a 1D coordination polymer. Cyan: Mo; blue: N; red: O; grey: C. All hydrogen atoms have been omitted for clarity. Reproduced from Ref. [9] with permission from the Royal Society of Chemistry.

- **Coordination network**

A coordination network is "a coordination compound extending, through repeating coordination entities, in 1 dimension, but with cross-links between two or more individual chains, loops, or spiro-links, or a coordination compound extending through repeating coordination entities in 2 or 3 dimensions".[8]

IUPAC task group strictly underlines that coordination polymers and coordination networks are not synonyms, since the latter are a subset of the former. According to these definitions, structures containing repeated tubular, necklace, rhomboid chains, or (4,4) net topology, can be classified as coordination networks. Conversely, zig-zag, arched, and helical chains belong to the group of 1D-CPs (Figure 1.3).[10]

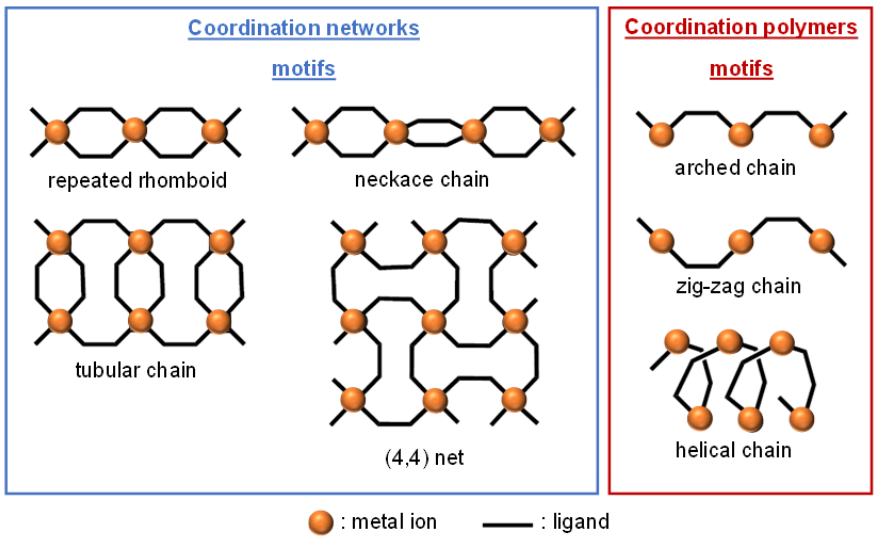

Figure 1.3. Some examples of structural motifs observed for coordination networks and coordination polymers. This picture is reproduced according to Ref. [10].

An example of coordination networks is showed in Figure 1.4.

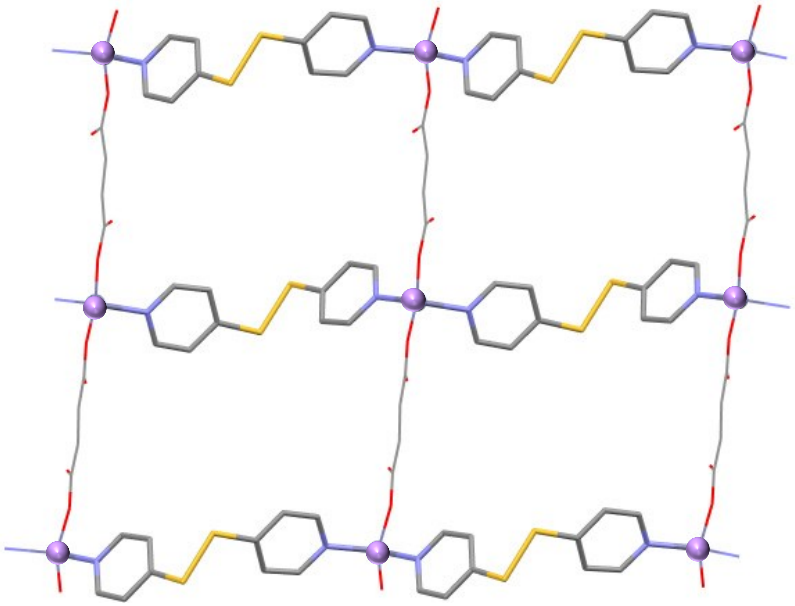

Figure 1.4. 2D-coordination network with (4,4) net topology. Mauve: Zn; yellow: S; light blue: N, grey: C; red: O. All hydrogen atoms have been omitted for clarity. This picture is reproduced according to Ref. [10].

- **Metal-organic framework**

A metal–organic framework is "a coordination network with organic ligands containing potential voids".[8]

One of the criteria MOFs need to fulfil is the presence of potential voids. However, IUPAC clarifies that no physical measurements of porosity or other properties are required. This is related to the fact that many systems are dynamic. Then, modifications in structure and, consequently, in potential porosity or solvent (and/or guest) filled voids can occur depending on external stimuli (e.g., temperature and pressure). For these reasons it is also not demanded for MOFs to be crystalline. Figure 1.5 shows an example of MOF.

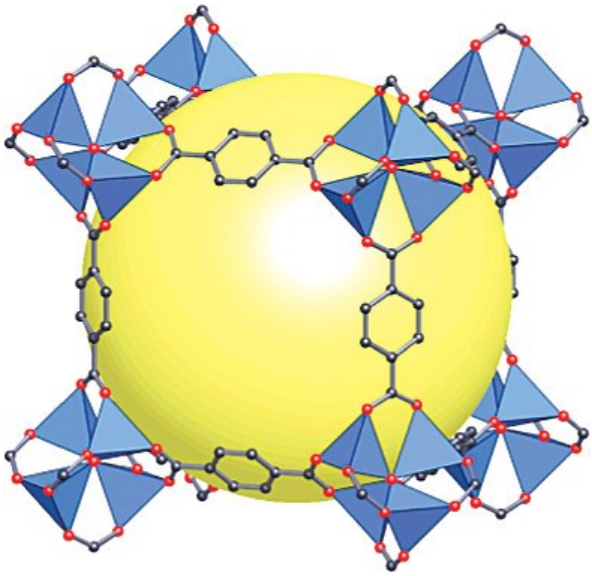

Figure 1.5. Example of MOF. Blue: Zn; red: O; grey: C (a). The yellow sphere in the middle highlights the presence of a cavity. All hydrogen atoms have been omitted for clarity. Reprinted with permission from [11]. Copyright 2007 American Chemical Society.

1.1.2 Organic ligands and metal sites

Several metal centres with specific points of extension can be connected to each other by a wide range of organic ligands through coordination bonds. This yields a numerous diversity of MOFs, especially in terms of topology. To the best of our knowledge, the flexibility with which geometry, size, and functionality of MOF constituents can be varied has led to more than 20,000 different structures in the past decades, proving an exceptional chemical tailoring of these materials.[12]

Commonly, two groups of ligands are used in MOFs: N-donors and carboxylates. Linkers are further classified as di-topic, tri-topic, tetra-topic, etc., according to the number of sites which they can use to bind a metal centre. Figure 1.6 reports some examples of carboxylate ligands, which are known as hard donors.[13]

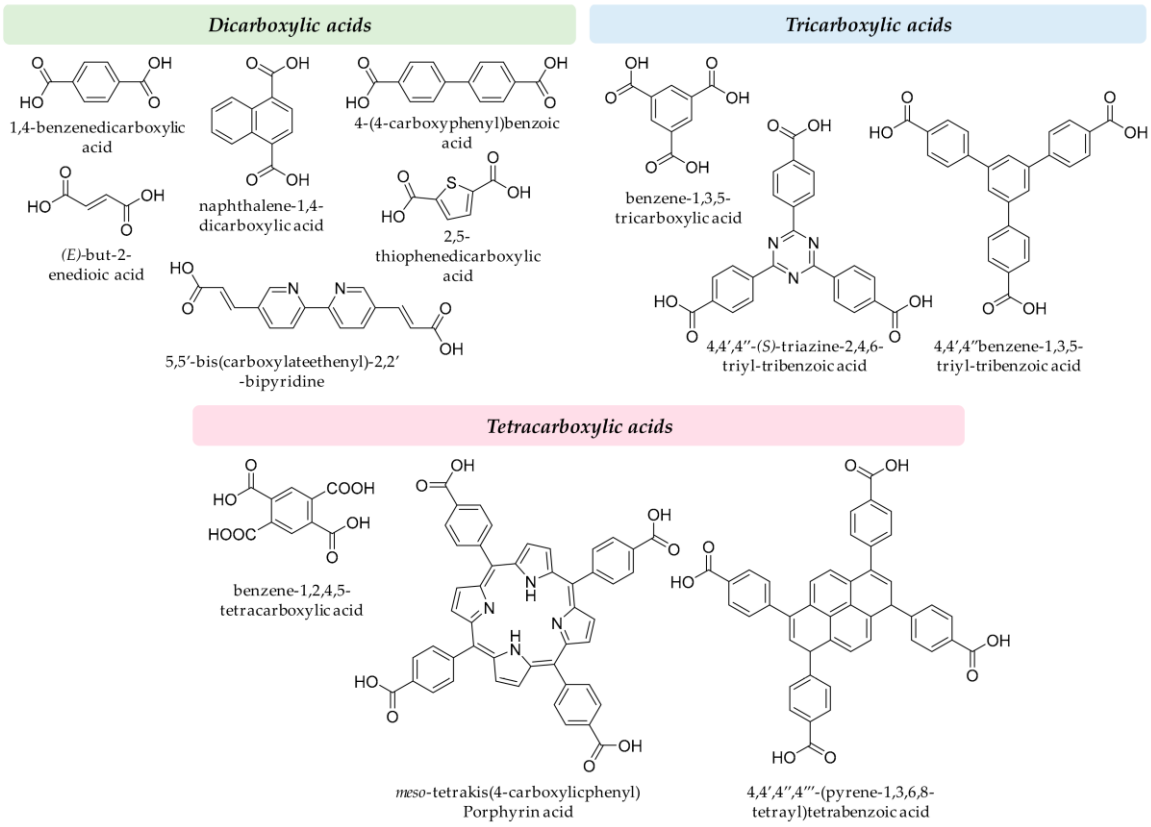

Figure 1.6. Examples of carboxylate ligands used for MOF synthesis. This picture is reproduced according to Ref. [13].

N-donors, such as bipyridines and imidazolates, are classified as neutral soft ligands. Some examples of N-donor ligands are given in Figure 1.7.

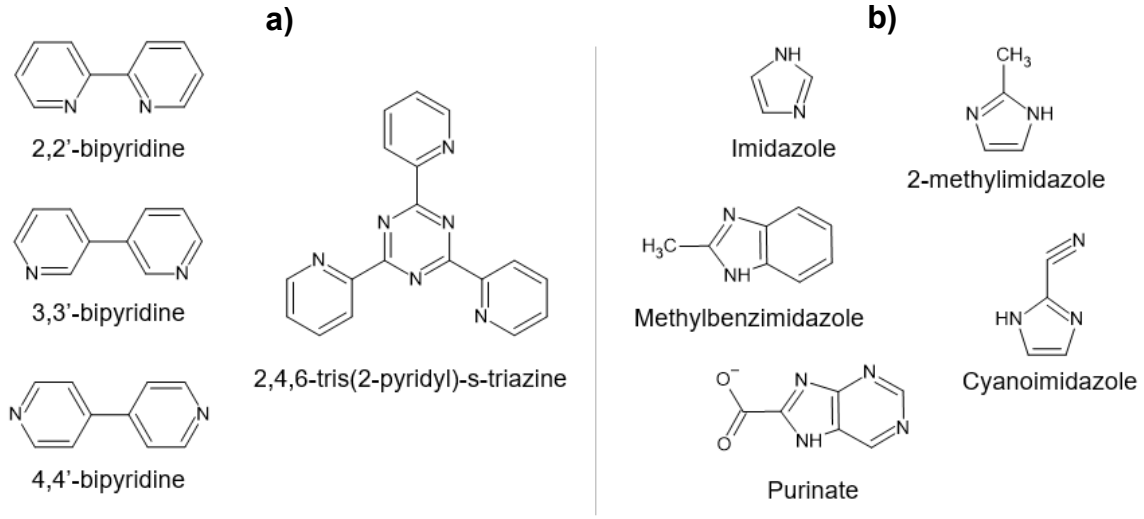

Figure 1.7. Examples of N-donor ligands based on bipyridine (a) and imidazolate (b).

Pore size of MOFs can be modulated by using ligands with different length. The use of the isoreticular principle in the design of MOFs, varying the size and nature of a structure without changing its underlying topology, can lead to ultrahigh porosity and unusually large pore openings. A representative example of linker extension strategy is given by Omar Yaghi et al., who developed a straightforward method to fabricate larger pores in MOFs by changing the extension of the bridging ligand length while keeping the framework topology (Figure 1.8).[14]

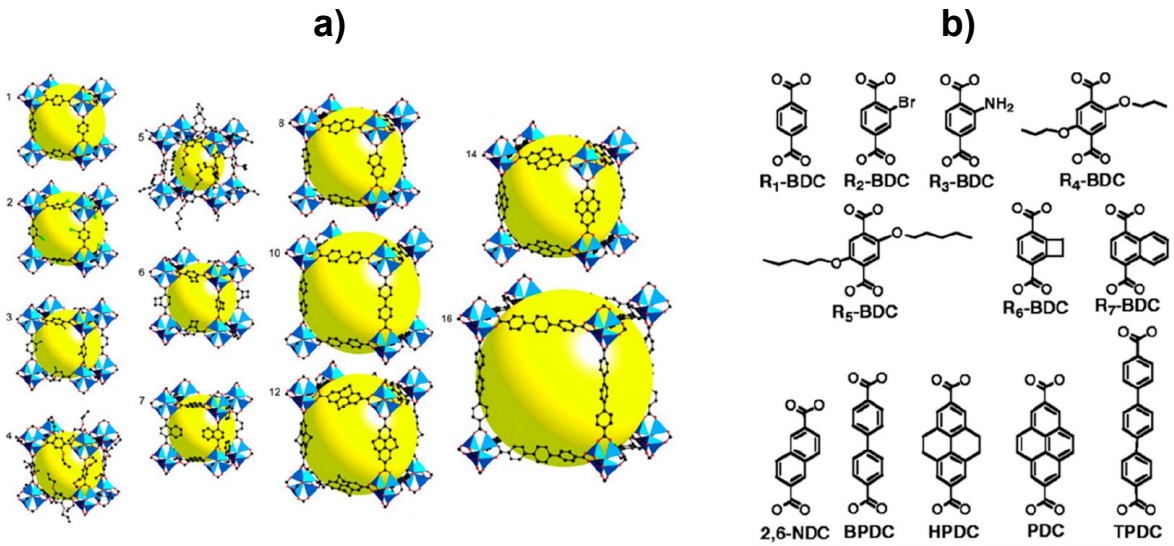

Figure 1.8. MOF series (a) obtained via isoreticular principle (IRMOF) using organic ligands with different length (b). Reprinted from [14] with permission from AAAS.

The presence of metals in MOFs has a significant role in the catalytic performance, as well as in the extraction and adsorption capacities, due to their partial positive charge and the possibility to create open sites. Metal centres can be constituted by single metal ions or metal-cluster entities, called secondary building units (SBUs).[15]

Figure 1.9 provides an example of MOF self-assembly in a simple metal-and-ligand construction mode: metal ions are linked by di-topic ligands (e.g., 4,4'-bipyridine), giving a flexible structure where each vertex represents a metal ion.[5] A variety of framework structures has been produced by assembling metal ions with di-, tri-, and poly-topic organic ligands. However, attempts to evacuate and/or exchange guests within the pores without compromising structural integrity, with few exceptions,[16,17] provoked the collapse of the host framework.[15]

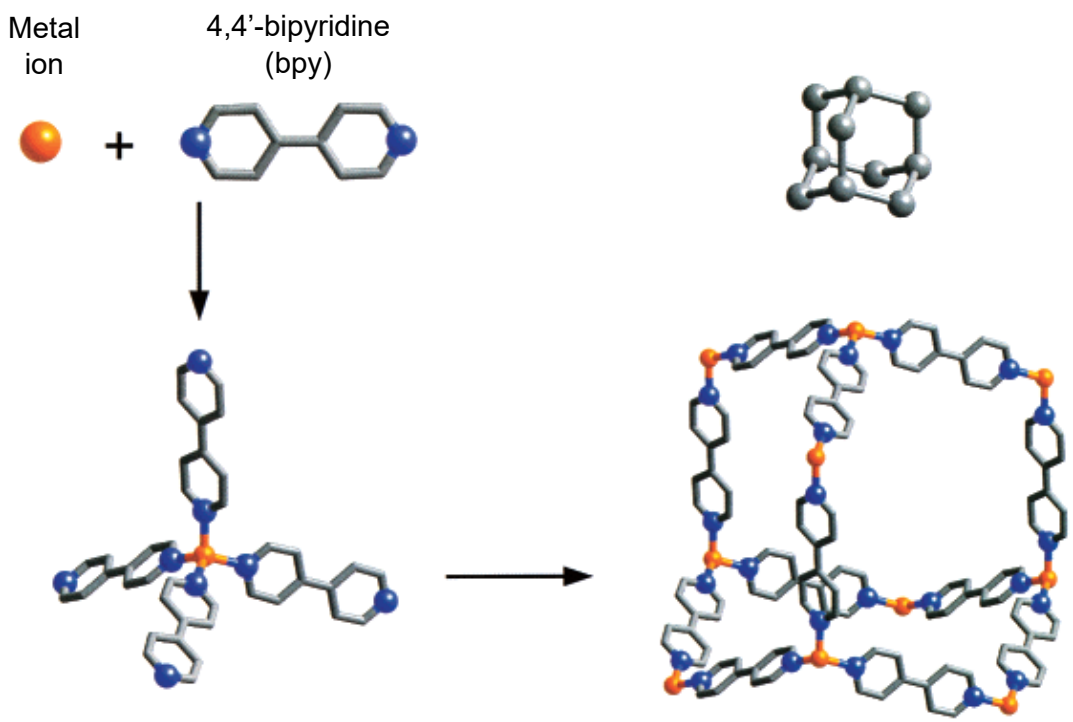

Figure 1.9. Assembly of MOFs based on the copolymerisation of organic linkers with metal ions, giving a flexible metal-ligand structure with expanded diamond topology. M, orange; C, grey, N, blue. All hydrogen atoms have been omitted for clarity. Adapted with permission from [15]. Copyright 2001 American Chemical Society.

Conversely, one or more metal ions can be coordinated by carboxylates or other coordination modes of poly-topic ligands to form SBUs, as shown in Figure 1.10. The replacement of metal vertices by clusters of vertices is called decoration. It provides higher rigidity and structural stability and lower interpenetration tendency to the resulting framework compared to single metal nodes, since metal ions result locked in their position within large rigid vertices, which in turn can be joined by rigid organic ligands to produce extended frameworks.[18]

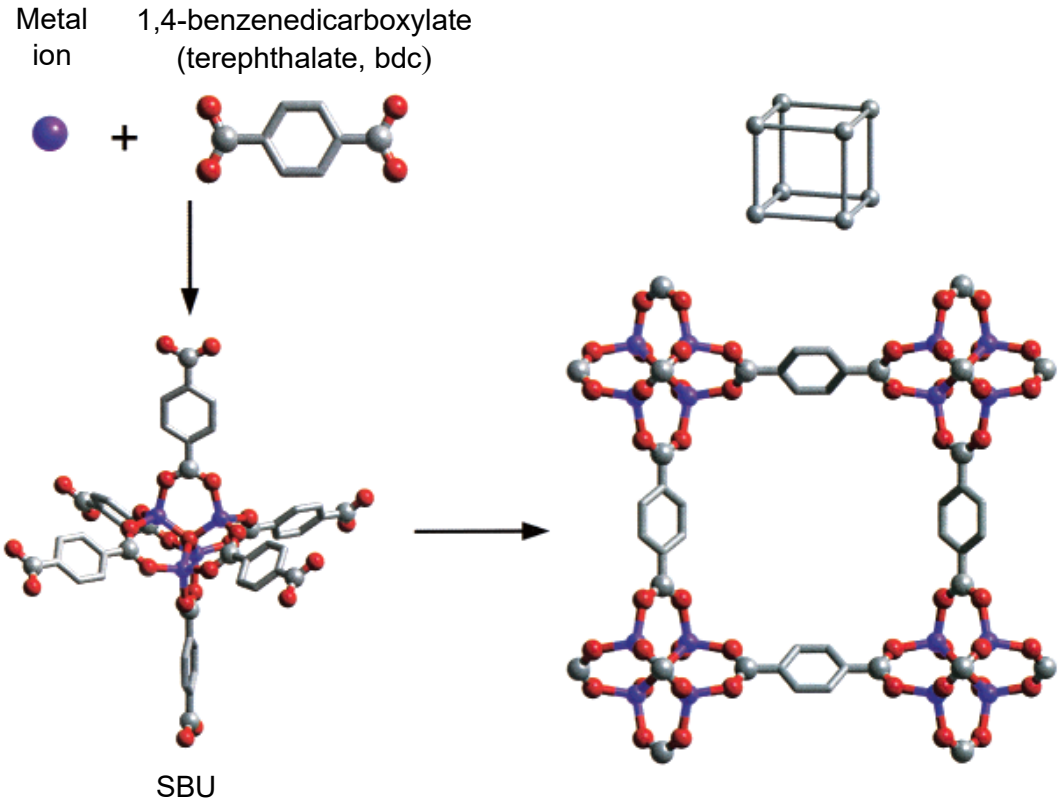

Figure 1.10. Assembly of MOFs by the copolymerisation of organic linkers with metal ions to give rigid metal-ligand clusters. Such SBUs can be in turn linked by organic ligand "struts" forming rigid extended frameworks. Each cluster acts as a large octahedron-decorated vertex in a cube. M, purple; O, red; C, grey. All hydrogen atoms have been omitted for clarity. Adapted with permission from [15]. Copyright 2001 American Chemical Society.

SBUs can be classified depending on the number of metal ions composing a cluster. Figure 1.11 shows same examples of SBUs divided according to the different number of metal ions.

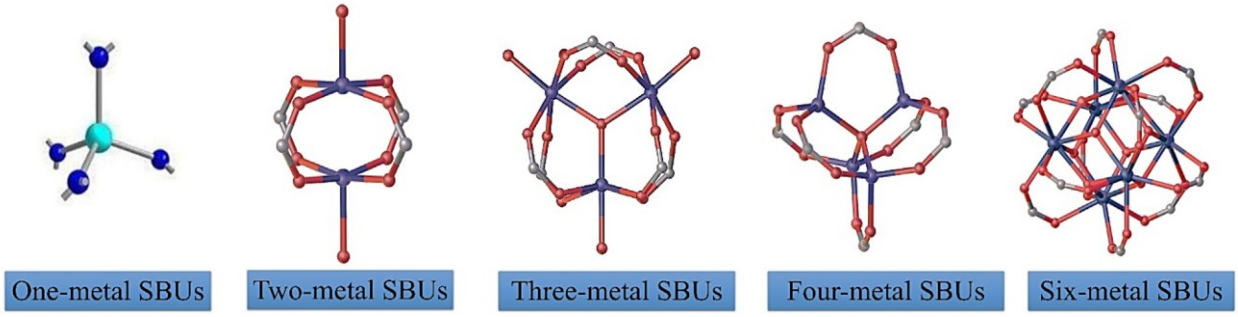

Figure 1.11. Different examples of secondary building units (SBUs). Reprinted from [5]. Copyright 2021, with permission from Elsevier.

One-metal SBUs composed of $M(N)_4$ cores (M: Zn, Co; N: imidazolate) feature in the ZIF-n family (ZIF: zeolitic imidazolate framework) (Figure 1.12).[19]

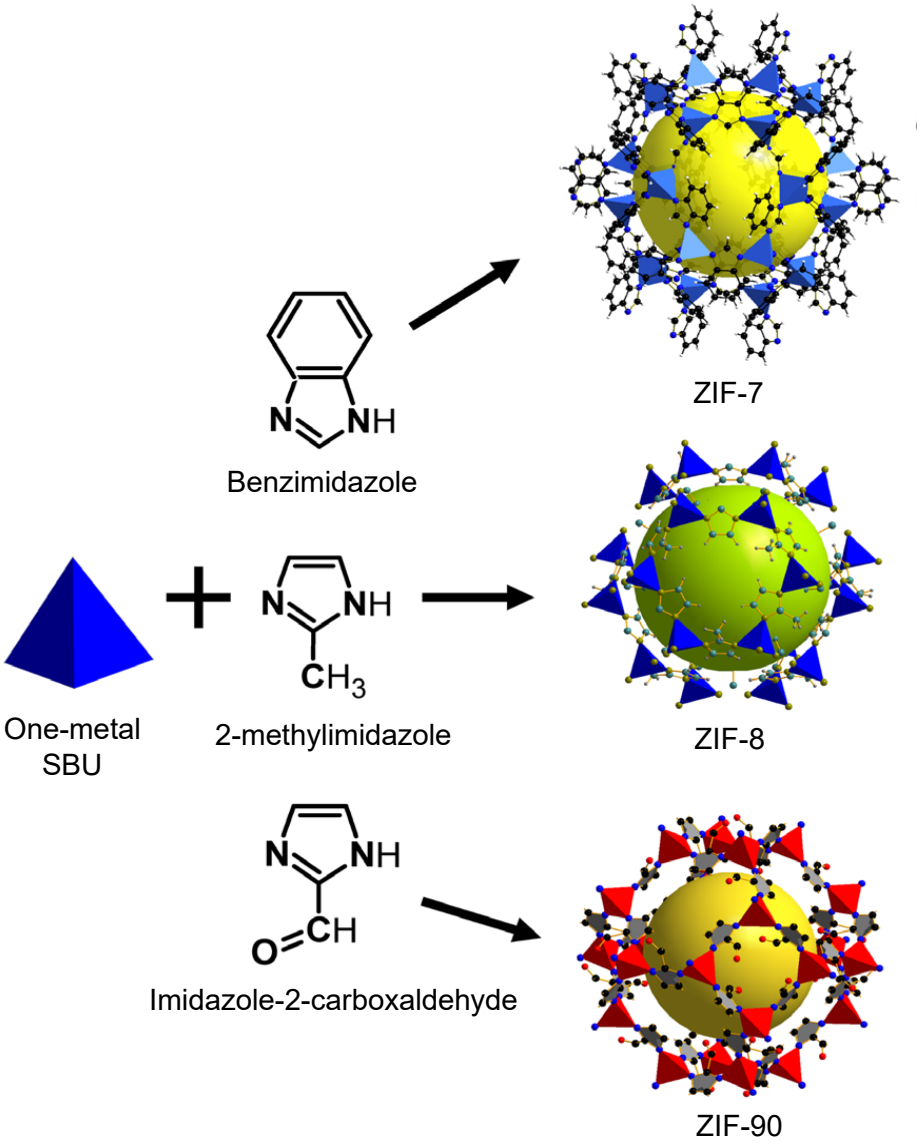

Figure 1.12. Examples of ZIFs derived from the linkage of one-metal SUBs and imidazolates. This picture is reproduced according to Ref. [20].

Two-metal SBUs can be found in MOF-199, also known as HKUST-1 (HKUST: Hong Kong University of Science and Technology), with paddle-wheel $Cu_2(RCOO)_4$ cores (R: H, alkyl, aryl), as shown in Figure 1.13.[21]

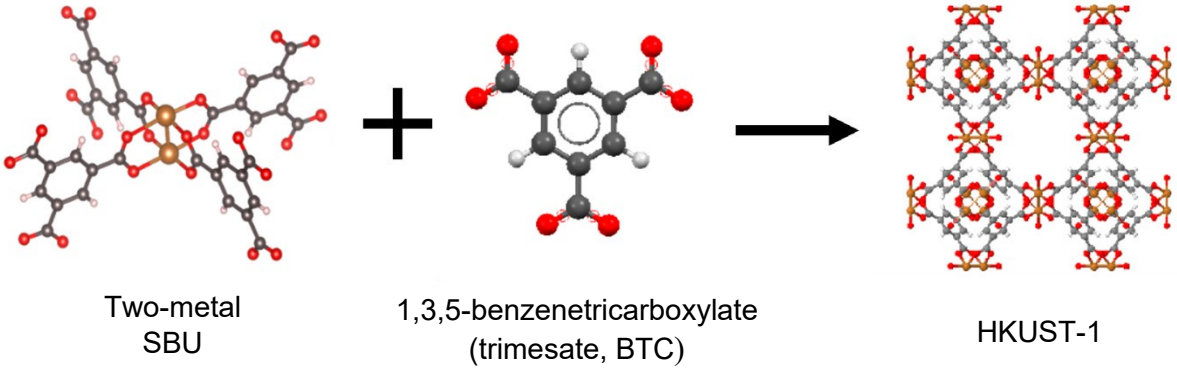

Figure 1.13. Structure of HKUST-1 based on two-metal SBUs and trimesate. This picture is reproduced according to Ref. [22].

Three-metal SBUs are typical of the terephthalate (BDC) based MIL-101 and the trimesate (BTC) based MIL-100 (MIL: Material Institute of Lavoisier) with $[M_3(\mu_3\text{-}O)(RCOO)_6]$ cores (M: Cr, Fe, Al, Sc, V) (Figure 1.14);[23,24]

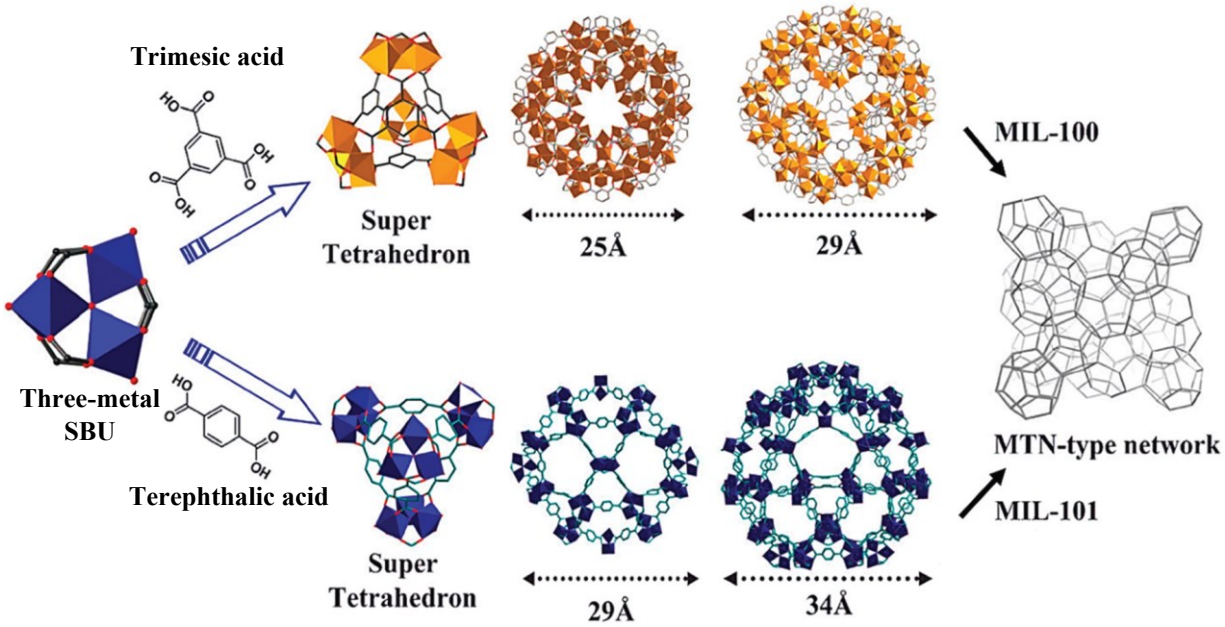

Figure 1.14. Structure of MIL-100 and 101 formed by three-metal SBUs linked through BTC and BDC, respectively, into supertetrahedra, which further assembles into hexagonal and pentagonal cages constituting a porous framework with the zeolite MTN topology (MTN = zeolite socony mobil – thirty-nine). Reproduced from Ref. [25] with permission from the Royal Society of Chemistry.

Four-metal SBUs with a $[Zn_4(\mu_4\text{-}O)(RCOO)_6]$ core are arranged in MOF-5, also known as IRMOF-1, (Figure 1.15).[26]

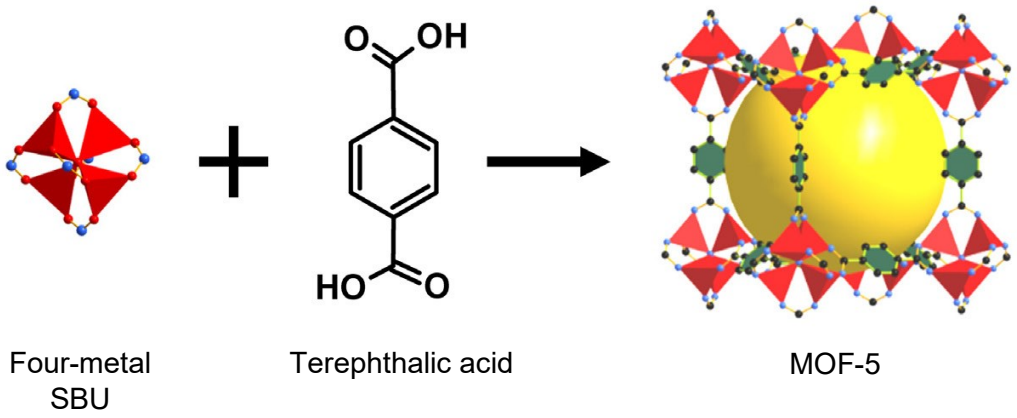

Figure 1.15. Structure of MOF-5 based on four-metal SBUs and terephthalate. This picture is reproduced according to Ref. [20].

The UiO-n family (UiO: University in Oslo) consists of six-metal SBUs with a $Zr_6O_4(OH)_4(RCOO)_{12}$ core (Figure 1.16).[27]

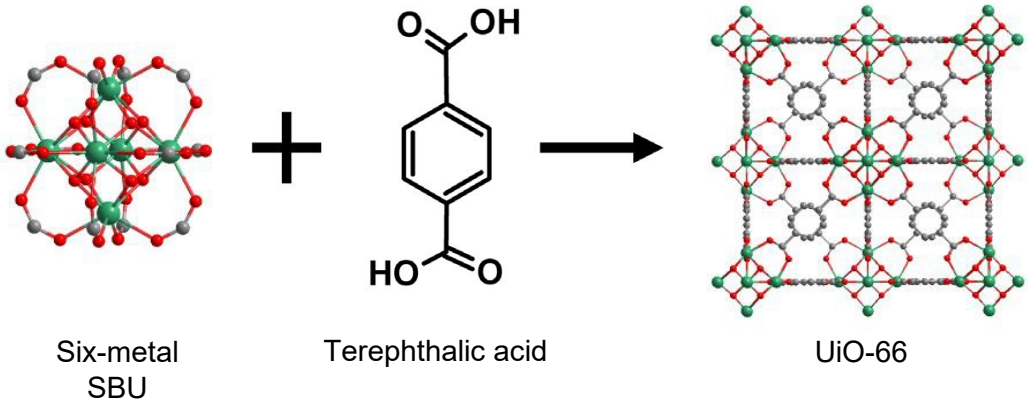

Figure 1.16. Structure of UiO-66 based on six-metal SBUs and terephthalate. Adapted with permission from [28]. Copyright 2019 American Chemical Society.

SBUs can also consist of infinite rods of linked metal-centred polyhedra (Figure 1.17). This is the case of the so-called rod MOFs including MOF-71, MIL-47, and MIL-53.[29]

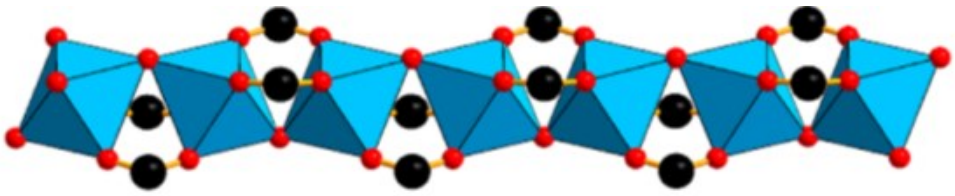

Figure 1.17. One rod of MOF-71 of composition $[Co_2O(RCOO)_4]_\infty$. Reprinted with permission from [29]. Copyright 2016 American Chemical Society.

1.2. Iron(III) trimesate MOFs

Among the wide existing variety of MOFs, structures derived from the linkage of iron(III) and 1,3,5-benzenetricarboxylate (trimesate, btc), constituting the iron(III) trimesate family of MOFs, have aroused great interest in the last decade. This is due to the combination of attractive features of both iron, which is environmentally benign, non-toxic, cheap and possesses redox properties, and 3D-architectures with remarkable air- and water-stability, high specific surface areas (up to 2800 m^2/g), large accessible pores and permanent porosity.[24]

1.2.1 MIL-100(Fe) and Fe-BTC

MIL-100(Fe) was the first synthesised iron trimesate MOF by Patricia Horcajada et al. in 2007 under hydrothermal conditions.[30] It is a zeotype architecture based on trimers of iron(III) octahedra sharing a common μ_3-O vertex. These trinuclear SBUs are linked through trimesate ligands to build supertetrahedra, which in turn assemble into a zeolitic MTN topology. This is characterised by the existence of two types of mesoporous cavities of free diameter of ca. 25 and 29 Å, accessible through pentagonal and hexagonal microporous windows with a free diameter of ca. 5.5 and 8.6 Å, respectively (Figure 1.18). The structure formula reported for MIL-100(Fe) is $Fe_3O(H_2O)_2X\cdot\{C_6H_3(CO_2)_3\}_2\cdot nH_2O$ (n ~14.5) (X = F^- or OH^-). It possesses a crystalline cubic structure with a Fd-3m space group.

To the best of our knowledge, *in lieu* of Fe, many other trivalent metals, including Cr,[31] Sc,[32] Al[33] and V[34] can be used to build MIL-100 structure with the same organic linker. Moreover, synthesis of mixed-metal MIL-100(Sc,M) (M=Al, Cr, Fe) have been reported. However, unlike the above mentioned trivalent metals, iron can also form the semicrystalline iron(III) trimesate material, commonly called Fe-BTC, which is the disordered counterpart of MIL-100(Fe). The relationship between Fe-BTC and MIL-100(Fe) has received great attention over the past decade.[35] Among the huge family of MOFs, only another semicrystalline-full crystalline pair of materials have been recently reported.[36] Fe-BTC and MIL-100 have proven to possess same composition,[37] thermal stability,[38] and comparable nature/structure of metal clusters.[39] Sciortino et al. have related the disordered structure of Fe-BTC to the presence of terminal carboxyl groups belonging to extra-framework or partially deprotonated trimesic acid molecules which interrupt the order of the network.[39] The structure of Fe-BTC still remains almost unknown. Nevertheless, it has been recently identified that Fe-BTC contains both

crystalline and amorphous domains.[40] Therefore, Fe-BTC material is not ascribable as amorphous, but rather as disordered.

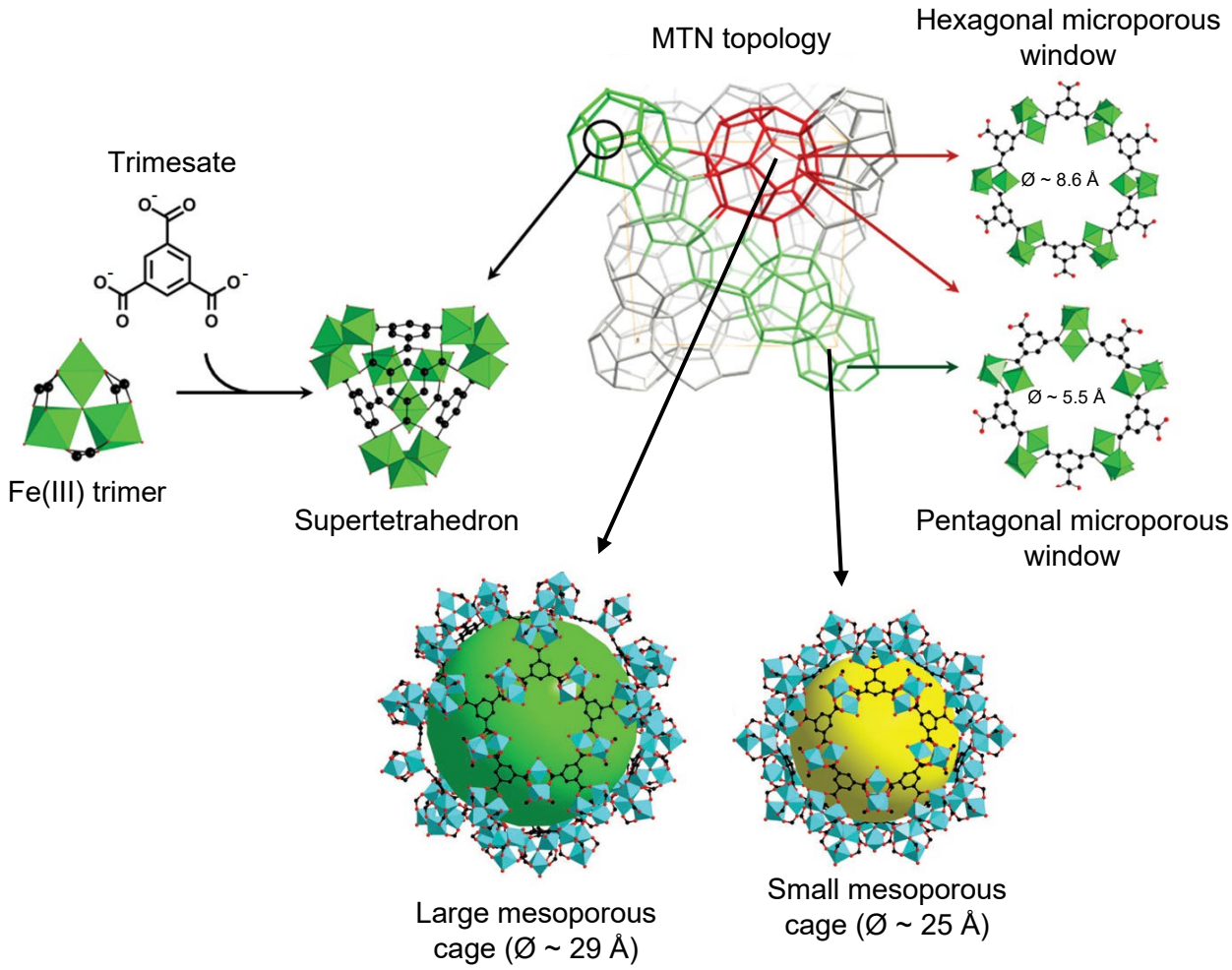

Figure 1.18. The structure of MIL-100(Fe), based on the coordination of Fe(III) trimers and trimesates, creating hybrid supertetrahedra which further assemble into a zeotypic MTN architecture consisting of small mesoporous cages, delimited by pentagonal microporous windows, and large mesoporous cages accessible through pentagonal and hexagonal microporous openings. Reprinted from [41]. Copyright 2013, with permission from John Wiley & Sons.

The interest in Fe-BTC is such that it was one of the first MOFs to be commercialised, as so-called Basolite®F300 by BASF/Aldrich.[42] Indeed, despite the disordered structure, Fe-BTC is widely used for the same applications of MIL-100, sometimes even surpassing its crystalline counterpart as heterogeneous catalysts, especially when Lewis acid sites are required by the reaction.[35] Catalysts can be divided into two main types, homogeneous and heterogeneous, depending on whether the catalyst is in the same phase as the reactants (homogeneous reaction), or in a different phase from the reactants (heterogeneous reaction), respectively. Heterogenous catalysis provide much easier and faster recovery and product separation compared homogeneous reactions. A variety of MOFs, including iron trimesate family, have attracted

significant attention as archetypical heterogeneous catalysts. MIL-100(Fe) was exploited as porous catalyst in numerous Friedel−Crafts type reactions, including the catalytic conversion of benzyl chloride (BZC) to diphenylmethane (DPM).[30] Dhakshinamoorthy et al. have compared the catalytic activity of MIL-100(Fe) and commercial Fe-BTC.[35] Four representative reactions have been selected, two of them requiring Lewis acidity (epoxide ring-opening reaction and aldehyde acetalization) and another two that are oxidation reactions (aerobic oxidation of thiophenol and benzylic oxidation of diphenylmethane (DPM) by TBHP). It was found that Fe-BTC performs better for catalytic processes requiring strong Lewis acid sites. Conversely, MIL-100(Fe) is the preferred catalyst for oxidation reactions. This has been related to the existence in Fe-BTC of structural defects (presence of extra Brønsted acid sites) compared to MIL-100(Fe). So, the use of whether MIL-100(Fe) or Fe-BTC as heterogeneous catalysts results interchangeable depending on the selected reaction type. The leaching of metal sites from the solid catalyst to the liquid phase is one of the main issues in heterogeneous catalysis. Therefore, to confirm that the process is heterogeneous and, thus, not related to the leaching of iron in solution, in the above-mentioned study Dhakshinamoorthy et al. also performed leaching tests for all reactions. A negligible detection of iron has been found in solution for both MIL-100(Fe) and Fe-BTC, proving that iron trimesates are valid catalyst with high catalytic activity.[35]

In addition, iron trimesate MOFs have recently shown great potential for electrochemical performance as electrode materials for high power Li-ion batteries applications because of their notable framework stability and redox reactivity. Among the currently available electrochemical energy storage devices, rechargeable batteries, including lithium-ion batteries (LIBs), possess high energy densities and are suitable for large-scale energy storage systems, electric vehicles, and portable electronic devices.[43] It has been reported an outstanding electrochemical performance for Fe-BTC MOFs, showing capacities up to 408 and 436 mA h g^{-1} after 400 cycles at a current density of 1000 and 500 mA g^{-1}, respectively.[44] Nowadays, there is great interest in exploiting MOFs for LIB applications, due to their high thermal stability, high surface area and porosity, controllable structures for lithium-ion intercalation and deintercalation, and tunable redox properties.[45] Moreover, both organic ligands and metal sites in MOFs can serve as active sites for electrochemical processes.[46]

1.2.2. Stability in water and physiological media

The stability in water of MOFs is of much interest for their industrial applications, especially in the context of wastewater remediation, liquid phase separation, and drug delivery, in which MOFs are used in aqueous media.[47] Iron(III) trimesate MOFs are remarkably promising regarding water stability, which has been widely studied in terms of water adsorption capability. Water adsorption firstly occurs on the available metal sites of these materials. Water molecules avoid the hydrophobic areas of the surface, preferably adsorbing on the hydrophilic centres. Iron(III) trimesate MOFs have polar sites due to the metal oxygen clusters and non-polar regions due to the organic aromatic linkers, which represent the major fraction of the inner surface. The filling of the mesopores then takes place, by filling of the smaller 25 Å pores followed by the larger 29 Å pores. Adsorption of water molecules eventually occurs in the inter particulate voids of the powder. This phenomenon has been clarified by Stefan Kaskel et al. on the basis of the so-called "bridging effect" (Figure 1.19): after the formation of a monolayer of water molecules, additional water can be hydrogen-bonded to these water nucleation sites forming water clusters in the pores. Finally, pores result filled by water agglomerates with free voids between them.[48]

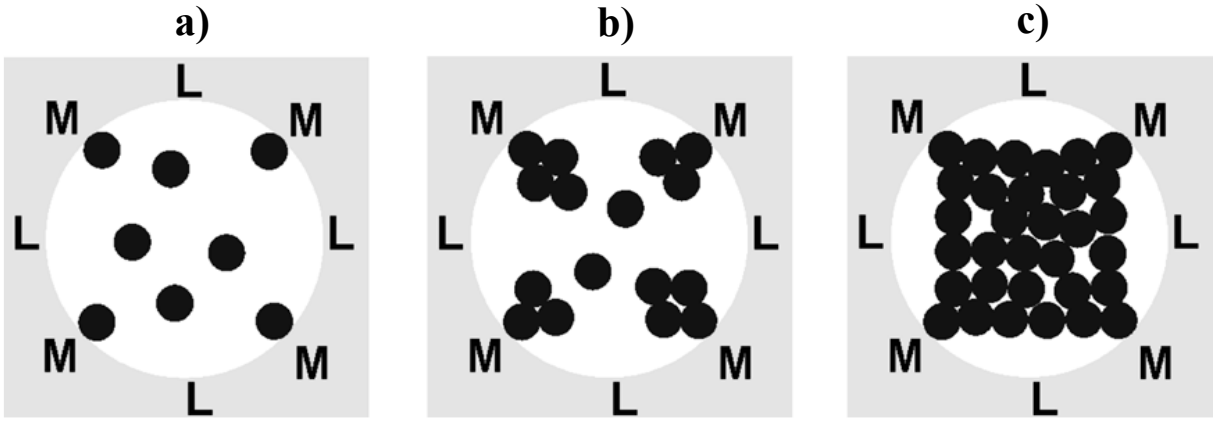

Figure 1.19. Bridging effect: (a) adsorption of single water molecules to the hydrophilic centres; (b) formation of water clusters via hydrogen bonds; (c) filled pore with free voids between the water agglomerates. L and M depict the organic linker and the metal cluster, respectively. Black dots represent the water molecules. Reprinted from [48]. Copyright 2009, with permission from Elsevier.

As promising material in water adsorption-related processes, iron trimesate has proven to be an efficient water vapor adsorbent dehumidification systems and water purification.[49,50] MIL-100(Fe) showed much higher water adsorption uptakes (up to 0.873 g H_2O per g dry adsorbent), compared to commercial adsorbents, such as SAPO-34 (0.330 g g^{-1}), NaX (0.336 g g^{-1}), and silica gel (0.327 g g^{-1}), and other representative MOFs (e.g., MOF-74, UiO-66-NH_2, and

HKUST-1).[51] Unlike the conventional porous materials which require a dehydration at high temperature before use, iron trimesate MOF need to be dehydrated at 30 °C. Recently, an efficient adsorption process based on iron trimesate MOF for water harvesting from air has been designed, contributing to address an actual global issue, that is water crisis.[52] In addition to a remarkable stability to water vapor at elevated temperatures, iron trimesate also remains stable in boiling water for up to 7 days.[49] Such an excellent stability arises from strong metal−ligand bonds given by the highly charged trivalent metals used to assemble the structure.[47]

In the context of drug delivery, the stability of iron(III) trimesate has been examined in the presence of various simulated physiological fluids for oral and intravenous administration.[53] Phosphate groups in PBS (PBS: phosphate buffered saline) have been found to replace the carboxylates from the MOF's structure, resulting in a progressive degradation of the material under intravenous conditions. A departure of the constitutive organic linkers occurs associated with an amorphization. It has also been highlighted that this degradation phenomenon is phosphate concentration-dependent since faster degradation of the material occurs at higher concentration of phosphates in PBS. Figure 1.20 presents a typical image of iron trimesate particles before (a) and after 8 days degradation in PBS (b). The morphology of particles changed with the appearance of a red-coloured core delimited by a grey shell.[54]

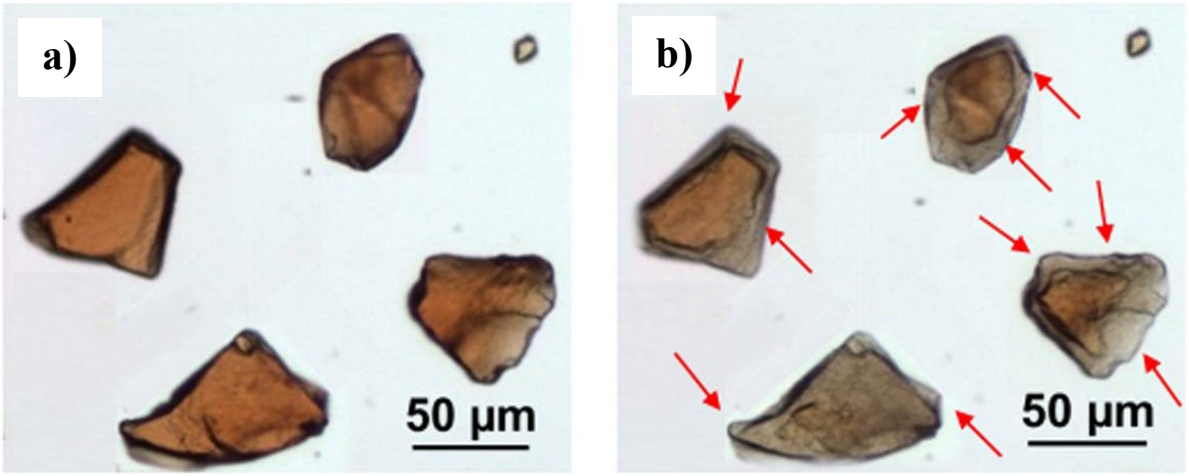

Figure 1.20. Images of iron trimesate observed by Raman-microscopy before (a) and after (b) degradation in PBS for 8 days. This picture is reproduced according to Ref. [54].

In order to overcome these drawbacks, several efforts have been done. For instance, the presence of BSA in the solution has been observed to lead to the formation of a protein corona, which decreases the degradation rate and improves the overall colloidal stability of the material under intravenous conditions by introducing steric hindrance.[53]

The degradation of the particles under gastric and intestinal conditions has proven to be comparable to that in PBS, with a gradual degradation up to 6 h reaching a plateau over 24 h. The presence of phosphates in intestinal conditions progressively replaces the carboxylic linkers, provoking the dissembling of the structure. Conversely, highly acidic conditions (pH 1.2) in gastric media favour the presence of soluble $Fe^{3+/2+}$ species as well as protonated linker, leading to a progressive structure degradation. However, it has been observed that in the presence of mucin, iron trimesate can interact with glycosylated proteins, promoting a degree of grafting to the intestinal mucosa after oral administration. Overall, iron trimesate displays an optimal stability for the first 6 h after immersion in simulated digestive media. A good stability for oral administration is ensured, considering the small bowel residence time (3.5−8 h).[53]

Thus, iron trimesates exhibit optimal stability during the first stages of incubation in both intravenous and oral conditions, demonstrating their potential in acting as drug nanocarriers. An efficient nontoxic nanocarrier material for drug delivery should meet requirements including high drug loadings, controllable drug release and matrix degradation. Because of their high surface areas and large mesoporous cavities, iron trimesate MOFs have been widely applied as drug-delivery systems.[55] It has been proven by Horcajada et al. that iron trimesate MOFs can efficiently act as nanocarriers for a variety of retroviral and antitumoral drugs (e.g., cidofovir, doxorubicin, azidothymidine, busulfan or triphosphate) against AIDS and cancer, respectively.[56] Drug entrapment efficiency was found to be larger than that of other existing carrier materials including MIL-53 and MIL-89 MOFs, demonstrating that iron trimesates could act like sponges through the encapsulation of drugs with various functional groups, polarities, and sizes. The *in vivo* acute toxicity of high doses of iron trimesate nanoparticles (NPs) have been intravenously investigated by evaluating their distribution, metabolism and excretion in rats.[57] The rats kept alive without any toxicity effect for 7 days after intravenous administration. It has been found that, such NPs are rapidly sequestered by the liver and spleen, and further biodegraded into their constitutive components (i.e., organic linkers and metal subunits), which could be directly eliminated in urine and/or faeces without metabolization and substantial toxicity. The controllable release of drugs from iron trimesate was exploited by Simon-Yarza et al.[58] The anticancer compound gemcitabine monophosphate (GMP) was

chosen to be encapsulated into the MOF for lung targeting. The colloidal suspension of this nanocarrier remained stable in the blood at pH < 6.5, while forming aggregates at pH > 6.5. Then the aggregates disaggregated releasing the drug molecules within the lung tissue. The controllable release of drugs could be also achieved through the degradation of the framework due to the high content of hydrogen peroxide at the site of infection caused by the bacteria.[59] A functionalisation approach of an iron trimesate MOF through the external surface covalent attachment of functional polymers has been reported.[60] Amino-polyethylene glycol (PEG5000) and Stp10-C were chosen as representative compounds due to their potential applications in multimodal imaging and biomedicine. The resulting functionalised iron trimesate NPs showed optimal chemical and colloidal stability in aqueous environments. The *in vivo* visualisation of functionalised NPs allowed to evaluate their distribution and accumulation. Moreover, such NPs displayed high uptake by cells without cytotoxicity even at high concentrations for more than 24 h.

1.2.3. Intrinsic peroxidase-like activity

Several non-protein materials have been found to possess intrinsic peroxidase-like activity, exhibiting catalytic activity similar to that found in natural peroxidases. Intrinsic peroxidase-like activity of MIL-100(Fe) has been reported for the first time by Zhang et al. in 2014. The optimal pH range was found to be 2.5 – 5.0 and the best temperature range was 35 – 55 °C.[61] Along with MIL-100(Fe), also disordered Fe-BTC material shows an intrinsic peroxidase-like activity.[62] Furthermore, peroxidase mimics include Fe-based MIL-53,[63] MIL-88(Fe),[64] and MIL-101(Fe) MOFs,[65] as well as Fe_3O_4,[66] Au nanoparticles,[67] Ce nanoparticles,[68] graphene oxide,[69] carbon nanotubes,[70] and carbon nanodots.[71]

It has been proposed that peroxidase mimic activity of MIL-100(Fe) originates from its catalytic activation of H_2O_2 through electron transfer, which leads to ·OH radicals, by a Fenton-like reaction.[72] Unlike Fenton reaction, which involves Fe^{2+} ions and hydrogen peroxide, a Fenton-like reaction is the reaction of hydrogen peroxide with Fe^{3+} ions, as shown in Eqs.(1) – (4).[73]

$$Fe^{3+} + H_2O_2 \rightleftarrows Fe \cdots OOH^{2+} + H^+ \quad (1)$$

$$Fe \cdots OOH^{2+} \longrightarrow HO_2 \cdot + Fe^{2+} \quad (2)$$

$$Fe^{2+} + H_2O_2 \longrightarrow OH \cdot + OH^- + Fe^{3+} \quad (3)$$

$$OH \cdot + RH \longrightarrow R \cdot + H_2O \quad (4)$$

The resulting ·OH radicals can react with chromogenic dyes, such as *o*-phenylenediamine (OPD), 2,2′-azino-bis(3-ethylbenzothiazoline-6-sulfonic acid) diammonium salt (ABTS), or 3,3',5,5'-tetramethylbenzidine (TMB), producing a colour change in the reaction.

Enzyme mimics have received the most attention over the past decade, since they overcome the drawbacks of using enzymes.[74] Indeed, enzymes easily get denatured upon heating or chemical changes. Moreover, their isolation, purification, and storage are relatively expensive and time-consuming.[75]

An archetypical example of peroxidase is given by horseradish peroxidase, also called, hydrogen peroxide oxidoreductase or HRP (EC Number: 1.11.1.7). It is a predominantly α-helical single-chain glycoprotein of 44 kDa containing four disulfide bridges and 18% carbohydrate (Figure 1.21). HRP, isolated from the roots of horseradish (*Amoracia rusticana*), belongs to the ferroprotoporphyrin group of peroxidases.[76]

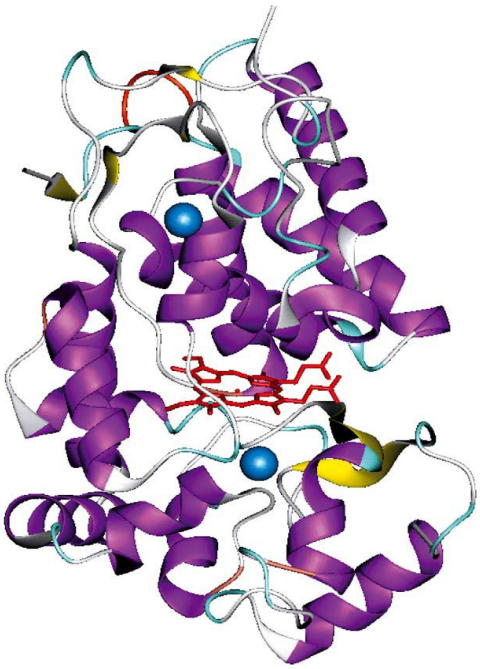

Figure 1.21. Three-dimensional representation of the horseradish peroxidase isoenzyme C (Brookhaven accession code 1H5A). The heme group (red) is located between the distal and proximal domains, containing one calcium atom (blue) for each domain. α-helical and β-sheet regions of the enzyme are coloured in purple and yellow, respectively. Reprinted from [76]. Copyright 2004, with permission from Elsevier.

HRP can combine with hydrogen peroxide (H_2O_2) and the resultant [HRP-H_2O_2] complex readily oxidises a wide range of hydrogen donors. Peroxidase reaction can be simply summarised by the following equation:[77]

$$2RH + H_2O_2 \rightarrow 2R\cdot + 2H_2O$$

Peroxidase mimics possess great potential in many fields, including catalysis, and sensing for the detection of hydrogen peroxide, ascorbic acid, and other peroxidase substrates.[61,62,64] Sensors are analytical devices that estimate the chemical response of a chemical reaction, by producing a signal as a function of the concentration of an analyte in the chemical reaction. They are applied into a wide range of fields, ranging from food and environment safety (pollutant detection, microorganism identification, etc.) to biomedicine (disease monitoring, drug discovery, etc.). Iron(III) trimesate MOFs have been extensively employed in biosensing.[55] Patra et al. have developed a bioelectrode for glucose detection combining MIL-100(Fe) with platinum nanoparticles (Pt-NPs) as immobilisation matrix for glucose oxidase enzyme (GOx). The biosensor was prepared through the step-by-step deposition of each component at the surface of the carbon ink electrodes (CIE). It exhibited interesting results in terms of sensitivity, response time, reproducibility, and time stability. After one week of storage, the bioelectrode retained 96% of its original response, and after 21 days it retained 90% under wet and 78% under dry conditions. Electrochemical biosensor prepared with MIL-100(Fe) was also compared to bioelectrodes containing other MIL-100 MOFs, such as aluminium and chromium-based ones. MIL-100(Fe)-based biosensors showed advantages in terms of limit of detection, linear concentration range, detection time, and sensitivity over the other MOFs. This behaviour was explained by the synergetic of the intrinsic peroxidase-like activity of iron trimesate MOF and catalytic activity of GOx. The enzyme mimic iron trimesate catalysed the decomposition of H_2O_2, the main product of glucose oxidation by GOx, by a Fenton-like reaction.[78] Iron trimesate MOFs have been also studied for colorimetric biosensing. Colorimetric sensors became very popular and widespread in recent years. They are a class of optical sensors that provides a colour-change when influenced by external stimuli. Unlike electrochemical sensors, they possess higher accessibility and ease of use, lower costs and more sensitive and selective responses toward various analytes.[79] Zhang et al. exploited the peroxidase mimic activity of iron trimesate MOF for a colorimetric method to quantitatively determine hydrogen peroxide.[61] In the presence of H_2O_2, iron trimesate produces ·OH radicals which can oxidise 3,3′,5,5′-tetramethylbenzidine (TMB), a chromogenic substrate molecule, simultaneously giving rise to the blue-coloured oxidised TMB (oxTMB). oxTMB gives intense

characteristic absorbance peaks at 370 and 652 nm in the UV-vis spectra, accounting for the blue colour of the solution. Since the absorbance of oxTMB is dependent on the concentration of H_2O_2 in the solution, this method has been used for the quantitative evaluation of hydrogen peroxide.

1.2.4. Coordinatively unsaturated metal sites (CUS)

The existence of metal sites surrounded by labile ligands that can be eliminated to create a coordinatively unsaturated site (also called open-metal sites or CUS) is of great interest in MOFs' research. The existence of CUS can strongly modify interactions with gases or liquid adsorbates, playing a key role in gas storage and separations. Moreover, since CUS act as Lewis acid sites, they have been tested for their efficacy in a broad range of Lewis acid-catalysed reactions, proving exceptional chemical turnovers while maintaining the structural integrity of the porous material.[80]

In 2010 Gérard Férey et al. have demonstrated that a controlled and partial reduction of Fe^{3+} to Fe^{2+} sites in MIL-100 structure upon heating under vacuum gives rise to open-metal sites. These CUS exhibit strong interactions with unsaturated molecules, such as propylene, CO and NO, through π-back donation, consisting in the donation of an electron from the partially filled d orbital of the metal to the antibonding orbital of the unsaturated adsorptive.[81] It has been shown that an activation of the material at a temperature T > 150 °C under vacuum leads to the departure from the framework of terminal water molecules coordinated to iron, giving rise to a large number of Fe^{3+} CUS. Conversely, the activation under vacuum at a temperature 150 °C < T < 250 °C, further leads to the creation of Fe^{2+} CUS, which is not due to the direct reduction of Fe^{3+} sites but rather to the departure of the anionic ligand (F^- and OH^-) (Figure 1.22).

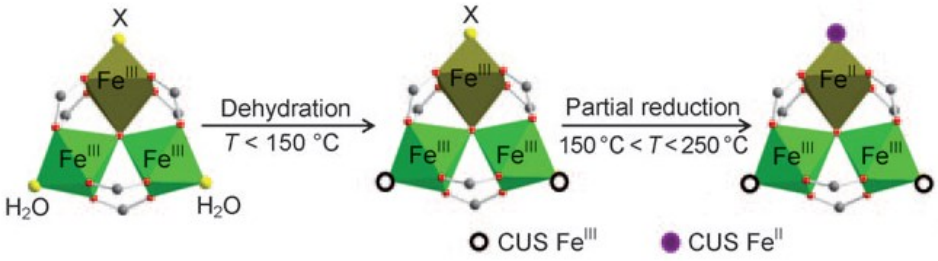

Figure 1.22. Formation of Fe^{3+} and Fe^{2+} CUS in an octahedral iron trimer of MIL-100(Fe) by dehydration and partial reduction. Reprinted from [81]. Copyright 2010, with permission from John Wiley & Sons.

Fe^{3+} CUS showed better adsorption capacity of propylene compared to propane while Fe^{2+} CUS showed higher performance on CO adsorption than CO_2 adsorption due to the different metal-gas interaction.[80] Therefore, different amounts of Fe^{3+} and Fe^{2+} CUS, easily tunable by exploiting a variety of activation conditions, lead to gas adsorbents with different selectivity.

The multivalent nature of the MIL-100, given by the compresence of Fe^{2+} and Fe^{3+} unsaturated metal sites, makes iron trimesate materials promising gases adsorbents with high adsorption selectivity. Finding suitable porous materials for gas adsorption and separation in industry can be very challenging. Besides activated carbons, silica gels, zeolites and polymers, MOFs represents interesting candidates for industrial adsorption and separation processes due to their high thermal and chemical stability and high specific surface areas.[24] Iron trimesates have been found to show good performances in gas adsorption and separation. Recently, an iron trimesate MOF has been employed to prepare polylactic acid (PLA) mixed matrix membranes, which were used in the pervaporation process for the separation of ethanol/methyl tert-butyl-ether mixtures at the azeotropic point.[82]

1.2.6. Synthesis methods

1.2.6.1. Green Chemistry principles

Before examining in detail the different synthesis approaches reported for the preparation of iron(III) trimesate MOFs, a briefly discussion on green chemistry is necessary. Green chemistry is defined as the "design of chemical products and processes to reduce or eliminate the use and generation of hazardous substances".[83] Since this concept was proposed, several governmental programs and initiative on green chemistry have been introduced around the world.[84] The main green chemistry's aim is to achieve sustainability. This is also in agreement with the current 2030 Agenda for Sustainable Development, adopted by all United Nations Member States in 2015, which is based on 17 Sustainable Development Goals for peace and prosperity for people and the planet, now and into the future (Figure 1.23).[85]

Figure 1.23. The 17 Sustainable Development Goals.[85]

Given its sustainability purposes, it is not surprising that green chemistry has been applied to a large range of industry fields, from automobile, aerospace, electronics, energy, household, cosmetic products, pharmaceutical, to agriculture and so on.[86] Green chemistry criteria can be summarised into the Twelve Principles of Green Chemistry (Figure 1.24), introduced in 1998 by John Warner and Paul Anastas,[83] as follow:

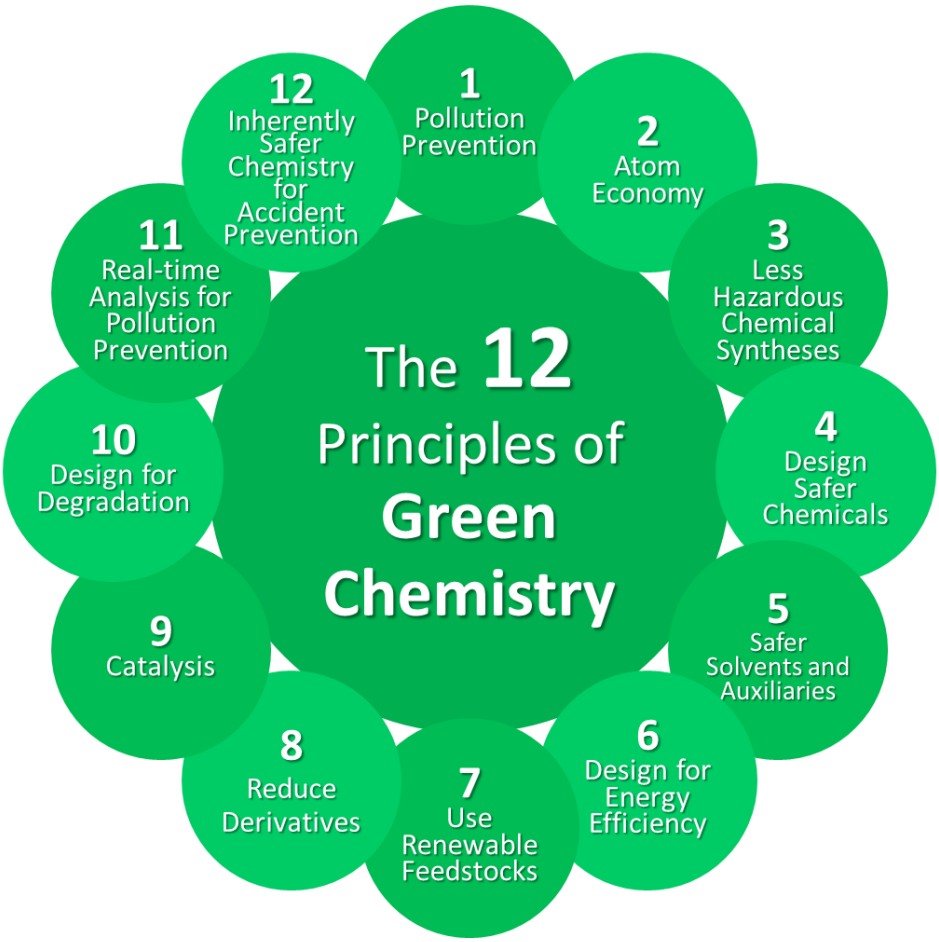

Figure 1.24. The 12 principles of green chemistry.

1. ***Prevention.*** "It is better to prevent waste than to treat or clean up waste after it is formed".[86] In order to define the environmental acceptability of a manufacturing process, the concept of E-Factor has been proposed to quantify the amount of waste produced per kg of product.[87]

2. ***Atom Economy.*** "Synthetic methods should be designed to maximise the incorporation of all materials used in the process into final product".[86]

3. ***Less Hazardous Chemical Synthesis.*** "Whenever practicable, synthetic methodologies should be designed to use and generate substances that pose little or no toxicity to human health and the environment".[86]

4. ***Designing Safer Chemicals.*** "Chemical products should be designed to preserve efficacy of the function while reducing toxicity".[86]

5. ***Safer Solvents and Auxiliaries.*** "The use of auxiliary substances (e.g., solvents, separation agents, etc.) should be made unnecessary whenever possible and, when used,

innocuous".[86] Where possible, the use of any solvent should be avoided because including an auxiliary inevitably implies energy and efforts to remove it from a designated system. Hence, the ideal situation would be devoted to developing solventless systems.

6. Design for Energy Efficiency. "Energy requirements of chemical processes should be recognised for their environmental and economic impacts and should be minimised. If possible, synthetic methods should be conducted at ambient temperature and pressure".[86]

7. Use of Renewable Feedstocks. "A raw material or feedstock should be renewable rather than depleting whenever technically and economically practicable".[86]

8. Reduce Derivatives. "Unnecessary derivatisation (use of blocking groups, protection/deprotection, temporary modification of physicochemical processes) should be minimised or avoided, if possible, because such steps require additional reagents and can generate waste".[86]

9. Catalysis. "Catalytic reagents (as selective as possible) are superior to stoichiometric reagents".[86]

10. Design for Degradation. "Chemical products should be designed so that at the end of their function they break down into innocuous degradation products and do not persist in the environment".[86]

11. Real-Time Analysis for Pollution Prevention. "Analytical methodologies need to be further developed to allow for real-time, in-process monitoring and control prior to the formation of hazardous substances".[86]

12. Inherently safer Chemistry for Accident Prevention. "Substances and the form of a substance used in a chemical process should be chosen to minimise the potential for chemical accidents, including releases, explosions, and fires".[86]

Given the above-illustrated discussion, synthesis method can be divided into traditional (or conventional), and alternative methods. The former does not strictly follow green chemistry criteria, mainly due to harsh synthesis conditions, use of large amounts of solvents and hazardous chemicals, and long reaction times. Conversely, the latter has been developed in agreement with green chemistry principles, characterised by mild reaction conditions, short reaction times, use of safe chemicals and little amounts of solvents.

1.2.6.2. Conventional methods

MIL-100(Fe) was synthesised for the first time by Horcajada et al. in 2007 via hydrothermal method.[30] Metallic iron, trimesic acid (H_3BTC), hydrofluoric acid (HF), nitric acid (HNO_3) and water (reaction mixture of composition 1.0 Fe^0 : 0.66 H_3BTC : 2.0 HF : 1.2 HNO_3 : 280 H_2O) were placed into a Teflon-coated autoclave and held at 150 °C for 6 days with an initial heating ramp of 12 h and a final cooling ramp of 24 h (Figure 1.25). The pH remained acid (< 1) during the synthesis. After being recovered by filtration, the resulting orange solid was washed with deionised water. In order to decrease the amount of residual trimesic acid, the sample was treated in hot deionised water (80 °C) for 3 h. Finally, the sample was dried at RT. This synthesis protocol yielded a highly crystalline material using HF as efficient mineralizing agent. However, HF is corrosive and difficult to handle. In addition, the requirement of long reaction time, high pressure and temperature, and acidic pH did not address green chemistry criteria, leading to the need for more eco-compatible routes to prepare the material.

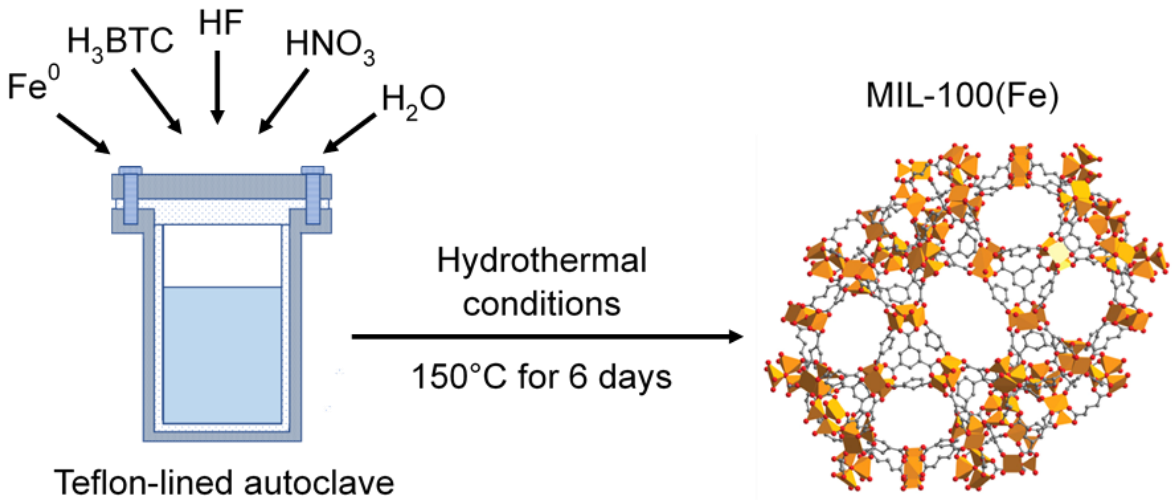

Figure 1.25. Schematic representation of hydrothermal synthesis of MIL-100(Fe). The picture of MIL-100(Fe) structure is reprinted with permission from [88]. Copyright 2018 American Chemical Society.

In the context of hydrothermal methods, many efforts have been done by Canioni et al., developing a HF-free-synthesis of MIL-100(Fe) without compromising the obtainment of a crystalline pure material.[89] $FeCl_3 \cdot 6H_2O$ and trimethyl 1,3,5-benzenetricarboxylate were dispersed in 5 mL of water and heated at 130 °C for three days in a Teflon-lined autoclave. Then, the orange solid, recovered by filtration, and washed with acetone, is finally dried under air. This new route provided many advantages in comparison to the previously reported method, since it required shorter reaction times (3 days vs 6 days), it avoided the use of corrosive acids HF and HNO_3. Moreover, the use of trimethyl 1,3,5-benzenetricarboxylate instead of 1,3,5-

benzenetricarboxylic allowed a better control of the reaction kinetics, since the slow hydrolysis of ester moieties helped leading to a well crystalline solid. Based on this protocol, García Márquez et al. developed a microwave-assisted synthesis of MIL-100(Fe) which gave rise to a nanometric solid.[90]

A large-scale hydrothermal synthesis of a HF-free MIL-100(Fe) was developed by Seo et al. in 2012.[91] After dissolving $Fe(NO_3)_3 \cdot 9H_2O$ in water, trimesic acid was added, stirring at RT for 1 h. The resulting reactant mixture was loaded in a Teflon-lined autoclave and heated at 160 °C for 12 h. After the hydrothermal reaction, the orange solid was recovered by filtration and washed with deionised water. Then, the as-synthesised MIL-100(Fe) was purified by a two-step process: (i) double solvent extraction with hot water and ethanol; (ii) chemical treatment with an aqueous solution of NH_4F. The sample was finally air-dried at less than 100 °C. The synthesis was also conducted by using different iron precursors (e.g., metallic iron or iron chloride), always leading to lower porosity and product yield compared to iron nitrate. Despite the improvements compared to the first synthesis of MIL-100(Fe) by Horcajada et al., the synthesis still suffered of requiring acidic conditions, high temperature and pressure, long reaction times (including time-consuming purification steps), as well as the use large amounts of solvents (the reactor volume was up to 10 L). These harsh conditions are not eco-friendly and raise the costs of the overall process, which is not desirable in the context of an efficient industrial production.

In 2015 Sanchez-Sanchez et al. partially overcame such drawbacks proposing a batch-based method for the preparation of an iron(III) trimesate MOF under atmospheric pressure at room temperature.[37] They did not obtain a crystalline MIL-100(Fe) but its disordered analogous Fe-BTC. For a typical synthesis (Figure 1.26) two solutions are prepared. The first one was obtained by dissolving trimesic acid in a NaOH aqueous solution. The second solution was prepared by dissolving of $FeCl_3 \cdot 6H_2O$ in water. The latter solution was added dropwise over the former under stirring, immediately generating a brownish orange solid. The resultant suspension (pH = 2.1) was maintained under magnetic stirring at RT for 10 minutes. The molar ratio of the mixture was 1.5 Fe : 1.0 H_3BTC : 3.0 NaOH : 880 H_2O. After being recovered by centrifugation, the solid was washed with deionised water and ethanol, and finally dried at room temperature. This synthesis strategy avoided the use of high temperature and pressure and required short reaction times. However, the pH remained acidic throughout the synthesis, despite the use of NaOH, which is also irritating and strongly corrosive. In addition, the

formation of a brownish orange solid upon dropwise mixing the solutions revealed a lack of homogeneity within the reaction mixture.

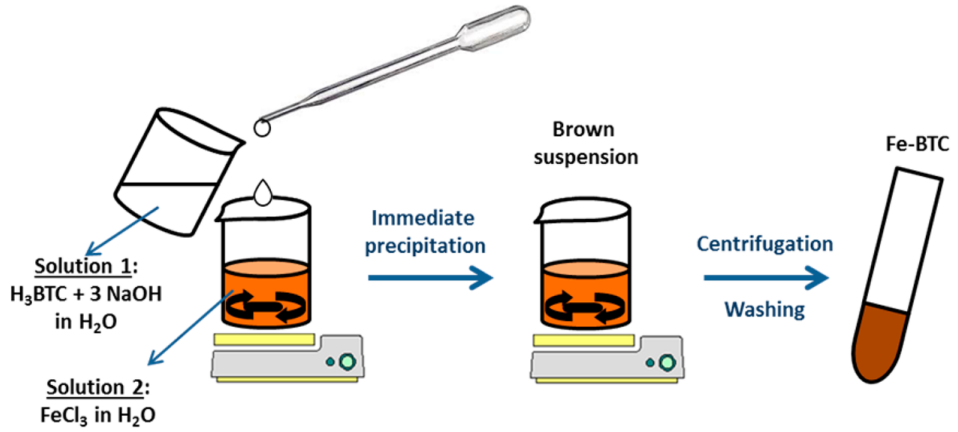

Figure 1.26. Schematic representation of a solution-based synthesis of Fe-BTC. Reprinted with permission from [38]. Copyright 2017 American Chemical Society.

Based on this synthesis, further research led Sanchez-Sanchez's group to develop a solution-based preparation of crystalline MIL-100(Fe) (Figure 1.27). The only distinctions compared to the previous protocol were the use of an iron(II) source, $FeCl_2 \cdot 4H_2O$ in place of $FeCl_3 \cdot 6H_2O$, and a longer reaction time (24 hours vs 10 minutes). The pH of the suspension after adding dropwise the NaOH aqueous solution of trimesic acid into the iron(II) chloride solution was around 5.2. However, long reaction times, in addition to the use of corrosive NaOH, are still not feasible for a sustainable industrial scale-up of the synthesis.

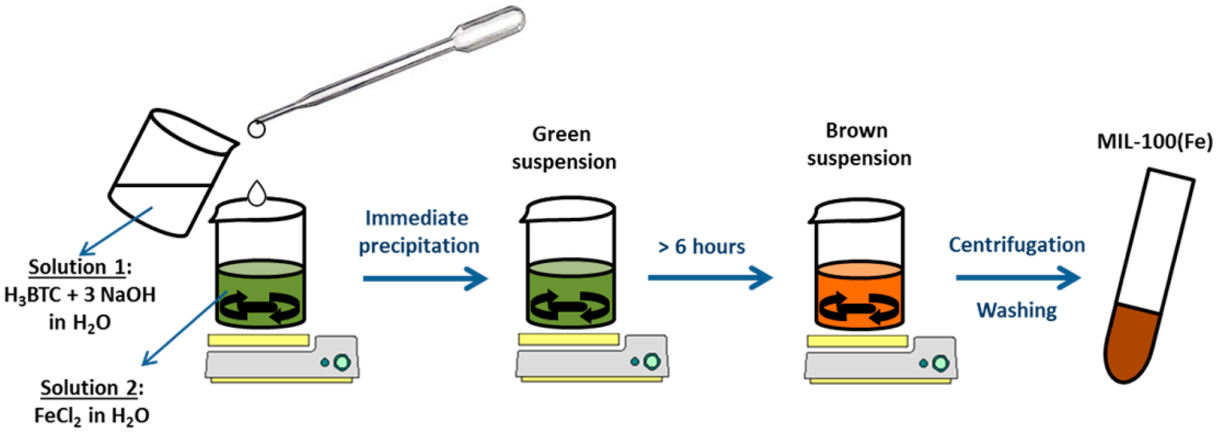

Figure 1.27. Schematic representation of a solution-based synthesis of MIL-100(Fe). Reprinted with permission from [38]. Copyright 2017 American Chemical Society.

1.2.6.3. Alternative methods

In order to overcome the disadvantages of conventional synthesis methods, greener and milder synthetic conditions have been attained by employing alternative methods. In the following section, alternative synthesis routes of iron(III) trimesate based on electrochemical, sonochemical and mechanochemical methods are described.

Electrochemical method

Commercially available Fe-BTC MOF is produced as Basolite®F300 by BASF/Aldrich via electrochemical approach.[92] Electrochemical synthesis uses the anode oxidation under an applied electric field for supplying metal ions to the reaction solution, which also contains dissolved ligand molecules and an electrolyte. The as-synthesised samples are then washed and dried (Figure 1.28).[93]

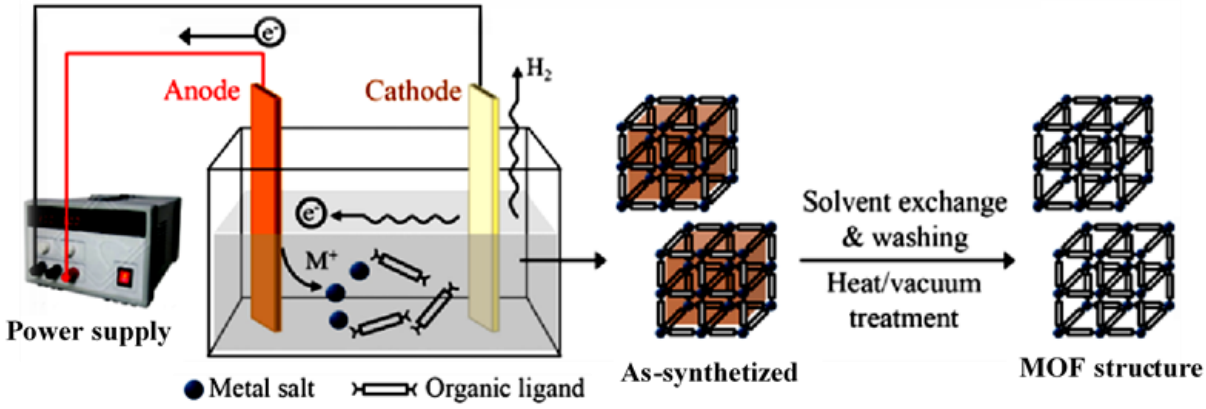

Figure 1.28. Schematic representation of an electrochemical synthesis of MOFs. Reprinted from [94]. Copyright 2013, with permission from Springer Nature.

The synthetic parameters, which can be modulated, include solvent, voltage, electrolyte, and synthesis temperature. The metal deposition on the cathode is avoided by using protic solvents, and H_2 is formed in the process. This method can be performed at atmospheric pressure and room temperature, and it is significantly fast and cost-efficient for MOFs' production. Moreover, it is feasible for industrial scale-up since it provides high yields coupled with short fabrication times under milder conditions compared to conventional batch reactions. Another advantage of the electrochemical route for industrial applications is the possibility to run a continuous process. It gives high levels of purity, since it avoids the reaction between anions and metal in a salt solution.[95] However, only a few MOFs can be prepared using electrochemical method. BASF researchers has so far achieved the electrochemical synthesis

of 5 types of MOFs, namely Basolite®F300 (Fe-BTC), Basolite®Z1200 (ZIF-8), Basolite®Z377 (MOF-177), Basolite®C300 (HKUST-1), and Basolite®A100 (MIL-53(Al).[96] One of the main disadvantages of this method is the inferior quality of MOFs compared to other techniques. Schlesinger et al. synthesised HKUST-1 using both electrochemical and solvothermal routes, investigating the effect of synthesis procedures on its properties. It has been found that the electrochemically-prepared product possessed lower quality because of the salt's conduction and/or the linker's inclusion in the pores during crystallisation.[97]

Sonochemical method

The sonochemical method is based on the irradiation of reaction solution with high frequencies ultrasonic waves (20 kHz – 10 MHz). The use of ultrasounds (US) for material synthesis has been extensively exploited over many years, becoming one of the most powerful tools to synthesise nanostructured materials.[98] Starting in 2008, it was also applied for the synthesis of MOFs, representing a fast, facile, energy-efficient, environmentally friendly, room temperature method.[99] This is of main interest for industrial scale-up of MOFs' synthesis. In addition, nanocrystalline particles, which are often obtained by sonochemical syntheses, establish further advantage for their application.[95] Compared to other energy sources (e.g., heat, radiations, electric potential, etc.), ultrasonic irradiations provides short durations of extremely high pressures and temperatures in liquids, which cannot be achieved by other methods.[100] Interestingly, these unique reaction conditions do not arise directly from US itself. Indeed, acoustic wavelengths are much larger than molecular dimensions. Therefore, no direct, molecular level interaction between the chemical species and ultrasound could take place. Several theories have been proposed to explain how sonic radiation with frequency ranging from 20 kHz to 10 MHz could break chemical bonds. They all agree that the main event accounting for the chemical effects of ultrasound is the formation, growth, and collapse of bubbles that are formed in the liquid.[101] This phenomenon, driven by high intensity ultrasounds, is called acoustic cavitation (Figure 1.29). When liquids are irradiated with US, the alternating expansive and compressive acoustic waves creates cyclic alternating areas of compression (high pressure) and rarefaction (low pressure). In the rarefaction regions, the pressure drops below the vapor pressure of the solvent and small bubbles (i.e., cavities) are formed. The resulting bubbles starting to oscillate because of the alternating pressure. The oscillating bubbles can accumulate ultrasonic energy while growing to a certain size (typically tens of μm) through the diffusion of solute vapor into the volume of the bubble. Once the

bubbles reach their maximum size, they become unstable and subsequently collapse, releasing the stored energy within a very short time (heating and cooling rates > 10^{10} K s^{-1}). This cavitation implosion is very localised and transient, giving rise to hot spots with a temperature of ca. 5000 K and a pressure of ca. 1000 bar.[100] Such a fast kinetics prompt by US results in accelerated and homogeneous nucleation. However, it does not permit the growth of the nuclei, since in each collapsing bubble a few nucleation centres are formed but their growth is limited by the short collapse. Subsequently, despite varying in size, shape, structure, and solid phase (amorphous or crystalline), this process gives rise to nanometric particles and reduced crystallisation times compared with other synthesis techniques.[92]

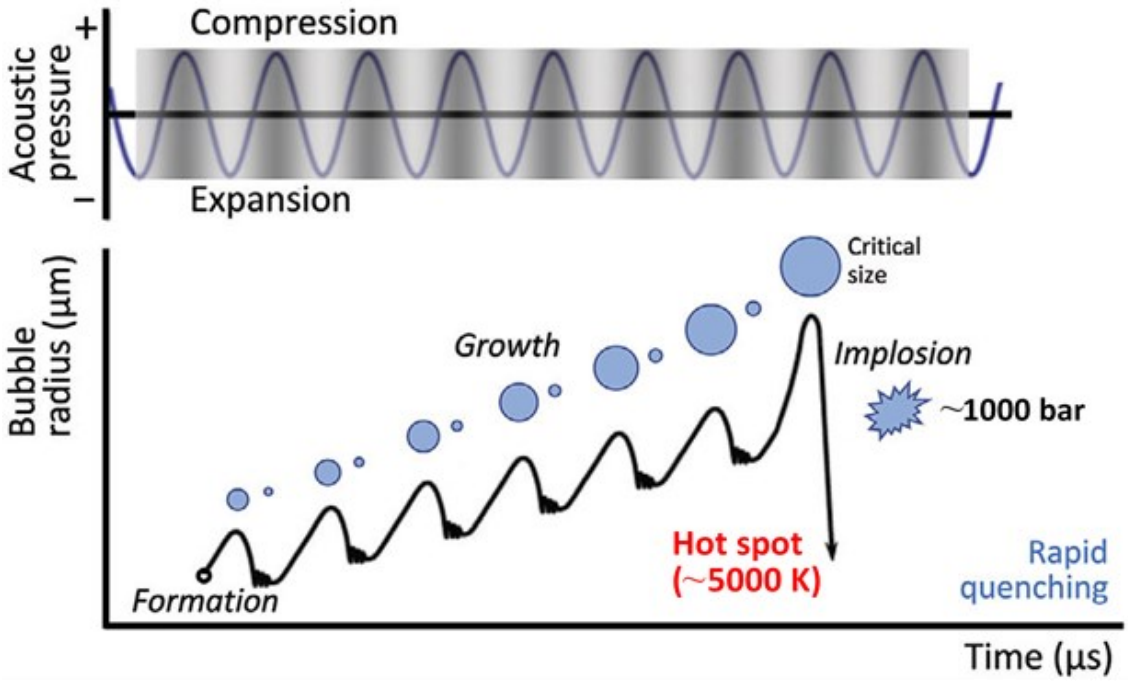

Figure 1.29. Schematic representation of transient acoustic cavitation. Reproduced with permission from [98]. Copyright 2013, Royal Society of Chemistry.

Sonochemical process variables and apparatuses

Cavitation occurs over a very wide range of frequencies (20 kHz – 10 MHz). At higher frequencies the intrinsic viscosity of liquids prevents cavitation phenomenon. In general, cavitational heating of collapsing bubbles occurs at higher frequencies, whereas physical effects of ultrasounds (e.g., surface damage and emulsification) are more dominant at lower frequencies.[100] The formation of cavities and the intensity of their collapse is governed by a wide range of parameters: acoustic frequency and intensity, which depend on the equipment used, temperature, gas atmosphere, and vapor pressure, viscosity, and chemical reactivity of the liquid. Volatile organic solvents are not optimal media for sonochemical reactions since the

high vapor pressure reduces the intensity of bubbles collapse and thus the resulting temperatures and pressures.[95]

The source of the US irradiation is a piezoelectric material, such as ceramic (PZT), lead–zirconate–titanate or quartz. It is subjected to high-voltage alternating current with an ultrasonic frequency, expanding and contracting in this electric field and converting electrical energy into sound energy.[102]

A variety of sonochemical apparatuses are commercially available, including ultrasonic cleaning baths, flow reactors, and direct-immersion ultrasonic horns. Most cleaning baths (Figure 1.30) operate near 40 kHz. Commonly, they have insufficient intensity for most applications. However, they are useful for liquid-solid reactions with reactive and easily passivated solids (e.g., Li, Mg).[100]

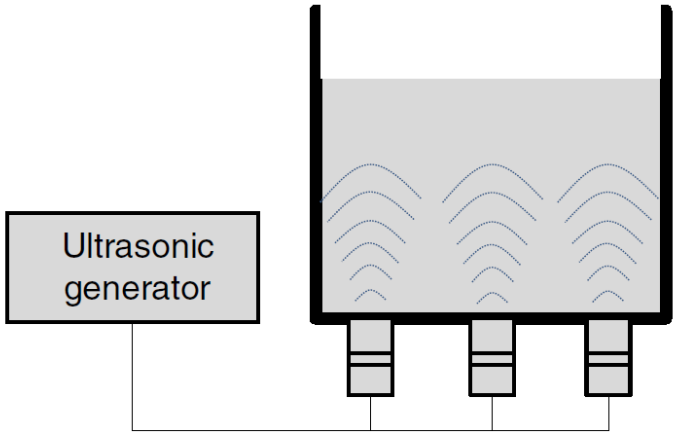

Figure 1.30. Schematic representation of transient acoustic cavitation. Reprinted from [103], Copyright 2015, with permission from Elsevier.

In a typical laboratory-scale sonochemical apparatus (Figure 1.31) a high-intensity ultrasonic titanium horn, driven by a piezoelectric transducer, is directly introduced into a thermostatic glass reactor. Commonly, high intensity ultrasonic horns operate at 20 or 40 kHz.

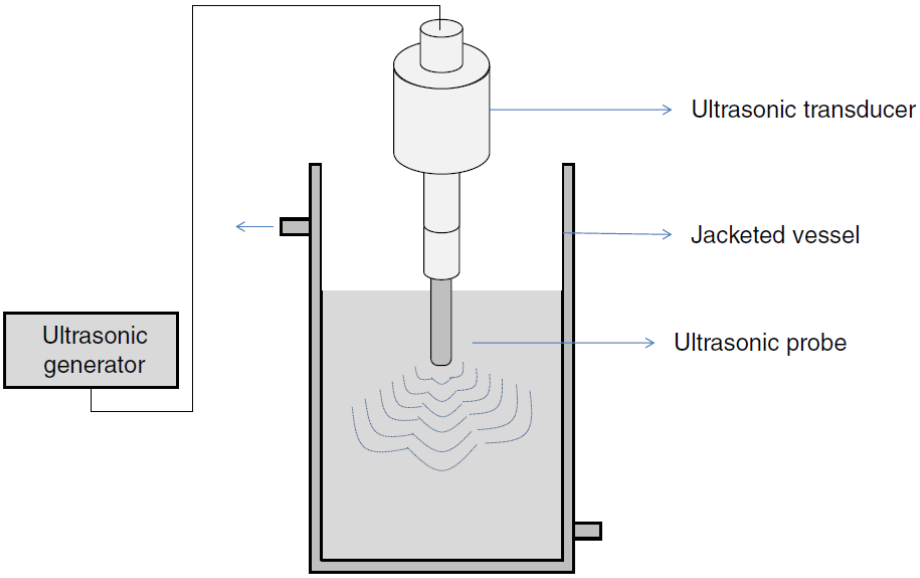

Figure 1.31. Schematic representation of transient acoustic cavitation. Reprinted from [103], Copyright 2015, with permission from Elsevier.

Sonochemical reactions can be carried out continuously through flow reactors (Figure 1.32), which are highly feasible for industrial scale-up.[104]

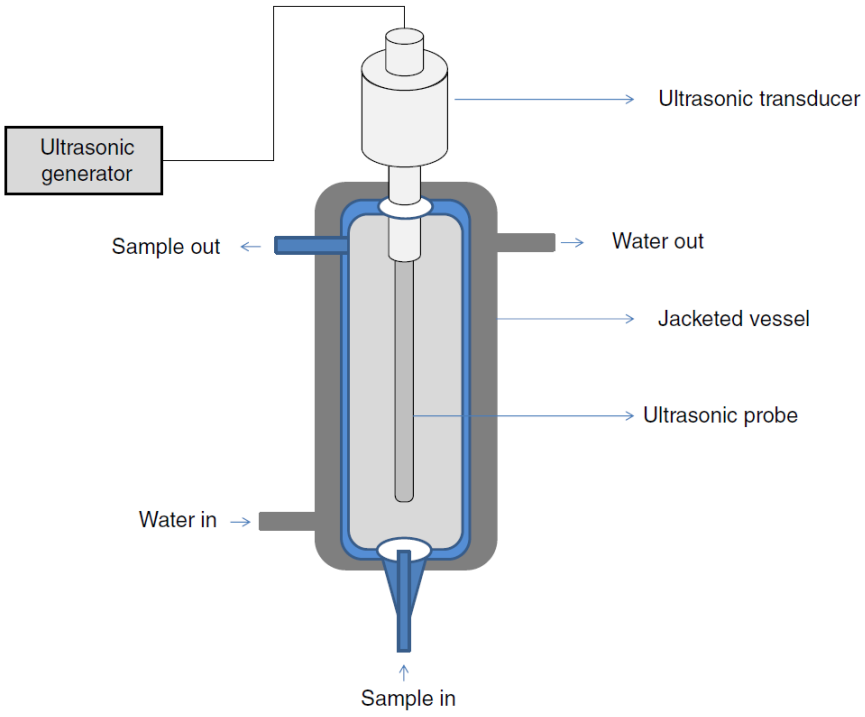

Figure 1.32. Scheme of the continuous flow ultrasonic reactor. Reprinted from [103], Copyright 2015, with permission from Elsevier.

Mechanochemical method

According to the International Union of Pure and Applied Chemistry (IUPAC), a mechanochemical reaction is defined as a "chemical reaction that is induced by the direct absorption of mechanical energy".[105] Mechanical energy can be imparted into the system through a variety of mechanical treatments, including compression, impact, grinding, stretching, and shearing. Besides reactions initiated by mechanical actions, this definition of mechanochemical reaction includes reactions involving reagents pre-treated by mechanically activation.[106] The mechanical action can reduce particle size, create active sites for chemical reactivity, and generate (and/or increase) active surfaces of substances which can more efficiently contact, coalesce and react.[107] Mechanochemistry is widely adopted in a range of areas such as pharmaceutical, organic and inorganic chemistry, polymer science, etc.[108] The first mechanochemical synthesis of MOFs was reported in 2006 by James et al.[109] The interest in mechanochemical synthesis of MOFs is mostly due to the opportunity to carry out reactions at room temperature, minimising, or completely avoiding, the use of solvents throughout synthetic routes, from laboratory-scale to large-scale set-ups. Solvent-free, or nearly solvent-free, synthetic routes are particularly advantageous in an age where the need to develop more eco-friendly chemical syntheses is remarkably demanding. Moreover, mechanochemical reactions can lead to quantitative yields in relatively short reaction times (normally in the range of 10 – 60 min), and products containing small particles are generally obtained.[95]

Mechanochemical tools and equipment

The most ubiquitous and easy-to-use mechanochemical tool is the traditional mortar and pestle (Figure 1.33). However, manual grinding is affected by variable factors, both human and environmental. First, the manual force applied is inevitably variable between individuals and over time. In addition, variability of atmospheric conditions, such as ambient humidity, which differs in the seasons and latitudes, may negatively affect the reaction outcome, especially in the case of moisture- and/or air-sensitive reagents. Safety concerns should be also considered, especially when handling toxic or volatile compounds. Owing to these variables being very difficult to control, results obtained by mortar and pestle are often unreproducible.[110]

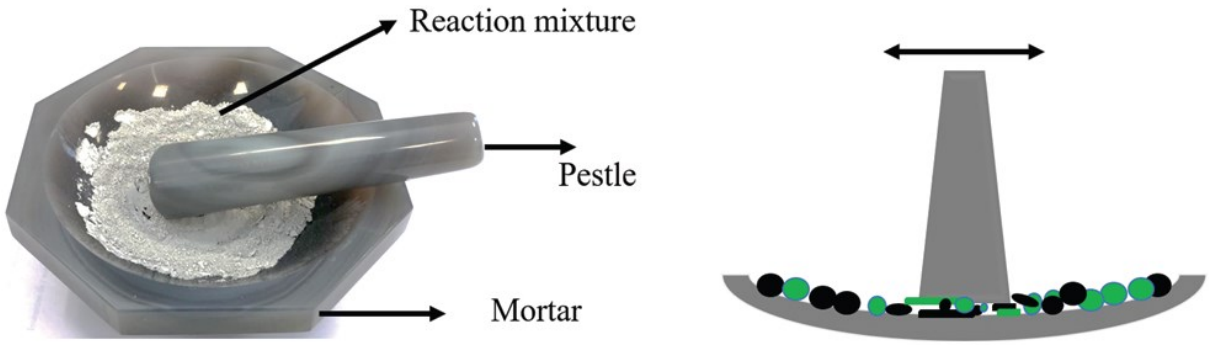

Figure 1.33. Traditional mortar and pestle to conduct manual grinding. Reproduced with permission from [111]. Copyright 2021, Royal Society of Chemistry.

Nowadays, laboratory-scale mechanochemical reactions are preferentially conducted using automatised grinders. Unlike mortar and pestle, they ensure more controlled conditions, homogeneous and intense grinding, also for prolonged reaction times (e.g., several hours) which are sometimes required to obtain very small particle sizes and/or amorphization of reagents. An archetypical example of automated grinder is represented by ball mills, which include a closed reaction vessel, called jar, containing balls. There are several types of ball mills commercially available, such as shaker or mixer mills, planetary and attritor mills.[112] Despite differing by the way in which the mechanical energy is imparted to the system, they are all based on a simple working principle, using the mechanical energy generated by impacting the reaction mixture with balls inside a closed jar. During the periodic motion of the mill, balls inside the reactor collide with each other, with the reactants and with the jar walls at a high velocity, exerting a mechanical loading to the processed powder particles.

Planetary and attritor ball mills are characterised by low compressive and high shear forces. In a planetary ball mill the jar movement is compared to the motion of spinning planets along their orbit around a sun (thus, the term planetary). Indeed, cylindrical jars spin around their main axis while rotating eccentrically about the sun wheel axis. Two forces (centrifugal and Coriolis forces) combine inside the vessels, leading to a disordered dynamic of milling balls involving frictional and impulsive processes of powders. A typical planetary mill consists of two or more jars that rotate around their axis (with angular velocity ω_d) installed on a disc (so-called solar wheel), which also rotates (generally in the opposite direction) with angular velocity ω_r. Depending on the relative speeds of these two rotation modes, this motion causes the balls to move around the surfaces of the walls (attrition mode) or jump across the vessel and impact against the sides (collision mode). Fritsch GmbH released one of the most common planetary

mills, which offers capacities between 12 and 500 mL, and rotational speeds up to 1100 rpm, giving rise to a centrifugal acceleration up to almost 100 times the Earth's gravity (Figure 1.34).

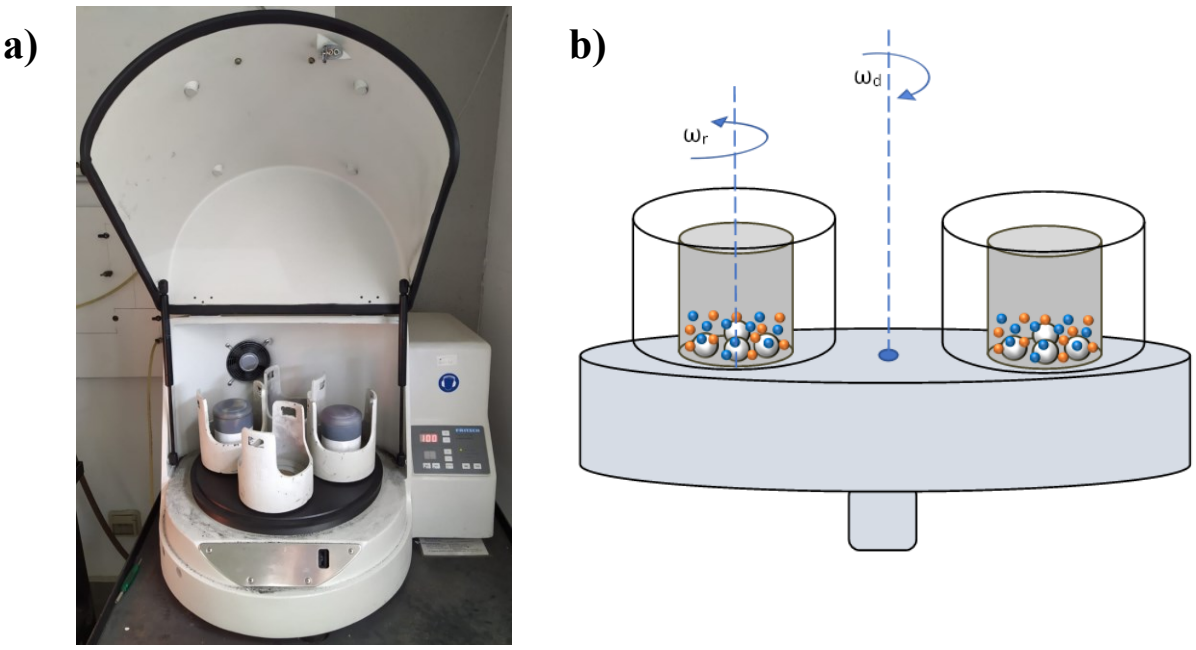

Figure 1.34. (a) A Fritsch-pulverisette 5 planetary ball mill. (b) Schematic representation of the movement of the balls inside the jar in a planetary mill.

Planetary systems with adapters holding multiple vessels (with capacities between 2 and 250 mL) and able to process up to 48 samples simultaneously are also commercially available. This multisampling approach is called parallel mechanochemistry.[113] As above mentioned for conventional planetary ball mills, the adaptors containing several vials rotate at an angular frequency ω_d, and at an angular frequency ω_r in the opposite direction. The distance between the adaptors and the support disc is constant (R), but not in the case of the vial (A) (Figure 1.35). Consistently, during the milling process, the vials (A) are not always placed at the same distance from the disc centre over the time. Vials positioned at the periphery of the adapters (at a distance r_1) experiment most force, while vials positioned more toward the centre are at a distance r_2 and experience less force. This movement is named lunar and is typical of multisampling planetary mills.[106,113]

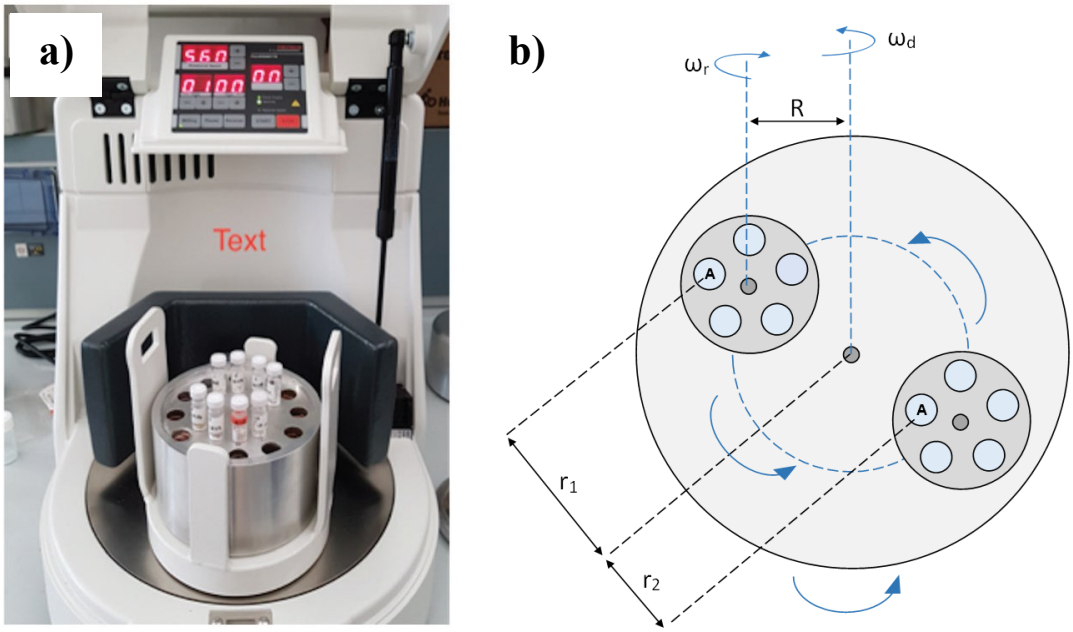

Figure 1.35. (a) A multisample planetary mill. Reproduced with permission from [113]. Copyright 2020, Royal Society of Chemistry. (b) Schematic representation of a multisampling planetary mill. R = distance between the solar wheel axis and the jar axis; r_1 = distance between the solar wheel axis and the vial A placed at the edge; r_2 = distance between the solar wheel axis and the vial A placed toward the centre (after 180° rotation).

Another example of mill is the attritor ball mill in which the agitator has a rotating shaft with perpendicular arms (Figure 1.36). This type of mills causes a differential movement between the powder and the balls, providing a large degree of surface contact. The kinetic energy imparted depends on the speed of rotation of the attritor shaft. Attritors are characterised by a relatively low energy, translating in frictional dynamics. Impulsive dynamics can also be present depending on the operational conditions.[112]

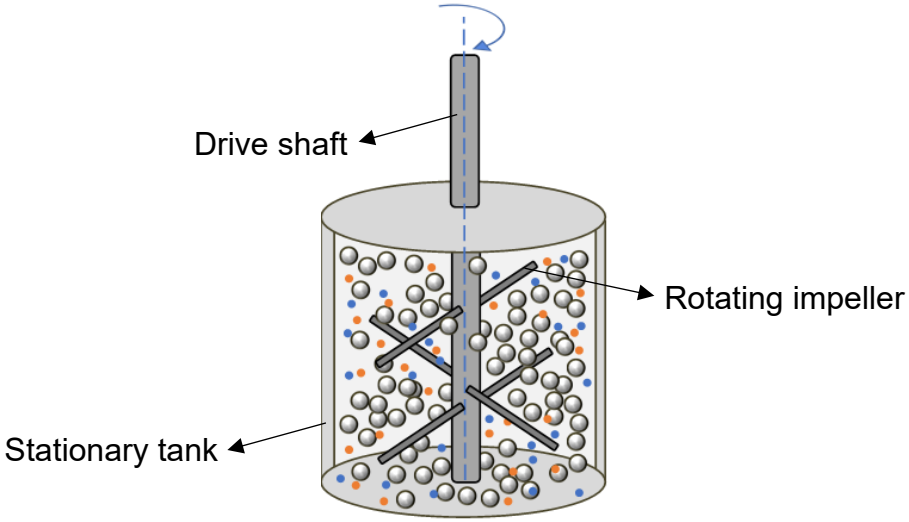

Figure 1.36. Schematic representation of an attritor mill.

In contrast with attritor and planetary ball mills, mixer ball mills (also called shaker or vibratory mills) are characterised by low shear forces and high compressive. In mixer mills, the reaction jars are horizontally or vertically rapidly shaken at a frequency up to 60 Hz, grinding and shearing the reactants together (Figure 1.37). Since mixer mills can process sample quantities between 0.01 and 50 mL, they are suitable for laboratory-scale investigations up to a gram scale.

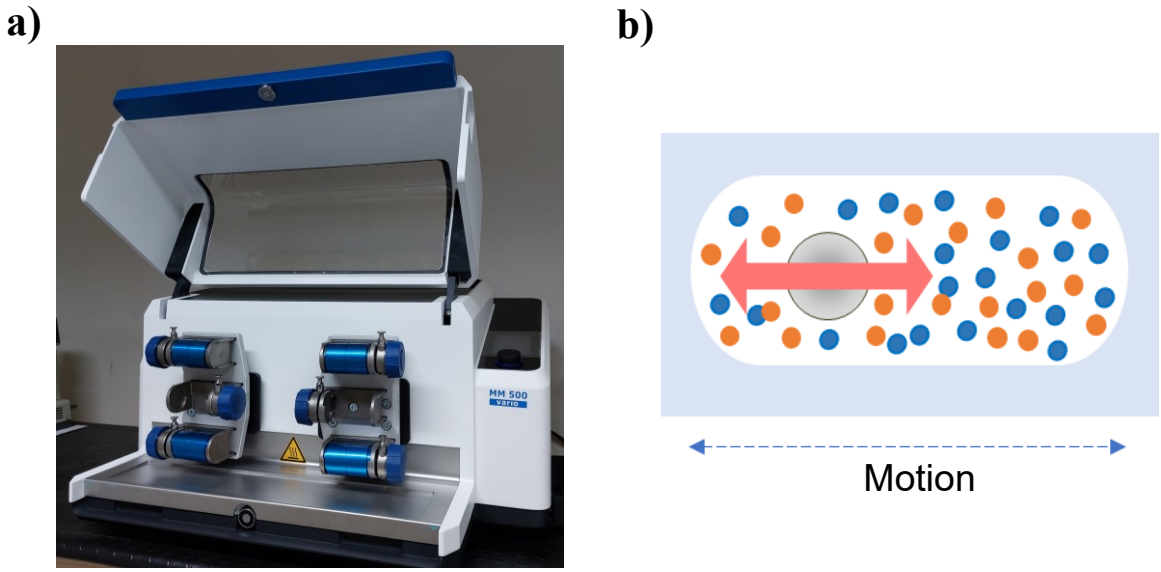

Figure 1.37. (a) An example of shaker mill; (b) schematic cross section for horizontally oscillating mixer mill.

Mixer mills with a so-called "shape of 8" movement are also available: the reactor undergoes simultaneously a rotation in the equatorial plane and an angular harmonic displacement. Typically, operational frequency is ca. 18 – 30 Hz (Figure 1.38).

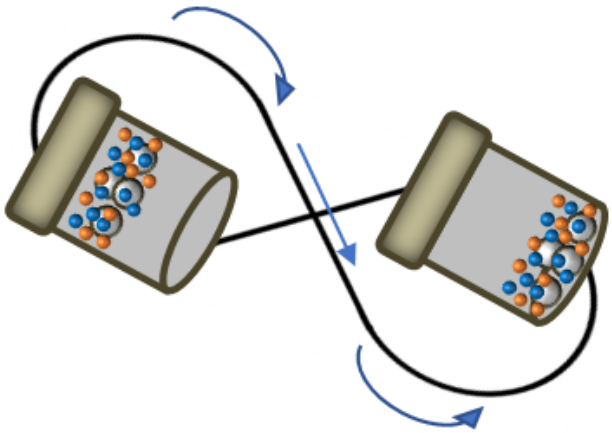

Figure 1.38. Schematic representation of the "shape of 8" movement of the reaction chamber in a SPEX mixer mill.

One of the most complicated three-dimensional milling movements is characteristic of the SPEX Mixer/Mill 8000. The vessel moves at high frequency in a complex cycle that involves motion in three orthogonal directions. The centre of the jar vibrates in two directions (x and y axis) with the same frequency and different amplitude, while its slanted axis rotates around the third direction (z axis). Rotation and vibration movements occur at the same frequency (Figure 1.39).[114]

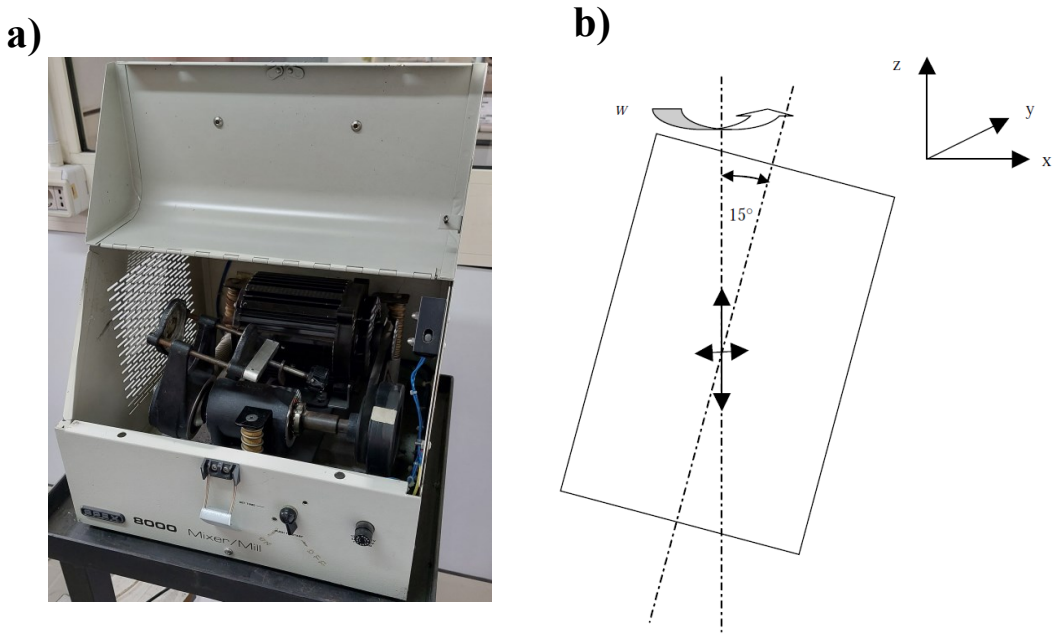

Figure 1.39. SPEX 8000 mixer/mill (a); schematic representation of the movement of the SPEX 8000 (b) reproduced according to ref [114].

In addition to ball milling, twin-screw extrusion (TSE) is a another mechanochemical equipment. In this apparatus solid reagents are ground together by a pair of counter-rotatory screws while the mixture is transported along the extrusion path through a barrel (Figure 1.40). Different type of sections of the screw are available to enable several mechanical actions (e.g., simple mixing, conveying, or grinding). The reagent feed-rate, screw rotating speed and screw and barrel lengths can be modulated to optimise reaction conditions.[107] Since the mechanochemical reaction occurs in a continuous process, TSE represents a solid-state equivalent to solution-based flow-reactors. Moreover, TSE has been successfully employed for large-scale preparation of MOFs, proving exceptional feasibility of mechanochemistry for industrial scale-up.[115]

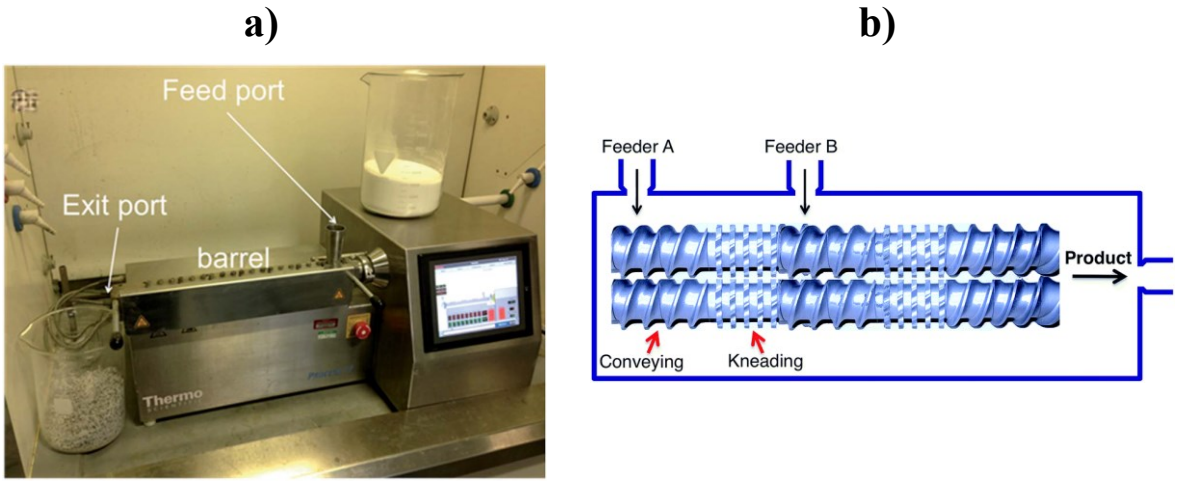

Figure 1.40. Twin screw extruder (a); schematic twin-screw extrusion setup (b). Reproduced from Ref. [115,116] with permission from the Royal Society of Chemistry.

Mechanochemical process variables

The energy transfer which occurs during the mechanical milling is affected by a variety of processing parameters. They are often intertwined because of the complex ball and powder dynamics, and include: the type of mill, the materials composing jars and balls (constituting the so-called milling media), the number and size of milling balls, the milling frequency, the duration of milling, the temperature of milling, dry or wet milling, ball-to-powder ratio, and (balls + powder)/empty jar volume ratio.[107,117] The milling media (i.e., the jars and balls), can be made from a variety of materials, such as Teflon, stainless-steel, zirconia, tungsten carbide, etc. The kinetic energy of the balls is a function of their mass and square velocity. Therefore, since milling media can vary in their density (ρ), they allow to control energy input and, hence, reactivity. Steel and tungsten carbide are dense materials (ρ_{steel} = 7.8 g/cm^3 and $\rho_{tungsten\ carbide}$ = 15.8 g/cm^3), so, they carry higher kinetic energy during the milling process than less dense materials (ρ_{Teflon} = 2.3 g/cm^3; ρ_{agate} = 2.6 g/cm^3; $\rho_{zirconia}$ = 5.7 g/cm^3). The appropriate milling material need to be carefully evaluated mostly depending on the nature of the substances composing the reaction mixture.[107] For example, less dense materials are more suitable compared to more dense material especially when dealing with biomolecules which require mild reaction conditions. Since the milling medium influences the kinetic energy of the balls, it also influences the temperature during milling. In addition, milling media can differ in their chemical resistance. For instance, stainless-steel milling media corrode in contact with strong acids.[118] Moreover, metal contamination or chemical leaching of metal ions (e.g., Co, Fe, etc.) can occur during prolonged milling, affecting the reaction outcome. In this context, milling

media made from chemically resistant materials, such as Teflon, can avoid these contamination issues. However, being much softer, the Teflon milling media shows faster wear and tear rate.[119] The volume ratio (balls + powder)/empty jar should be optimised on the basis of the mill used. Higher volume ratio reduces the mean free path of the ball motion and friction mode is promoted. Vice versa, the impact mode is dominant with lower volume ratio. The grinding speed and the duration of milling influence the kinetics. The faster the milling speed, the higher the energy input, and generally the reaction is faster. Conversely, high speeds can result in higher temperatures, that may cause side reactions or contaminations from the jar material.[120] Ball-to-reagent-ratio (BRR) is another pivotal experimental parameter to consider in ball milling reactions. It is defined as the total mass of the milling balls in the media divided by the total mass of the reagents in the reaction. It has been shown that BRR influences reaction kinetics and can be varied to finely optimise and tune mechanochemical reactions.[121] BRR can be summarised as follow:

$$Ball - to - reagent - ratio\ (BRR)\ = \frac{Total\ mass\ of\ balls}{Total\ mass\ of\ reagents}$$

Neat grinding (NG) and Liquid-Assisted Grinding (LAG)

Mechanosynthesis can be carried out using small amounts of solvent (LAG - Liquid-Assisted Grinding) or without using any additional solvent (NG – Neat Grinding).

The term liquid-assisted grinding (LAG) has been introduced to describe and unify mechanochemical reactions in which a defined volume of liquid is added.[122] In order to assess a systematic distinction between the various grinding techniques, a parameter (η), defined as the ratio of liquid volume (in μL) to the combined mass of solid reactants (in mg), has been proposed.[108]

$$\eta\ = \frac{Added\ liquid\ (\mu L)}{Mass\ of\ solid\ reactants\ (mg)}$$

According to this classification (Figure 1.41), NG correspond to $\eta = 0$, while LAG correspond to $0 < \eta < 1$. Higher values ($\eta > 1$) correspond to the formation of slurries and homogenously dissolved reactions.[121]

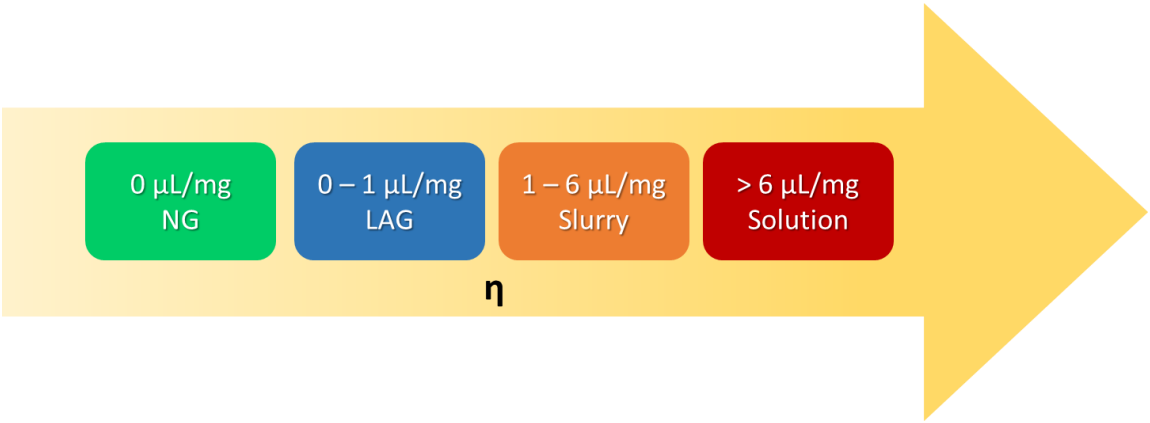

Figure. 1.41. Ranges of η values.

Besides NG and LAG, other grinding techniques have been exploited, such as polymer-assisted grinding (POLAG), vapour-assisted grinding (VAG), and ion- and liquid-assisted grinding (ILAG). These approaches involve the addition of sub-stoichiometric amounts of additives to the grinding process, leading to a better control of chemical selectivity and reactivity.[110]

In its simplest form, NG mechanochemical synthesis involves reaction between dry reactants. Nevertheless, some reactions in this category can involve the release of liquid during the reaction.[123] This is the case of hydrate reactants or liquid by-products, such as acetic acid or water, which are generated as condensates during the reaction. These kinds of reactions proceed rapidly under mechanochemical conditions, suggesting that the presence of liquid may accelerate the reaction. For instance, Fernández-Bertrán et al. demonstrated that mechanochemical reactions were accelerated when the analyte was a hydrate.[124] This is the case of the reaction occurring when milling and pressing analytes with alkali halides to form disks for IR experiments. Conversely, LAG approach refers to mechanochemical synthesis in which a small quantity of liquid is intentionally added to the reaction mixture. It has been showed that adding small amounts of liquid can dramatically accelerate, and even enable, mechanochemical reactions between solids. The amounts of solvents used are much inferior than the quantities typically used in solution-based reactions.[123] Hence, both NG and LAG methods result more environment-friendly and sustainable than conventional approaches.

Compared to conventional solution-based approaches, alternative methods require shorter reaction times and the use of lower amounts of solvents. Moreover, alternative approaches avoid high temperature and pressure. Such features result in reduced costs of the overall production processes and contribute to further improve environmental footprint of reactions. This is not only appealing to industrial scale-up, but it is also in agreement with green chemistry principles for a sustainable and conscious development. Both electrochemical, sonochemical and mechanochemical approaches give rise to Fe-BTC materials, the disordered phase of MIL-100(Fe) containing both crystalline and amorphous domains.[40] Fe-BTC MOF is commercially available as Basolite®F300 by BASF/Aldrich.[42] It has grabbed great attention in the last decades because of its remarkable activity as heterogeneous catalysts, performing even better than its crystalline counterpart (i.e., MIL-100(Fe)) for Lewis acid reactions. Therefore, despite the disordered structure, Fe-BTC is widely used for the same applications of MIL-100(Fe) and it is sometimes preferred owing to the milder reaction conditions required for its synthesis.

According to the framework formation proposed by Seo et al., the synthesis pathways under hydrothermal conditions of crystalline MIL-100(Fe) undergo four important steps: hydrolysis, deprotonation, self-assembly, and condensation.[91] In the very early reaction stage, the hydrolysis of Fe(III) salts forms monomeric $[Fe(H_2O)_{6-n}(OH)_n]^{(3-n)+}$ octahedra which readily arrange to produce inorganic clusters with a triangular arrangement of Fe(III) atoms through H-bonds. Full deprotonation of trimesic acid ($pK_{a1} = 3.12$; $pK_{a2} = 3.89$; $pK_{a3} = 4.70$)[125] is needed to promote condensation. Once trimeric inorganic units are formed, the self-assembly of the inorganic trimers and carboxylic acids can take place. Carboxylate moieties of deprotonated trimesic acid orient properly towards inorganic trimers. Then, the condensation occurs, leading to the final phase of the material, with the formation of the iron trimers based supertetrahedral building blocks of MIL-100(Fe). Although trimesic acid deprotonation is favoured at basic conditions, low pH allows a better control of the reaction kinetics.[89] Indeed, a slow rate of deprotonation leads to a more ordered arrangement of carboxylate moieties towards trimeric iron(III) clusters, leading to the obtainment of highly porous and ordered solids. Moreover, acidic conditions stabilised iron trimers over monomeric octahedra. This mechanism clearly explains why acidic conditions, as well as high temperature and pressure and long reaction time, are required for to obtain a well-defined and crystalline MIL-100(Fe), and why milder conditions under short reaction times at ambient pressure and temperature generally give rise to disordered Fe-BTC materials. Given the same features between MIL-100(Fe) and Fe-BTC in terms of composition,[37] thermal stability,[38] and nature/structure of metal clusters,[39] and

the comparable applications,[35] milder and alternative synthesis of disordered iron(III) trimesate MOFs are generally preferred over the harsh conditions required for conventional preparation of crystalline MIL-100(Fe). However, despite the enormous advantages given by alternative methods, they have been scarcely exploited for the synthesis of Fe-BTC[126,127], which is rather widely carried out in solution according to the method developed by Sanchez-Sanchez.[37] As previously discussed in section 1.2.6.2, a typical synthesis with this batch-based protocol requires ambient temperature and pressure, short reaction times (10 minutes). However, the pH remains acidic throughout the synthesis (pH = 2.1), despite the use of alkaline solutions. In addition, the formation of a brownish orange solid upon dropwise mixing the solutions of the precursors does not ensure homogeneity within the reaction mixture. Mechanochemical approach has been used to synthesise a Fe-BTC MOF, exhibiting crystallinity and better textural properties compared to the commercial Basolite®F300.[126] Synthesis was carried out grinding ferric nitrate nonahydrate and trimesic acid together with a small amount of an aqueous solution of tetramethyl ammonium hydroxide pentahydrate ($TMAOH{\cdot}5H_2O$) for one hour. Despite the use of base, the pH remained acidic ($pH \approx 1$) throughout the synthesis, similarly to the traditional solvo/hydrothermal protocol. These acidic conditions can limit the use of iron(III) trimesate materials, especially for biomedical purposes. Therefore, milder synthesis conditions still need to be addressed. This is prominent when using MOFs as support for the immobilisation of pH-sensitive molecules (e.g., proteins, nucleic acids, drugs etc.), since they can easily undergo upon denaturation if exposed to harsh temperature, pressure, and pH conditions. Before entering more in detail into the advantages of employing alternative synthesis methods to achieve mild and bio-friendly encapsulation of biomolecules, an extensive and detailed discussion on existing immobilisation strategies is provided in the next section.

1.3. Protein immobilisation

Proteins are indisputably one of the most important biomacromolecules for life, serving a variety of functions within the body. Some of them are involved in structural support and movement (contractile proteins), or in defending the body from antigens (antibodies), others are receptors or messenger proteins which help coordinating life-sustaining biological functions (hormones). Other proteins possess catalytic activity (enzymes), which generally far exceeds artificial catalysts efficiency.[128] Consistently, the interest in applying proteins for *ex vivo* applications has rapidly grown in recent years owing to circumventing the laborious design and synthesis of artificial molecules. Proteins have been extensively studied to explore diverse and unique applications from food and environment safety to biomedicine, including sensing, drug delivery and biocatalysis.[129] However, the use of free proteins for practical applications is hindered by their instability in harsh operational conditions, low shelf-life, difficult recovery and poor reusability.[130] Indeed, enzymes, and more generally proteins, possess a labile nature owing to their low thermal stabilities, narrow optimum pH ranges, low tolerances to most organic solvents and many metal ions. Furthermore, proteins themselves represent a source of contamination in the desired product, resulting in inevitable purification and separation steps.[131] In order to overcome such drawbacks, several protein immobilisation strategies on solid supports have been exploited. The term "immobilised proteins" refers to "enzymes physically confined or localised in a certain defined region of space with retention of their catalytic activities, and which can be used repeatedly and continuously".[132] Unlike using proteins homogeneously, the major benefits of employing heterogeneous immobilised proteins include enhanced stability in storage and operational conditions, easy separation from the reaction mixture, adjustability of their properties, reusability, prevention of microbial contaminations and/or protein contamination in the product.[133] Moreover, protein immobilisation can lead to enhanced activity and/or selectivity.[134] The improved stability and reusability of immobilised proteins is significantly beneficial for their industrial application.

Immobilised proteins or enzymes are widely employed in biomedical fields, food industry and environmental monitoring.[135] Encapsulated proteins are used in different types of bioreactors for the separation of metabolites from body fluids or for the improvement of metabolic deficiency in the human body.[136] Some applications of bioreactors used in human medicine include the degradation of organophosphate in organophosphate poisoning by the use of organophosphate hydrolases,[137] DNA damage repair in skin aging and cancer by DNA repair

enzymes,[138] and hydrolysis of phospholipids in hypercholesterolemia using phospholipase A2.[139] The development of controlled drug delivery systems for dosing of proteins or enzymes into cells is another important application of immobilised enzymes in biomedicine, especially in cancer treatment. Usually, chemotherapeutics tends to show weak targeting effects and/or causes toxic effects on normal cells during cancer treatment. One strategy to overcome such limitations is to employ nontoxic prodrugs metabolised by enzymes to generate cytotoxic products in a tumour microenvironment.[140] However, enzymes are generally present at very low levels in cells, which leads to the poor selectivity and unsatisfactory results for this enzyme-activated prodrug therapies. An ideal method is to deliver exogenous enzymes to tumour cells.[130] Nevertheless, enzymes tend to suffer from the internal environment during the delivery process. This problem can be overcome by the immobilisation of enzymes on solid supports, which emerges as excellent matrixes to deliver enzymes to the cancer cells.[141] Several immobilised enzymes are commonly used as biocatalysts for the production of active pharmaceutical ingredients (APIs), cosmetic additives for personal care, and food ingredients due to their high regio-, chemo- and enantioselectivity, operating in conditions which were extreme for a wild type enzymes.[142] Biosensors represent a major application of immobilised proteins, not only in medicine and clinical diagnostics[143] but also in environmental monitoring,[144] food safety,[145] as well as agricultural industry.[146] Immobilised antibodies, receptors, and enzymes have been reported for the detection of different bioactive compounds in medical diagnosis or food and/or environment contaminants, including glucose,[147] urea[148], cholesterol,[149] hydrogen peroxide[150], organophosphates pesticides[151] and so on. Such biosensors use high reactivity and specificity of enzymes towards their substrates and possess high accuracy, sensitivity, reliability, ease of handling. Moreover, they are relatively cost efficient compared to traditional analytical methods.[152] Depending on the assay type, enzymatic biosensors can be classified in two fundamental categories. In the first group, the enzyme detects the presence of co-factor/co-substrate, or a substrate. A typical example of this approach is given by glucose biosensors employed for blood glucose monitoring in people affected by diabetes.[153] The second group is based on the detection of enzyme inhibitors in the presence of a substrate. One of the most common example is the detection of organophosphate compounds used as warfare nerve agents or pesticides.[154]

Besides the advantages given by enzyme immobilisation, it is also important to consider that physical and chemical properties of proteins can suffer changes after immobilisation depending on the choice of immobilisation method and support.[131] Therefore, it is pivotal to identify immobilisation technique and matrix that produce the minimum loss of protein integrity and functionality.

1.3.1. Solid supports

Various solid materials have been employed as supports for enzyme immobilisation, including porous and non-porous materials. Non-porous materials (mainly magnetic nanoparticles) showed several disadvantages, such as very low protein-loading capabilities. Moreover, enzymes are exposed to the external surface, often requiring covering the immobilised proteins with polymers.[155] Conversely, protein immobilisation on porous solids enables an increased contact surface and, therefore, stronger binding with the protein and higher loading capacity compared to flat surfaces, because of the large surface area and void volume. A considerably inferior protein leaching is observed when using porous materials, since the proteins result confined within the pores after immobilisation. In addition, immobilisation on porous supports can stabilise the enzyme against interaction with the enzymatic extract, preventing autolysis or proteolysis by proteases.[134] Further, the spatial separation of proteins within the pores of the support can avoid their distortion, deactivation, and/or aggregation. However, diffusion restrictions can represent a disadvantage when immobilise proteins in porous materials.[136] Porous materials such as hydrogels, sol–gel matrices, mesoporous silica, organic microparticles, and metal-organic frameworks are interesting candidate materials for protein immobilisation and have attracted great attention over the past years.[131] Sol-gel matrices can prevent enzyme leaching due to entrapment within their intrinsically porous structure. However, it has been observed that the disordered structures of sol-gels can favour enzymes denaturation. In addition, the entry of bulky substrates into enzyme active sites is sometimes hindered by the small pore size of such matrixes.[156] Enzymes immobilisation using hydrogels or organic microparticles as supports suffer from limited mass transfer, leaching (owing to the degradation or swelling of the matrices), and enzyme denaturation.[157] In this regard, mesoporous silica nanoparticles represents a better choice for protein immobilisation, because of their ordered structure and large pore size.[158,159] However, the one-dimensional-channel structure of mesoporous silica gives rise to fewer interactions between enzymes and the inner channel surface of support, causing the leaching of enzymes after multiple cycles of use.

Furthermore, the challenges of rational structural design, the presence of surface charges which can provoke a reduction of enzyme loading and/or enzyme denaturation, together with the possibility of aggregation inside the channel, often hinder the use of mesoporous silica as a protein support.

Among porous materials, MOFs show unique properties such as high surface area and pore volume, and specific molecular adsorptions, which make them very promising as supports for protein immobilisation. The strong interaction between MOFs and proteins is one of the main advantages of using MOFs over other support materials, especially mesoporous silica. Indeed, these strong interactions between the organic components of the framework and protein molecules (e.g., π-π interactions) lead to a lower extent of protein leaching-out from supports during applications, whereas the lack of specific interactions between the proteins and mesoporous silica materials causes severe protein leakage.[160] Furthermore, unlike other porous materials including zeolites and mesoporous silicas, chemical functionality and pore dimensions of MOFs can be precisely tuned for the immobilisation of specific. This is a distinct advantage of MOFs as potent supporting matrices for protein immobilisation. Another relevant aspect of MOF chemistry regarding protein encapsulation is that biocompatible synthesis conditions (room temperature, H_2O) have been developed, for a number of examples, especially ZIFs.[161,162] In the last decade, various applications have been explored using MOFs as a platform for the immobilisation of proteins, enzymes, drugs, and DNA.[163] To the best of our knowledge, MOFs were applied to immobilise a wide range of proteins and enzymes, such as cholesterol oxidase,[164] acetylcholinesterase,[165] glucose oxidase,[166] uricase,[167] and hemin[168] for cholesterol, methyl parathion, glucose, uric acid and 2,4,6-trichlorophenol detection, respectively, lipase to catalyse warfarin synthesis[169] and esterification reactions,[170] carbonic anhydrase to promote CO_2 capture,[171] organophosphate hydrolase for nerve agent detoxification,[172] insulin to favour oral drug delivery for diabetes treatment,[173] tyrosinase for cancer therapy,[141] and so on. Besides enzymes and proteins, MOFs have been combined with several bioentities, including drugs,[174], nucleic acids (DNA[175] and RNA[176]), antibodies,[177] cells and viruses.[178]

1.3.2. Immobilisation strategies

Given the above-mentioned advantages of using MOFs as support for protein immobilisation, significant efforts have been made for the preparation of protein-MOF hybrid composites in the last decades. Several strategies have been developed to immobilise numerous proteins on MOFs. There are mainly two ways to prepare protein-MOF composites in terms of how guest molecules bind to the supports. One consists of the immobilisation of guests into the MOF during its building-up process and it is called *in situ/de novo* approach. The other involves post-synthetic methods where proteins are introduced into the pre-synthesised MOF, and includes surface adsorption, covalent binding, and pore entrapment. Typically, protein/MOF-based biocomposites are termed as follow:[161]

- *protein@MOF*; proteins are embedded within the MOF structure since (i) the MOF is synthesised in the presence of an enzyme (*in situ* immobilisation), or (ii) the enzyme is introduced within the pore network of a pre-synthesised MOF (pore entrapment).
- *protein-on-MOF*: proteins are anchored to the surface of a pre-synthesised MOF via (i) covalent bonds (covalent binding), or (ii) noncovalent interactions (surface adsorption).

First, post-synthetic approaches such as surface adsorption, covalent binding, and pore entrapment are discussed in sequence. Then, *in situ* immobilisation is examined.

1.3.2.1. Surface adsorption

This is a fast, cost-efficient, simple, and most widely used method to immobilise proteins solid supports. It is a reversible process performed by simply bringing protein and support into contact with each other. Physical attachment of proteins on the support surface is usually an effect of simple non-covalent interactions, including van der Waals forces, hydrogen bonding ionic binding, and hydrophobic forces.[179] Because of the variety of functional groups in proteins, given by the presence of various amino acids, the binding is not site-specific and a distinction among the forces is generally difficult. Conversely, the minimum activation step is one of the advantages of enzyme immobilisation by adsorption method. Moreover, it is an easy and inexpensive strategy of immobilisation. However, since proteins results exposed to the external surface, any change of salt concentrations and/or pH could strongly affect the electrostatic protein-support interactions and eventually lead to the leaching-out of the protein.[130] Recently, a surface adsorption approach has been used by Zhong et al. to immobilise GOx on a Zr-based porphyrin MOF matrix (Figure 1.42).[166] In the case of protein

surface adsorption, the selected framework should have large enough pores to adsorb a specific protein.[180]

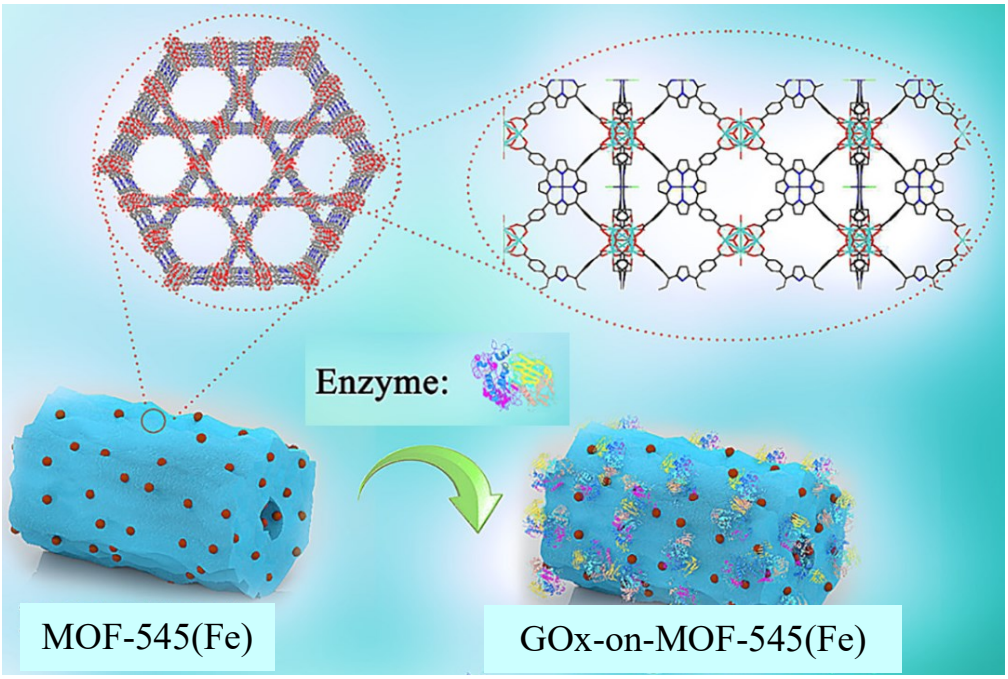

Figure 1.42. Schematic representation of the preparation of GOx-on-MOF-545(Fe) composites via surface adsorption strategy. Reprinted from [166], Copyright 2009, with permission from Elsevier.

When MOFs possess smaller pore size than the corresponding protein, an alternative strategy, called dye-tagging method, can be pursued to achieve surface immobilisation. Firstly, protein molecules are conjugated via covalent bond to small molecules, such as dyes. Then the dye can diffuse within the pores of MOFs, whereas the enzyme molecules remain adsorbed on the external surface.[163] Since single- or multi-point covalent attachment are necessary, protein chemical modifications and/or rigidification/distortion can occur and should be taken into account.[181] Based on this strategy, Liu et al. carried out the immobilisation of trypsin on various MOF supports (CYCU-4-(Al) and MIL-101(Cr)), using fluorescein isothiocyanate (FITC) as dye (Figure 1.43). FTIC molecules possess much inferior size compared to the MOF pores. Therefore, dye molecules could be used to gain trypsin access into the pores of the MOFs designed as supports. Indeed, trypsin is a macromolecule, therefore its entry into the pores of MOFs would be hindered.[182]

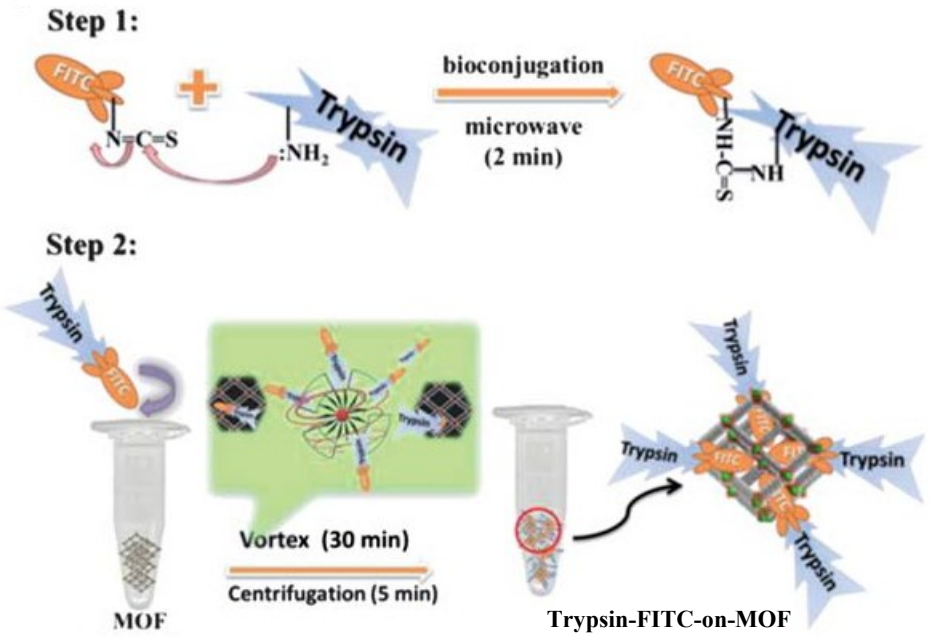

Figure 1.43. Schematic representation of trypsin surface immobilisation on a MOF support via dye-tagging strategy. Reproduced with permission from [182]. Copyright 2013, Royal Society of Chemistry.

1.3.2.2. Covalent binding

Covalent binding is a widely used method for protein immobilisation. Unlike weak interactions given by physical adsorption, covalent binding is irreversible and it can be attained by direct linkage of the protein on the surface of support materials via covalent bonds.[183] Generally, covalent binding method involves an activation step before protein immobilisation. This activation step requires the introduction of an electrophilic group to the support material, giving rise to strong covalent bonds with protein nucleophilic groups.[184] Furthermore, the strong interactions between protein and support favour protein rigidification, stabilizing proteins against harsh conditions and reducing protein leakage. The covalent binding method suffers from some intrinsic limitations, since it involves numerous steps, including activation of the support, covalent binding, and blocking of reactive groups, making this strategy time-consuming and expensive. Moreover, the activity of enzymes may decrease after the immobilisation due to the chemical modification of the enzyme by covalent binding. Multipoint covalent linkage is postulated to be one of the most robust chemical bonds to conjugate biomolecules.[134] However, the creation of multiple interactions between the protein and the support can diminish the conformational flexibility of the guest, often leading to protein distortion.[163] In addition, similarly to adsorption strategies, proteins resulted exposed to the

external surface, thus they may not be fully shielded from pH, solvent, and temperature conditions, which can cause the deactivation of proteins. Shih et al. have successfully exploited covalent binding strategy to immobilise trypsin on a range of MOF supports (MIL-88B(Cr), MIL-88B-NH_2(Cr), and MIL-101(Cr)).[185] First, dicyclohexylcarbodiimide (DCC, a common enzyme coupling agent) was used to activate the free carboxylate groups of the MOFs. Then, the DCC-activated carboxylates reacted with the amine groups present on trypsin via nucleophilic attack (Figure 1.44).

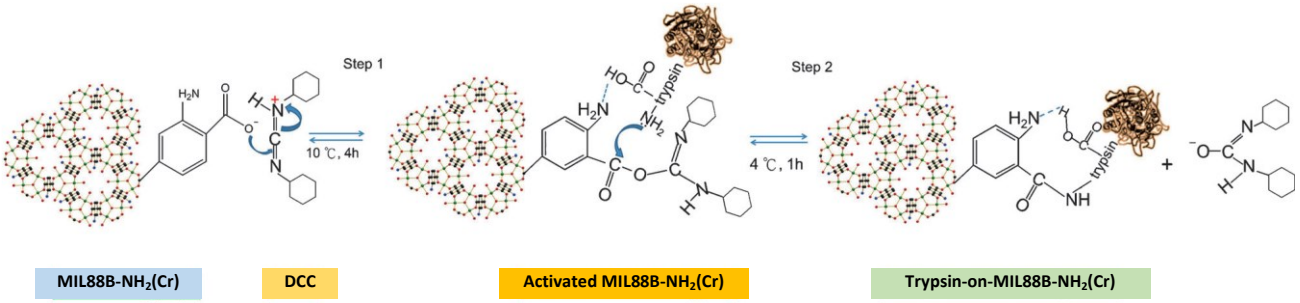

Figure 1.44. Schematic representation of trypsin immobilisation on a MOF support via covalent binding strategy. Reprinted from [185], Copyright 2012, with permission from John Wiley & Sons.

1.3.2.3. Pore entrapment

Cage inclusion, also known as pore/cage entrapment or encapsulation, is performed as a second step after the synthesis of the support. Protein inclusion in porous materials reduces protein leaching owing to introducing physical barriers. A wide variety of proteins can, in principle, be immobilised within the pores if the size of the protein is smaller than those of support channels.[130] Unlike surface adsorption, in which proteins are exposed on the MOF surface, pore entrapment contributes to improved stability and reduced leaching in recycle since proteins result physically adsorbed within the cavity of the support. The pores of the framework can provide size selectivity for specific substrates, which can hardly be attained with surface immobilisation strategies. Pore entrapment provides an additional protective layer, since enzyme interfering species need to diffuse through the pore channels before access the enzyme. This also prevents aggregation by physical separation of enzyme molecules.[131] However, only a few reported MOFs possess enzyme-compatible pores.[169,186] It has been explored the synthesis of big-pore-size MOFs feasible for enzyme immobilisation. However, owing to requiring complex synthetic procedures involving long organic ligands, this generally resulted in unstable systems.[187] Chen et al. have achieved the encapsulation of cytochrome c (Cyt c) in a nanoporous MOF, despite the much smaller pore sizes of the MOF compared to the larger

molecular dimension of the protein. This mechanism, depicted in (Figure 1.45), firstly involved the surface adsorption of the protein (a) followed by a partial unfolding (b). Then, the partially unfolded protein, after partitioning between the surface and exterior pores (c), finally migrated into the large interior cavity of the MOF (d).[188]

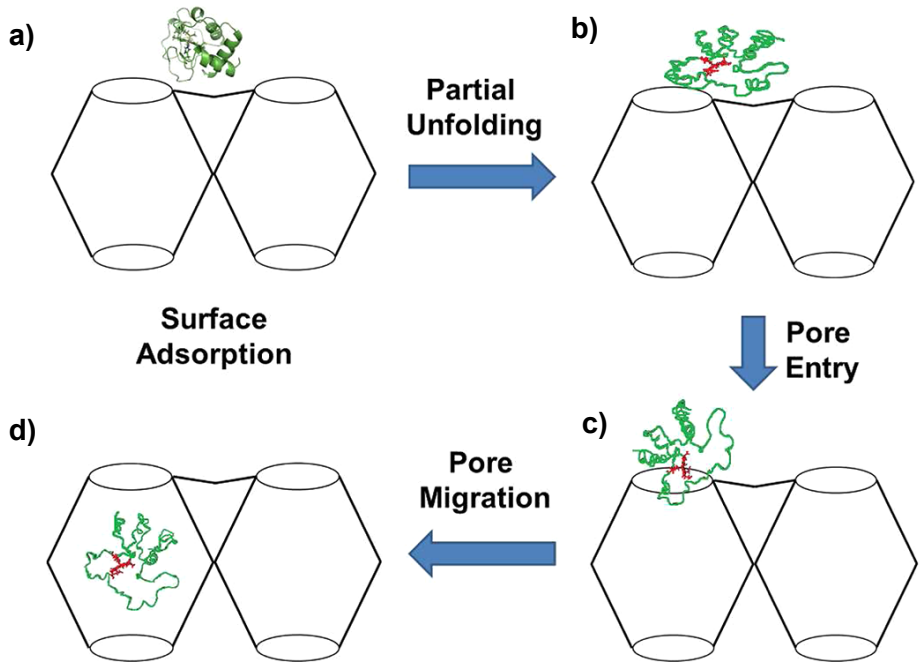

Figure 1.45. Example of protein immobilisation through pore entrapment, involving surface adsorption of the protein (a); partial protein unfolding (b); protein partitioning between the surface and exterior pores (c); migration of the protein into the large interior cavity (d). Reprinted with permission from [188]. Copyright 2012 American Chemical Society.

Huo et al. reported a different encapsulation method for the immobilisation of proteins such as β-galactosidase (β-gal), and Candida Antarctica lipase B (CalB) on ZIF-8 MOF.[189] They employed an agarose hydrogel droplet containing the enzyme and stabilised by magnetite nanoparticles and UiO-66. Such droplets acted as a template around which a hierarchically structured ZIF-8 shell was deposited (Figure 1.46). The resulting microcapsular structures were highly microporous and robust to encapsulate proteins and successfully fabricate β-gal@ZIF-8 and CalB@ZIF-8 materials. This encapsulation strategy configures MOFs into hollow microcapsules. Therefore, encapsulation of biomolecules within the capsule interior did not significantly affect ZIF-8's porosity, allowing for the immobilisation of large proteins. Despite the great potential, post-synthetic pore entrapment strategies require numerous additional steps, resulting expensive and time consuming.

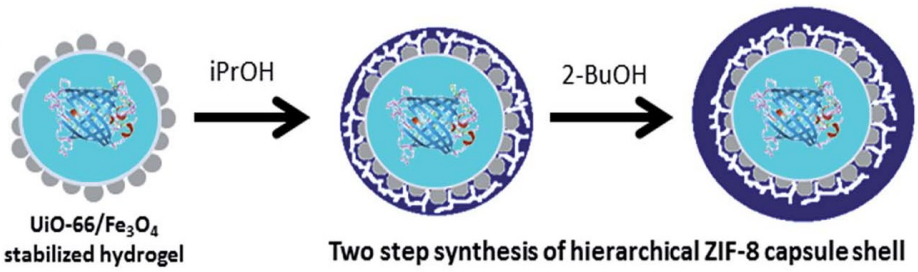

Figure 1.46. Schematic representation of the two-step synthesis of ZIF-8 capsule shell. Reproduced from [189] with permission from the Royal Society of Chemistry.

1.3.2.4. In situ immobilisation

Protein immobilisation strategies based on adsorption or covalent linkage into support surfaces cause a significant decrease of MOF porosity, owing to the large protein molecules blocking the apertures to the available porosity of the framework. This could be an issue in terms of molecular diffusion and selectivity for biocatalytic applications. Moreover, direct adsorption/attachment of proteins into the pores of MOFs is achievable only when the size of the proteins is such that can enter the pores. Most of the reported MOFs possess pore size inferior to the molecular size of proteins. Pore entrapment has been proved to allow for the inclusion of guest molecules whose size are larger than the pores of supports. However, this strategy is limited by the multi-step pathways and the overall time-, cost- and chemical-consumption. Furthermore, conformational changes of proteins, that could decrease their biocatalytic potentials, are often needed.[136] In this regard, an alternative strategy, named *in situ* (*de novo* or one-pot) immobilisation, leads to the immobilisation of proteins into the MOF during its synthesis in a one-step process. Unlike post-synthetical approaches, pre-formed supports are not required since nucleation and growth of MOF proceed simultaneously with protein encapsulation. Proteins result embedded into MOF, and their size can be larger than the pore openings of supports.[131] This not only reduces, or even avoids, leaching, but also remarkably enlarges the selection of proteins and MOFs, making this immobilisation strategy generally applicable for numerous applications.[136]

The encapsulation of biomolecules into MOFs by *in situ* approach mainly depends on the synthetic conditions. Mild and biocompatible operating conditions are pivotal for *de novo* strategies, where proteins are mixed with MOF precursors (organic ligands and metal ions).[187] Only a few MOFs are the candidates for this immobilisation method. This is for example the case for zeolitic imidazolate frameworks (ZIFs), which represent one of the most widely used

MOFs to immobilise biomolecules via *in situ* approach because of their extremely mild synthetic conditions.[130] Lyu et al. introduced this one-pot method for the synthesis of enzyme-MOF composites in 2014.[190] They selected cytochrome c (Cyt c) as model protein and ZIF-8 as MOF support. In principle, Cyt c cannot gain access into the pores of the MOF, owing to Cyt c having much larger size than the pores of ZIF-8. However, protein immobilisation was easily achieved by one-pot synthesis method. In this experiment, a methanol solution of zinc nitrate hexahydrate and 2-ethylimidazole is mixed with a solution of both Cyt c and polyvinylpyrrolidone (PVP), yielding Cyt c@ZIF-8 crystals (Figure 1.47). PVP promoted the stabilisation and dispersion of the protein in methanol. This strategy has been also used to immobilise proteins such as lipase (LP) and horseradish peroxidase (HRP) into ZIF-8 and ZIF-10 MOF, showing the versatility of *in situ* approach.[190] Nevertheless, the above-mentioned enzyme–MOF composites were synthesised in methanol, thus, it is suitable only for methanol resistant proteins.

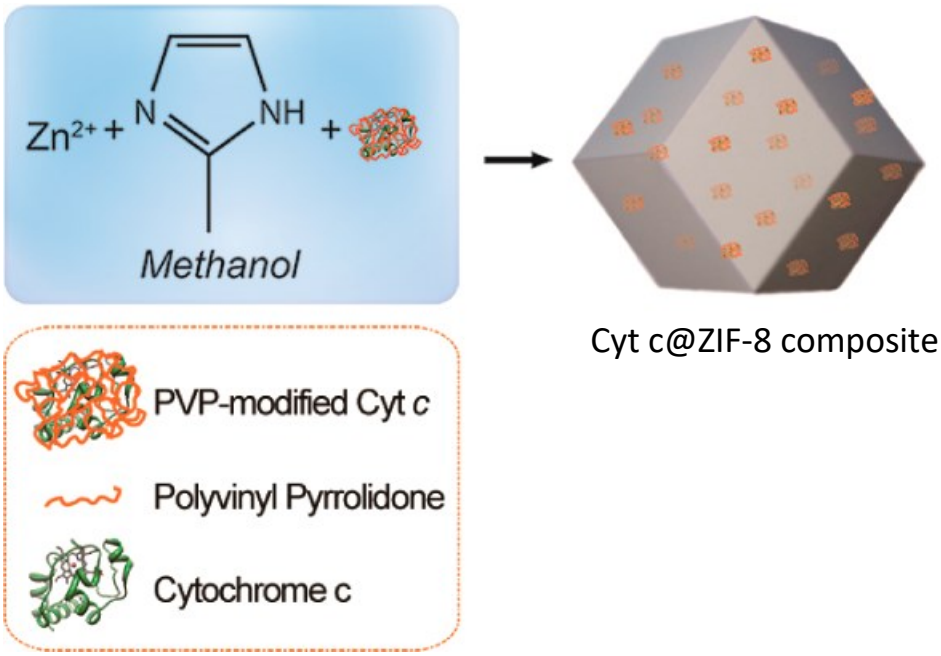

Figure 1.47. One-pot synthesis of a Cyt c/ZIF-8 composite. Adapted with permission from [190]. Copyright 2014 American Chemical Society.

Efforts have been done to perform one-pot immobilisation in aqueous solution, making the preparation of protein–MOF hybrid biocomposites suitable to be expanded to a very large pool of biomolecules and MOF materials.[162,191–193] Liao et al. immobilised Catalase (CAT) protein molecules into the ZIF-90 MOF support via one-pot synthesis strategy, by using water as solvent.

To fabricate CAT@ZIF-90 composites an aqueous zinc nitrate solution was stirred at room temperature with an aqueous solution containing catalase, imidazolate-2-carboxaldehyde, and capping agent. The enzyme molecules resulted confined in the porous cavities left in the MOF crystals by growth of the framework around the enzyme. This confinement reduced the structural changes that lead to unfolding. Indeed, they exposed the embedded enzymes to denature reagent (e.g., urea) and high temperatures (e.g., 80 °C), monitoring their resulting catalytic activity and structural conformation changes. The results indicated that the confinement provided by the *in situ* approach reduces structural changes and retains enzymes functionality under denaturing reaction conditions, compared to free enzymes (Figure 1.48).[193]

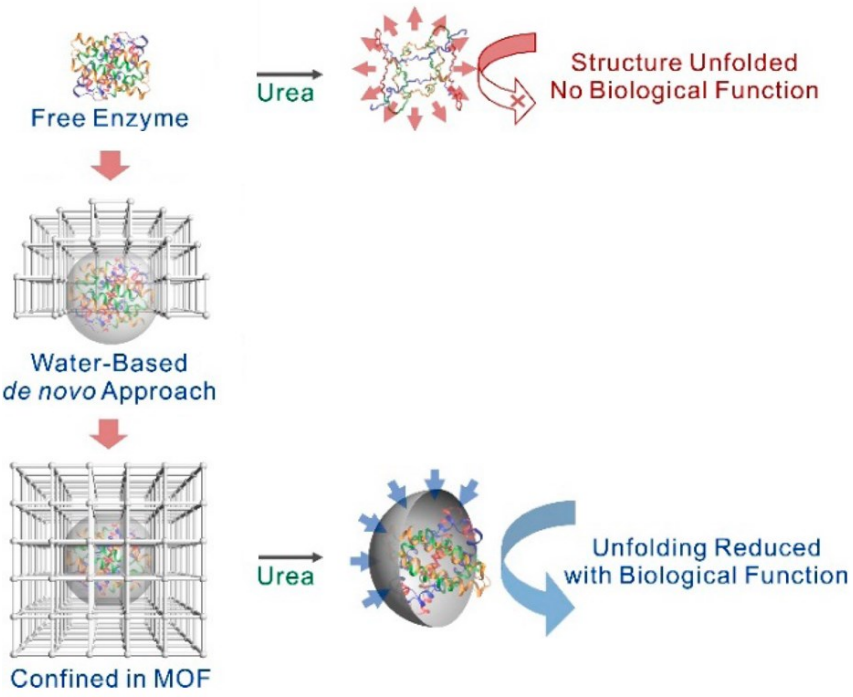

Figure 1.48. *De novo* approach for the preparation of enzyme-MOF composites. The resulting structural confinement ensure the retainment of biological function under a wider range of conditions (e.g., exposure to urea) after being embedded into MOFs. Reprinted with permission from [193]. Copyright 2017 American Chemical Society.

The one-step immobilisation method can be also exploited to encapsulate two or more proteins within a support in order to develop multi-enzyme systems which are able to catalyse multi-step tandem (or cascade) reactions. For instance, horseradish peroxidase (HRP) and glucose oxidase (GOx) were co-immobilised within ZIF-8 by Wu et al. using an *in situ* approach.[162] The multi-enzyme/ZIF-8 composite also exhibited high stability, selectivity, and sensitivity in glucose detection (Figure 1.49).

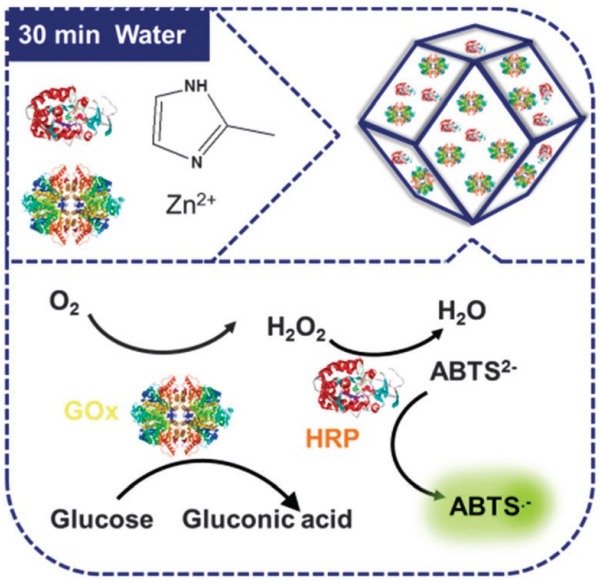

Figure 1.49. Schematic one-pot synthesis of GOx&HRP@ZIF-8 and GOx-HRP cascade reaction. Reproduced with permission from [162]. Copyright 2015, Royal Society of Chemistry.

In situ immobilisation strategies include co-precipitations methods, where enzymes are stabilised by a capping agent (e.g., PVP), and biomimetic mineralisation approaches, which are carried out in the absence of capping agents. Liang et al. compared the stability of urease@ZIF-8 composites obtained by co-precipitation and biomimetic mineralisation one-pot strategies (Figure 1.50). Both approaches showed comparable encapsulation efficiencies suggesting that capping agents do not help enhancing biomolecule loading. Furthermore, it has been reported that the biomimetic mineralisation approach is able to improve the bioactive temperature range of enzymes compared to both the enzymes encapsulated via the controlled co-precipitation method and free enzymes. Therefore, biomimetic mineralisation offers enhanced protection than the co-precipitation method over a range of temperatures. Furthermore, the co-precipitation method typically exposes the enzymes to the external environment. Conversely, the biomimetic mineralisation approach leads to a homogeneous distribution of cavities in the sample.[194]

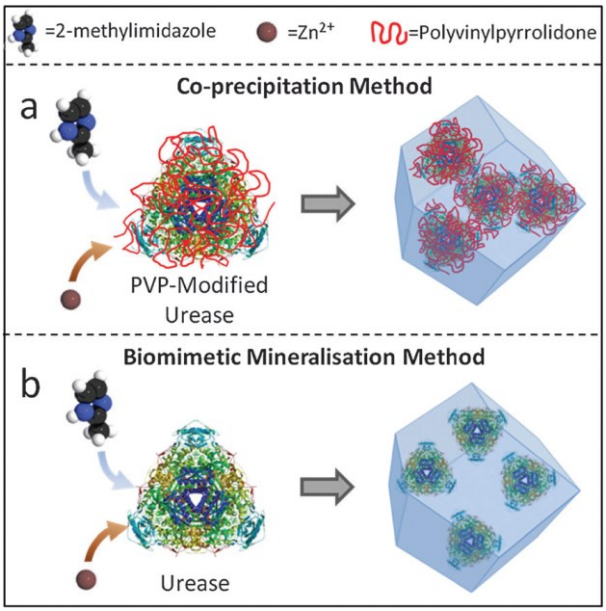

Figure 1.50. Schematic representation of the synthesis of urease@ZIF-8 composite by (a) co-precipitation in the presence PVP, and (b) biomimetic mineralisation method. Reproduced with permission from [194]. Copyright 2016, Royal Society of Chemistry.

Besides proteins and enzymes, *in situ* immobilisation strategy can be further extended to the encapsulation of a variety of biomacromolecules (Figure 1.51), including DNA, into MOFs.[192]

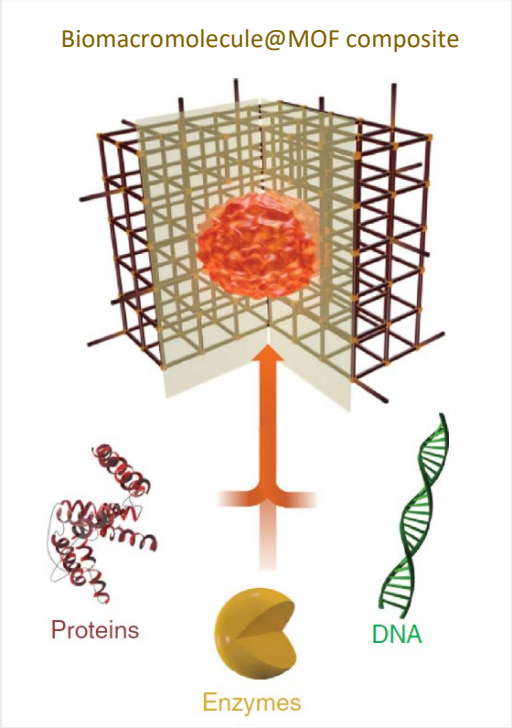

Figure 1.51. Schematic representation of a hybrid biocomposite in which a biomacromolecule (e.g., DNA, protein, or enzyme) is encapsulated within the crystalline, porous shell of a MOF. This picture is reproduced according to ref [192].

One-pot immobilisation of biomolecules in MOFs offers retained activity and integrity of guests, as well as enhanced stability, and reduced leaching from supports. However, biocomposites selectivity and efficiency does not depend exclusively on biomolecule integrity and/or concentration but also on its spatial localisation and dispersion.[130] Determining the orientation of guest molecules confined on solid supports, can be extremely challenging because of the interferences given by background signals of the MOF. Pan et al. were the first to employ site-directed spin labelling (SDSL) in combination with Electron Paramagnetic Resonance (EPR) spectroscopy to allow the evaluation of the spatial orientation of lysozyme *in situ* immobilised on ZIF-8. surfaces.[195] Their findings showed the presence of both buried and solvent-exposed enzymes. Buried enzymes include the enzyme molecules whose active sites are either buried deep inside MOF framework or partially buried below MOF surface (Figure 1.52).

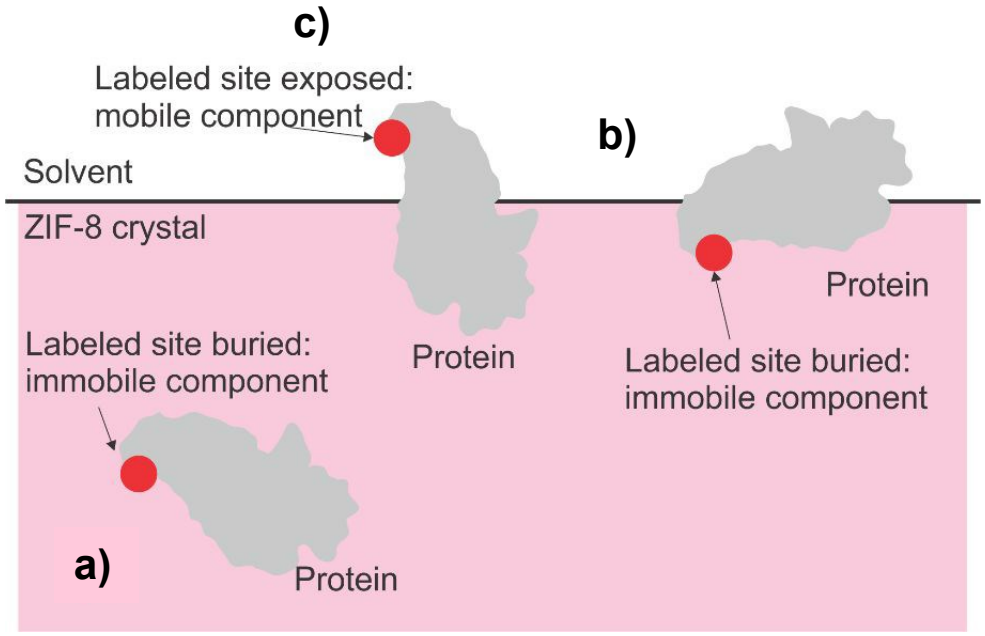

Figure 1.52. Schematic representation of deeply (a) or partially (b) buried and solvent-exposed (c) enzymes. Reprinted with permission from [195]. Copyright 2018 American Chemical Society.

Being able to control enzyme localisation on MOF could enable a fine tuning of substrate selectivity depending on its size and/or affinity to MOFs. In this regard, an orientation keeping the active site away from solvent bulk could favour the accessibility of small substrates over large ones. Conversely, the partial block of the active sites can help discriminating among small substrates with different sizes, whereas an orientation directing the active site towards the solvents is preferred in the case of large substrates.[195]

In situ immobilisation represents a very promising strategy for the synthesis of biomolecule–MOF composites, due to its simple operation (one-step process), wide applicability to a variety of available guest molecules and facile extension to multi-enzyme systems.[196] Since encapsulation occurs concurrently with the synthesis of the support, one-pot immobilisation implies that the support must be capable of being formed in the presence of biomolecules under conditions that do not significatively alter their structure/functionality. Indeed, biomolecules stability is affected by chemical, physical, and biological factors, therefore the immobilisation conditions (temperature, pH, concentrations) need to be carefully evaluated.[161] However, only a few MOFs are synthesised under biocompatible, mild conditions suitable for this immobilisation method.[190] Whenever the synthesis of the support cannot be carried out in aqueous media under mild temperature and pH, post-synthetical immobilisation approaches are indisputably required.[187] This involves additional steps, resulting in the use of more reagents and higher costs. Post-synthetical immobilisation strategies are generally needed for iron(III) trimesate MOFs, whose traditional hydrothermal synthesis conditions are far from biocompatibility, requiring long reaction times, high temperature, high pressure, and acidic pH which would hinder the retention of the biological activity of designed guest molecules.[174,197,198] Hence, applications of iron(III) trimesate MOFs as protein support are often restricted, although the great potentialities of this framework. On the one hand, iron is environmentally benign, non-toxic, and cheap. On the other hand, such MOFs show remarkable air- and water-stability, high specific surface areas (up to 2800 m^2/g), large mesoporous cavities accessible through micropores and permanent porosity. Moreover, iron(III) trimesate possesses intrinsic peroxidase-like activity, therefore it constitutes a nanozymes, namely a nanostructure with enzymatic-like activity.[199] Nanozymes, have attracted great attention because of the lowered costs, improved stability, and excellent recyclability compared to natural enzymes. In this regard, trying to shift MOFs' harsh synthesis conditions to those demanded to avoid the biomolecule denaturation would fully open up their application spectrum. This would eventually result in time-, cost-efficient, and sustainable *in situ* immobilisation approaches which overcome the above-mentioned disadvantages given by post-synthetical strategies. Nevertheless, tailoring the synthetic conditions of support to a bio-friendly level without compromising its textural and structural features represents the one of the main challenges of the one-pot immobilisation approach. To the best of our knowledge, only conventional solution-based strategies have been reported so far to attain one-pot enzyme immobilisation on iron(III) trimesate MOFs. Gascon et al. encapsulated lipase B, GOx, and alcohol dehydrogenase (ADH) during the synthesis of the MOF.[200–202] An enzyme-containing aqueous solution was mixed

with a NaOH solution of trimesic acid. Then, an aqueous solution containing $FeCl_3$ was slowly added. The resulting suspension was stirred for 10 minutes at RT. A similar protocol was followed by Tocco et al. to integrated laccase (LAC) on ZIF-zni and Fe-BTC, finding much higher catalytic activity for ZIF-zni based biocatalyst compared to Fe-BTC.[203] Zhao et al. *in situ* encapsulated GOx on iron(III) trimesate MOF through solution-based synthesis.[204] An aqueous solution containing GOx and PVP was mixed with an ethanolic solution of trimesic acid. Then, an aqueous solution containing ferric chloride was dropwise added, keeping under magnetic stirring for 30 minutes. Analogously, a CAT@Fe-BTC composite was synthesised via *de novo* method by Jing et al.[205] An aqueous solution of the enzyme was added to an ethanolic solution containing trimesic acid. An aqueous solution containing ferric nitrate was then added, keeping the resulting suspension under magnetic stirring for 4 hours. All the above-mentioned protocols required ambient temperature and pressure conditions and relatively short reaction times (from 10 minutes to 4 hours). Nevertheless, enzymes result expose to either organic solvents (ethanol) or NaOH solutions. Moreover, the pH of the resulting suspensions has not been reported. pH is pivotal when dealing with biomolecules, as they can easily undergo upon denaturation and consequent loss of functionality. To fully retain biocatalytic activity, immobilisation strategies using Fe-BTC could be further improved. Also, the contact between the biomolecule and solvent can be minimised, or even completely avoided, by using mechanochemical methods. Very fast kinetics prompted by ultrasounds makes also sonochemical approaches interesting for *de novo* immobilisation. Moreover, the preparation of protein@MOF composites through these alternative methods appeals to industrial scale-up, minimizing the environmental footprint of the process while providing the same efficiency of traditional routes. Nevertheless, neither mechanochemistry nor sonochemistry have been exploited for one-pot encapsulation of biomolecules within iron(III) trimesate structure. Indeed, only a few studies reported the synthesis of iron(III) trimesate MOF via alternative mechanochemical and sonochemical approaches and none of them is conducted under biocompatible conditions. Zadeh et al. prepared a Fe-BTC material via sonochemical method by irradiating a DMF solution of ferric nitrate in DMF and trimesic acid under 50 kHz ultrasound, at 70 °C for 120 min.[127] Furthermore, Pilloni et al. obtained an iron(III) trimesate material by grinding ferric nitrate and trimesic acid with 5 mL of an aqueous solution of tetramethyl ammonium hydroxide for 1 hour.[126] Despite the use of base, the pH remained acidic (pH ≈ 1) throughout the synthesis, similarly to the traditional method. Therefore, huge improvements can be done in order to further widespread the unexpressed potential of alternative methods for one-pot encapsulation of biomolecules.

1.4. Aim of this research

The present Ph.D. research project deals with the development of new synthesis protocols for the preparation of enzymes-MOFs hybrid composite materials using alternative mechanochemical and sonochemical methods under green, mild conditions. In particular, this study focused on the innovative synthesis, characterisation and catalytic determination of GOx@Fe-BTC hybrid composites. One of the advantages of using Fe-BTC, beside its biocompatibility and low cost, is its enzyme-mimic nature. Indeed, enzyme-enzyme mimic cascade reaction can be carried out without requiring the immobilisation of additional peroxidase enzymes. Hence, this MOF does not act as a mere passive platform for the immobilisation of GOx, but rather performs a double function serving as support and concurrently taking part to a tandem reaction. Disordered Fe-BTC was preferred over crystalline MIL-100(Fe) owing to the milder and more sustainable reaction conditions required for its synthesis. Glucose oxidase isolated from the fungus *Aspergillus niger*, also called 1-oxidoreductase, β-D-glucose:oxygen or GOx (EC Number: 1.1.3.4.), is a dimer consisting of two 80 kDa equal subunits (Figure 1.53). Each subunit contains one mole of iron and one flavin adenine dinucleotide (FAD) moiety. GOx is a glycoprotein containing approximately 2% amino sugars and 16% neutral sugar.[206] It also contains 3 cysteine residues and 8 potential sites for N-linked glycosylation.[207]

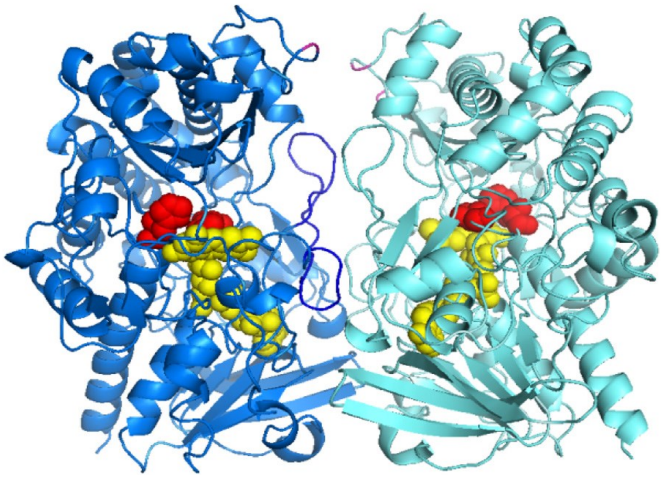

Figure 1.53. Schematic representation of GOx: monomers coloured in dark blue and light blue, FAD in yellow and active sites in red. Reprinted from [213], Copyright 2016, with permission from Elsevier.

GOx catalyses the oxidation of β-D-glucose by molecular oxygen to form hydrogen peroxide and D-glucono-δ-lactone, which subsequently hydrolyses spontaneously to gluconic acid.[208] The reaction can be summarised as follows:

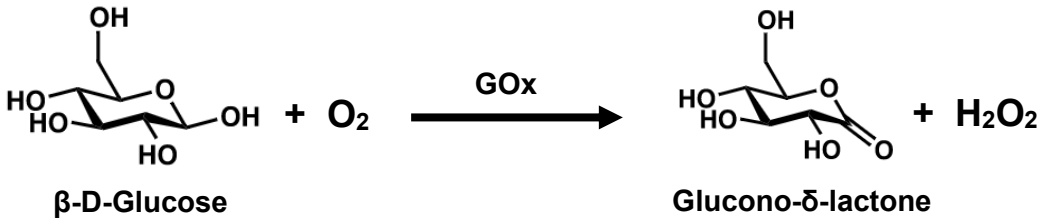

Glucose oxidase is commonly used to accomplish enzymatic determination of D-glucose in solution.[209] Since GOx oxidises β-D-glucose to D-glucono-δ-lactone and hydrogen peroxide, HRP is often exploited as the coupling enzyme in glucose sensing.[210] *In lieu* of peroxidases, peroxidase-mimics can also be employed to catalyse the oxidation of peroxidase substrates, including chromogenic molecules, giving rise to a sensitive colorimetric detection of glucose concentrations.[211] Such peroxidase-mimics include iron(III) trimesate materials. The pH optimum for GOx (isoelectric point: 4.2) is 5.5, while it possesses a broad activity in a pH range between 4 and 7.[212] Conversely, iron(III) trimesate materials possess intrinsic peroxidase-like activity in the pH range 2.5 – 5.0.[61]

Therefore, the first part of this research work dealt with the evaluation of the optimal synthesis conditions enabling a balance between the retainment of both GOx stability/activity and Fe-BTC enzyme-mimic feature, and the preservation of Fe-BTC integrity, robustness, and porosity to efficiently coated the enzyme. The effect of pH on textural properties, thermal stability, and microstructure of Fe-BTC MOF was evaluated. Once determined the best conditions, one-pot synthesis of GOx@Fe-BTC biocomposites have been carried-out via two different synthesis methods, namely mechanochemical and sonochemical approaches. Because of their advantages in terms of reduced reaction times, and minimal use of solvents compared to traditional methods, these alternative methods enable synthesis conditions feasible to preserve biomolecules integrity/functionality.

Then, in the final part of this study, hybrid GOx@Fe-BTC composites prepared via mechanochemical and sonochemical approaches under mild conditions were exploited as biosensors to perform colorimetric detection of glucose. Such a biosensing uses a cascade reaction involving the peroxidase-mimic activity of Fe-BTC and the catalytic activity of GOx. First, GOx catalyses the oxidation of D-glucose, producing D-glucono-δ-lactone and H_2O_2. Then, in the presence of hydrogen peroxide Fe-BTC is able to catalyse the oxidation of chromogenic molecules, such as TMB into its blue-coloured oxidised form (called oxTMB), as shows in Figure 1.54.

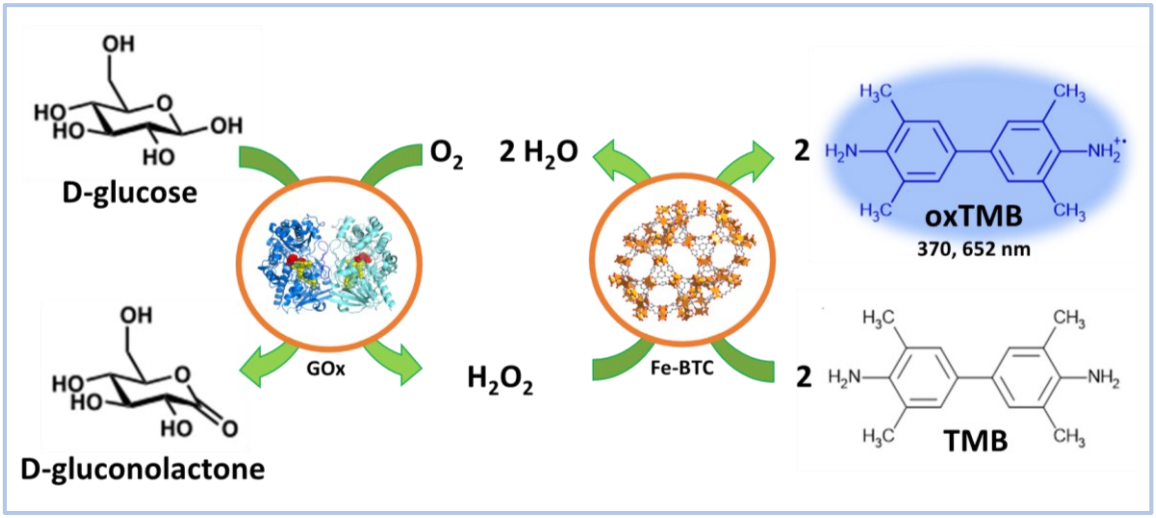

Figure 1.54. Schematic representation of the enzyme-enzyme mimic cascade reaction involving GOx and Fe-BTC. GOx picture is reprinted from [213], Copyright 2016, with permission from Elsevier. Fe-BTC picture is reprinted with permission from [88]. Copyright 2018 American Chemical Society.

TMB is a colourless diamine with absorbance maximum (λ_{max}) at 285 nm. Compared to other peroxidase substrate dyes used for diagnostic purposes (e.g., ABTS and OPD), TMB shows the highest detection sensitivity.[214] The oxidation of TMB by peroxidase or peroxidase-mimic gives rise to coloured products. First, a blue product is obtained, passing through a green stage, and finally a yellow coloration is observed. The blue product arises from the one-electron oxidation of TMB (λ_{max} = 370, 652 nm), whereas the yellow product is the two-electron diimine product (λ_{max} = 450 nm). The one-electron oxidation product of TMB is a radical cation, which is in rapid chemical equilibrium with a charge transfer complex (CTC) consisting of a yellow coloured diimine form (electron acceptor) and a colourless diamine form (electron donor).[215] TMB oxidation product intermediates are depicted in Figure 1.55. Typically, colorimetric sensing using TMB relies on the detection of the one-electron oxidation product of TMB recording the absorbance at 370 or 652 nm. Indeed, a complete and rapid oxidation of TMB into its diimine form requires a large excess of peroxidase/peroxidase-mimic and/or highly acidic conditions (pH = 1) to lead to the complete dissociation of the CTC.[216]

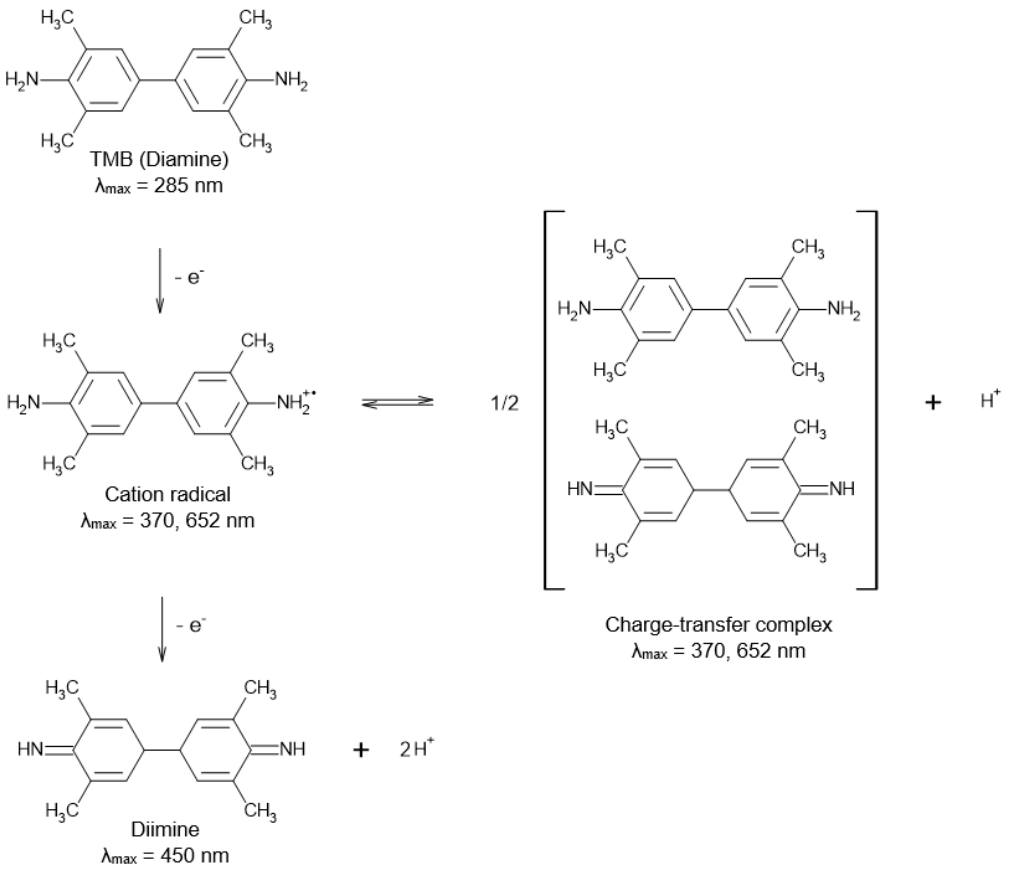

Figure 1.55. Oxidation product intermediates of TMB.

The development of hybrid composites via alternative mechanochemical and sonochemical approaches under *ad hoc* selected mild conditions, aims to minimise the enzyme activity loss during its immobilisation. A full retention of catalytic activity is a key factor in the field of *ex vivo* applications of biomolecules. Therefore, this work looks at a new generation of biomolecule@MOF composites to achieve a green, easy, and sustainable fabrication of highly performing biocatalysts, drug delivery systems, and biosensors.

1.5. References

[1] Hong-Cai, Z.; Jeffrey R., L.; Omar M., Y. Introduction to Metal − Organic Frameworks. *Chem. Rev.* **2012**, *112* (2), 673–674. https://doi.org/https://doi.org/10.1021/cr300014x.

[2] Yaghi, O. M.; Li, H. Hydrothermal Synthesis of a Metal-Organic Framework Containing Large Rectangular Channels. *J. Am. Chem. Soc.* **1995**, *117*, 10401–10402. https://doi.org/https://doi.org/10.1021/ja00146a033.

[3] Safaei, M.; Foroughi, M. M.; Ebrahimpoor, N.; Jahani, S.; Omidi, A.; Khatami, M. A Review on Metal-Organic Frameworks: Synthesis and Applications. *TrAC - Trends Anal. Chem.* **2019**, *118*, 401–425. https://doi.org/10.1016/j.trac.2019.06.007.

[4] Shi, J. Z.; Zhu, X. L.; Li, L.; Chen, X. M. Zeolite Ceramics with Ordered Microporous Structure and High Crystallinity Prepared by Cold Sintering Process. *J. Am. Ceram. Soc.* **2021**, *104* (11), 5521–5528. https://doi.org/10.1111/jace.17964.

[5] Bazargan, M.; Ghaemi, F.; Amiri, A.; Mirzaei, M. Metal–Organic Framework-Based Sorbents in Analytical Sample Preparation. *Coord. Chem. Rev.* **2021**, *445*, 214107. https://doi.org/10.1016/j.ccr.2021.214107.

[6] IUPAC. *Nomenclature of Inorganic Chemistry, IUPAC Recommendations 2005 (the "Red Book").*; 2005.

[7] Jenkins, A. D.; Stepto, R. F. T.; Kratochvíl, P.; Suter, U. W. Glossary of Basic Terms in Polymer Science (IUPAC Recommendations 1996). *Pure Appl. Chem.* **1996**, *68* (12), 2287–2311. https://doi.org/10.1351/pac199668122287.

[8] Batten, S. R.; Champness, N. R.; Chen, X. M.; Garcia-Martinez, J.; Kitagawa, S.; Öhrström, L.; O'Keeffe, M.; Suh, M. P.; Reedijk, J. Terminology of Metal-Organic Frameworks and Coordination Polymers (IUPAC Recommendations 2013). *Pure Appl. Chem.* **2013**, *85* (8), 1715–1724. https://doi.org/10.1351/PAC-REC-12-11-20.

[9] Li, M. M.; Claire, F. J.; Solomos, M. A.; Tenney, S. M.; Ivanov, S. A.; Siegler, M. A.; Kempa, T. J. Molecular Chains of Coordinated Dimolybdenum Isonicotinate Paddlewheel Clusters. *RSC Adv.* **2019**, *9* (29), 16492–16495. https://doi.org/10.1039/c9ra03572a.

[10] Seidel, R. W.; Goddard, R.; Oppel, I. M. Structural Diversity of Metallosupramolecular Assemblies Based on the Bent Bridging Ligand 4,4'-Dithiodipyridine. *Polymers (Basel).* **2013**, *5* (2), 527–575. https://doi.org/10.3390/polym5020527.

[11] Kaye, S. S.; Dailly, A.; Yaghi, O. M.; Long, J. R. Impact of Preparation and Handling on the Hydrogen Storage Properties of Zn4O(1,4-Benzenedicarboxylate)3 (MOF-5). *J. Am. Chem. Soc.* **2007**, *129* (46), 14176–14177. https://doi.org/10.1021/ja076877g.

[12] Furukawa, H.; Cordova, K. E.; O'Keeffe, M.; Yaghi, O. M. The Chemistry and Applications of Metal-Organic Frameworks. *Science* **2013**, *341*, 12304444. https://doi.org/10.1126/science.1230444.

[13] Rocío-Bautista, P.; Taima-Mancera, I.; Pasán, J.; Pino, V. Metal-Organic Frameworks in Green Analytical Chemistry. *Separations* **2019**, *6* (3), 1–21. https://doi.org/10.3390/separations6030033.

[14] Eddaoudi, M.; Kim, J.; Rosi, N.; Vodak, D.; Wachter, J.; O'Keeffe, M.; Yaghi, O. M. Systematic Design of Pore Size and Functionality in Isoreticular MOFs and Their Application in Methane Storage. *Science* **2002**, *295* (5554), 469–472. https://doi.org/10.1126/science.1067208.

[15] Eddaoudi, M.; Moler, D. B.; Li, H.; Chen, B.; Reineke, T. M.; O'Keeffe, M.; Yaghi, O. M. Modular Chemistry: Secondary Building Units as a Basis for the Design of Highly Porous and Robust Metal-Organic Carboxylate Frameworks. *Acc. Chem. Res.* **2001**, *34* (4), 319–330. https://doi.org/10.1021/ar000034b.

[16] Kepert, C. J.; Rosseinsky, M. J. Zeolite-like Crystal Structure of an Empty Microporous Molecular Framework. *Chem. Commun.* **1999**, *536* (4), 375–376. https://doi.org/10.1039/a809746a.

[17] Biradha, K.; Hongo, Y.; Fujita, M. Open Square-Grid Coordination Polymers of the Dimensions 20 × 20 Å: Remarkably Stable and Crystalline Solids Even after Guest Removal. *Angew. Chemie (International Ed. English)* **2000**, *39* (21), 3843–3845. https://doi.org/10.1002/1521-3773(20001103)39:21<3843::aid-anie3843>3.0.co;2-#.

[18] Kalmutzki, M. J.; Hanikel, N.; Yaghi, O. M. Secondary Building Units as the Turning Point in the Development of the Reticular Chemistry of MOFs. *Sci. Adv.* **2018**, *4* (10). https://doi.org/10.1126/sciadv.aat9180.

[19] Kouser, S.; Hezam, A.; Khadri, M. J. N.; Khanum, S. A. A Review on Zeolite Imidazole Frameworks: Synthesis, Properties, and Applications. *J. Porous Mater.* **2022**, *29* (3), 663–681. https://doi.org/10.1007/s10934-021-01184-z.

[20] Perez, E. V.; Karunaweera, C.; Musselman, I. H.; Balkus, K. J.; Ferraris, J. P. Origins and Evolution of Inorganic-Based and MOF-Based Mixed-Matrix Membranes for Gas Separations. *Processes* **2016**, *4* (3).

https://doi.org/10.3390/pr4030032.
[21] Chui, S. S. Y.; Lo, S. M. F.; Charmant, J. P. H.; Orpen, A. G.; Williams, I. D. A Chemically Functionalizable Nanoporous Material [Cu3(TMA)2 (H2O)3](N). *Science* **1999**, *283* (5405), 1148–1150. https://doi.org/10.1126/science.283.5405.1148.
[22] Zhang, Q.; Pramudya, Y.; Wenzel, W.; Wöll, C. Modeling the Layer-by-Layer Growth of HKUST-1 Metal-Organic Framework Thin Films. *Nanomaterials* **2021**, *11* (7). https://doi.org/10.3390/nano11071631.
[23] Zorainy, M. Y.; Gar Alalm, M.; Kaliaguine, S.; Boffito, D. C. Revisiting the MIL-101 Metal-Organic Framework: Design, Synthesis, Modifications, Advances, and Recent Applications. *J. Mater. Chem. A* **2021**, *9* (39), 22159–22217. https://doi.org/10.1039/d1ta06238g.
[24] Zhong, G.; Liu, D.; Zhang, J. Applications of Porous Metal-Organic Framework MIL-100(M) (M = Cr, Fe, Sc, Al, V). *Cryst. Growth Des.* **2018**, *18* (12), 7730–7744. https://doi.org/10.1021/acs.cgd.8b01353.
[25] Rivera-Torrente, M.; Mandemaker, L. D. B.; Filez, M.; Delen, G.; Seoane, B.; Meirer, F.; Weckhuysen, B. M. Spectroscopy, Microscopy, Diffraction and Scattering of Archetypal MOFs: Formation, Metal Sites in Catalysis and Thin Films. *Chem. Soc. Rev.* **2020**, *49* (18), 6694–6732. https://doi.org/10.1039/d0cs00635a.
[26] Li, H.; Eddaoudi, M.; O'Keeffe, M.; Yaghi, O. M. Design and Synthesis of an Exceptionally Stable and Highly. *Nature* **1999**, *402*, 276–279. https://doi.org/https://doi.org/10.1038/46248.
[27] Ru, J.; Wang, X.; Wang, F.; Cui, X.; Du, X.; Lu, X. UiO Series of Metal-Organic Frameworks Composites as Advanced Sorbents for the Removal of Heavy Metal Ions: Synthesis, Applications and Adsorption Mechanism. *Ecotoxicol. Environ. Saf.* **2021**, *208*, 111577. https://doi.org/10.1016/j.ecoenv.2020.111577.
[28] Wei, R.; Gaggioli, C. A.; Li, G.; Islamoglu, T.; Zhang, Z.; Yu, P.; Farha, O. K.; Cramer, C. J.; Gagliardi, L.; Yang, D.; Gates, B. C. Tuning the Properties of Zr 6 O 8 Nodes in the Metal Organic Framework UiO-66 by Selection of Node-Bound Ligands and Linkers. *Chem. Mater.* **2019**, *31* (5), 1655–1663. https://doi.org/10.1021/acs.chemmater.8b05037.
[29] Schoedel, A.; Li, M.; Li, D.; O'Keeffe, M.; Yaghi, O. M. Structures of Metal-Organic Frameworks with Rod Secondary Building Units. *Chem. Rev.* **2016**, *116* (19), 12466–12535. https://doi.org/10.1021/acs.chemrev.6b00346.
[30] Horcajada, P.; Surblé, S.; Serre, C.; Hong, D. Y.; Seo, Y. K.; Chang, J. S.; Grenèche, J. M.; Margiolaki, I.; Férey, G. Synthesis and Catalytic Properties of MIL-100(Fe), an Iron(III) Carboxylate with Large Pores. *Chem. Commun.* **2007**, No. 27, 2820–2822. https://doi.org/10.1039/b704325b.
[31] Mao, Y.; Qi, H.; Ye, G.; Han, L.; Zhou, W.; Xu, W.; Sun, Y. Green and Time-Saving Synthesis of MIL-100(Cr) and Its Catalytic Performance. *Micropor. Mesopor. Mater.* **2019**, *274* (May 2018), 70–75. https://doi.org/10.1016/j.micromeso.2018.07.026.
[32] Mitchell, L.; Gonzalez-Santiago, B.; Mowat, J. P. S.; Gunn, M. E.; Williamson, P.; Acerbi, N.; Clarke, M. L.; Wright, P. A. Remarkable Lewis Acid Catalytic Performance of the Scandium Trimesate Metal Organic Framework MIL-100(Sc) for C-C and C=N Bond-Forming Reactions. *Catal. Sci. Technol.* **2013**, *3* (3), 606–617. https://doi.org/10.1039/c2cy20577g.
[33] Steenhaut, T.; Filinchuk, Y.; Hermans, S. Aluminium-Based MIL-100(Al) and MIL-101(Al) Metal-Organic Frameworks, Derivative Materials and Composites: Synthesis, Structure, Properties and Applications. *J. Mater. Chem. A* **2021**, *9* (38), 21483–21509. https://doi.org/10.1039/d1ta04444c.
[34] Hou, Y.; Mao, H.; Xu, L. MIL-100(V) and MIL-100(V)/RGO with Various Valence States of Vanadium Ions as Sulfur Cathode Hosts for Lithium-Sulfur Batteries. *Nano Res.* **2017**, *10* (1), 344–353. https://doi.org/10.1007/s12274-016-1326-0.
[35] Dhakshinamoorthy, A.; Alvaro, M.; Horcajada, P.; Gibson, E.; Vishnuvarthan, M.; Vimont, A.; Grenèche, J. M.; Serre, C.; Daturi, M.; Garcia, H. Comparison of Porous Iron Trimesates Basolite F300 and MIL-100(Fe) as Heterogeneous Catalysts for Lewis Acid and Oxidation Reactions: Roles of Structural Defects and Stability. *ACS Catal.* **2012**, *2* (10), 2060–2065. https://doi.org/10.1021/cs300345b.
[36] Flores, J. G.; Delgado-García, R.; Sánchez-Sánchez, M. Semiamorphous Fe-BDC: The Missing Link between the Highly-Demanded Iron Carboxylate MOF Catalysts. *Catal. Today* **2022**, *390–391*, 237–245. https://doi.org/10.1016/j.cattod.2021.11.004.
[37] Sanchez-Sanchez, M.; De Asua, I.; Ruano, D.; Diaz, K. Direct Synthesis, Structural Features, and Enhanced Catalytic Activity of the Basolite F300-like Semiamorphous Fe-BTC Framework. *Cryst. Growth Des.* **2015**, *15* (9), 4498–4506. https://doi.org/10.1021/acs.cgd.5b00755.
[38] Guesh, K.; Caiuby, C. A. D.; Mayoral, Á.; Díaz-García, M.; Díaz, I.; Sanchez-Sanchez, M. Sustainable Preparation of MIL-100(Fe) and Its Photocatalytic Behavior in the Degradation of Methyl Orange in Water. *Cryst. Growth Des.* **2017**, *17* (4), 1806–1813. https://doi.org/10.1021/acs.cgd.6b01776.
[39] Sciortino, L.; Alessi, A.; Messina, F.; Buscarino, G.; Gelardi, F. M. Structure of the FeBTC Metal-Organic Framework: A Model Based on the Local Environment Study. *J. Phys. Chem. C* **2015**, *119* (14), 7826–7830. https://doi.org/10.1021/acs.jpcc.5b01336.

[40] Sapnik, A. F.; Bechis, I.; Collins, S. M.; Johnstone, D. N.; Divitini, G.; Smith, A. J.; Chater, P. A.; Addicoat, M. A.; Johnson, T.; Keen, D. A.; Jelfs, K. E.; Bennett, T. D. Mixed Hierarchical Local Structure in a Disordered Metal–Organic Framework. *Nat. Commun.* **2021**, *12*, 2062. https://doi.org/10.1038/s41467-021-22218-9.

[41] Agostoni, V.; Chalati, T.; Horcajada, P.; Willaime, H.; Anand, R.; Semiramoth, N.; Baati, T.; Hall, S.; Maurin, G.; Chacun, H.; Bouchemal, K.; Martineau, C.; Taulelle, F.; Couvreur, P.; Rogez-Kreuz, C.; Clayette, P.; Monti, S.; Serre, C.; Gref, R. Towards an Improved Anti-HIV Activity of NRTI via Metal-Organic Frameworks Nanoparticles. *Adv. Healthc. Mater.* **2013**, *2* (12), 1630–1637. https://doi.org/10.1002/adhm.201200454.

[42] Czaja, A. U.; Trukhan, N.; Müller, U. Industrial Applications of Metal–Organic Frameworks. *Chem. Soc. Rev.* **2009**, *38* (5), 1284–1293. https://doi.org/10.1039/b804680h.

[43] Chu, J.; Wang, Y.; Zhong, F.; Feng, X.; Chen, W.; Ai, X.; Yang, H.; Cao, Y. Metal/ Covalent-organic Frameworks for Electrochemical Energy Storage Applications . *EcoMat* **2021**, No. March 2020. https://doi.org/10.1002/eom2.12133.

[44] Hu, X.; Lou, X.; Li, C.; Ning, Y.; Liao, Y.; Chen, Q.; Mananga, E. S.; Shen, M.; Hu, B. Facile Synthesis of the Basolite F300-like Nanoscale Fe-BTC Framework and Its Lithium Storage Properties. *RSC Adv.* **2016**, *6* (115), 114483–114490. https://doi.org/10.1039/C6RA22738D.

[45] Wang, L.; Han, Y.; Feng, X.; Zhou, J.; Qi, P.; Wang, B. Metal-Organic Frameworks for Energy Storage: Batteries and Supercapacitors. *Coord. Chem. Rev.* **2016**, *307*, 361–381. https://doi.org/10.1016/j.ccr.2015.09.002.

[46] Zhang, Z.; Yoshikawa, H.; Awaga, K. Monitoring the Solid-State Electrochemistry of Cu(2,7-AQDC) (AQDC = Anthraquinone Dicarboxylate) in a Lithium Battery: Coexistence of Metal and Ligand Redox Activities in a Metal-Organic Framework. *J. Am. Chem. Soc.* **2014**, *136* (46), 16112–16115. https://doi.org/10.1021/ja508197w.

[47] Burtch, N. C.; Jasuja, H.; Walton, K. S. Water Stability and Adsorption in Metal-Organic Frameworks. *Chem. Rev.* **2014**, *114* (20), 10575–10612. https://doi.org/10.1021/cr5002589.

[48] Küsgens, P.; Rose, M.; Senkovska, I.; Fröde, H.; Henschel, A.; Siegle, S.; Kaskel, S. Characterization of Metal-Organic Frameworks by Water Adsorption. *Micropor. Mesopor. Mater.* **2009**, *120* (3), 325–330. https://doi.org/10.1016/j.micromeso.2008.11.020.

[49] Seo, Y. K.; Yoon, J. W.; Lee, J. S.; Hwang, Y. K.; Jun, C. H.; Chang, J. S.; Wuttke, S.; Bazin, P.; Vimont, A.; Daturi, M.; Bourrelly, S.; Llewellyn, P. L.; Horcajada, P.; Serre, C.; Férey, G. Energy-Efficient Dehumidification over Hierachically Porous Metal-Organic Frameworks as Advanced Water Adsorbents. *Adv. Mater.* **2012**, *24* (6), 806–810. https://doi.org/10.1002/adma.201104084.

[50] Han, Q.; Wang, Z.; Chen, X.; Jiao, C.; Li, H.; Yu, R. Facile Synthesis of Fe-Based MOFs(Fe-BTC) as Efficient Adsorbent for Water Purifications. *Chem. Res. Chinese Univ.* **2019**, *35* (4), 564–569. https://doi.org/10.1007/s40242-019-8415-z.

[51] Schoenecker, P. M.; Carson, C. G.; Jasuja, H.; Flemming, C. J. J.; Walton, K. S. Effect of Water Adsorption on Retention of Structure and Surface Area of Metal-Organic Frameworks. *Ind. Eng. Chem. Res.* **2012**, *51* (18), 6513–6519. https://doi.org/10.1021/ie202325p.

[52] Silva, M. P.; Ribeiro, A. M.; Silva, C. G.; Ho Cho, K.; Lee, U. H.; Faria, J. L.; Loureiro, J. M.; Chang, J. S.; Rodrigues, A. E.; Ferreira, A. Atmospheric Water Harvesting on MIL-100(Fe) upon a Cyclic Adsorption Process. *Sep. Purif. Technol.* **2022**, *290* (February). https://doi.org/10.1016/j.seppur.2022.120803.

[53] Bellido, E.; Guillevic, M.; Hidalgo, T.; Santander-Ortega, M. J.; Serre, C.; Horcajada, P. Understanding the Colloidal Stability of the Mesoporous MIL-100(Fe) Nanoparticles in Physiological Media. *Langmuir* **2014**, *30* (20), 5911–5920. https://doi.org/10.1021/la5012555.

[54] Li, X.; Lachmanski, L.; Safi, S.; Sene, S.; Serre, C.; Grenèche, J. M.; Zhang, J.; Gref, R. New Insights into the Degradation Mechanism of Metal-Organic Frameworks Drug Carriers. *Sci. Rep.* **2017**, *7* (1), 1–11. https://doi.org/10.1038/s41598-017-13323-1.

[55] Quijia, C. R.; Lima, C.; Silva, C.; Alves, R. C.; Frem, R.; Chorilli, M. Application of MIL-100(Fe) in Drug Delivery and Biomedicine. *J. Drug Deliv. Sci. Technol.* **2021**, *61*, 102217. https://doi.org/10.1016/j.jddst.2020.102217.

[56] Horcajada, P.; Chalati, T.; Serre, C.; Gillet, B.; Sebrie, C.; Baati, T.; Eubank, J. F.; Heurtaux, D.; Clayette, P.; Kreuz, C.; Chang, J. S.; Hwang, Y. K.; Marsaud, V.; Bories, P. N.; Cynober, L.; Gil, S.; Férey, G.; Couvreur, P.; Gref, R. Porous Metal-Organic-Framework Nanoscale Carriers as a Potential Platform for Drug Deliveryand Imaging. *Nat. Mater.* **2010**, *9* (2), 172–178. https://doi.org/10.1038/nmat2608.

[57] Baati, T.; Njim, L.; Neffati, F.; Kerkeni, A.; Bouttemi, M.; Gref, R.; Najjar, M. F.; Zakhama, A.; Couvreur, P.; Serre, C.; Horcajada, P. In Depth Analysis of the in Vivo Toxicity of Nanoparticles of Porous Iron(Iii) Metal–Organic Frameworks. *Chem. Sci.* **2013**, *4* (4), 1597–1607. https://doi.org/10.1039/c3sc22116d.

[58] Simon-Yarza, T.; Giménez-Marqués, M.; Mrimi, R.; Mielcarek, A.; Gref, R.; Horcajada, P.; Serre, C.;

Couvreur, P. A Smart Metal–Organic Framework Nanomaterial for Lung Targeting. *Angew. Chemie - Int. Ed.* **2017**, *56* (49), 15565–15569. https://doi.org/10.1002/anie.201707346.

[59] Mao, D.; Hu, F.; Kenry; Ji, S.; Wu, W.; Ding, D.; Kong, D.; Liu, B. Metal–Organic-Framework-Assisted In Vivo Bacterial Metabolic Labeling and Precise Antibacterial Therapy. *Adv. Mater.* **2018**, *30* (18), 1–7. https://doi.org/10.1002/adma.201706831.

[60] Zimpel, A.; Preiß, T.; Röder, R.; Engelke, H.; Ingrisch, M.; Peller, M.; Rädler, J. O.; Wagner, E.; Bein, T.; Lächelt, U.; Wuttke, S. Imparting Functionality to MOF Nanoparticles by External Surface Selective Covalent Attachment of Polymers. *Chem. Mater.* **2016**, *28* (10), 3318–3326. https://doi.org/10.1021/acs.chemmater.6b00180.

[61] Zhang, J. W.; Zhang, H. T.; Du, Z. Y.; Wang, X.; Yu, S. H.; Jiang, H. L. Water-Stable Metal–Organic Frameworks with Intrinsic Peroxidase-like Catalytic Activity as a Colorimetric Biosensing Platform. *Chem. Commun.* **2014**, *50* (9), 1092–1094. https://doi.org/10.1039/c3cc48398c.

[62] Thakur, B.; Karve, V. V.; Sun, D. T.; Semrau, A. L.; Weiß, L. J. K.; Grob, L.; Fischer, R. A.; Queen, W. L.; Wolfrum, B. An Investigation into the Intrinsic Peroxidase-Like Activity of Fe-MOFs and Fe-MOFs/Polymer Composites. *Adv. Mater. Technol.* **2021**, *6* (5), 2001048. https://doi.org/10.1002/admt.202001048.

[63] Ai, L.; Li, L.; Zhang, C.; Fu, J.; Jiang, J. MIL-53(Fe): A Metal-Organic Framework with Intrinsic Peroxidase-like Catalytic Activity for Colorimetric Biosensing. *Chem. - A Eur. J.* **2013**, *19* (45), 15105–15108. https://doi.org/10.1002/chem.201303051.

[64] Fu, M.; Chai, B.; Yan, J.; Wang, C.; Fan, G.; Song, G.; Xu, F. Facile Preparation of MIL-88B-Fe Metal–Organic Framework with High Peroxidase-like Activity for Colorimetric Detection of Hydrogen Peroxide in Milk and Beer. *Appl. Phys. A Mater. Sci. Process.* **2021**, *127* (12). https://doi.org/10.1007/s00339-021-05082-8.

[65] Ortiz-Gómez, I.; Salinas-Castillo, A.; García, A. G.; Álvarez-Bermejo, J. A.; de Orbe-Payá, I.; Rodríguez-Diéguez, A.; Capitán-Vallvey, L. F. Microfluidic Paper-Based Device for Colorimetric Determination of Glucose Based on a Metal-Organic Framework Acting as Peroxidase Mimetic. *Microchim. Acta* **2018**, *185* (1). https://doi.org/10.1007/s00604-017-2575-7.

[66] Wei, H.; Wang, E. Fe3O4 Magnetic Nanoparticles as Peroxidase Mimetics and Their Applications in H2O2 and Glucose Detection Use of the Novel Properties of Fe3O4 MNPs as Peroxidase. *Anal. Chem.* **2008**, *80* (6), 2250–2254.

[67] Jv, Y.; Li, B.; Cao, R. Positively-Charged Gold Nanoparticles as Peroxidiase Mimic and Their Application in Hydrogen Peroxide and Glucose Detection. *Chem. Commun.* **2010**, *46* (42), 8017–8019. https://doi.org/10.1039/c0cc02698k.

[68] Asati, A.; Santra, S.; Kaittanis, C.; Nath, S.; Perez, J. M. Oxidase-like Activity of Polymer-Coated Cerium Oxide Nanopartieles. *Angew. Chemie - Int. Ed.* **2009**, *48* (13), 2308–2312. https://doi.org/10.1002/anie.200805279.

[69] Garg, B.; Bisht, T.; Ling, Y. C. Graphene-Based Nanomaterials as Efficient Peroxidase Mimetic Catalysts for Biosensing Applications: An Overview. *Molecules* **2015**, *20* (8), 14155–14190. https://doi.org/10.3390/molecules200814155.

[70] Song, Y.; Wang, X.; Zhao, C.; Qu, K.; Ren, J.; Qu, X. Label-Free Colorimetric Detection of Single Nucleotide Polymorphism by Using Single-Walled Carbon Nanotube Intrinsic Peroxidase-like Activity. *Chem. - A Eur. J.* **2010**, *16* (12), 3617–3621. https://doi.org/10.1002/chem.200902643.

[71] Shi, W.; Wang, Q.; Long, Y.; Cheng, Z.; Chen, S.; Zheng, H.; Huang, Y. Carbon Nanodots as Peroxidase Mimetics and Their Applications to Glucose Detection. *Chem. Commun.* **2011**, *47* (23), 6695–6697. https://doi.org/10.1039/c1cc11943e.

[72] Tang, J.; Wang, J. Fe-Based Metal Organic Framework/Graphene Oxide Composite as an Efficient Catalyst for Fenton-like Degradation of Methyl Orange. *RSC Adv.* **2017**, *7* (80), 50829–50837. https://doi.org/10.1039/c7ra10145g.

[73] Wang, S. A Comparative Study of Fenton and Fenton-like Reaction Kinetics in Decolourisation of Wastewater. *Dye. Pigment.* **2008**, *76* (3), 714–720. https://doi.org/10.1016/j.dyepig.2007.01.012.

[74] Yang, Y.; Shen, D.; Long, Y.; Xie, Z.; Zheng, H. Intrinsic Peroxidase-like Activity of Ficin. *Sci. Rep.* **2017**, *7* (February), 1–8. https://doi.org/10.1038/srep43141.

[75] Sellami, K.; Couvert, A.; Nasrallah, N.; Maachi, R.; Abouseoud, M.; Amrane, A. Peroxidase Enzymes as Green Catalysts for Bioremediation and Biotechnological Applications: A Review. *Sci. Total Environ.* **2022**, *806*. https://doi.org/10.1016/j.scitotenv.2021.150500.

[76] Veitch, N. C. Horseradish Peroxidase: A Modern View of a Classic Enzyme. *Phytochemistry* **2004**, *65* (3), 249–259. https://doi.org/10.1016/j.phytochem.2003.10.022.

[77] Lopes, G. R.; Pinto, D. C. G. A.; Silva, A. M. S. Horseradish Peroxidase (HRP) as a Tool in Green Chemistry. *RSC Adv.* **2014**, *4* (70), 37244–37265. https://doi.org/10.1039/c4ra06094f.

[78] Patra, S.; Hidalgo Crespo, T.; Permyakova, A.; Sicard, C.; Serre, C.; Chaussé, A.; Steunou, N.; Legrand,

L. Design of Metal Organic Framework-Enzyme Based Bioelectrodes as a Novel and Highly Sensitive Biosensing Platform. *J. Mater. Chem. B* **2015**, *3* (46), 8983–8992. https://doi.org/10.1039/c5tb01412c.
[79] Ebralidze, I. I.; Laschuk, N. O.; Poisson, J.; Zenkina, O. V. *Colorimetric Sensors and Sensor Arrays*; Elsevier Inc., 2019. https://doi.org/10.1016/B978-0-12-814505-0.00001-1.
[80] Hall, J. N.; Bollini, P. Structure, Characterization, and Catalytic Properties of Open-Metal Sites in Metal Organic Frameworks. *Reaction Chemistry and Engineering*. Royal Society of Chemistry February 1, 2019, pp 207–222. https://doi.org/10.1039/c8re00228b.
[81] Yoon, J. W.; Seo, Y. K.; Hwang, Y. K.; Chang, J. S.; Leclerc, H.; Wuttke, S.; Bazin, P.; Vimont, A.; Daturi, M.; Bloch, E.; Llewellyn, P. L.; Serre, C.; Horcajada, P.; Grenèche, J. M.; Rodrigues, A. E.; Férey, G. Controlled Reducibility of a Metal-Organic Framework with Coordinatively Unsaturated Sites for Preferential Gas Sorption. *Angew. Chemie - Int. Ed.* **2010**, *49* (34), 5949–5952. https://doi.org/10.1002/anie.201001230.
[82] Msahel, A.; Galiano, F.; Pilloni, M.; Russo, F.; Hafiane, A.; Castro-Muñoz, R.; Kumar, V. B.; Gedanken, A.; Ennas, G.; Porat, Z.; Scano, A.; Ben Hamouda, S.; Figoli, A. Exploring the Effect of Iron Metal-Organic Framework Particles in Polylactic Acid Membranes for the Azeotropic Separation of Organic/Organic Mixtures by Pervaporation. *Membranes* **2021**, *11* (1), 1–18. https://doi.org/10.3390/membranes11010065.
[83] Anastas, P. T.; Warner, J. C. *Green Chemistry: Theory and Practice*; Oxford University Press, New York, 1998.
[84] Anastas, P. T. Meeting the Challenges to Sustainability through Green Chemistry. *Green Chem.* **2003**, *5* (2), 29–34. https://doi.org/10.1039/b211620k.
[85] *https://www.un.org/sustainabledevelopment*.
[86] Anastas, P.; Eghbali, N. Green Chemistry: Principles and Practice. *Chem. Soc. Rev.* **2010**, *39* (1), 301–312. https://doi.org/10.1039/b918763b.
[87] Sheldon, R. A. The E Factor: Fifteen Years On. *Green Chem.* **2007**, *9* (12), 1273–1283. https://doi.org/10.1039/b713736m.
[88] Fan, G.; Dundas, C. M.; Zhang, C.; Lynd, N. A.; Keitz, B. K. Sequence-Dependent Peptide Surface Functionalization of Metal-Organic Frameworks. *ACS Appl. Mater. Interfaces* **2018**, *10* (22), 18601–18609. https://doi.org/10.1021/acsami.8b05148.
[89] Canioni, R.; Roch-Marchal, C.; Sécheresse, F.; Horcajada, P.; Serre, C.; Hardi-Dan, M.; Férey, G.; Grenèche, J. M.; Lefebvre, F.; Chang, J. S.; Hwang, Y. K.; Lebedev, O.; Turner, S.; Van Tendeloo, G. Stable Polyoxometalate Insertion within the Mesoporous Metal Organic Framework MIL-100(Fe). *J. Mater. Chem.* **2011**, *21* (4), 1226–1233. https://doi.org/10.1039/c0jm02381g.
[90] García Márquez, A.; Demessence, A.; Platero-Prats, A. E.; Heurtaux, D.; Horcajada, P.; Serre, C.; Chang, J. S.; Férey, G.; De La Peña-O'Shea, V. A.; Boissière, C.; Grosso, D.; Sanchez, C. Green Microwave Synthesis of MIL-100(Al, Cr, Fe) Nanoparticles for Thin-Film Elaboration. *Eur. J. Inorg. Chem.* **2012**, *100* (32), 5165–5174. https://doi.org/10.1002/ejic.201200710.
[91] Seo, Y. K.; Yoon, J. W.; Lee, J. S.; Lee, U. H.; Hwang, Y. K.; Jun, C. H.; Horcajada, P.; Serre, C.; Chang, J. S. Large Scale Fluorine-Free Synthesis of Hierarchically Porous Iron(III) Trimesate MIL-100(Fe) with a Zeolite MTN Topology. *Micropor. Mesopor. Mater.* **2012**, *157*, 137–145. https://doi.org/10.1016/j.micromeso.2012.02.027.
[92] Abdelkareem, M. A.; Abbas, Q.; Mouselly, M.; Alawadhi, H.; Olabi, A. G. High-Performance Effective Metal–Organic Frameworks for Electrochemical Applications. *J. Sci. Adv. Mater. Devices* **2022**, *7* (3), 100465. https://doi.org/10.1016/j.jsamd.2022.100465.
[93] Anumah, A.; Louis, H.; Magu, T. O.; Amos, P. I. Metal-Organic Frameworks (MOFs): Recent Advances in Synthetic Methodologies and Some Applications. *Chem. Methodol.* **2019**, No. January 2019. https://doi.org/10.22034/CHEMM.2018.139807.1067.
[94] Lee, Y. R.; Kim, J.; Ahn, W. S. Synthesis of Metal-Organic Frameworks: A Mini Review. *Korean J. Chem. Eng.* **2013**, *30* (9), 1667–1680. https://doi.org/10.1007/s11814-013-0140-6.
[95] Stock, N.; Biswas, S. Synthesis of Metal-Organic Frameworks (MOFs): Routes to Various MOF Topologies, Morphologies, and Composites. *Chem. Rev.* **2012**, *112* (2), 933–969. https://doi.org/10.1021/cr200304e.
[96] Mueller, U.; Puetter, H.; Hesse, M.; Schubert, M.; Wessel, H.; Huff, J.; Guzmann, M.; Organic. Method for Electrochemical Production of a Crystalline Porous Metal Organic Skeleton Material, Google Patents, 2011.
[97] Schlesinger, M.; Schulze, S.; Hietschold, M.; Mehring, M. Evaluation of Synthetic Methods for Microporous Metal-Organic Frameworks Exemplified by the Competitive Formation of [Cu2(Btc)3(H2O)3] and [Cu2(Btc)(OH)(H2O)]. *Micropor. Mesopor. Mater.* **2010**, *132* (1–2), 121–127. https://doi.org/10.1016/j.micromeso.2010.02.008.
[98] Hangxun, X.; Zeiger, B. W.; Suslick, K. S. Sonochemical Synthesis of Nanomaterials. *Chem. Soc. Rev.*

2013, *42* (7), 2555–2567. https://doi.org/10.1039/c2cs35282f.
[99] Son, W. J.; Kim, J.; Kim, J.; Ahn, W. S. Sonochemical Synthesis of MOF-5. *Chem. Commun.* **2008**, No. 47, 6336–6338. https://doi.org/10.1039/b814740j.
[100] Bang, J. H.; Suslick, K. S. Applications of Ultrasound to the Synthesis of Nanostructured Materials. *Adv. Mater.* **2010**, *22* (10), 1039–1059. https://doi.org/10.1002/adma.200904093.
[101] Gedanken, A. Using Sonochemistry for the Fabrication of Nanomaterials. *Ultrason. Sonochem.* **2004**, *11* (2), 47–55. https://doi.org/10.1016/j.ultsonch.2004.01.037.
[102] Hussein, E. M.; Khairou, K. S. Sonochemistry: Synthesis of Bioactive Heterocycles. *Synth. Commun.* **2014**, *44* (15), 2155–2191. https://doi.org/10.1080/00397911.2014.893360.
[103] Zinoviadou, K. G.; Galanakis, C. M.; Brnčić, M.; Grimi, N.; Boussetta, N.; Mota, M. J.; Saraiva, J. A.; Patras, A.; Tiwari, B.; Barba, F. J. Fruit Juice Sonication: Implications on Food Safety and Physicochemical and Nutritional Properties. *Food Res. Int.* **2015**, *77*, 743–752. https://doi.org/10.1016/j.foodres.2015.05.032.
[104] Gogate, P. R.; Sutkar, V. S.; Pandit, A. B. Sonochemical Reactors: Important Design and Scale up Considerations with a Special Emphasis on Heterogeneous Systems. *Chem. Eng. J.* **2011**, *166* (3), 1066–1082. https://doi.org/10.1016/j.cej.2010.11.069.
[105] Horie, K.; Barón, M.; Fox, R. B.; He, J.; Hess, M.; Kahovec, J.; Kitayama, T.; Kubisa, P.; Maréchal, E.; Mormann, W.; Stepto, R. F. T.; Tabak, D.; Vohlídal, J.; Wilks, E. S.; Work, W. J. Definitions of Terms Relating to Reactions of Polymers and to Functional Polymeric Materials: (IUPAC Recommendations 2003). *Pure Appl. Chem.* **2004**, *76* (4), 889–906. https://doi.org/10.1351/pac200476040889.
[106] Colacino, E.; Ennas, G.; Halasz, I.; Porcheddu, A.; Scano, A. *Mechanochemistry - A Practical Introduction from Soft to Hard Materials*; De Gruyter, 2020.
[107] Tan, D.; García, F. Main Group Mechanochemistry: From Curiosity to Established Protocols. *Chem. Soc. Rev.* **2019**, *48* (8), 2274–2292. https://doi.org/10.1039/c7cs00813a.
[108] James, S. L.; Adams, C. J.; Bolm, C.; Braga, D.; Collier, P.; Frišcic, T.; Grepioni, F.; Harris, K. D. M.; Hyett, G.; Jones, W.; Krebs, A.; Mack, J.; Maini, L.; Orpen, A. G.; Parkin, I. P.; Shearouse, W. C.; Steed, J. W.; Waddell, D. C. Mechanochemistry: Opportunities for New and Cleaner Synthesis. *Chem. Soc. Rev.* **2012**, *41* (1), 413–447. https://doi.org/10.1039/c1cs15171a.
[109] Pichon, A.; Lazuen-Garay, A.; James, S. L. Solvent-Free Synthesis of a Microporous Metal-Organic Framework. *CrystEngComm* **2006**, *8* (3), 211–214. https://doi.org/10.1039/b513750k.
[110] Howard, J. L.; Cao, Q.; Browne, D. L. Mechanochemistry as an Emerging Tool for Molecular Synthesis: What Can It Offer? *Chem. Sci.* **2018**, *9* (12), 3080–3094. https://doi.org/10.1039/c7sc05371a.
[111] Mateti, S.; Mathesh, M.; Liu, Z.; Tao, T.; Ramireddy, T.; Glushenkov, A. M.; Yang, W.; Chen, Y. I. Mechanochemistry: A Force in Disguise and Conditional Effects towards Chemical Reactions. *Chem. Commun.* **2021**, *57* (9), 1080–1092. https://doi.org/10.1039/d0cc06581a.
[112] Porcheddu, A.; Colacino, E.; De Luca, L.; Delogu, F. Metal-Mediated and Metal-Catalyzed Reactions under Mechanochemical Conditions. *ACS Catal.* **2020**, *10* (15), 8344–8394. https://doi.org/10.1021/acscatal.0c00142.
[113] Martina, K.; Rotolo, L.; Porcheddu, A.; Delogu, F.; Bysouth, S. R.; Cravotto, G.; Colacino, E. High Throughput Mechanochemistry: Application to Parallel Synthesis of Benzoxazines. *Chem. Commun.* **2018**, *54* (5), 551–554. https://doi.org/10.1039/c7cc07758k.
[114] Chen, W.; Schoenitz, M.; Ward, T. S.; Dave, R. N.; Dreizin, E. L. Numerical Simulation of Mechanical Alloying in a Shaker Mill by Discrete Element Method. *KONA Powder Part. J.* **2005**, *23* (March), 152–162. https://doi.org/10.14356/kona.2005018.
[115] Crawford, D.; Casaban, J.; Haydon, R.; Giri, N.; McNally, T.; James, S. L. Synthesis by Extrusion: Continuous, Large-Scale Preparation of MOFs Using Little or No Solvent. *Chem. Sci.* **2015**, *6* (3), 1645–1649. https://doi.org/10.1039/c4sc03217a.
[116] Leonardi, M.; Villacampa, M.; Menéndez, J. C. Multicomponent Mechanochemical Synthesis. *Chem. Sci.* **2018**, *9* (8), 2042–2064. https://doi.org/10.1039/c7sc05370c.
[117] Michalchuk, A. A. L.; Tumanov, I. A.; Boldyreva, E. V. Ball Size or Ball Mass-What Matters in Organic Mechanochemical Synthesis? *CrystEngComm* **2019**, *21* (13), 2174–2179. https://doi.org/10.1039/c8ce02109k.
[118] Hernández, J. G.; Bolm, C. Altering Product Selectivity by Mechanochemistry. *J. Org. Chem.* **2017**, *82* (8), 4007–4019. https://doi.org/10.1021/acs.joc.6b02887.
[119] Andersen, J.; Mack, J. Mechanochemistry and Organic Synthesis: From Mystical to Practical. *Green Chem.* **2018**, *20* (7), 1435–1443. https://doi.org/10.1039/c7gc03797j.
[120] Garay, A. L.; Pichon, A.; James, S. L. Solvent-Free Synthesis of Metal Complexes. *Chem. Soc. Rev.* **2007**, *36* (6), 846–855. https://doi.org/10.1039/b600363j.
[121] Do, J. L.; Friščić, T. Mechanochemistry: A Force of Synthesis. *ACS Cent. Sci.* **2017**, *3* (1), 13–19. https://doi.org/10.1021/acscentsci.6b00277.

[122] Tan, D.; Loots, L.; Friščić, T. Towards Medicinal Mechanochemistry: Evolution of Milling from Pharmaceutical Solid Form Screening to the Synthesis of Active Pharmaceutical Ingredients (APIs). *Chem. Commun.* **2016**, *52* (50), 7760–7781. https://doi.org/10.1039/c6cc02015a.

[123] Bowmaker, G. A. Solvent-Assisted Mechanochemistry. *Chem. Commun.* **2013**, *49* (4), 334–348. https://doi.org/10.1039/c2cc35694e.

[124] Fernández-Bertrán, J.; Reguera, E. Mechanochemical Reactions in Alkali Halide Pressed Disks. *Solid State Ionics* **1997**, *93*, 139–146.

[125] Tao, L.; Han, J.; Tao, F. M. Correlations and Predictions of Carboxylic Acid PKa Values Using Intermolecular Structure and Properties of Hydrogen-Bonded Complexes. *J. Phys. Chem. A* **2008**, *112* (4), 775–782. https://doi.org/10.1021/jp710291c.

[126] Pilloni, M.; Padella, F.; Ennas, G.; Lai, S.; Bellusci, M.; Rombi, E.; Sini, F.; Pentimalli, M.; Delitala, C.; Scano, A.; Cabras, V.; Ferino, I. Liquid-Assisted Mechanochemical Synthesis of an Iron Carboxylate Metal Organic Framework and Its Evaluation in Diesel Fuel Desulfurization. *Micropor. Mesopor. Mater.* **2015**, *213*, 14–21. https://doi.org/10.1016/j.micromeso.2015.04.005.

[127] Hossein Zadeh, M.; Keramati, N.; Mehdipour Ghazi, M. Ultrasonic-Assisted Synthesis of New Photocatalyst Based on Fe–Benzenetricarboxylic (Fe–BTC) Metal Organic Framework: Characterization and Photocatalytic Properties. *J. Iran. Chem. Soc.* **2019**, *16* (2), 401–409. https://doi.org/10.1007/s13738-018-1519-4.

[128] Cooper, G. M. *The Cell: A Molecular Approach*, 2nd editio.; Sinauer Associates, Ed.; Sunderland (MA), 2000.

[129] Bhavaniramya, S.; Ramar, V.; Vishnupriya, Selvaraju Premkumar, K.; Al-Aboody, Mohammad S. Vijayakumar, Rajendran Dharmar, B. Enzyme Immobilization on Nanomaterials for Biosensor and Biocatalyst in Food and Biomedical Industry. *Curr. Pharm. Des.* **2019**, *25* (24), 2661–2676. https://doi.org/10.2174/1381612825666190712181403.

[130] Xia, H.; Li, N.; Zhong, X.; Jiang, Y. Metal-Organic Frameworks: A Potential Platform for Enzyme Immobilization and Related Applications. *Front. Bioeng. Biotechnol.* **2020**, *8*, 1–16. https://doi.org/10.3389/fbioe.2020.00695.

[131] Lian, X.; Fang, Y.; Joseph, E.; Wang, Q.; Li, J.; Banerjee, S.; Lollar, C.; Wang, X.; Zhou, H. C. Enzyme-MOF (Metal-Organic Framework) Composites. *Chem. Soc. Rev.* **2017**, *46* (11), 3386–3401. https://doi.org/10.1039/c7cs00058h.

[132] Tosa, T.; Mori, T.; Fuse, N.; Chibata, I. Studies on Continuous Enzyme Reactions. I. Screening of Carriers for Preparation of Water-Insoluble Aminoacylase. *Enzymologia* **1966**, *31* (4), 214–224.

[133] Bornscheuer, U. T. Immobilizing Enzymes: How to Create More Suitable Biocatalysts. *Angew. Chemie - Int. Ed.* **2003**, *42* (29), 3336–3337. https://doi.org/10.1002/anie.200301664.

[134] Mateo, C.; Palomo, J. M.; Fernandez-Lorente, G.; Guisan, J. M.; Fernandez-Lafuente, R. Improvement of Enzyme Activity, Stability and Selectivity via Immobilization Techniques. *Enzyme Microb. Technol.* **2007**, *40* (6), 1451–1463. https://doi.org/10.1016/j.enzmictec.2007.01.018.

[135] Homaei, A. A.; Sariri, R.; Vianello, F.; Stevanato, R. Enzyme Immobilization: An Update. *J. Chem. Biol.* **2013**, *6* (4), 185–205. https://doi.org/10.1007/s12154-013-0102-9.

[136] Raja, D. S.; Liu, W. L.; Huang, H. Y.; Lin, C. H. Immobilization of Protein on Nanoporous Metal-Organic Framework Materials. *Comments Inorg. Chem.* **2015**, *35* (6), 331–349. https://doi.org/10.1080/02603594.2015.1059827.

[137] Petrikovics, I.; Hong, K.; Omburo, G.; Hu, Q. Z.; Pei, L.; McGuinn, W. D.; Sylvester, D.; Tamulinas, C.; Papahadjopoulos, D.; Jaszberenyi, J. C.; Way, J. L. Antagonism of Paraoxon Intoxication by Recombinant Phosphotriesterase Encapsulated within Sterically Stabilized Liposames. *Toxicol. Appl. Pharmacol.* **1999**, *156* (1), 56–63. https://doi.org/10.1006/taap.1998.8620.

[138] Yarosh, D. B.; O'Connor, A.; Alas, L.; Potten, C.; Wolf, P. Photoprotection by Topical DNA Repair Enzymes: Molecular Correlates of Clinical Studies. *Photochem. Photobiol.* **1999**, *69* (2), 136–140. https://doi.org/10.1111/j.1751-1097.1999.tb03265.x.

[139] Jørgensen, K.; Kiebler, T.; Hylander, I.; Vermehren, C. Interaction of a Lipid-Membrane Destabilizing Enzyme with PEG-Liposomes. *Int. J. Pharm.* **1999**, *183* (1), 21–24. https://doi.org/10.1016/S0378-5173(99)00036-8.

[140] Giang, I.; Boland, E. L.; Poon, G. M. K. Prodrug Applications for Targeted Cancer Therapy. *AAPS J.* **2014**, *16* (5), 899–913. https://doi.org/10.1208/s12248-014-9638-z.

[141] Lian, X.; Huang, Y.; Zhu, Y.; Fang, Y.; Zhao, R.; Joseph, E.; Li, J.; Pellois, J. P.; Zhou, H. C. Enzyme-MOF Nanoreactor Activates Nontoxic Paracetamol for Cancer Therapy. *Angew. Chemie - Int. Ed.* **2018**, *57* (20), 5725–5730. https://doi.org/10.1002/anie.201801378.

[142] Truppo, M. D.; Hughes, G. Development of an Improved Immobilized CAL-B for the Enzymatic Resolution of a Key Intermediate to Odanacatib. *Org. Process Res. Dev.* **2011**, *15* (5), 1033–1035. https://doi.org/10.1021/op200157c.

[143] Habimana, J. de D.; Ji, J.; Sun, X. Minireview: Trends in Optical-Based Biosensors for Point-Of-Care Bacterial Pathogen Detection for Food Safety and Clinical Diagnostics. *Anal. Lett.* **2018**, *51* (18), 2933–2966. https://doi.org/10.1080/00032719.2018.1458104.
[144] Hart, J. P.; Serban, S.; Jones, L. J.; Biddle, N.; Pittson, R.; Drago, G. A. Selective and Rapid Biosensor Integrated into a Commercial Hand-Held Instrument for the Measurement of Ammonium Ion in Sewage Effluent. *Anal. Lett.* **2006**, *39* (8), 1657–1667. https://doi.org/10.1080/00032710600713545.
[145] Gazel, N.; Yildiz, H. B. Enzyme-Based Biosensors in Food Industry via Surface Modifications. *Surf. Treat. Biol. Chem. Phys. Appl.* **2016**, 227–252. https://doi.org/10.1002/9783527698813.ch7.
[146] Verma, M. L. Nanobiotechnology Advances in Enzymatic Biosensors for the Agri-Food Industry. *Environ. Chem. Lett.* **2017**, *15* (4), 555–560. https://doi.org/10.1007/s10311-017-0640-4.
[147] Si, P. Hierarchically Structured One- Dimensional TiO 2 for Protein Glucose Sensing. *ACS Nano* **2011**, *5* (9), 7617–7626.
[148] Kim, J.; Sung, G. Y.; Park, M. Efficient Portable Urea Biosensor Based on Urease Immobilized Membrane for Monitoring of Physiological Fluids. *Biomedicines* **2020**, *8* (12), 1–11. https://doi.org/10.3390/biomedicines8120596.
[149] Singh, S.; Solanki, P. R.; Pandey, M. K.; Malhotra, B. D. Cholesterol Biosensor Based on Cholesterol Esterase, Cholesterol Oxidase and Peroxidase Immobilized onto Conducting Polyaniline Films. *Sensors Actuators, B Chem.* **2006**, *115* (1), 534–541. https://doi.org/10.1016/j.snb.2005.10.025.
[150] Wang, L.; Wang, E. A Novel Hydrogen Peroxide Sensor Based on Horseradish Peroxidase Immobilized on Colloidal Au Modified ITO Electrode. *Electrochem. commun.* **2004**, *6* (2), 225–229. https://doi.org/10.1016/j.elecom.2003.12.004.
[151] Kim, C. S.; Choi, B. H.; Seo, J. H.; Lim, G.; Cha, H. J. Mussel Adhesive Protein-Based Whole Cell Array Biosensor for Detection of Organophosphorus Compounds. *Biosens. Bioelectron.* **2013**, *41* (1), 199–204. https://doi.org/10.1016/j.bios.2012.08.022.
[152] Achparaki, M.; Thessalonikeos, E.; Tsoukali, H.; Mastrogianni, O.; Zaggelidou, E.; Chatzinikolaou, F.; Vasilliades, N.; Raikos, N.; Isabirye, M.; Raju, D. V. .; Kitutu, M.; Yemeline, V.; Deckers, J.; J. Poesen Additional. Micro- and Nanocarriers for Immobilization of Enzymes. *Intech* **2012**, 13.
[153] Basso, A.; Serban, S. Industrial Applications of Immobilized Enzymes—A Review. *Mol. Catal.* **2019**, *479* (August). https://doi.org/10.1016/j.mcat.2019.110607.
[154] Rajangam, B.; Daniel, D. K.; Krastanov, A. I. Progress in Enzyme Inhibition Based Detection of Pesticides. *Eng. Life Sci.* **2018**, *18* (1), 4–19. https://doi.org/10.1002/elsc.201700028.
[155] Tacias-Pascacio, V. G.; Ortiz, C.; Rueda, N.; Berenguer-Murcia, Á.; Acosta, N.; Aranaz, I.; Civera, C.; Fernandez-Lafuente, R.; Alcántara, A. R. Dextran Aldehyde in Biocatalysis: More than a Mere Immobilization System. *Catalysts* **2019**, *9* (7). https://doi.org/10.3390/catal9070622.
[156] Datta, S.; Christena, L. R.; Rajaram, Y. R. S. Enzyme Immobilization: An Overview on Techniques and Support Materials. *3 Biotech* **2013**, *3* (1), 1–9. https://doi.org/10.1007/s13205-012-0071-7.
[157] Lee, K. Y.; Yuk, S. H. Polymeric Protein Delivery Systems. *Prog. Polym. Sci.* **2007**, *32* (7), 669–697. https://doi.org/10.1016/j.progpolymsci.2007.04.001.
[158] Hudson, S.; Magner, E.; Cooney, J.; Kieran, B. Methodology for the Immobilization of Enzymes onto Mesoporous Materials. *J. Phys. Chem. B* **2005**, *109* (41), 19496–19506. https://doi.org/10.1021/jp052102n.
[159] Hudson, S.; Cooney, J.; Magner, E. Proteins in Mesoporous Silicates. *Angew. Chemie - Int. Ed.* **2008**, *47* (45), 8582–8594. https://doi.org/10.1002/anie.200705238.
[160] Chen, Y.; Han, S.; Li, X.; Zhang, Z.; Ma, S. Why Does Enzyme Not Leach from Metal-Organic Frameworks (MOFs)? Unveiling the Interactions between an Enzyme Molecule and a MOF. *Inorg. Chem.* **2014**, *53* (19), 10006–10008. https://doi.org/10.1021/ic501062r.
[161] Liang, W.; Wied, P.; Carraro, F.; Sumby, C. J.; Nidetzky, B.; Tsung, C. K.; Falcaro, P.; Doonan, C. J. Metal-Organic Framework-Based Enzyme Biocomposites. *Chem. Rev.* **2021**, *121* (3), 1077–1129. https://doi.org/10.1021/acs.chemrev.0c01029.
[162] Wu, X.; Ge, J.; Yang, C.; Hou, M.; Liu, Z. Facile Synthesis of Multiple Enzyme-Containing Metal-Organic Frameworks in a Biomolecule-Friendly Environment. *Chem. Commun.* **2015**, *51* (69), 13408–13411. https://doi.org/10.1039/c5cc05136c.
[163] Bilal, M.; Adeel, M.; Rasheed, T.; Iqbal, H. M. N. Multifunctional Metal-Organic Frameworks-Based Biocatalytic Platforms: Recent Developments and Future Prospects. *J. Mater. Res. Technol.* **2019**, *8* (2), 2359–2371. https://doi.org/10.1016/j.jmrt.2018.12.001.
[164] Zhao, M.; Li, Y.; Ma, X.; Xia, M.; Zhang, Y. Talanta Adsorption of Cholesterol Oxidase and Entrapment of Horseradish Peroxidase in Metal-Organic Frameworks for the Colorimetric Biosensing of Cholesterol. *Talanta* **2019**, *200*, 293–299. https://doi.org/10.1016/j.talanta.2019.03.060.
[165] Dong, S.; Peng, L.; Wei, W.; Huang, T. Three MOF-Templated Carbon Nanocomposites for Potential Platforms of Enzyme Immobilization with Improved Electrochemical Performance. *ACS Appl. Mater.*

Interfaces **2018**, *10* (17), 14665–14672. https://doi.org/10.1021/acsami.8b00702.
[166] Zhong, X.; Xia, H.; Huang, W.; Li, Z.; Jiang, Y. Biomimetic Metal-Organic Frameworks Mediated Hybrid Multi-Enzyme Mimic for Tandem Catalysis. *Chem. Eng. J.* **2020**, *381*, 122758. https://doi.org/10.1016/j.cej.2019.122758.
[167] Badoei-dalfard, A.; Sohrabi, N.; Karami, Z.; Sargazi, G. Fabrication of an Efficient and Sensitive Colorimetric Biosensor Based on Uricase/ Th-MOF for Uric Acid Sensing in Biological Samples. *Biosens. Bioelectron.* **2019**, *141*, 111420. https://doi.org/10.1016/j.bios.2019.111420.
[168] Zhang, T.; Wang, L.; Gao, C.; Zhao, C.; Wang, Y.; Wang, J. Hemin Immobilized into Metal-Organic Frameworks as an Electrochemical Biosensor for 2,4,6-Trichlorophenol. *Nanotechnology* **2018**, *29* (7), 74003. https://doi.org/10.1088/1361-6528/aaa26e.
[169] Liu, W. L.; Yang, N. S.; Chen, Y. T.; Lirio, S.; Wu, C. Y.; Lin, C. H.; Huang, H. Y. Lipase-Supported Metal-Organic Framework Bioreactor Catalyzes Warfarin Synthesis. *Chem. - A Eur. J.* **2015**, *21* (1), 115–119. https://doi.org/10.1002/chem.201405252.
[170] Cao, Y.; Wu, Z.; Wang, T.; Xiao, Y.; Huo, Q.; Liu, Y. Immobilization of: Bacillus Subtilis Lipase on a Cu-BTC Based Hierarchically Porous Metal-Organic Framework Material: A Biocatalyst for Esterification. *Dalt. Trans.* **2016**, *45* (16), 6998–7003. https://doi.org/10.1039/c6dt00677a.
[171] Ren, S.; Feng, Y.; Wen, H.; Li, C.; Sun, B.; Cui, J.; Jia, S. Immobilized Carbonic Anhydrase on Mesoporous Cruciate Flower-like Metal Organic Framework for Promoting CO2 Sequestration. *Int. J. Biol. Macromol.* **2018**, *117*, 189–198. https://doi.org/10.1016/j.ijbiomac.2018.05.173.
[172] Wei, T. H.; Wu, S. H.; Huang, Y. Da; Lo, W. S.; Williams, B. P.; Chen, S. Y.; Yang, H. C.; Hsu, Y. S.; Lin, Z. Y.; Chen, X. H.; Kuo, P. E.; Chou, L. Y.; Tsung, C. K.; Shieh, F. K. Rapid Mechanochemical Encapsulation of Biocatalysts into Robust Metal–Organic Frameworks. *Nat. Commun.* **2019**, *10*, 5002. https://doi.org/10.1038/s41467-019-12966-0.
[173] Chen, Y.; Li, P.; Modica, J. A.; Drout, R. J.; Farha, O. K. Acid-Resistant Mesoporous Metal-Organic Framework toward Oral Insulin Delivery: Protein Encapsulation, Protection, and Release. *J. Am. Chem. Soc.* **2018**, *140* (17), 5678–5681. https://doi.org/10.1021/jacs.8b02089.
[174] Li, X.; Semiramoth, N.; Hall, S.; Tafani, V.; Josse, J.; Laurent, F.; Salzano, G.; Foulkes, D.; Brodin, P.; Majlessi, L.; Ghermani, N. E.; Maurin, G.; Couvreur, P.; Serre, C.; Bernet-Camard, M. F.; Zhang, J.; Gref, R. Compartmentalized Encapsulation of Two Antibiotics in Porous Nanoparticles: An Efficient Strategy to Treat Intracellular Infections. *Part. Part. Syst. Charact.* **2019**, *36* (3), 1–9. https://doi.org/10.1002/ppsc.201800360.
[175] Wang, S.; McGuirk, C. M.; Ross, M. B.; Wang, S.; Chen, P.; Xing, H.; Liu, Y.; Mirkin, C. A. General and Direct Method for Preparing Oligonucleotide-Functionalized Metal-Organic Framework Nanoparticles. *J. Am. Chem. Soc.* **2017**, *139* (29), 9827–9830. https://doi.org/10.1021/jacs.7b05633.
[176] He, C.; Lu, K.; Liu, D.; Lin, W. Nanoscale Metal-Organic Frameworks for the Co-Delivery of Cisplatin and Pooled SiRNAs to Enhance Therapeutic Efficacy in Drug-Resistant Ovarian Cancer Cells. *J. Am. Chem. Soc.* **2014**, *136* (14), 5181–5184. https://doi.org/10.1021/ja4098862.
[177] Feng, Y.; Wang, H.; Zhang, S.; Zhao, Y.; Gao, J.; Zheng, Y.; Zhao, P.; Zhang, Z.; Zaworotko, M. J.; Cheng, P.; Ma, S.; Chen, Y. Antibodies@MOFs: An In Vitro Protective Coating for Preparation and Storage of Biopharmaceuticals. *Adv. Mater.* **2019**, *31* (2), 1–7. https://doi.org/10.1002/adma.201805148.
[178] Riccò, R.; Liang, W.; Li, S.; Gassensmith, J. J.; Caruso, F.; Doonan, C.; Falcaro, P. Metal-Organic Frameworks for Cell and Virus Biology: A Perspective. *ACS Nano* **2018**, *12* (1), 13–23. https://doi.org/10.1021/acsnano.7b08056.
[179] Hanefeld, U.; Gardossi, L.; Magner, E. Understanding Enzyme Immobilisation. *Chem. Soc. Rev.* **2009**, *38* (2), 453–468. https://doi.org/10.1039/b711564b.
[180] Lykourinou, V.; Chen, Y.; Wang, X.; Meng, L.; Hoang, T.; Ming, L.; Musselman, R. L.; Ma, S. Immobilization of MP-11 into a Mesoporous Metal-Organic Framework, MP-11@mesoMOF: A New Platform for Enzymatic Catalysis. *J. Am. Chem. Soc.* **2011**, *133* (27), 10382–10385. https://doi.org/10.1021/ja2038003.
[181] Mehta, J.; Bhardwaj, N.; Bhardwaj, S. K.; Kim, K. H.; Deep, A. Recent Advances in Enzyme Immobilization Techniques: Metal-Organic Frameworks as Novel Substrates. *Coord. Chem. Rev.* **2016**, *322*, 30–40. https://doi.org/10.1016/j.ccr.2016.05.007.
[182] Liu, W. L.; Lo, S. H.; Singco, B.; Yang, C. C.; Huang, H. Y.; Lin, C. H. Novel Trypsin-FITC@MOF Bioreactor Efficiently Catalyzes Protein Digestion. *J. Mater. Chem. B* **2013**, *1* (7), 928–932. https://doi.org/10.1039/c3tb00257h.
[183] Lu, S. W.; Thirlway, J.; Micklefield, J. Direct Site-Selective Covalent Protein Immobilization Catalyzed by a Phosphopantetheinyl Transferase. *J. Am. Chem. Soc.* **2008**, *130* (37), 12456–12464. https://doi.org/10.1021/ja8030278.
[184] Guisan, J. M. *Immobilization of Enzymes and Cells*, 2nd Editio.; Humana Press: Totowa, NJ, 2006. https://doi.org/10.1007/978-1-59745-053-9.

[185] Shih, Y. H.; Lo, S. H.; Yang, N. S.; Singco, B.; Cheng, Y. J.; Wu, C. Y.; Chang, I. H.; Huang, H. Y.; Lin, C. H. Trypsin-Immobilized Metal-Organic Framework as a Biocatalyst in Proteomics Analysis. *Chempluschem* **2012**, *77* (11), 982–986. https://doi.org/10.1002/cplu.201200186.
[186] Deng, H.; Grunder, S.; Cordova, K. E.; Valente, C.; Furukawa, H.; Hmadeh, M.; Gándara, F.; Whalley, A. C.; Liu, Z.; Asahina, S.; Kazumori, H.; O'Keeffe, M.; Terasaki, O.; Stoddart, J. F.; Yaghi, O. M. Large-Pore Apertures in a Series of Metal-Organic Frameworks. *Science* **2012**, *336*, 1018–1023. https://doi.org/10.1017/cbo9781139167291.033.
[187] Asunción Molina, M.; Gascón-Pérez, V.; Sánchez-Sánchez, M.; Blanco, R. M. Sustainable One-Pot Immobilization of Enzymes in/on Metal-Organic Framework Materials. *Catalysts* **2021**, *11*, 1002. https://doi.org/10.3390/catal11081002.
[188] Chen, Y.; Lykourinou, V.; Vetromile, C.; Hoang, T.; Ming, L. J.; Larsen, R. W.; Ma, S. How Can Proteins Enter the Interior of a MOF? Investigation of Cytochrome c Translocation into a MOF Consisting of Mesoporous Cages with Microporous Windows. *J. Am. Chem. Soc.* **2012**, *134* (32), 13188–13191. https://doi.org/10.1021/ja305144x.
[189] Huo, J.; Aguilera-Sigalat, J.; El-Hankari, S.; Bradshaw, D. Magnetic MOF Microreactors for Recyclable Size-Selective Biocatalysis. *Chem. Sci.* **2015**, *6* (3), 1938–1943. https://doi.org/10.1039/c4sc03367a.
[190] Lyu, F.; Zhang, Y.; Zare, R. N.; Ge, J.; Liu, Z. One-Pot Synthesis of Protein-Embedded Metal − Organic Frameworks with Enhanced Biological Activities. *Nano Lett.* **2014**, *14*, 5761–5765. https://doi.org/10.1021/nl5026419.
[191] Shieh, F. K.; Wang, S. C.; Yen, C. I.; Wu, C. C.; Dutta, S.; Chou, L. Y.; Morabito, J. V.; Hu, P.; Hsu, M. H.; Wu, K. C. W.; Tsung, C. K. Imparting Functionality to Biocatalysts via Embedding Enzymes into Nanoporous Materials by a de Novo Approach: Size-Selective Sheltering of Catalase in Metal-Organic Framework Microcrystals. *J. Am. Chem. Soc.* **2015**, *137* (13), 4276–4279. https://doi.org/10.1021/ja513058h.
[192] Liang, K.; Ricco, R.; Doherty, C. M.; Styles, M. J.; Bell, S.; Kirby, N.; Mudie, S.; Haylock, D.; Hill, A. J.; Doonan, C. J.; Falcaro, P. Biomimetic Mineralization of Metal-Organic Frameworks as Protective Coatings for Biomacromolecules. *Nat. Commun.* **2015**, *6*, 1–8. https://doi.org/10.1038/ncomms8240.
[193] Liao, F. S.; Lo, W. S.; Hsu, Y. S.; Wu, C. C.; Wang, S. C.; Shieh, F. K.; Morabito, J. V.; Chou, L. Y.; Wu, K. C. W.; Tsung, C. K. Shielding against Unfolding by Embedding Enzymes in Metal-Organic Frameworks via a de Novo Approach. *J. Am. Chem. Soc.* **2017**, *139* (19), 6530–6533. https://doi.org/10.1021/jacs.7b01794.
[194] Liang, K.; Coghlan, C. J.; Bell, S. G.; Doonan, C.; Falcaro, P. Enzyme Encapsulation in Zeolitic Imidazolate Frameworks: A Comparison between Controlled Co-Precipitation and Biomimetic Mineralisation. *Chem. Commun.* **2016**, *52* (3), 473–476. https://doi.org/10.1039/c5cc07577g.
[195] Pan, Y.; Li, H.; Farmakes, J.; Xiao, F.; Chen, B.; Ma, S.; Yang, Z. How Do Enzymes Orient When Trapped on Metal-Organic Framework (MOF) Surfaces? *J. Am. Chem. Soc.* **2018**, *140* (47), 16032–16036. https://doi.org/10.1021/jacs.8b09257.
[196] Wu, X.; Hou, M.; Ge, J. Metal-Organic Frameworks and Inorganic Nanoflowers: A Type of Emerging Inorganic Crystal Nanocarrier for Enzyme Immobilization. *Catal. Sci. Technol.* **2015**, *5* (12), 5077–5085. https://doi.org/10.1039/c5cy01181g.
[197] Bikiaris, N. D.; Ainali, N. M.; Christodoulou, E.; Kostoglou, M.; Kehagias, T.; Papasouli, E.; Koukaras, E. N.; Nanaki, S. G. Dissolution Enhancement and Controlled Release of Paclitaxel Drug via a Hybrid Nanocarrier Based on Mpeg-Pcl Amphiphilic Copolymer and Fe-Btc Porous Metal-Organic Framework. *Nanomaterials* **2020**, *10* (12), 1–30. https://doi.org/10.3390/nano10122490.
[198] Lajevardi, A.; Hossaini Sadr, M.; Badiei, A.; Armaghan, M. Synthesis and Characterization of Fe3O4@SiO2@MIL-100(Fe) Nanocomposite: A Nanocarrier for Loading and Release of Celecoxib. *J. Mol. Liq.* **2020**, *307*, 112996. https://doi.org/10.1016/j.molliq.2020.112996.
[199] Cheng, H.; Zhang, L.; He, J.; Guo, W.; Zhou, Z.; Zhang, X.; Nie, S.; Wei, H. Integrated Nanozymes with Nanoscale Proximity for in Vivo Neurochemical Monitoring in Living Brains. *Anal. Chem.* **2016**, *88* (10), 5489–5497. https://doi.org/10.1021/acs.analchem.6b00975.
[200] Gascón, V.; Jiménez, M. B.; Blanco, R. M.; Sanchez-Sanchez, M. Semi-Crystalline Fe-BTC MOF Material as an Efficient Support for Enzyme Immobilization. *Catal. Today* **2018**, *304*, 119–126. https://doi.org/10.1016/j.cattod.2017.10.022.
[201] Gascón, V.; Carucci, C.; Jiménez, M. B.; Blanco, R. M.; Sánchez-Sánchez, M.; Magner, E. Rapid In Situ Immobilization of Enzymes in Metal–Organic Framework Supports under Mild Conditions. *ChemCatChem* **2017**, *9* (7), 1182–1186. https://doi.org/10.1002/cctc.201601342.
[202] Carucci, C.; Bruen, L.; Gascón, V.; Paradisi, F.; Magner, E. Significant Enhancement of Structural Stability of the Hyperhalophilic ADH from Haloferax Volcanii via Entrapment on Metal Organic Framework Support. *Langmuir* **2018**, *34* (28), 8274–8280. https://doi.org/10.1021/acs.langmuir.8b01037.
[203] Tocco, D.; Carucci, C.; Todde, D.; Shortall, K.; Otero, F.; Sanjust, E.; Magner, E.; Salis, A. Enzyme

Immobilization on Metal Organic Frameworks: Laccase from Aspergillus Sp. Is Better Adapted to ZIF-Zni Rather than Fe-BTC. *Colloids Surfaces B Biointerfaces* **2021**, *208*, 112147. https://doi.org/10.1016/j.colsurfb.2021.112147.

[204] Zhao, Z.; Pang, J.; Liu, W.; Lin, T.; Ye, F.; Zhao, S. A Bifunctional Metal Organic Framework of Type Fe(III)-BTC for Cascade (Enzymatic and Enzyme-Mimicking) Colorimetric Determination of Glucose. *Microchim. Acta* **2019**, *186* (5). https://doi.org/10.1007/s00604-019-3416-7.

[205] Jing, Y.; Li, J.; Zhang, X.; Sun, M.; Lei, Q.; Li, B.; Yang, J.; Li, H.; Li, C.; Yang, X.; Xie, L. Catalase-Integrated Metal-Organic Framework with Synergetic Catalytic Activity for Colorimetric Sensing. *Environ. Res.* **2022**, *207*, 112147. https://doi.org/10.1016/j.envres.2021.112147.

[206] Tsuge, H.; Natsuaki, O.; Ohashi, K. Purification, Properties, and Molecular Features of Glucose Oxidase from Aspergillus Niger. *J. Biochem.* **1975**, *78* (4), 835–843. https://doi.org/10.1093/oxfordjournals.jbchem.a130974.

[207] Frederick, K. R.; Tung, J.; Emerick, R. S.; Masiarz, F. R.; Chamberlain, S. H.; Vasavada, A.; Rosenberg, S.; Chakraborty, S.; Schopter, L. M.; Massey, V. Glucose Oxidase from Aspergillus Niger. Cloning, Gene Sequence, Secretion from Saccharomyces Cerevisiae and Kinetic Analysis of a Yeast-Derived Enzyme. *J. Biol. Chem.* **1990**, *265* (7), 3793–3802. https://doi.org/10.1016/s0021-9258(19)39664-4.

[208] Leskovac, V.; Trivić, S.; Wohlfahrt, G.; Kandrač, J.; Peričin, D. Glucose Oxidase from Aspergillus Niger: The Mechanism of Action with Molecular Oxygen, Quinones, and One-Electron Acceptors. *Int. J. Biochem. Cell Biol.* **2005**, *37* (4), 731–750. https://doi.org/10.1016/j.biocel.2004.10.014.

[209] Yee, Y. C.; Hashim, R.; Mohd Yahya, A. R.; Bustami, Y. Colorimetric Analysis of Glucose Oxidase-magnetic Cellulose Nanocrystals (CNCS) for Glucose Detection. *Sensors (Switzerland)* **2019**, *19* (11), 1–12. https://doi.org/10.3390/s19112511.

[210] Lian, X.; Chen, Y. P.; Liu, T. F.; Zhou, H. C. Coupling Two Enzymes into a Tandem Nanoreactor Utilizing a Hierarchically Structured MOF. *Chem. Sci.* **2016**, *7* (12), 6969–6973. https://doi.org/10.1039/c6sc01438k.

[211] Chen, Y.; Zhong, Q.; Wang, Y.; Yuan, C.; Qin, X.; Xu, Y. Colorimetric Detection of Hydrogen Peroxide and Glucose by Exploiting the Peroxidase-like Activity of Papain. *RSC Adv.* **2019**, *9* (29), 16566–16570. https://doi.org/10.1039/c9ra03111a.

[212] Pazur, J. H.; Kleppe, K. The Oxidation of Glucose and Related Compounds by Glucose Oxidase from Aspergillus Niger. *Biochemistry* **1964**, *3* (4), 578–583. https://doi.org/10.1021/bi00892a018.

[213] Janati-fard, F.; Reza, M.; Monhemi, H. Investigation of Structural Stability and Enzymatic Activity of Glucose Oxidase and Its Subunits. *J. Mol. Catal. B Enzym.* **2016**, *134*, 16–24. https://doi.org/10.1016/j.molcatb.2016.09.008.

[214] Hosoda, H.; Takasaki, W.; Oe, T.; Tsukamoto, R.; Nambara, T. A Comparison of Chromogenic Substrates for Horseradish Peroxidase as a Label in Steroid Enzyme Immunoassay. *Chem. Pharm. Bull.* **1986**, *34* (10), 4177–4182. https://doi.org/10.1248/cpb.34.4177.

[215] Josephy, P. D.; Eling, T.; Mason, R. P. The Horseradish Peroxidase-Catalyzed Oxidation of 3,5,3',5'-Tetramethylbenzidine. Free Radical and Charge-Transfer Complex Intermediates. *J. Biol. Chem.* **1982**, *257* (7), 3669–3675. https://doi.org/10.1016/s0021-9258(18)34832-4.

[216] Bally, R. W.; Gribnau, T. C. J. Some Aspects of the Chromogen 3, 3', 5, 5'-Tetramethylbenzidine as Hydrogen Donor in a Horseradish Peroxidase Assay. *Clin. Chem. Lab. Med.* **1989**, *27* (10), 791–796. https://doi.org/10.1515/cclm.1989.27.10.791.

Chapter 2:

Mechanochemical synthesis, characterisation, and intrinsic peroxidase-like activity of Fe-BTC

2. Mechanochemical synthesis, characterisation, and intrinsic peroxidase-like activity of Fe-BTC

2.1. Experimental section

2.1.1. Reagents and materials

Iron(III) nitrate nonahydrate ($Fe(NO_3)_3 \cdot 9H_2O$, 98%), tetramethyl ammonium hydroxide pentahydrate ($TMAOH \cdot 5H_2O$, 97%), 1,3,5-benzenetricarboxylic acid (H_3BTC, 95%), hydrogen peroxide solution (H_2O_2, 30% (w/w) in H_2O), 3,3′,5,5′-tetramethylbenzidine (TMB, ≥99%), glacial acetic acid (AcOH, ≥99%), sodium acetate trihydrate ($NaAc \cdot 3H_2O$), Ethanol (EtOH, ≥99.8%), and horseradish peroxidase (EC 1.11.1.7) were supplied by Sigma-Aldrich and used as received without further purification. Valsartan ((S)-3-methyl-2-(N-{[2′-(2H-1,2,3,4-tetrazol-5-yl)biphenyl-4-yl]methyl} pentanamido) butanoic acid) was supplied by Novartis.

2.1.2. Synthesis

1.29 g of $Fe(NO_3)_3 \cdot 9H_2O$, 0.47 g of H_3BTC, proper amounts of $TMAOH \cdot 5H_2O$ (1.63, 1.81 or 1.99 g to obtain a pH of 3, 4 or 5, respectively), and 13.7 g of zirconia balls were placed in a 32 mL stainless-steel Teflon coated grinding jar. No additional solvents were added. The reaction mixture was grinded using a Spex 8000 Mixer/Mill (Figure 2.1). Then, the resulting dense, orange-coloured slurry was dispersed in 20 mL of Milli-Q deionised water. The pH of the obtained dispersion was measured. The dispersion was centrifugated for 10 min at 2500 rpm, the precipitate was washed twice with Milli-Q deionised water, and finally dried. The resulting dry orange sample was collected and stored.

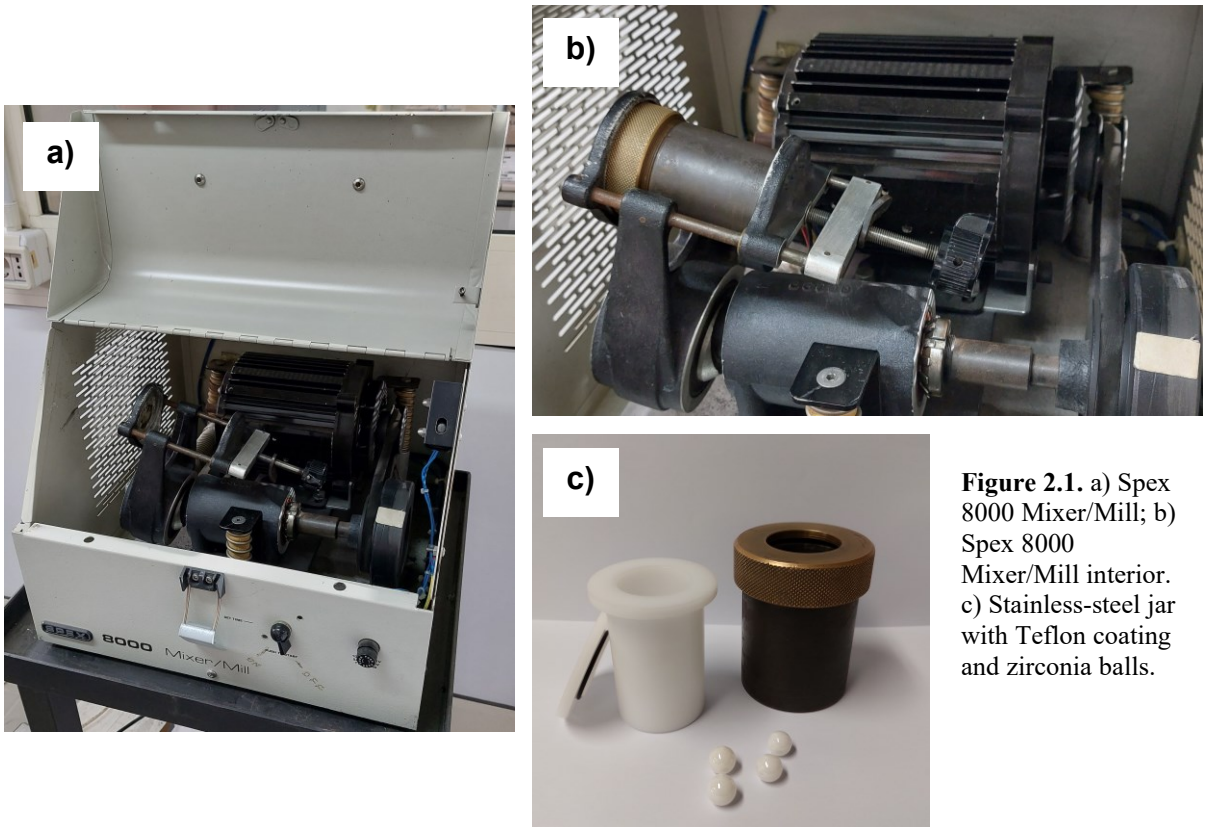

Figure 2.1. a) Spex 8000 Mixer/Mill; b) Spex 8000 Mixer/Mill interior. c) Stainless-steel jar with Teflon coating and zirconia balls.

To identify the most suitable conditions for the *in situ* immobilisation of biomolecules during MOF mechanosynthesis, the effect of different synthesis parameters on the properties of the material was investigated. In particular, the use of balls with different sizes was evaluated (5- and 10-mm diameter). Synthesis was performed in a range of grinding time from 6 to 60 minutes. Several drying conditions were also explored, such as air-drying at room temperature and freeze-drying (samples were stored at -80 °C prior to lyophilisation) to identify the best sample storage conditions. Indeed, freeze drying, also called lyophilisation, offers several advantages in terms of storage stability and product shelf-life. It is a three-stage process consisting in removing water from frozen samples by sublimation and desorption. Firstly, (i) an initial freezing step leads to the formation of ice nuclei which separate from the solute phase. Then, (ii) ice is removed by sublimation. Finally, (iii) remaining water is desorbed by increasing the temperature.[1]

For comparison purposes, a LAG synthesis using 4 mL of deionised water as solvent was also carried out.

In a typical NG synthesis, 10-mm diameter zirconia balls are employed, the reaction mixture is grinded for 1 hour and samples are dried under air at room temperature, unless otherwise stated.

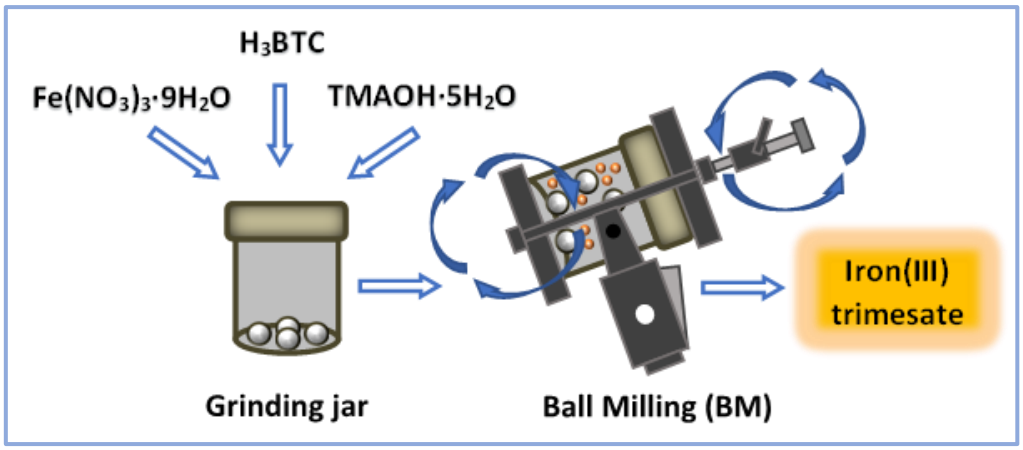

Figure 2.2. Schematic representation of a mechanochemical synthesis of Fe-BTC MOF.

2.1.3. Characterisation

Fourier-transform infrared (FT-IR) spectra were recorded using a Bruker Tensor 27 spectrophotometer within the 400-4000 cm^{-1} scanning range. X-ray powder diffraction (XRPD) patterns were collected on a Bruker D8 Advance Diffractometer using Cu-Kα radiation (λ = 1.54056 Å, I = 30 mA, V = 40 kV) in a scanning range between 7° and 80° 2-theta (step size = 0.05° 2-theta). Due to the high iron fluorescence radiation emission stimulated by the Kα copper radiation, to obtain a satisfactory signal-to-noise ratio in the XRPD pattern an appropriate acquisition time was selected. Differential scanning calorimetry analysis (DSC) and thermogravimetric analysis (TGA) were carried out on a Perkin-Elmer STA 6000 simultaneous thermal analyser in a temperature range between 25 and 850 °C (heating rate = 10 °C/min) under O_2 flow (40 mL/min). Scanning electron microscopy (SEM) images were obtained on a FEI Quanta 200 microscope. N_2 physisorption was performed on a Sorptomatic 1990 CE apparatus (Fisons Instruments) at -196 °C. Prior to measurement, all the samples were outgassed at 150 °C under vacuum for 17 h. Pore size distribution was estimated by using Horvath-Kavazoe (HK) equation to the adsorption branches of the N_2 isotherms. Specific Surface Area (SSA) was determined from adsorption data by applying Dubinin-Radushkevich (DR) method.

2.1.4. Evaluation of the intrinsic peroxidase-mimic activity of Fe-BTC

To evaluate the intrinsic peroxidase-like activity of Fe-BTC, four reaction systems were examined: (1) Fe-BTC (250 μg/mL), TMB (0.4 mM) and H_2O_2 (0.5 mM) in acetate buffer (10

mM, pH = 4); (2) Fe-BTC (250 μg/mL), and TMB (0.4 mM) in acetate buffer (10 mM, pH = 4); (3) TMB (0.4 mM) and H_2O_2 (0.5 mM) in acetate buffer (10 mM, pH = 4); (4) TMB (0.4 mM) in acetate buffer (10 mM, pH = 4). The solution mixtures were incubated at 35 °C under magnetic stirring (150 rpm) for 1 hour. Then, the test samples were centrifugated at 5000 rpm for 10 minutes and supernatants were collected. Absorbance spectra of the supernatants were collected from 500 to 800 nm on a BioTek Synergy H1 Plate Reader.

2.1.5. pH, temperature, catalyst concentration and incubation time dependence on Fe-BTC peroxidase-mimic activity

pH profile of Fe-BTC peroxidase-mimic activity was examined over the pH range 3 – 5 (acetate buffer, 10 mM). Experiments were performed by adding Fe-BTC (250 μg/mL) or free HRP (0.2 ng/mL), TMB (0.4 mM) and H_2O_2 (0.5 mM) in the appropriate buffer. The solution mixtures were incubated at 35 °C under magnetic stirring (150 rpm) for 1 hour. The influence of temperature on the peroxidase-mimic activity of Fe-BTC was investigated in the temperature range between 25 and 55 °C. Experiments were carried out by adding Fe-BTC (250 μg/mL) or HRP (0.2 ng/mL), TMB (0.4 mM) and H_2O_2 (0.5 mM) in acetate buffer (10 mM, pH = 4). The solution mixtures were incubated at the appropriate temperature under magnetic stirring (150 rpm) for 1 hour. Incubation time dependence on Fe-BTC peroxidase-mimic activity was evaluated considering a time range between 30 and 120 minutes. Experiments were carried out by adding Fe-BTC (250 μg/mL), TMB (0.4 mM) and H_2O_2 (0.5 mM) in acetate buffer (10 mM, pH = 4). The solution mixtures were incubated at 35 °C under magnetic stirring (150 rpm) for the appropriate incubation time. The effect of Fe-BTC concentration on its peroxidase-mimic activity was considered. Experiments were carried out by adding different concentration of Fe-BTC (250, 500 or 800 μg/mL), TMB (0.4 mM) and H_2O_2 (0.5 mM) in acetate buffer (10 mM, pH = 4). The solution mixtures were incubated at 35 °C under magnetic stirring (150 rpm) for 1 hour.

After the appropriate incubation time, the test samples of all above-mentioned experiments were centrifugated at 5000 rpm for 10 minutes and supernatants were collected. Absorbance of the supernatants was then recorded at 652 nm on a BioTek Synergy H1 Plate Reader. All measurements were performed in triplicate and the average value reported.

The relative activity was calculated using the following formula:[2]

$$Relative\ activity\ (\%) = \frac{A}{A_{max}} \times 100\%$$

where A_{max} is the maximum absorbance recorded, and A is the absorbance measured at same conditions.

2.1.6. Colorimetric biosensing of H_2O_2

A dose-response curve for H_2O_2 detection (A_{652nm} vs H_2O_2 conc.) using Fe-BTC under the optimum conditions was obtained. Experiments were carried out by adding Fe-BTC (250 μg/mL), TMB (0.4 mM) and different concentrations of H_2O_2 (0-200 μM) in acetate buffer (10 mM, pH = 4). The solution mixtures were incubated at 35 °C under magnetic stirring (150 rpm) for 1 hour. Then, the test samples were centrifugated at 5000 rpm for 10 minutes and supernatants were collected. Absorbance of the supernatants was then recorded at 652 nm on a BioTek Synergy H1 Plate Reader. All measurements were performed in triplicate and the average value reported.

The limit of detection (LOD) and the limit of quantification (LOQ) for H_2O_2 were calculated by using the following equations:[3]

$$LOD = \frac{3\sigma}{s} \qquad ; \qquad LOQ = \frac{10\sigma}{s}$$

where σ denotes the standard deviation of ten blank tests and s represents the slope of the calibration curve.

2.1.7. Steady-state kinetic assay

Kinetic parameters of peroxidase-mimic Fe-BTC and horseradish peroxidase were evaluated by varying the concentration of one substrate at a fixed concentration of the second substrate. Experiments were carried out at room temperature in acetate buffer (10 mM; pH = 4) using Fe-BTC (250 μg/mL) or HRP (1 ng/mL) with a fixed concentration of TMB (0.2 mM) and varying concentrations of H_2O_2 (0.25 – 6 mM) or a fixed concentration of H_2O_2 (0.5 mM) and different concentrations of TMB (0.1 – 0.8 mM). The change in absorbance at 652 nm was monitored on a BioTek Synergy H1 Plate Reader for 180 sec. According to Michaelis−Menten equation:[4]

$$V_0 = \frac{V_{max} \cdot [S]}{K_m + [S]}$$

Where [S] is the substrate (TMB or H_2O_2) concentration and V_0 is the initial velocity. Moreover,

$$V_0 = \frac{\Delta A}{\Delta t \cdot \epsilon}$$

Where ΔA is the change in absorbance, Δt is the time variation and ε is the molar extinction coefficient (oxTMB molar extinction coefficient, $\varepsilon_{652nm} = 3.9 \times 10^4\ M^{-1}\ cm^{-1}$).[5]

The Michaelis–Menten constant (K_m) and the maximum reaction rate (V_{max}) can be calculated by using the double reciprocal of Michaelis−Menten equation:

$$\frac{1}{V_0} = \frac{K_m}{V_{max}} \frac{1}{[S]} + \frac{1}{V_{max}}$$

The plot $1/V_0$ vs. $1/[S]$ (known as Lineweaver–Burk or double reciprocal plot) is linear. V_{max} is obtained from the intercept and K_m is calculated from the slope.[4]

2.1.8. Drug encapsulation

Preliminary studies on the application of the mechanochemically-prepared Fe-BTC material as drug-delivery system were also carried out. Valsartan, an angiotensin II receptor type 1 antagonists widely used in treatment of hypertension, heart failure, myocardial infarction, and diabetic nephropathy,[6] was selected.

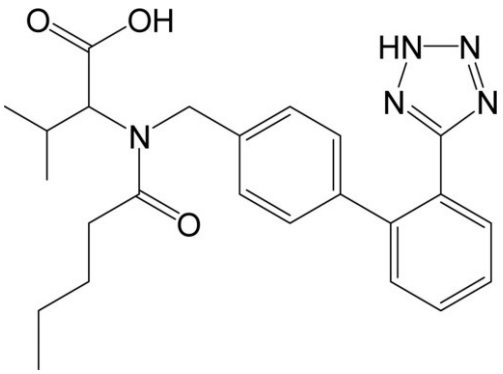

Figure 2.3. Chemical structure of Valsartan.

The encapsulation of Valsartan was performed by a simple impregnation method. Valsartan was dispersed into 10 mL of ethanol with a concentration of 10 mg/L, and then, 5 mg of Fe-BTC were added into the drug solution under magnetic stirring (150 rpm, RT) for 24 hours. The orange-coloured mixture was then centrifugated for 10 minutes (10000 rpm, RT). Supernatant was collected and absorbance at 250 nm was measured for the quantification of Valsartan loaded in Fe-BTC. Calibration curve was obtained by measuring the absorbance at 250 nm of Valsartan ethanolic solutions with concentrations ranging from 1 to 30 mg/L. Absorbance measurements were performed on a BioTek Synergy H1 Plate Reader. All measurements were performed in triplicate and the average value reported.

2.2. Results and Discussion

2.2.1. Effect of pH

Samples were characterised by N_2 physisorption, TGA, DSC, SEM, XRPD, and FT-IR in order to investigate the effect of pH on textural properties, thermal stability, morphology, and microstructure of the material. To distinguish among different working pH conditions, Fe-BTC samples were labelled as BM_pH3, BM_pH4 and BM_pH5 (BM stands for ball milling).

X-ray Powder Diffraction

XRPD patterns obtained for BM_pH3, BM_pH4 and BM_pH5 samples are depicted in Figure 2.4. All samples show a similar diffraction pattern in terms of position of diffraction peaks. This is consistent with XRPD patterns reported in the literature for Fe-BTC frameworks.[7,8] An intense diffraction peak centred at 10.65° 2-theta with a visible shoulder at ca. 14.30° 2-theta was observed for all samples. The following peaks at ca. 18.76, 23.83, 28.09, 33.36, 42.49° 2-theta are less intense and broader than the first one. The presence of broad diffraction peaks is in agreement with the disordered structure of Fe-BTC material in comparison with crystalline MIL-100(Fe).[9] Despite the different pH conditions, all samples do not show significant microstructural differences by XRPD.

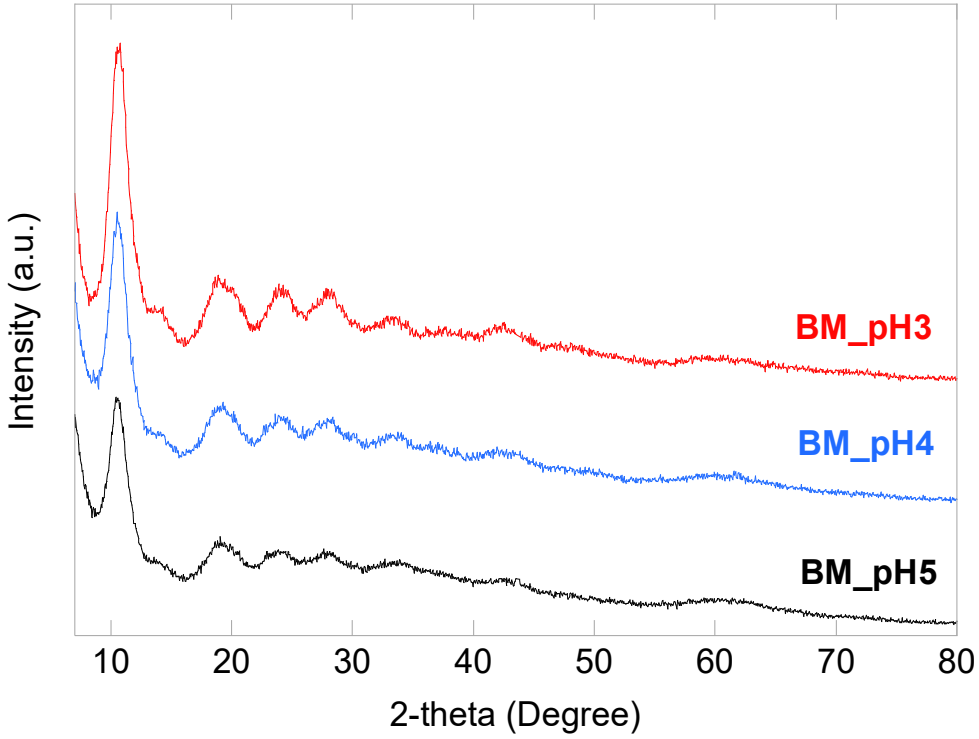

Figure. 2.4 XRPD patterns of BM_pH3, BM_pH4 and BM_pH5 recorded from 7 to 80° 2-theta.

Fourier-Transform Infrared Spectroscopy

Figure 2.5 reports FT-IR spectra obtained for BM_pH3, BM_pH4 and BM_pH5 in the 4000-400 cm^{-1} range. The presence of a broad band in region 3600-3100 cm^{-1} is attributed to the stretching vibrations of hydroxyl groups and water molecules coordinated to iron octahedra as well as adsorbed water molecules.[10,11] The relative intensity of this band slightly decreases with increasing pH. This suggested the presence of larger amounts of adsorbed water in BM_pH3, compared to samples obtained at pH 4 or 5. However, this is a negligible difference between samples owing to water adsorption being closely dependent on the extent of humidity and exposure time to air of samples.[12] The weak band at 3080 cm^{-1} is ascribable to the aromatic C–H stretching vibrations. A weak carbonyl band at 1703 cm^{-1} is visible in all samples. It is noteworthy that the relative intensity of this band gradually decreases at higher pH values. This is consistent with the presence of larger amounts of deprotonated trimesic acid at pH 5, which concur interrupting the order of the network.[13] Despite these slight differences, the spectra of the samples synthesised at different pH values are similar to each other as well as to FT-IR spectra reported in the literature for Fe-BTC materials.[14] The band at 1625 cm^{-1} is due to the C=O stretching of carboxylate groups, while the bands at ca. 1564 and 1371 cm^{-1} are ascribable to the asymmetric and symmetric stretching of the O–C–O group, respectively. The bands at

759 and 706 cm^{-1} are assigned to the C–H bending vibrations of aromatic rings, whereas the band at 463 cm^{-1} is attributed to the stretching vibrations of Fe-O bonds.[15–17]

Therefore, despite the different working pH conditions, samples do not show significant microstructural differences by FT-IR and XRPD.

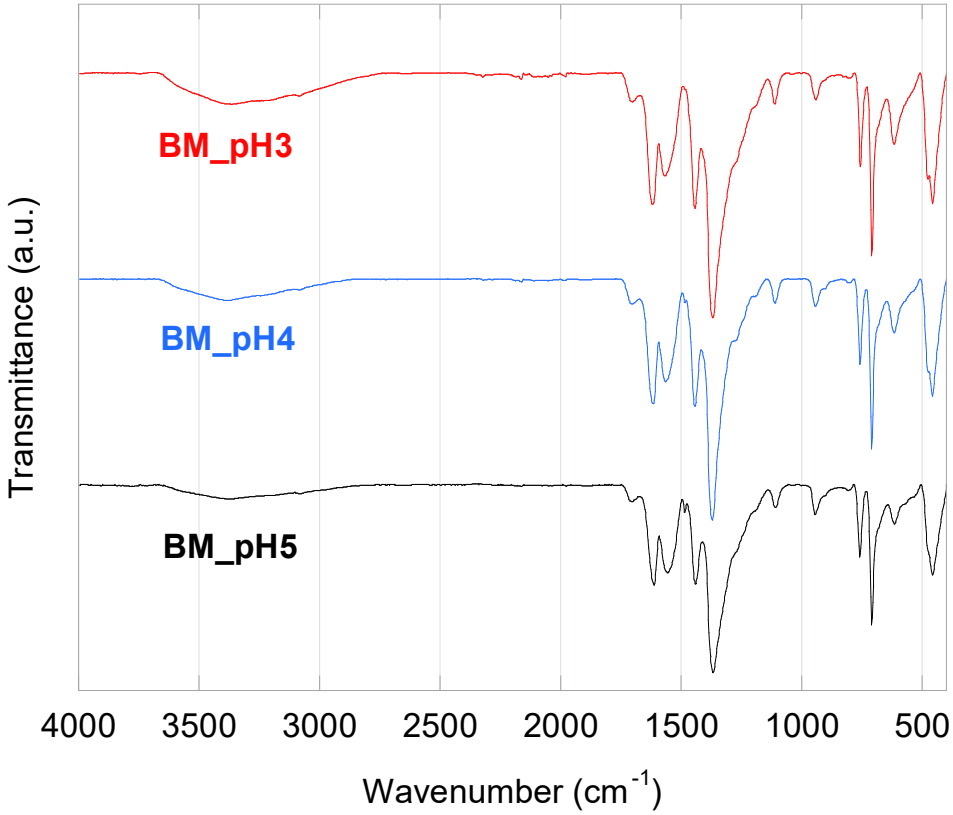

Figure 2.5. FT-IR spectra of BM_pH3, BM_pH4 and BM_pH5 from 400 to 4000 cm^{-1}.

Scanning Electron Microscopy

Samples microstructure was also examined by scanning electron microscopy. As shown in Figure 2.6, BM_pH3, BM_pH4 and BM_pH5 samples are constituted by agglomeration of particles which in turn are covered by much smaller particles. The presence of these smaller particles is mostly pronounced in the BM_pH4 sample (Figure 2.6 b).

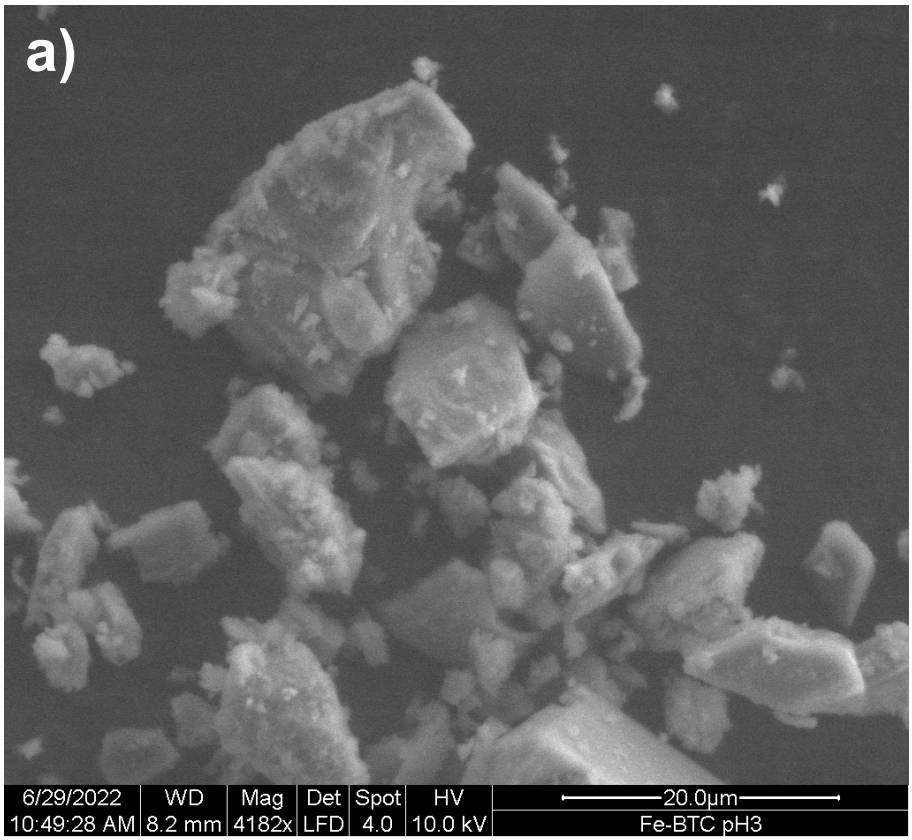
a)
6/29/2022
10:49:28 AM
WD
8.2 mm
Mag
4182x
Det
LFD
Spot
4.0
HV
10.0 kV
20.0µm
Fe-BTC pH3

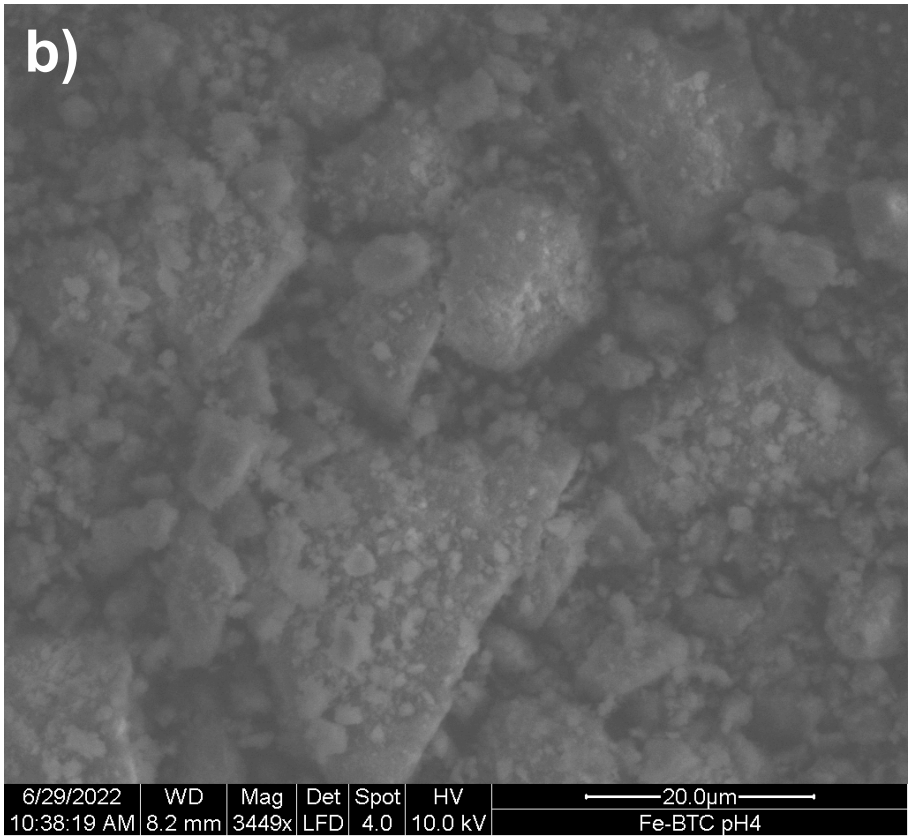
b)
6/29/2022
10:38:19 AM
WD
8.2 mm
Mag
3449x
Det
LFD
Spot
4.0
HV
10.0 kV
20.0µm
Fe-BTC pH4

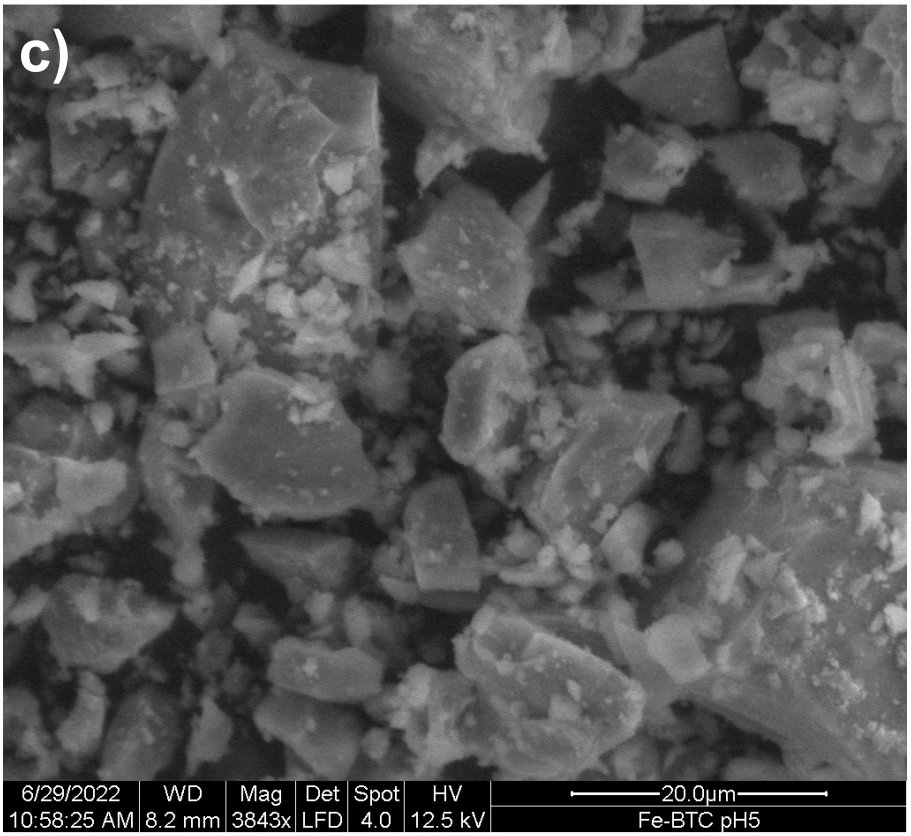

Figure 2.6. SEM images of BM_pH3 (a), BM_pH4 (b) and BM_pH5 (c).

Thermal Analysis

Thermal behaviour of samples was investigated under oxygen flow. Thermogravimetric (TG) curves, the corresponding derivative curves (dTG) and the DSC curves obtained for BM_pH3, BM_pH4 and BM_pH5 are shown in Figure 2.7. TG curves of all samples (Figure 2.7a) display three weight losses in the 25 – 850 °C range, as reported in the literature for this material.[18,19] The first weight loss occurs up to 150 °C and derives from the loss of adsorbed water molecules. Such a first loss is higher for BM_pH3 compared to BM_pH4 and BM_pH5. This is in agreement with the different amounts of adsorbed water observed also in FT-IR spectra. The second weight loss (150 – 260 °C) is attributed to the departure of water molecules coordinated to iron trimers. The third and last weight loss over the 260 – 450 °C range, is related to the decomposition of the framework into hematite by combustion, as confirmed by the presence of an intense exothermic peak at ca. 350 °C in the DSC curves of the samples (Figure 2.7c).

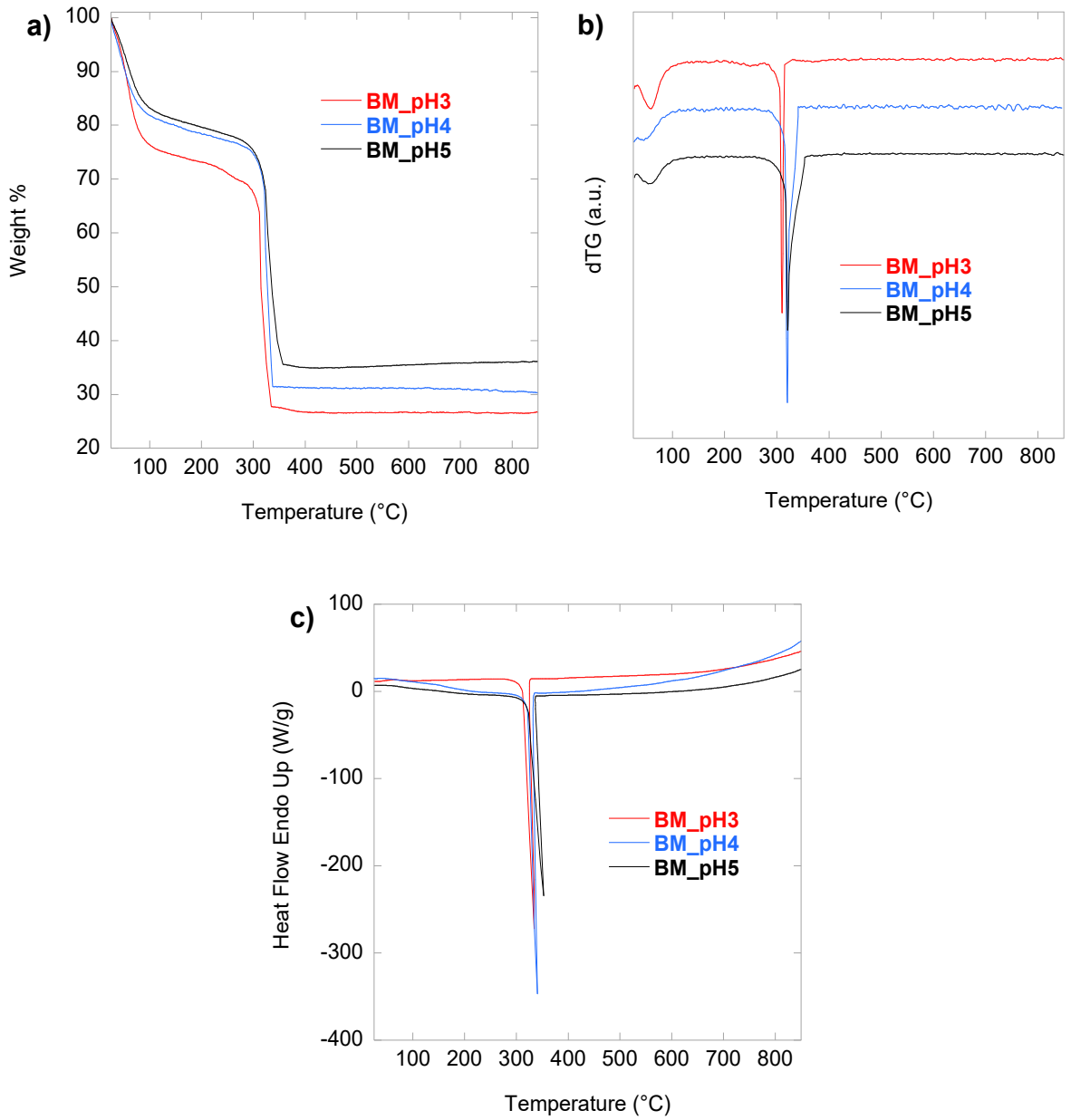

Figure 2.7. TG (a), dTG (b) and DSC (c) curves of BM_pH3, BM_pH4 and BM_pH5 samples, obtained between 25 and 850 °C (10 °C/min) under O_2 flow (40 ml/min).

Nitrogen physisorption

N_2 adsorption/desorption isotherms and pore size distributions for BM_pH3, BM_pH4 and BM_pH5 are shown in Figure 2.8a. All samples present a I-type isotherm, which is typical of microporous material.[20] BM_pH3 and BM_pH4 display a plateau at ca. $p/p^0 = 0.12$, while the plateau is reached at lower adsorbed volume and at lower relative pressure ($p/p^0 = 0.01$) for BM_pH5. Unlike BM_pH3 and BM_pH5 samples, the isotherm of BM_pH4 shows a hysteresis loop at p/p^0 0.83-0.99, due to capillary condensation occurring because of interparticle

mesoporosity. Indeed, BM_pH4 shows a relatively higher mesopore and macropore volume than BM_pH3 and BM_pH5 (Table 2.1). This suggests a different extent of particle aggregation for BM_pH4, which gives rise to interparticle meso- and macropores, as also evidenced by SEM analysis. The presence of a peak centred at around 6 Å in pore size distribution curves (Figure 2.8b) of both BM_pH3 and BM_pH4 testifies that the average dimension of a large fraction of pores is around 6 Å for these two samples. A small population of pores of higher dimensions (around 12 Å) is also observable, reminding of the presence of two types of cages in MIL-100(Fe). 6Å-diameter pores are absent in BM_pH5 which only shows a broad and less intense peak in the 10-15 Å region.

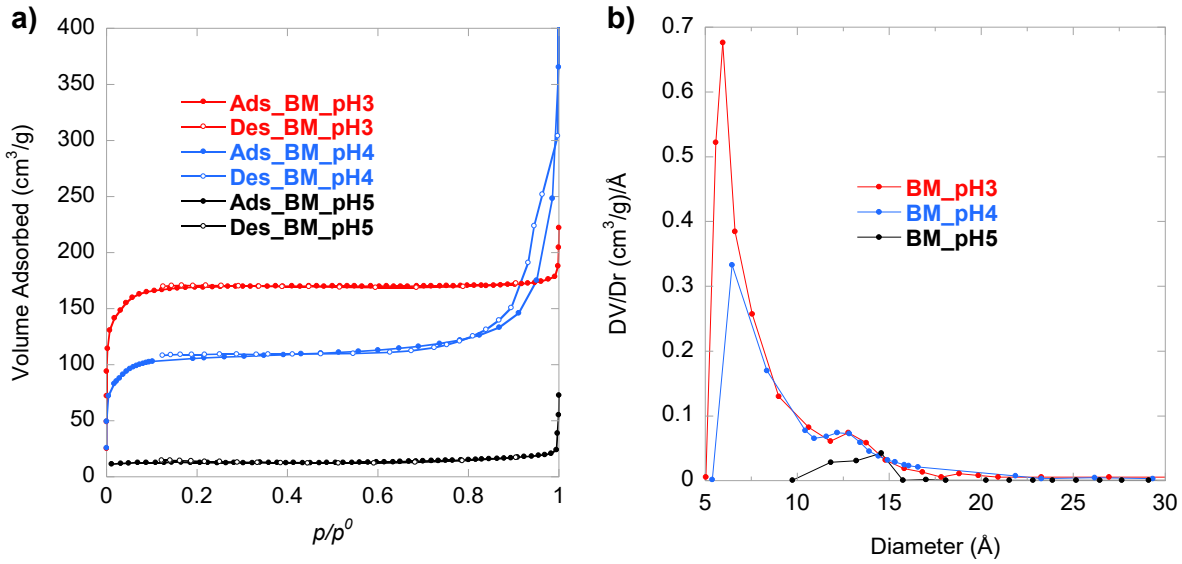

Figure 2.8. N_2 adsorption/desorption isotherms obtained at -196 °C (a) and pore size distributions (b) of BM_pH3, BM_pH4 and BM_pH5.

BM_pH3 sample showed the best results in terms of micropore volume (0.260 cm^3/g) and specific surface area (742 m^2/g). A decrease of both micropore volume and SSA with increasing pH was observed, as shown in Table 2.1. Such a decrease in micropore volume and SSA of the material as the pH increased is consistent with the framework formation mechanism proposed by Seo et al.[21] (previously reported in section 1.2.6.3). Although trimesic acid deprotonation and, therefore, condensation is favoured at basic conditions, low pH ensures a better control of the reaction kinetics because of the lower extent of hydrolysis of carboxyl groups.[22] Indeed, a slow condensation rate leads to a more ordered arrangement in space of carboxyl moieties towards trimeric iron(III) clusters, leading to the obtainment of highly porous and ordered solids. Hence, despite having a lower extent of extra-framework carboxyl groups which could

be assumed as a hint of a more ordered structure, as the pH increases the rate of condensation increases, hindering the formation of a sample with considerable permanent porosity. This explains the decreasing micropore volume and SSA observed increasing pH from 3 to 5.

Sample	SSA (m^2/g)	Micropore volume (cm^3/g)	Mesopore volume (cm^3/g)	Macropore volume (cm^3/g)
BM_pH3	742	0.260	0.007	0.003
BM_pH4	450	0.162	0.089	0.048
BM_pH5	57	0.020	0.008	0.002

Table 2.1. Specific Surface Area (SSA) and macro-, meso- and micropore volume of BM_pH3, BM_pH4 and BM_pH5. % Relative Standard Deviation (%RSD) SSA = 2; %RSD pore volume = 1.

Therefore, on the one hand textural properties of this material are noticeably affected by pH, having proved to be tuned by simply varying the amount of TMAOH. On the other hand, samples do not show any considerable differences in terms of thermal stability and microstructure.

Even though the best results in terms of SSA and micropore volume have been attained at pH 3, further investigation has been conducted on synthesis at pH 4. Since GOx shows a broad activity range (pH 4-7)[23] and iron(III) trimesate materials possess an intrinsic peroxidase-like activity in a pH range between 2.5 and 5,[24] synthesis at pH 4 represents the optimal balance between retention of GOx and Fe-BTC enzymatic and enzymatic-mimic activity, respectively, and satisfactory textural properties, physicochemical integrity of Fe-BTC.

2.2.2. Effect of solvents

In order to establish a comparison between NG and LAG approaches, mechanosynthesis of Fe-BTC at pH 4 was also conducted by adding a small amount of deionised water together with H_3BTC, $Fe(NO_3)_3 \cdot 9H_2O$ and $TMAOH \cdot 5H_2O$ in the grinding jar. To distinguish among NG and LAG synthesis, Fe-BTC samples were labelled as BM_NG, and BM_LAG. As reported in Figure 2.9, samples show a similar diffraction pattern. Therefore, the use of water did not affect the sample's microstructure.

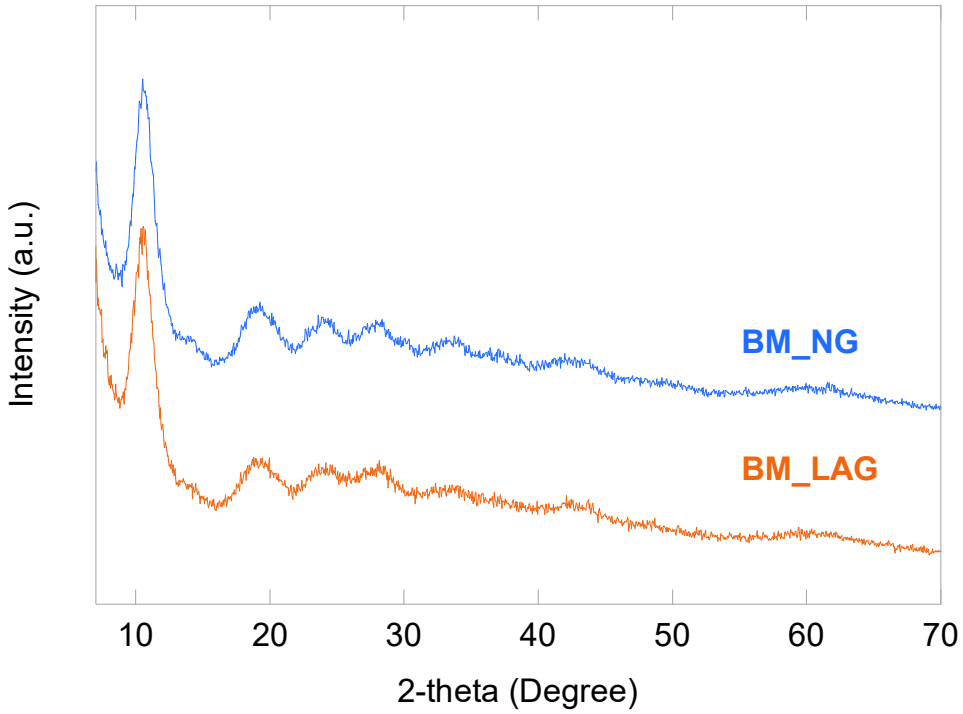

Figure. 2.9 XRPD patterns of BM_NG, and BM_LAG recorded from 7 to 70° 2-theta.

Conversely, LAG synthesis gave rise to lower SSA and micropore volume compared to the sample obtained without adding any solvents (Table 2.2). Consistently, the use of solvents proves to be completely unnecessary to obtain the material.

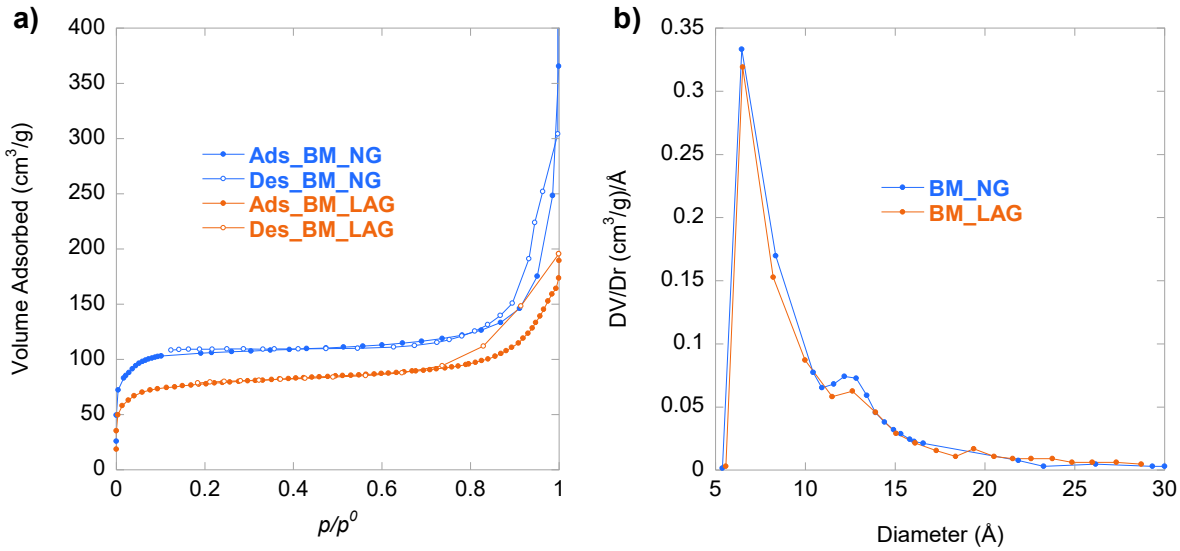

Figure 2.10. N_2 adsorption/desorption isotherms obtained at -196 °C (a) and pore size distributions (b) of BM_NG, and BM_LAG.

This represents an unprecedented breaking point for Fe-BTC synthesis, which is here successfully synthesised for the first time in solvent-free conditions. Avoiding the use of solvents, this approach fulfils both bio-friendly targets and green chemistry criteria. Moreover, biomolecules are generally more stable in powder than in solution.[25]

Sample	SSA (m^2/g)	Micropore volume (cm^3/g)	Mesopore volume (cm^3/g)	Macropore volume (cm^3/g)
BM_NG	450	0.162	0.089	0.048
BM_LAG	323	0.118	0.080	0.030

Table 2.2. Specific Surface Area (SSA) and macro-, meso- and micropore volume of BM_NG, and BM_LAG. %RSD SSA = 2; %RSD pore volume = 1.

2.2.3. Effect of milling media

The effect of milling media on the material was investigated by exploring the use of zirconia balls with different sizes. Fe-BTC samples were labelled as BM_5mm and BM_10mm to distinguish between samples obtained employing 5- or 10-mm diameter balls, respectively.

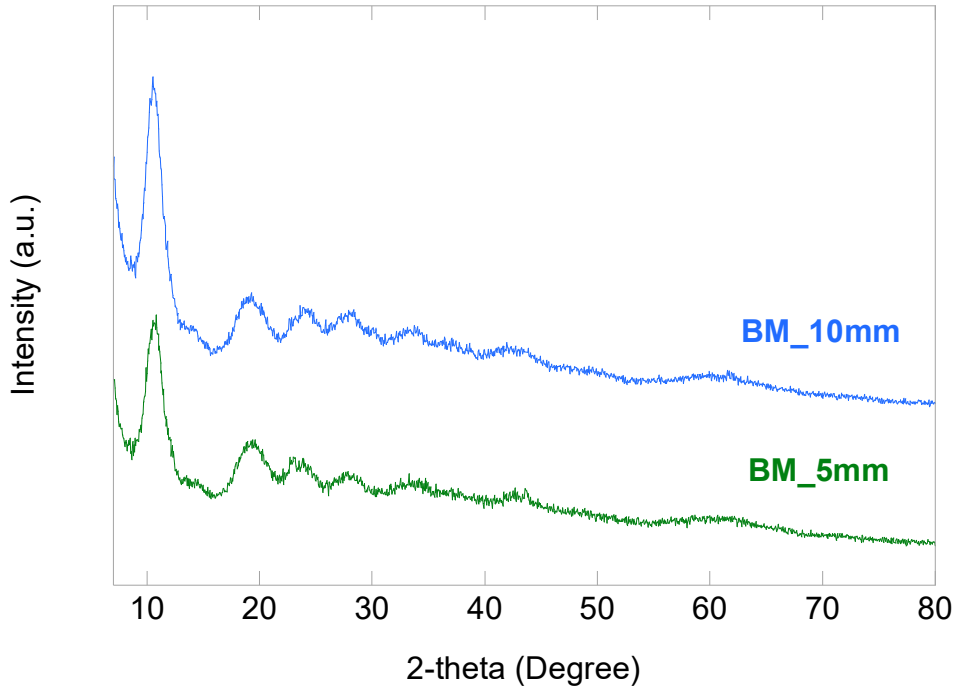

Figure. 2.11. XRPD patterns of BM_10mm and BM_5mm recorded from 7 to 80° 2-theta.

The use of balls with different sizes does not affect the microstructure of the material (Figure 2.11). Conversely, Fe-BTC material obtained by using small balls showed slightly lower SSA and micropore volume compared to BM_10mm (Table 2.3). Therefore, 10-mm diameter balls were preferred.

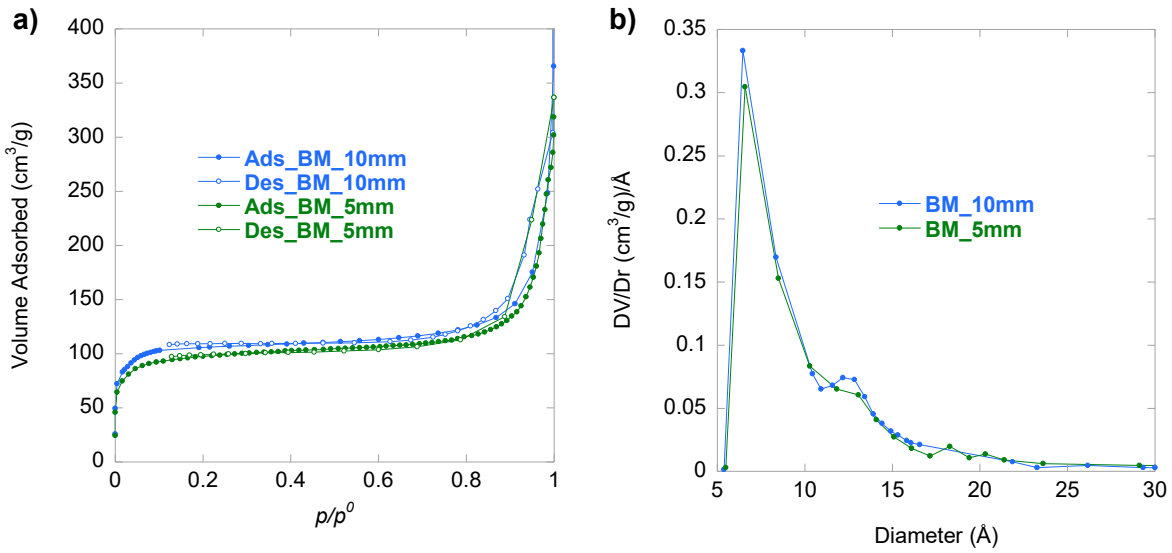

Figure 2.12. N_2 adsorption/desorption isotherms obtained at -196 °C (a) and pore size distributions (b) of BM_10mm and BM_5mm.

Sample	SSA (m^2/g)	Micropore volume (cm^3/g)	Mesopore volume (cm^3/g)	Macropore volume (cm^3/g)
BM_10mm	450	0.162	0.089	0.048
BM_5mm	410	0.148	0.091	0.075

Table 2.3. Specific Surface Area (SSA) and macro-, meso- and micropore volume of BM_10mm and BM_5mm. %RSD SSA = 2; %RSD pore volume = 1.

2.2.4. Effect of grinding time

The effect of grinding time on microstructure and textural properties of Fe-BTC was examined over a range between 6 and 60 minutes. Fe-BTC samples obtained grinding for 6, 30 or 60 minutes were labelled as BM_6min, BM_30min and BM_60min, respectively.

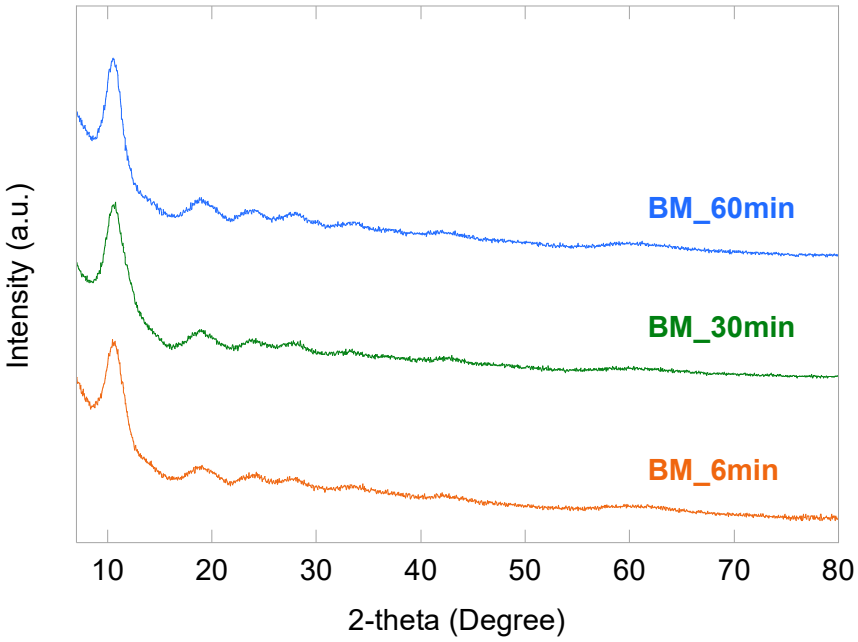

Figure. 2.13. XRPD patterns of BM_6min, BM_30min and BM_60min recorded from 7 to 80° 2-theta

.

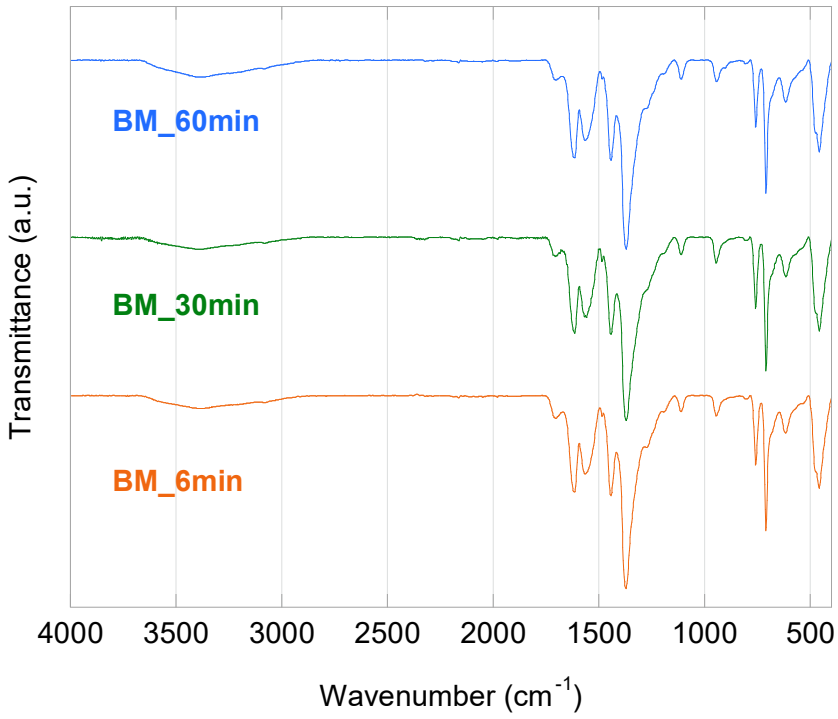

Figure 2.14. FT-IR spectra of BM_6min, BM_30min and BM_60min from 400 to 4000 cm^{-1}.

Despite the different grinding time, all samples do not show significant microstructural differences by XRPD (Figure 2.13) and FT-IR (Figure 2.14).

As displayed in Figure 2.15, all samples showed a I-type isotherm and comparable pore distribution size curves.

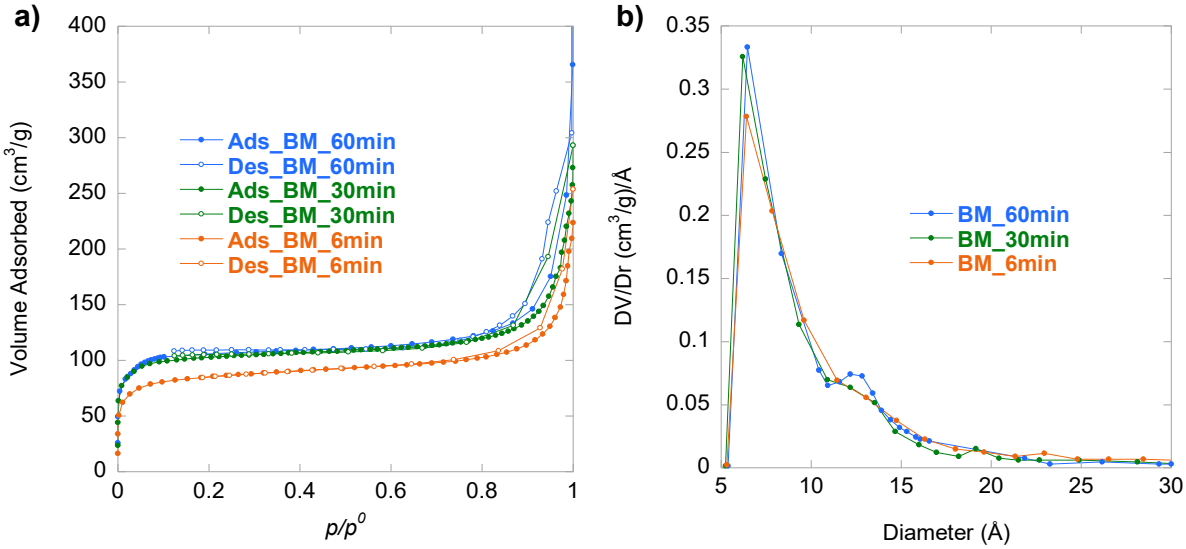

Figure 2.15. N_2 adsorption/desorption isotherms obtained at -196 °C (a) and pore size distributions (b) of BM_6min, BM_30min and BM_60min.

Samples obtained grinding for 30 or 60 minutes showed negligible differences in terms of SSA and pore volume. Conversely, a slight decrease of textural properties was observed when reducing grinding time from 30 to 6 minutes.

Sample	SSA (m^2/g)	Micropore volume (cm^3/g)	Mesopore volume (cm^3/g)	Macropore volume (cm^3/g)
BM_60min	450	0.162	0.089	0.048
BM_30min	449	0.157	0.078	0.043
BM_6min	370	0.129	0.065	0.030

Table 2.4. Specific Surface Area (SSA) and macro-, meso- and micropore volume of BM_6min, BM_30min and BM_60min. %RSD SSA = 2; %RSD pore volume = 1.

Given the physicochemical similarities between BM_60 min and BM_30min, 30-minute grinding should be preferred over 60-minute synthesis, in order to minimise potential effect of

grinding on biomolecules. Moreover, a time-saving procedure is more desirable for industrial scale-up contributing to lower the cost of the overall production process. In view of *in situ* immobilisation of biomolecules both 30-minute and 6-minute synthesis protocols provide an optimal compromise to preserve biomolecules structural/functional stability while displaying desirable textural properties of Fe-BTC.

2.2.5. Effect of drying conditions

Two different drying processes have been explored (air-drying at room temperature and freeze-drying) to identify the most suitable conditions to store the samples in sight of biomolecules immobilisation strategies. Fe-BTC samples undergone upon air-drying and freeze-drying are labelled as BM_air-dried and BM_freeze-dried, respectively.

Figure 2.16 shows the diffraction pattern of BM_air-dried and BM_freeze-dried samples. Such patterns do not significatively differ in terms of position of the diffraction peaks.

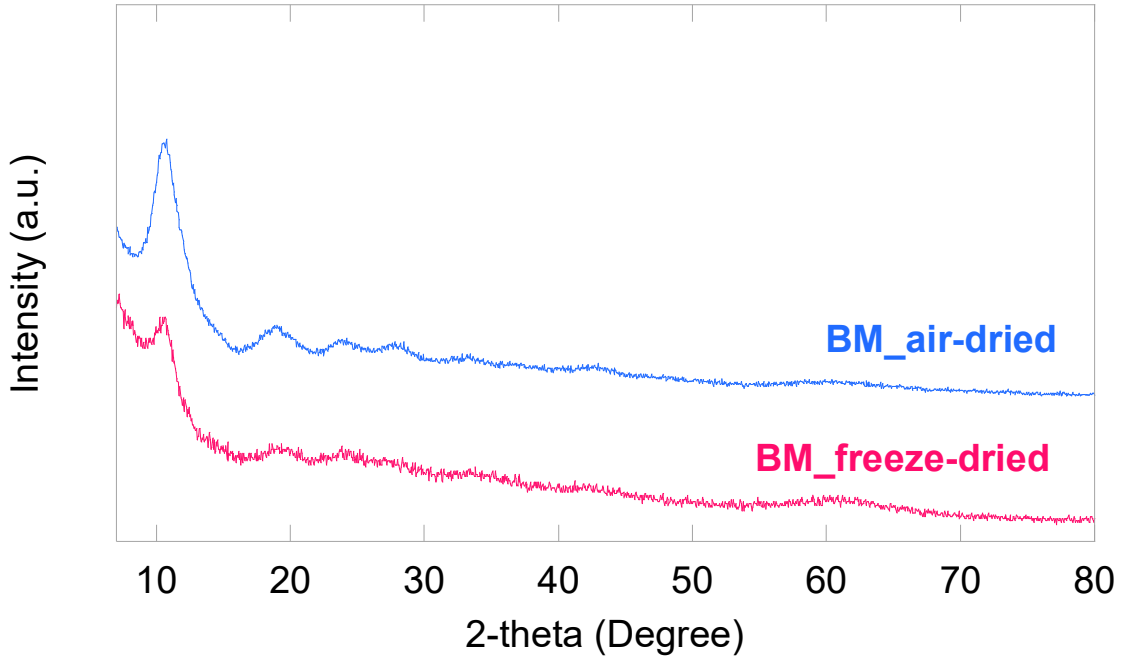

Figure. 2.16. XRPD patterns of BM_air-dried, and BM_freeze-dried recorded from 7 to 80° 2-theta.

As depicted in Figure 2.17, both air-dried and freeze-dried samples show the same thermal behaviour, consisting of three weight losses in the 25-900 °C range. The first loss up to 150 °C

is smaller for BM_freeze-dried compared to the air-dried sample. Such a lower amount of adsorbed water molecules in the lyophilised material is consistent with the removal of water by sublimation and desorption during the freeze-drying process.

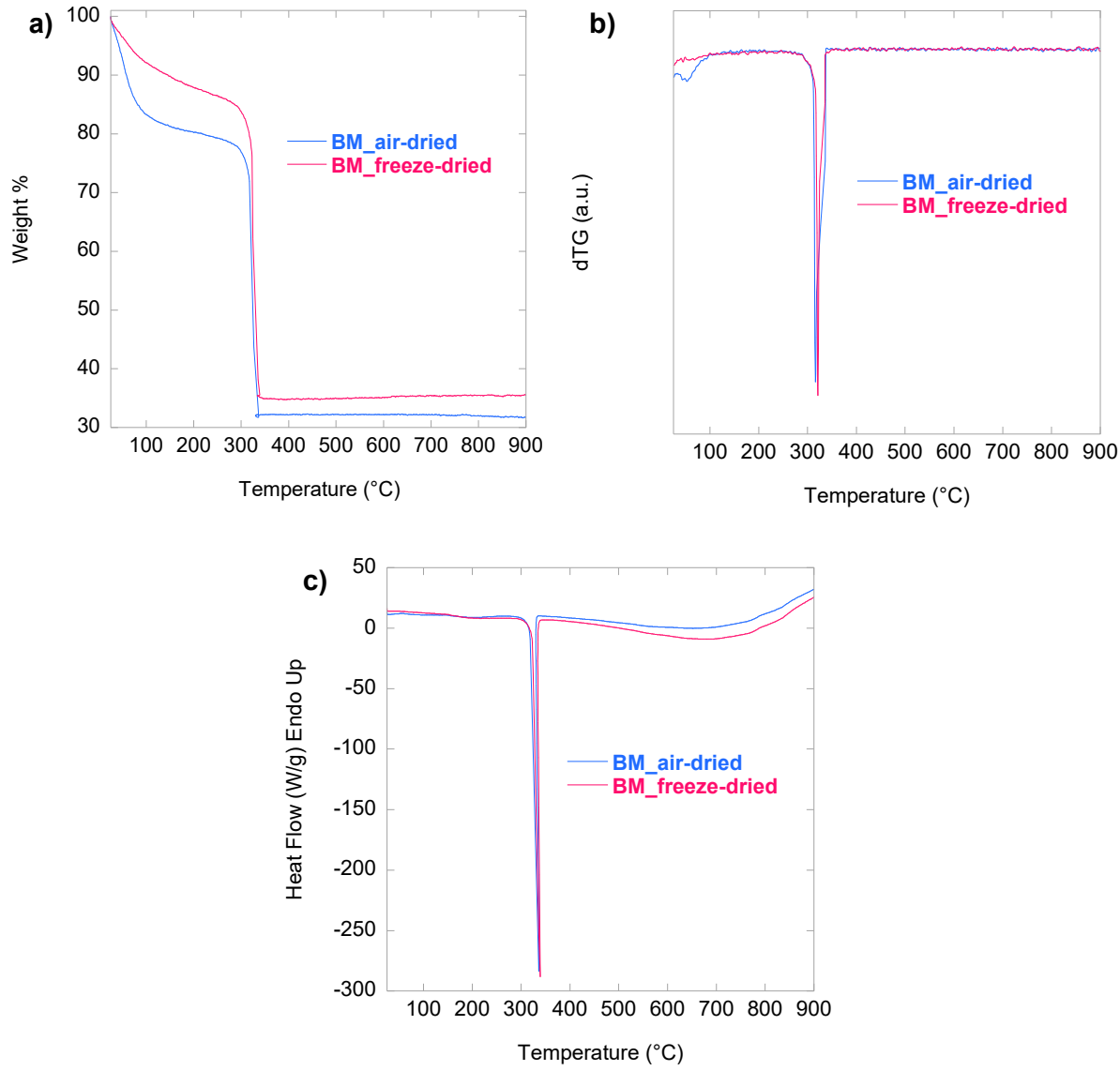

Figure 2.17. TG (a), dTG (b) and DSC (c) curves of BM_air-dried and BM_freeze-dried samples, obtained between 25 and 900 °C (10 °C/min) under O_2 flow (40 ml/min).

Both air-dried and freeze-dried samples show a I-type isotherm (Figure 2.18a). However, lyophilisation causes a severe decrease of both micropore volume and SSA, as displayed in Table 2.5.

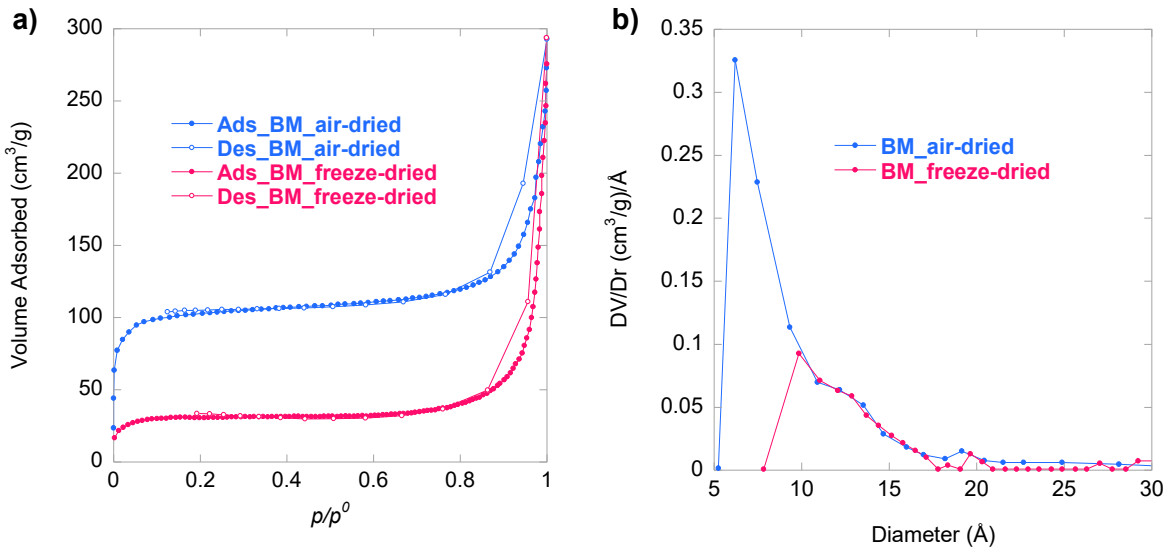

Figure 2.18. N_2 adsorption/desorption isotherms obtained at -196 °C (a) and pore size distributions (b) of BM_air-dried and BM_freeze-dried.

Furthermore, pore size distribution curves obtained for both materials differ in terms of intensity and peak positions (Figure 2.18b). BM_air-dried exhibits an intense peak at around 6 Å, attesting to a large fraction of pores with average dimension of ca 6 Å. Conversely, BM_freeze-dried sample shows a broad and less intense peak at higher diameter values, given by a population of pores with larger average dimensions (ca. 10 Å) compared to the air-dried Fe-BTC material.

Sample	SSA (m^2/g)	Micropore volume (cm^3/g)	Mesopore volume (cm^3/g)	Macropore volume (cm^3/g)
BM_air-dried	449	0.157	0.078	0.043
BM_freeze-dried	140	0.048	0.064	0.056

Table 2.5. Specific Surface Area (SSA) and macro-, meso- and micropore volume of BM_air-dried and BM_freeze-dried. %RSD SSA = 2; %RSD pore volume = 1.

Despite the potential advantages of lyophilisation regarding storage and shelf-life of the material, also in sight of its application of as biomolecule support, the decrease of textural properties of the Fe-BTC observed after freeze-drying proved the feasibility of air-drying to effectively retain a significant permanent porosity of the sample.

2.2.6. Intrinsic peroxidase-like activity

The intrinsic peroxidase-mimic activity of Fe-BTC material was evaluated by investigating the catalytic oxidation capacity of the material over a chromogenic peroxidase substrate (TMB) in the presence of H_2O_2. As shown in Figure 2.19, in the absence of both Fe-BTC and H_2O_2, the characteristic absorbance peak of oxidised TMB at 652 nm was not detected. A weak absorbance peak at 652 nm was visible for the reaction system consisting of TMB in the presence of Fe-BTC, revealing a weak capability of the MOF to oxidise TMB in the absence of H_2O_2. A slightly higher absorbance at 652 nm was observed for TMB in the presence of H_2O_2 but in the absence of Fe-BTC. A considerable increase in the absorbance at 652 nm and, thus, in the oxidation rate of TMB, was observed for the reaction system containing TMB together with both Fe-BTC and H_2O_2. This attested the significant intrinsic peroxidase-like activity of Fe-BTC, being able to catalyse the oxidation of peroxidase substrate in the presence of hydrogen peroxide.

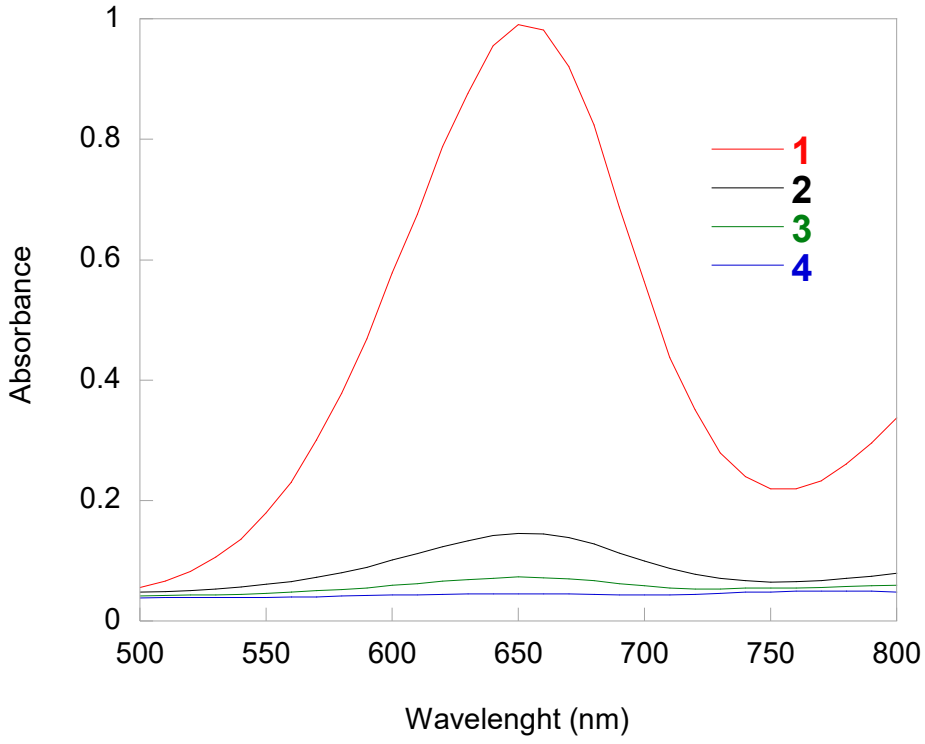

Figure 2.19. Absorption spectra of different reaction systems: TMB+H_2O_2+Fe-BTC (1, red), TMB+H_2O_2 (2, black), TMB+Fe-BTC (3, green), TMB (4, blue) in acetate buffer (10 mM, pH 4), at 35 °C after 1 hour incubation. The concentrations were 250 µg/mL for Fe-BTC, 0.4 mM for TMB and 0.5 mM for H_2O_2.

2.2.7. Effect of pH, temperature, catalyst concentration and incubation time

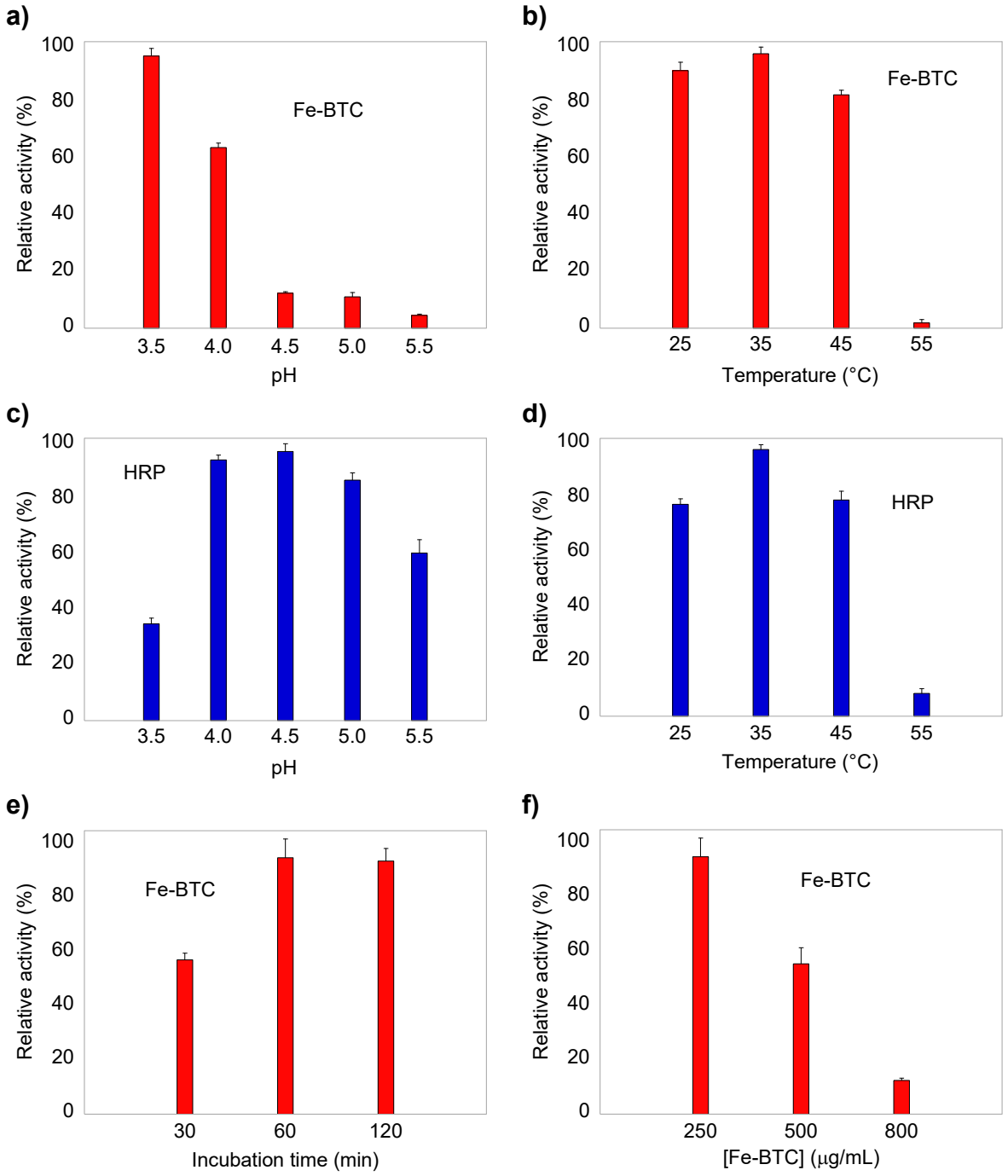

Figure 2.20. Effect of pH (a), temperature (b), incubation time (e) and catalyst concentration (f) on the intrinsic peroxidase-like activity of Fe-BTC. pH (c) and temperature (d) profile of HRP. Error bars represent the standard deviations of three independent experiments.

Similar to HRP, the intrinsic peroxidase-like activity of Fe-BTC is closely dependent on experimental conditions. The effect of pH, temperature, catalyst concentrations and incubation time on the relative activity of Fe-BTC was investigated. As shown in Figure 2.20 a, the activity of Fe-BTC gradually decreased from pH 3.5 to 4, while it decreased sharply at higher pH values. Although the maximal relative activity of Fe-BTC was found at pH 3.5, pH 4 was considered as optimal condition to gain a satisfactory balance between the intrinsic peroxidase-like activity of Fe-BTC and the catalytic activity of GOx in sight of the synthesis of GOx@Fe-BTC hybrid biocatalysts. The pH profile of Fe-BTC differed from that observed for HRP, whose relative activity increased from pH 3.5 to 4, reaching the maximum at 4.5, and finally decreasing from 5 to 5.5 (Figure 2.20 c). Regarding temperature dependence, Fe-BTC (Figure 2.20 b) and HRP (Figure 2.20 d) showed a similar profile with the maximal relative activity at 35 °C and a significant activity loss above 45 °C. The dependence on incubation was also investigated. It was found that maximal relative activity of Fe-BTC is reached in 60 minutes (Figure 2.20 e). As shown in Figure 2.20 f, a gradual decrease of Fe-BTC activity was observed while increasing the catalyst concentration. The higher the catalyst concentration, the higher is the surface of Fe-BTC available to adsorb oxTMB and remove it from solution. Therefore, a lower concentration of oxTMB in solution is detected. Figure 2.21 showed the increasing extent of Fe-BTC precipitate solid after centrifugation while increasing the catalyst concentration. The solid appears blue because of the adsorption of blue-coloured oxTMB on the Fe-BTC surface.

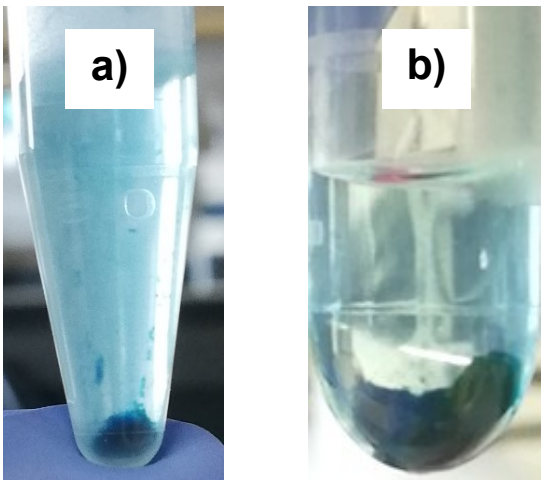

Figure 2.21. Blue-coloured solids after centrifugation of different reaction systems: a) Fe-BTC 250 µg/mL, TMB (0.4 mM), H_2O_2 (0.5 mM), b) Fe-BTC (800 µg/mL), TMB (0.4 mM), H_2O_2 (0.5 mM), in acetate buffer (10 mM, pH 4), at 35 °C after 1 hour incubation.

According to the experimental results above reported, the optimal pH, reaction temperature, incubation time, and Fe-BTC concentration were 4.0, 35 °C, 60 min, 250 µg/mL, respectively.

2.2.8. Steady-state kinetic assay

To further investigate the intrinsic peroxidase-mimic activity of Fe-BTC, steady-state kinetic experiments were performed. Typical Michaelis-Menten curves were obtained for both Fe-BTC (Figure 2.22 a,e) and HRP (Figure 2.22 c,g). Kinetic parameters K_m and V_{max}, summarised in Table 2.6, were obtained from Lineweaver–Burk double-reciprocal plots (Figure 2.22 b,d,f,h).

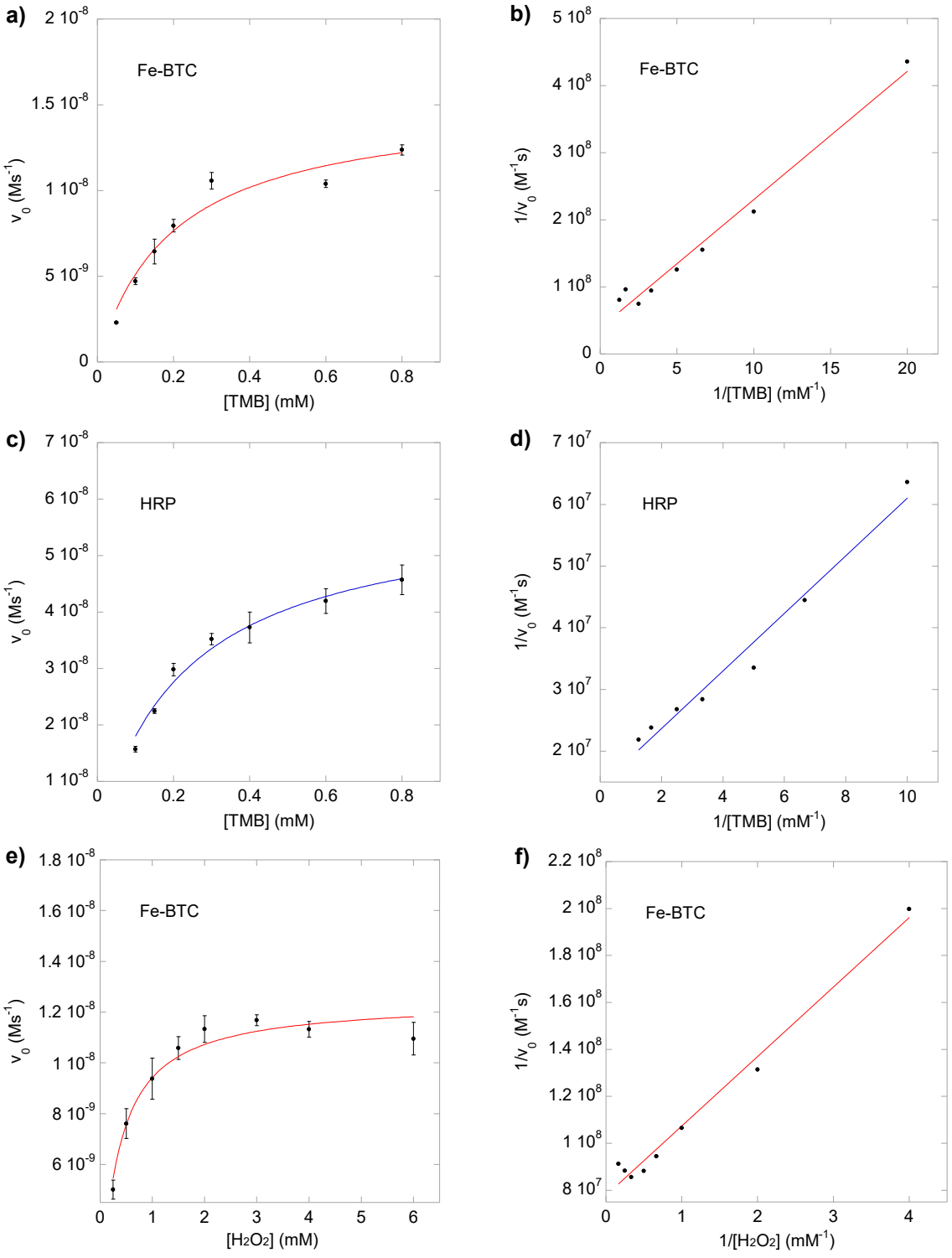

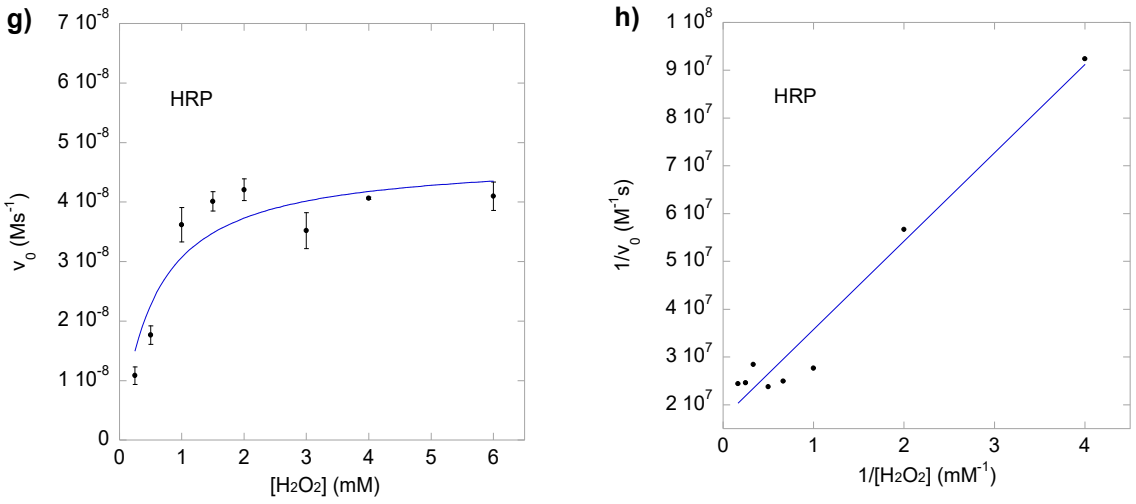

Figure 2.22. Steady-state kinetic analysis using the Michaelis–Menten model for Fe-BTC (a, e) and HRP (c, g) and the Lineweaver–Burk double-reciprocal plots for Fe-BTC (b, f) and HRP (d, h). Error bars represent the standard deviations of three independent experiments.

As shown in Table 2.6, the K_m value of Fe-BTC with TMB as substrate is slightly higher than the one calculated for HRP. Conversely, the V_{max} value of Fe-BTC with TMB as substrate is lower in comparison with HRP. These results revealed a slower reaction rate for Fe-BTC and a relatively lower affinity between TMB and catalyst for Fe-BTC compared to HRP. The K_m value calculated for Fe-BTC with H_2O_2 as substrate is ca. 2.8 times lower than the value obtained for HRP, revealing a much better affinity for Fe-BTC to H_2O_2 compared to HRP. The V_{max} value for Fe-BTC is lower compared to HRP, suggesting a relatively slower reaction rate for Fe-BTC than HRP.

Catalyst	Substrate	E (M)	K_m (mM)	V_{max} (M/s)
Fe-BTC	TMB	$2.85 \cdot 10^{-4}$	0.49	$2.57 \cdot 10^{-8}$
HRP	TMB	$2.27 \cdot 10^{-11}$	0.32	$6.95 \cdot 10^{-8}$
Fe-BTC	H_2O_2	$2.85 \cdot 10^{-4}$	0.38	$1.29 \cdot 10^{-8}$
HRP	H_2O_2	$2.27 \cdot 10^{-11}$	1.07	$5.80 \cdot 10^{-8}$

Table 2.6. Comparison of the kinetic parameters of Fe-BTC and HRP. [E] is the enzyme concentration, K_m is the Michaelis constant, V_{max} is the maximum reaction rate.

Because of its peroxidase-mimic activity and excellent affinity (especially towards H_2O_2), mechanochemically-prepared Fe-BTC could be used as a colorimetric assay platform to detect H_2O_2 concentrations.

2.2.9. H_2O_2 colorimetric detection

Hydrogen peroxide is widely applied as bleach agent and bactericide in many fields, including food industry and environmental protection, due to its strong oxidation.[3] However, H_2O_2 residues can be harmful for public health. Indeed, its accumulation in human body can lead to headaches, cardiovascular disease diabetes and cancer.[26] Therefore, a simple, accurate, and highly effective method for the detection of hydrogen peroxide is indispensable for environmental and food safety purposes.

Thus, a colorimetric biosensing of H_2O_2 was performed based on the above-mentioned optimal reaction conditions. Figure 2.23 showed the dose-response curve obtained in a [H_2O_2] range between 0 and 200 µM. The absorbance at 652 nm progressively increased with the increase of H_2O_2 concentration. A good linear response of the absorbance at 652 nm was found in the 7.5 - 75 µM [H_2O_2] range, with a correlation coefficient of 0.99961. LOD and LOQ were 0.24 and 0.79 µM, respectively.

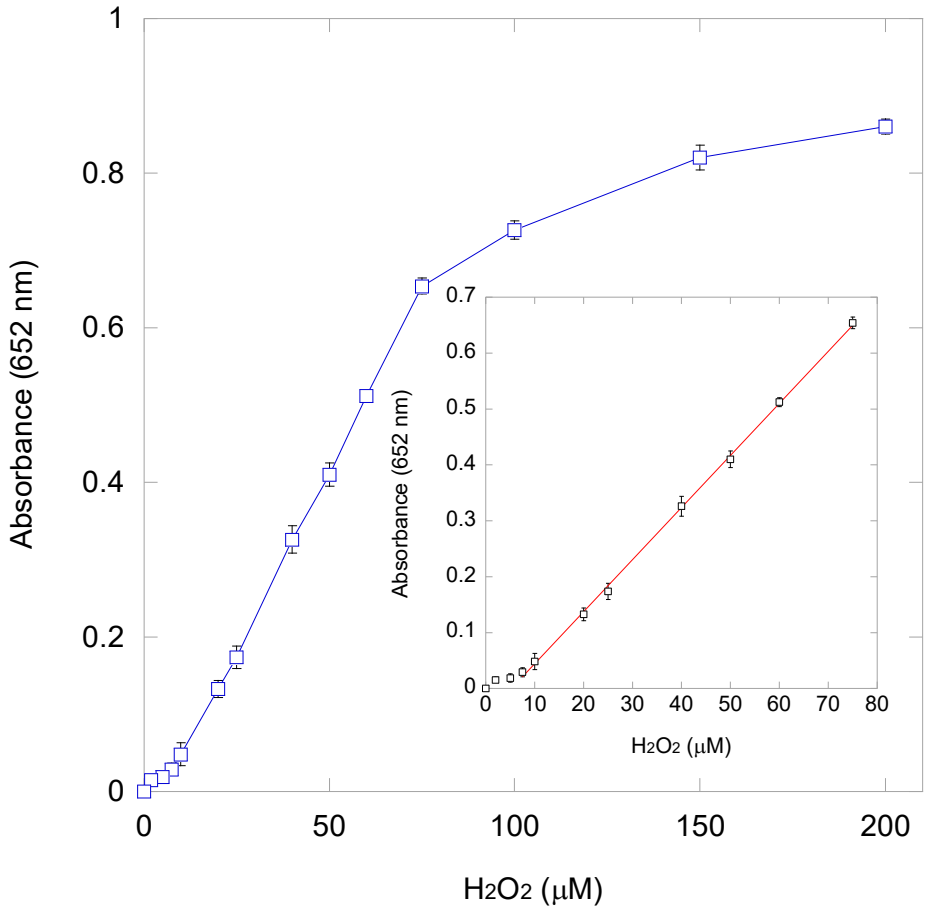

Figure 2.23. Dose–response curve for H_2O_2 detection in the 0 - 200 µM range. Inset: linear calibration plot between the absorbance at 652 nm and H_2O_2 concentration. Experiments were carried out using Fe-BTC (250 µg/mL), TMB (0.4 mM) and different concentration of H_2O_2 (0-200 µM) in acetate buffer (10 mM, pH = 4). The solution mixtures were incubated at 35 °C under magnetic stirring (150 rpm) for 1 hour. Error bars represent the standard deviations of three independent experiments.

Table 2.7 shows a comparison of various peroxidase-mimic materials used for the H_2O_2 detection. Compared to crystalline MIL-100(Fe), H_2O_2 biosensing platform Fe-BTC prepared via mechanochemical approach showed a wider linear range and similar LOD. Furthermore, LOD value obtained using Fe-BTC is significatively lower compared to other peroxidase-mimics, revealing a good sensitivity of the colorimetric detection assay developed in the present thesis work.

Catalyst	**Substrate**	**Linear range (µM) H_2O_2**	**LOD(µM) H_2O_2**	**Ref.**
MIL-100(Fe)	TMB	3 – 40	0.155	[24]
MIL-88B-Fe	TMB	10 – 100	0.60	[3]
Hemin@MIL-101(Al)-NH_2	TMB	5 – 200	2	[27]
MOF (Co/2Fe)	TMB	10 – 100	5	[28]
FeS_2 NPs	TMB	2 – 80	0.91	[29]
Fe-Ag_2S	TMB	10 – 150	7.82	[30]
Fe-BTC	TMB	7.5 – 75	0.24	This work

Table 2.7. Comparison of the characteristics of various peroxidase-mimics used for H_2O_2 colorimetric detection.

2.2.10. Drug encapsulation

Figure 2.24 shows the calibration curve obtained in a [Valsartan] range between 1 and 30 mg/L. The absorbance at 250 nm progressively increased as Valsartan concentration increased. The linear fitting equation is A_{250nm}= 0.030109c - 0.0024719 (mg/L) (R = 0.99991). Valsartan encapsulation was performed via impregnation method. 5 mg of mechanochemically-prepared Fe-BTC material were added to 5 mL of an ethanolic solution of Valsartan (10 mg/L). A_{250nm} of the supernatant collected after centrifugation of the Valsartan and Fe-BTC mixture was 0.148. This corresponded to [Valsartan] = 5 mg/L, attesting a Valsartan loading of ca. 50 % on Fe-BTC sample. These preliminary results testified the potential of Fe-BTC materials as drug-delivery systems. Further research is in progress in order to enhance Valsartan loading and perform drug release profile studies.

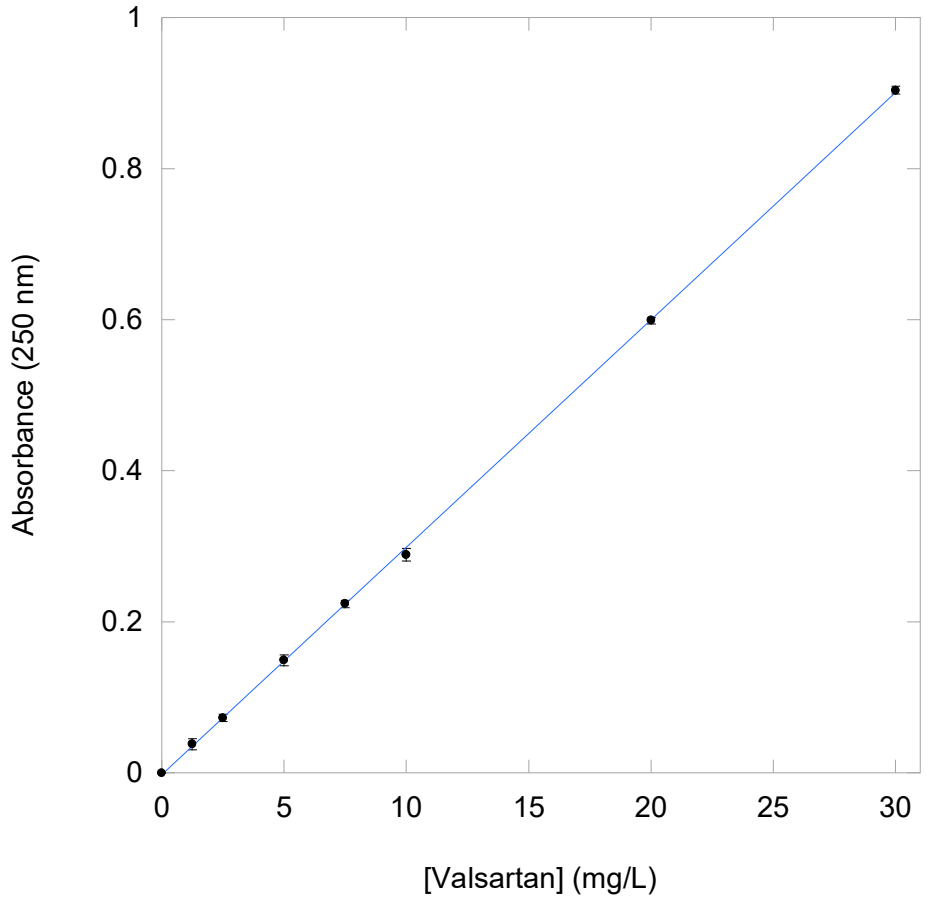

Figure 2.24. Calibration curve for Valsartan. Error bars represent the standard deviations.

2.3. References

[1] Roy, I.; Gupta, M. N. Freeze-Drying of Proteins: Some Emerging Concerns. *Biotechnol. Appl. Biochem.* **2004**, *39* (2), 165. https://doi.org/10.1042/ba20030133.

[2] Yan, Z.; Niu, Q.; Mou, M.; Wu, Y.; Liu, X.; Liao, S. A Novel Colorimetric Method Based on Copper Nanoclusters with Intrinsic Peroxidase-like for Detecting Xanthine in Serum Samples. *J. Nanoparticle Res.* **2017**, *19* (7). https://doi.org/10.1007/s11051-017-3904-9.

[3] Fu, M.; Chai, B.; Yan, J.; Wang, C.; Fan, G.; Song, G.; Xu, F. Facile Preparation of MIL-88B-Fe Metal–Organic Framework with High Peroxidase-like Activity for Colorimetric Detection of Hydrogen Peroxide in Milk and Beer. *Appl. Phys. A Mater. Sci. Process.* **2021**, *127* (12). https://doi.org/10.1007/s00339-021-05082-8.

[4] Nelson, D. L.; Cox, M. M. *Lehninger Principles of Biochemistry*, 7th ed.; WH Freeman, 2017.

[5] Metelitsa, D. I.; Naumchik, I. V.; Karaseva, E. I.; Polozov, G. I.; Shadyro, O. I. Inhibition of Peroxidase Oxidation of Aromatic Amines by Substituted Phenols. *Prikl. Biokhim. Mikrobiol.* **2003**, *39* (4), 401–412.

[6] Siddiqui, N.; Husain, A.; Chaudhry, L.; Alam, S. S.; Mitra, M.; Bhasin, P. S. Pharmacological and Pharmaceutical Profile of Valsartan: A Review. *J. Appl. Pharm. Sci.* **2011**, *1* (4), 12–19.

[7] Oveisi, A. R.; Khorramabadi-Zad, A.; Daliran, S. Iron-Based Metal-Organic Framework, Fe(BTC): An Effective Dual-Functional Catalyst for Oxidative Cyclization of Bisnaphthols and Tandem Synthesis of Quinazolin-4(3H)-Ones. *RSC Adv.* **2016**, *6* (2), 1136–1142. https://doi.org/10.1039/c5ra19013d.

[8] Bhattacharjee, S.; Matin, M. A. Hydroxylation of Phenol Catalyzed by Iron Metal-Organic Framework (Fe-BTC) with Hydrogen Peroxide. *J. Mater. Sci. Chem. Eng.* **2020**, *08* (02), 55–64. https://doi.org/10.4236/msce.2020.82006.

[9] Sapnik, A. F.; Bechis, I.; Collins, S. M.; Johnstone, D. N.; Divitini, G.; Smith, A. J.; Chater, P. A.; Addicoat, M. A.; Johnson, T.; Keen, D. A.; Jelfs, K. E.; Bennett, T. D. Mixed Hierarchical Local Structure in a Disordered Metal–Organic Framework. *Nat. Commun.* **2021**, *12*, 2062. https://doi.org/10.1038/s41467-021-22218-9.

[10] Leclerc, H.; Vimont, A.; Lavalley, J. C.; Daturi, M.; Wiersum, A. D.; Llwellyn, P. L.; Horcajada, P.; Férey, G.; Serre, C. Infrared Study of the Influence of Reducible Iron(Iii) Metal Sites on the Adsorption of CO, CO2, Propane, Propene and Propyne in the Mesoporous Metal-Organic Framework MIL-100. *Phys. Chem. Chem. Phys.* **2011**, *13* (24), 11748–11756. https://doi.org/10.1039/c1cp20502a.

[11] Autie-Castro, G.; Autie, M. A.; Rodríguez-Castellón, E.; Aguirre, C.; Reguera, E. Cu-BTC and Fe-BTC Metal-Organic Frameworks: Role of the Materials Structural Features on Their Performance for Volatile Hydrocarbons Separation. *Colloids Surf. A Physicochem. Eng. Asp.* **2015**, *481*, 351–357. https://doi.org/10.1016/j.colsurfa.2015.05.044.

[12] Mannias, G.; Scano, A.; Pilloni, M.; Magner, E.; Ennas, G. Tailoring MOFs to Biomedical Applications: A Chimera or a Concrete Reality? The Case Study of Fe-BTC by Bio-Friendly Mechanosynthesis. *Comments Inorg. Chem.* **2022**, *00* (00), 1–21. https://doi.org/10.1080/02603594.2022.2153837.

[13] Sciortino, L.; Alessi, A.; Messina, F.; Buscarino, G.; Gelardi, F. M. Structure of the FeBTC Metal-Organic Framework: A Model Based on the Local Environment Study. *J. Phys. Chem. C* **2015**, *119* (14), 7826–7830. https://doi.org/10.1021/acs.jpcc.5b01336.

[14] Pangkumhang, B.; Jutaporn, P.; Sorachoti, K.; Khamdahsag, P.; Tanboonchuy, V. Applicability of Iron (III) Trimesic (Fe-BTC) to Enhance Lignin Separation from Pulp and Paper Wastewater. *Sains Malays.* **2019**, *48* (1), 199–208. https://doi.org/10.17576/jsm-2019-4801-23.

[15] Lestari, W. W.; Hartono, J.; Adreane, M.; Nugrahaningtyas, K. D.; Purnawan, C.; Rahardjo, S. B. Electro-Synthetic Optimization of Host Material Based on MIL-100(Fe). *Molekul* **2016**, *11* (1), 61. https://doi.org/10.20884/1.jm.2016.11.1.195.

[16] Moradi, S. E.; Dadfarnia, S.; Haji Shabani, A. M.; Emami, S. Removal of Congo Red from Aqueous Solution by Its Sorption onto the Metal Organic Framework MIL-100(Fe): Equilibrium, Kinetic and Thermodynamic Studies. *Desalin. Water Treat.* **2015**, *56* (3), 709–721. https://doi.org/10.1080/19443994.2014.947328.

[17] Lv, H.; Zhao, H.; Cao, T.; Qian, L.; Wang, Y.; Zhao, G. Efficient Degradation of High Concentration Azo-Dye Wastewater by Heterogeneous Fenton Process with Iron-Based Metal-Organic Framework. *J. Mol. Catal. A Chem.* **2015**, *400*, 81–89. https://doi.org/10.1016/j.molcata.2015.02.007.

[18] Kuzminova, A.; Dmitrenko, M.; Mazur, A.; Ermakov, S.; Penkova, A. Novel Pervaporation Membranes Based on Biopolymer Sodium Alginate Modified by FeBTC for Isopropanol Dehydration. *Sustainability* **2021**, *13*, 6092. https://doi.org/10.3390/su13116092.

[19] Salazar-Aguilar, A. D.; Vega, G.; Casas, J. A.; Vega-Díaz, S. M.; Tristan, F.; Meneses-Rodríguez, D.; Belmonte, M.; Quintanilla, A. Direct Hydroxylation of Phenol to Dihydroxybenzenes by H2O2 and Fe-Based Metal-Organic Framework Catalyst at Room Temperature. *Catalysts* **2020**, *10*, 172.

https://doi.org/10.3390/catal10020172.
[20] F. Rouquerol; J. Rouquerol; K. Sing. *Adsorption by Powders and Porous Solids*; Elsevier, 1999.
[21] Seo, Y. K.; Yoon, J. W.; Lee, J. S.; Lee, U. H.; Hwang, Y. K.; Jun, C. H.; Horcajada, P.; Serre, C.; Chang, J. S. Large Scale Fluorine-Free Synthesis of Hierarchically Porous Iron(III) Trimesate MIL-100(Fe) with a Zeolite MTN Topology. *Micropor. Mesopor. Mater.* **2012**, *157*, 137–145. https://doi.org/10.1016/j.micromeso.2012.02.027.
[22] Canioni, R.; Roch-Marchal, C.; Sécheresse, F.; Horcajada, P.; Serre, C.; Hardi-Dan, M.; Férey, G.; Grenèche, J. M.; Lefebvre, F.; Chang, J. S.; Hwang, Y. K.; Lebedev, O.; Turner, S.; Van Tendeloo, G. Stable Polyoxometalate Insertion within the Mesoporous Metal Organic Framework MIL-100(Fe). *J. Mater. Chem.* **2011**, *21* (4), 1226–1233. https://doi.org/10.1039/c0jm02381g.
[23] Pazur, J. H.; Kleppe, K. The Oxidation of Glucose and Related Compounds by Glucose Oxidase from Aspergillus Niger. *Biochemistry* **1964**, *3* (4), 578–583. https://doi.org/10.1021/bi00892a018.
[24] Zhang, J. W.; Zhang, H. T.; Du, Z. Y.; Wang, X.; Yu, S. H.; Jiang, H. L. Water-Stable Metal–Organic Frameworks with Intrinsic Peroxidase-like Catalytic Activity as a Colorimetric Biosensing Platform. *Chem. Commun.* **2014**, *50* (9), 1092–1094. https://doi.org/10.1039/c3cc48398c.
[25] Wei, T. H.; Wu, S. H.; Huang, Y. Da; Lo, W. S.; Williams, B. P.; Chen, S. Y.; Yang, H. C.; Hsu, Y. S.; Lin, Z. Y.; Chen, X. H.; Kuo, P. E.; Chou, L. Y.; Tsung, C. K.; Shieh, F. K. Rapid Mechanochemical Encapsulation of Biocatalysts into Robust Metal–Organic Frameworks. *Nat. Commun.* **2019**, *10*, 5002. https://doi.org/10.1038/s41467-019-12966-0.
[26] Valko, M.; Leibfritz, D.; Moncol, J.; Cronin, M. T. D.; Mazur, M.; Telser, J. Free Radicals and Antioxidants in Normal Physiological Functions and Human Disease. *Int. J. Biochem. Cell Biol.* **2007**, *39* (1), 44–84. https://doi.org/10.1016/j.biocel.2006.07.001.
[27] Qin, F. X.; Jia, S. Y.; Wang, F. F.; Wu, S. H.; Song, J.; Liu, Y. Hemin@metal-Organic Framework with Peroxidase-like Activity and Its Application to Glucose Detection. *Catal. Sci. Technol.* **2013**, *3* (10), 2761–2768. https://doi.org/10.1039/c3cy00268c.
[28] Yang, H.; Yang, R.; Zhang, P.; Qin, Y.; Chen, T.; Ye, F. A Bimetallic (Co/2Fe) Metal-Organic Framework with Oxidase and Peroxidase Mimicking Activity for Colorimetric Detection of Hydrogen Peroxide. *Microchim. Acta* **2017**, *184* (12), 4629–4635. https://doi.org/10.1007/s00604-017-2509-4.
[29] Song, C.; Ding, W.; Zhao, W.; Liu, H.; Wang, J.; Yao, Y.; Yao, C. High Peroxidase-like Activity Realized by Facile Synthesis of FeS2 Nanoparticles for Sensitive Colorimetric Detection of H2O2 and Glutathione. *Biosens. Bioelectron.* **2020**, *151* (November 2019), 111983. https://doi.org/10.1016/j.bios.2019.111983.
[30] Ding, Y.; Liu, H.; Gao, L. N.; Fu, M.; Luo, X.; Zhang, X.; Liu, Q.; Zeng, R. C. Fe-Doped Ag2S with Excellent Peroxidase-like Activity for Colorimetric Determination of H2O2. *J. Alloys Compd.* **2019**, *785*, 1189–1197. https://doi.org/10.1016/j.jallcom.2019.01.225.

Chapter 3:

Mechanochemical synthesis, characterisation, and catalytic activity of GOx@Fe-BTC hybrid composite

3. Mechanochemical synthesis, characterisation, and catalytic activity of GOx@Fe-BTC hybrid composite

3.1. Experimental section

3.1.1. Reagents and materials

Iron(III) nitrate nonahydrate ($Fe(NO_3)_3 \cdot 9H_2O$, 98%), tetramethyl ammonium hydroxide pentahydrate ($TMAOH \cdot 5H_2O$, 97%), 1,3,5-benzenetricarboxylic acid (H_3BTC, 95%), and glucose oxidase from *Aspergillus niger* (EC 1.1.3.4), glucose (≥99.5%), 3,3′,5,5′-tetramethylbenzidine (TMB, ≥99%), glacial acetic acid (AcOH, ≥99%), sodium acetate trihydrate ($NaAc \cdot 3H_2O$), Ethanol (EtOH, ≥99.8%), and horseradish peroxidase (EC 1.11.1.7) were purchased by Sigma-Aldrich and used as received without further purification.

3.1.2. Synthesis

In situ immobilisation of glucose oxidase on Fe-BTC material was performed under optimal reaction conditions, according to the experimental results discussed in Chapter 2. In a typical mechanochemical synthesis of GOx@Fe-BTC hybrid composite 1.29 g of $Fe(NO_3)_3 \cdot 9H_2O$, 0.47 g of H_3BTC, 1.81 g of $TMAOH \cdot 5H_2O$, appropriate amounts of glucose oxidase (10, 25 or 50 mg), and 13.7 g of zirconia balls were place in a 32 mL stainless-steel Teflon coated grinding jar. No additional solvents were added. The reaction mixture was grinded for 6 or 30 minutes using a Spex 8000 Mixer/Mill. Then, the resulting dense, orange-coloured slurry was dispersed in 20 mL of Milli-Q deionised water. The pH of the obtained dispersion was ca. 4. The dispersion was centrifugated for 10 min at 2500 rpm, the precipitate was washed twice with Milli-Q deionised water, and finally air-dried. The resulting dry orange sample was collected and stored at 4 °C.

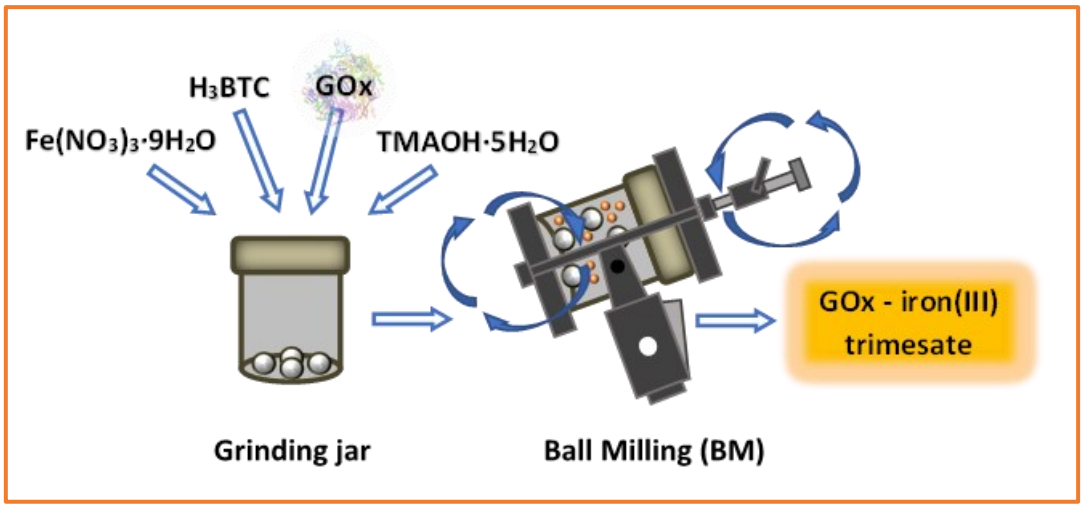

Figure 3.1. Schematic representation of a mechanochemical synthesis of GOx-iron(III)trimesate hybrid composite.

3.1.3. Characterisation

Fourier-transform infrared (FT-IR) spectra were recorded using a Bruker Tensor 27 spectrophotometer within the 400-4000 cm^{-1} scanning range. X-ray powder diffraction (XRPD) patterns were collected on a Bruker D8 Advance Diffractometer using Cu-Kα radiation (λ = 1.54056 Å, I = 30 mA, V = 40 kV) in a scanning range between 7° and 80° 2-theta (step size = 0.05° 2-theta). Due to the high iron fluorescence radiation emission stimulated by the Kα copper radiation, to obtain a satisfactory signal-to-noise ratio in the XRPD pattern an appropriate acquisition time was selected. Differential scanning calorimetry analysis (DSC) and thermogravimetric analysis (TGA) were carried out on a Perkin-Elmer STA 6000 simultaneous thermal analyser in a temperature range between 25 and 850 °C (heating rate = 10 °C/min) under O_2 flow (40 mL/min). N_2 physisorption was performed on a Sorptomatic 1990 CE apparatus (Fisons Instruments) at -196 °C. Prior to measurement, all the samples were outgassed at room temperature under vacuum for 24 h. Pore size distribution was estimated by using Horvath-Kavazoe (HK) equation to the adsorption branches of the N_2 isotherms. Specific Surface Area (SSA) was determined from adsorption data by applying Dubinin-Radushkevich (DR) method.

3.1.4. Catalytic activity of GOx@Fe-BTC

Biocatalytic activity of GOx@Fe-BTC hybrid biocomposite was evaluated. Experiments were performed by adding GOx@Fe-BTC (500 μg/mL), TMB (0.4 mM) and glucose (0.5 mM) in acetate buffer (pH 4, 10 mM). The solution mixtures were incubated at 35 °C under magnetic stirring (150 rpm) for 1 hour. Then, the test samples were centrifugated at 5000 rpm for 10 minutes and supernatants were collected. Absorbance of the supernatants was then recorded at 652 nm on a Cary 5000 UV-Vis-NIR spectrophotometer (Agilent Technologies). All measurements were performed in triplicate and the average value reported. The relative activity was calculated using the following formula:[1]

$$Relative\ activity\ (\%) = \frac{A}{A_{max}} \times 100\%$$

Where A_{max} is the maximum absorbance recorded, and A is the absorbance measured at same conditions.

3.1.5. Leaching test

Enzyme leaching-out from the support was investigated. In order to ascertain the degree of leaching after immobilisation process, catalytic activity of wastewater collected after the synthesis of GOx@Fe-BTC was measured. Wastewater was incubated at 35 °C under magnetic stirring (150 rpm) for 1 hour with TMB (0.4 mM), HRP (0.1 μg/mL), and glucose (0.5 mM) in acetate buffer (pH 4, 10 mM). Then, the test sample was centrifugated at 5000 rpm for 10 minutes and supernatants were collected. Absorbance of the supernatant was then recorded at 652 nm on a Cary 5000 UV-Vis-NIR spectrophotometer (Agilent Technologies). GOx leakage from the support was also evaluated by incubating GOx@Fe-BTC in acetate buffer (pH 4.0, 10 mM) for 24 hours. After centrifugation (5000 rpm for 10 minutes), enzymatic activity of supernatant was tested as described above. All measurements were performed in triplicate and the average value reported.

3.1.6. Temperature, storage conditions, and biocatalyst concentration dependence on GOx@Fe-BTC catalytic activity

The influence of temperature on the catalytic activity of GOx@Fe-BTC was investigated in the temperature range between 25 and 55 °C. Experiments were carried out by adding GOx@Fe-BTC (500 μg/mL) (or free GOx (0.2 μg/mL) and free HRP (0.1 μg/mL)), TMB (0.4 mM) and glucose (0.5 mM) in acetate buffer (10 mM, pH = 4). The solution mixtures were incubated at the appropriate temperature under magnetic stirring (150 rpm) for 1 hour. The effect of GOx@Fe-BTC concentration on its catalytic activity was examined. Experiments were carried out by adding different concentration of GOx@Fe-BTC (250, 500 or 1000 μg/mL), TMB (0.4 mM) and glucose (0.5 mM) in acetate buffer (10 mM, pH = 4). The solution mixtures were incubated at 35 °C under magnetic stirring (150 rpm) for 1 hour. The influence of storage conditions on the catalytic activity of GOx@Fe-BTC was investigated by measuring catalytic activity of samples (under conditions as described in Section 3.1.4) after storage at room temperature, 4 °C or – 20 °C for 24 hours.

After the appropriate incubation time, the test samples of all above-mentioned experiments were centrifugated at 5000 rpm for 10 minutes and supernatants were collected. Absorbance of the supernatants was then recorded at 652 nm on a Cary 5000 UV-Vis-NIR spectrophotometer (Agilent Technologies). All measurements were performed in triplicate and the average value reported.

3.1.7. Catalytic stability

Stability tests were performed by testing the catalytic activity of GOx@Fe-BTC hybrid biocomposite after storage at 4 °C for 1, 2, 3, 4 and 5 weeks. Experiments were carried out by adding GOx@Fe-BTC (500 μg/mL), TMB (0.4 mM) and glucose (0.5 mM) in acetate buffer (10 mM, pH = 4). The solution mixtures were incubated at 35 °C under magnetic stirring (150 rpm) for 1 hour. Then, the test samples were centrifugated at 5000 rpm for 10 minutes and supernatants were collected. Absorbance of the supernatants was then recorded at 652 nm Absorbance of the supernatants was then recorded at 652 nm on a Cary 5000 UV-Vis-NIR spectrophotometer (Agilent Technologies). All measurements were performed in triplicate and the average value reported.

3.2. Results and Discussion

GOx@Fe-BTC hybrid composite materials have been synthesised via mechanochemical approach adding different enzyme amounts and/or using various grinding times, as resumed in Table 3.1.

Sample	Grinding time (min)	pH	GOx added (mg)
Fe-BTC_6minM	6	4	0
GOx@Fe-BTC_6minM_10mg	6	4	10
GOx@Fe-BTC_6minM_25mg	6	4	25
GOx@Fe-BTC_6minM_50mg	6	4	50
Fe-BTC_30minM	30	4	0
GOx@Fe-BTC_30minM_10mg	30	4	10
GOx@Fe-BTC_30minM_25mg	30	4	25
GOx@Fe-BTC_30minM_50mg	30	4	50

Table 3.1. Samples prepared through mechanochemical approach and corresponding synthesis conditions.

3.2.1. Physicochemical characterisation

All Fe-BTC and GOx@Fe-BTC samples were characterised by X-ray powder diffraction. Fourier-Transform infrared spectroscopy, thermal analysis, and nitrogen physisorption.

X-ray Powder Diffraction

Samples' microstructure has been investigated by XRPD and FT-IR. Figure 3.2 shows XRPD patterns obtained for Fe-BTC and GOx@Fe-BTC samples. Despite the different grinding time and the different amount of enzyme, all samples showed a similar pattern in terms of position of diffraction peaks (ca. 10.65, 18.76, 23.83, 28.09, 33.36, and 42.49° 2-theta), proving the obtainment of a Fe-BTC material. Indeed, diffraction patterns obtained for both GOx@Fe-BTC_6minM_10,25,50mg and GOx@Fe-BTC_30minM_10,25,50mg samples do not differ

significantly from those of Fe-BTC_6minM and Fe-BTC_30minM, respectively. Such results demonstrated that the immobilisation of GOx did not significantly affect MOF's microstructure.

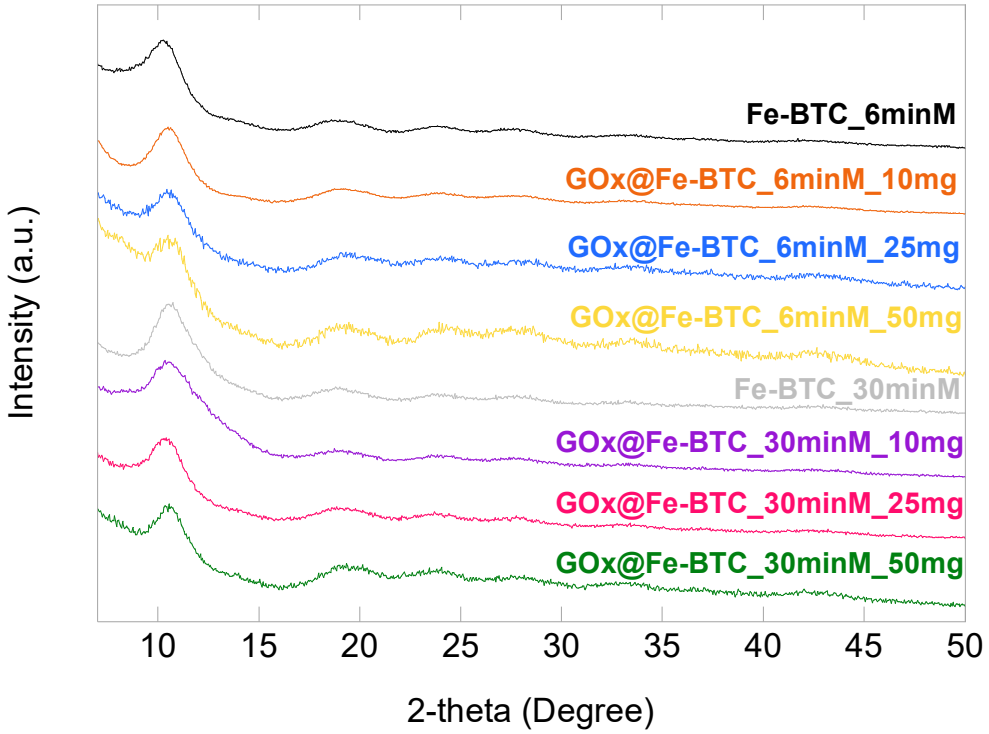

Figure 3.2. XRPD patterns of Fe-BTC and GOx@Fe-BTC samples recorded from 7 to 50° 2-theta.

Fourier-Transform Infrared Spectroscopy

Microstructure of samples was also investigated by FT-IR. The related spectra of Fe-BTC and GOx@Fe-BTC samples are shown in Figure 3.3. The spectra of all samples are similar as well as to the ones obtained for Fe-BTC material (see Chapter 2), and results reported in the literature for this MOF.[2] The broad band in the 3600-3100 cm^{-1} region can be attributed to the stretching vibrations of hydroxyl groups and water molecules coordinated to iron octahedra and adsorbed water molecules.[3] The band at 1625 cm^{-1} arising from the C=O stretching of carboxylate groups and the band at 1564 cm^{-1}, assigned to the asymmetric stretching of O–C–O groups, likely mask the bands characteristic of enzyme molecules (i.e., C=O stretching vibrations of peptide bonds, and a combination of C–N stretching and N–H in-plane bending vibrations of the peptide groups, respectively).[4] The band at 1371 cm^{-1} is ascribable to the symmetric stretching vibration of the O–C–O group. The bands at 759 and 706 cm^{-1} are attributed to the C–H bending vibrations of aromatic rings, while the band at 463 cm^{-1} is assigned to stretching of Fe-O bonds.[5–7]

Despite the different grinding time and/or the different amount of enzyme added, all samples showed no significant differences when comparing microstructure by FT-IR and XRPD. Therefore, enzyme immobilisation did not affect the MOF structure.

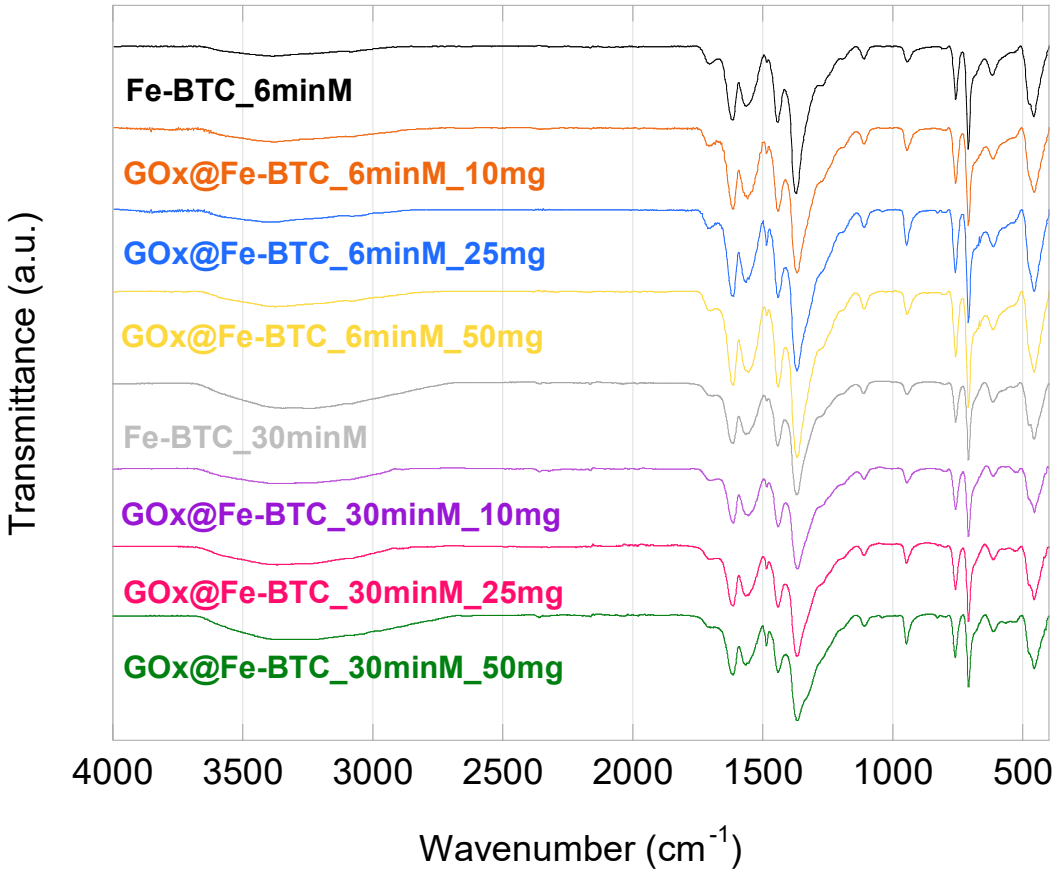

Figure 3.3. FT-IR spectra of Fe-BTC and GOx@Fe-BTC samples from 400 to 4000 cm^{-1}.

Thermal Analysis

Thermal behaviour of samples was examined under oxygen flow. Figure 3.4 and 3.5 showed TG, dTG and DCS curves of samples obtained grinding for 6 and 30 minutes, respectively. All samples showed three weight losses characteristic of Fe-BTC material: a first weight loss up to 150 °C arising from the departure of adsorbed water molecules; a second weight loss between 150 and 260 °C due to the loss of water molecules coordinated to iron trimers; a third and last weight loss over the range between 260 and 450 °C attributed to the decomposition of the framework by combustion, denoted by an exothermic peak at ca. 350 °C in the DSC curve, Figure 3.4 c and 3.5 c.

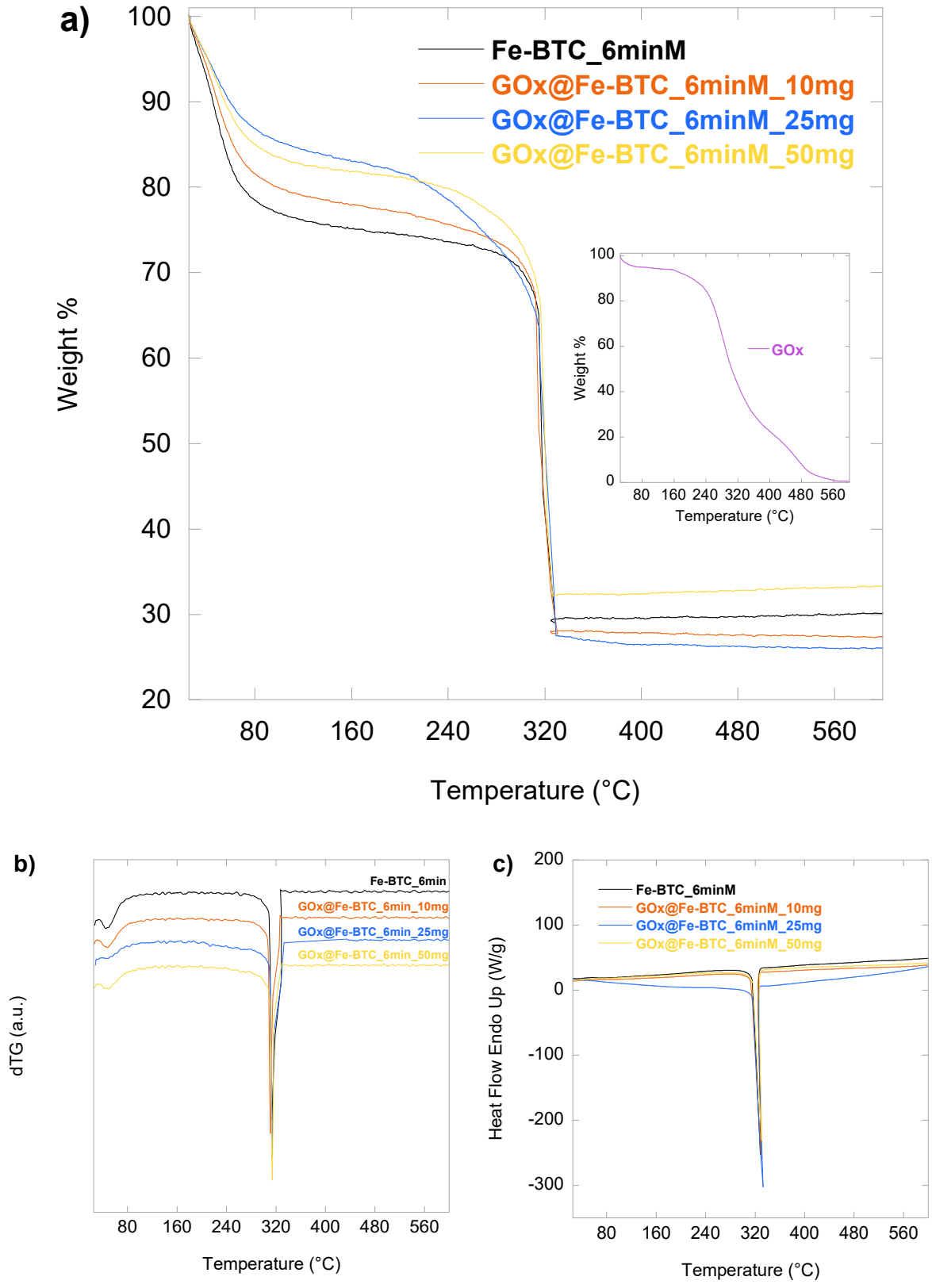

Figure 3.4. TG (a), dTG (b) and DSC (c) curves of Fe-BTC and GOx@Fe-BTC samples obtained in 6 min grinding (inset: GOx TG curve), in the temperature range between 25 and 600 °C (10 °C/min) under O_2 flow (40 ml/min).

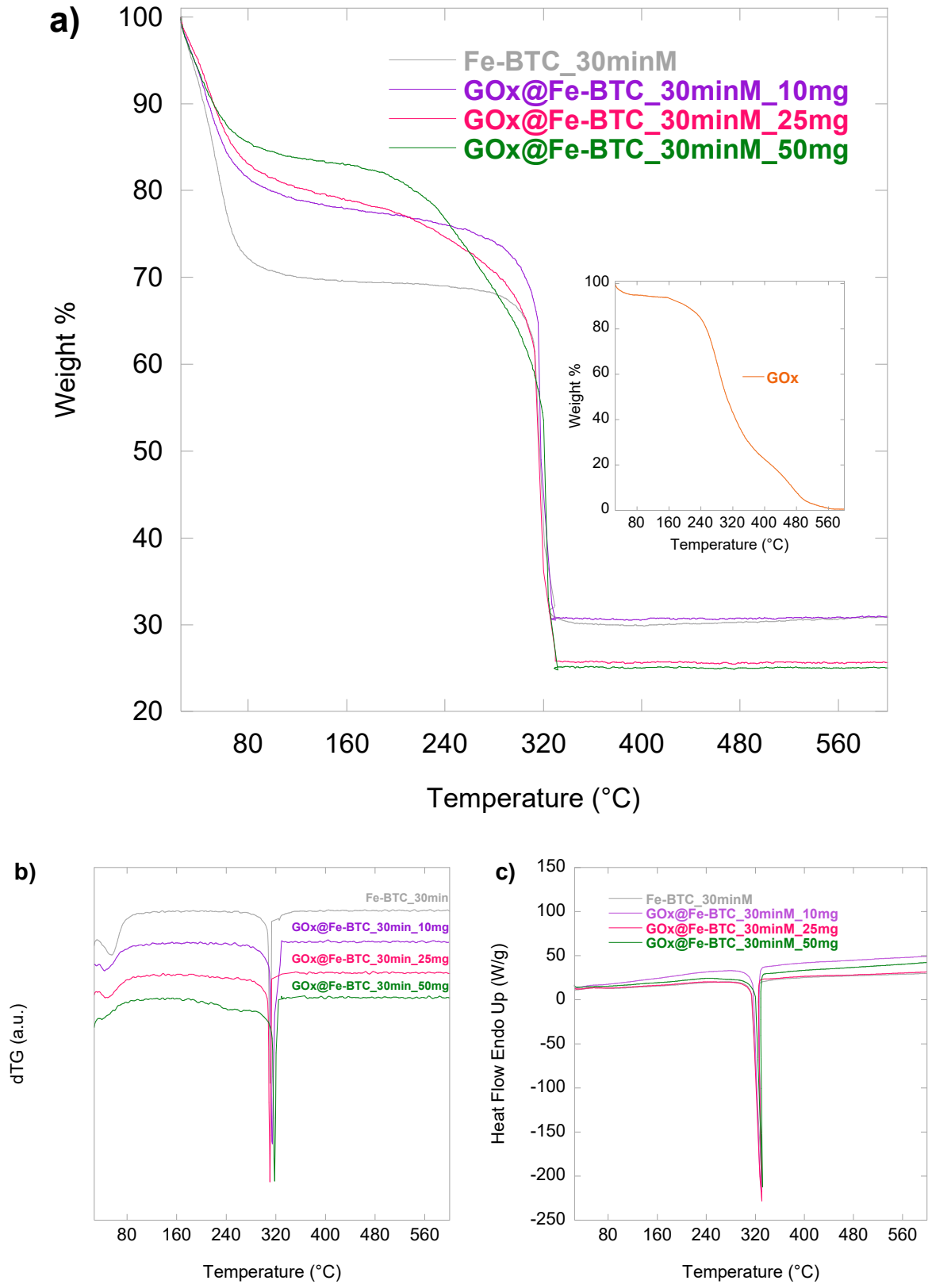

Figure 3.5. TG (a), dTG (b) and DSC (c) curves of Fe-BTC and GOx@Fe-BTC samples obtained in 30 min grinding (inset: GOx TG curve), in the temperature range between 25 and 600 °C (10 °C/min) under O_2 flow (40 ml/min).

The weight losses of Fe-BTC_6minM and Fe-BTC_30minM in the 25-150 °C range are higher than those observed for GOx@Fe-BTC_6minM and GOx@Fe-BTC_30minM samples, respectively. This could be attributed to the immobilisation of the enzyme into the pores of Fe-BTC. Indeed, due to the presence of GOx, a lower amount of water molecules could be adsorbed within the pores. Moreover, the weight loss in the 150-260 °C range increased by increasing the amount of enzyme added (Table 3.2), due to the degradation of GOx. GOx@Fe-BTC_6minM_50mg was the only exception, showing a weight loss between 150 and 260 °C lower than GOx@Fe-BTC_6minM_25mg, probably due to an ineffective immobilisation of GOx in this sample.

Sample	1st weight loss (25-150 °C)	2nd weight loss (150-260 °C)	3rd weight loss (260-450 °C)
Fe-BTC_6minM	24.0 %	3.4 %	43.4 %
GOx@Fe-BTC_6minM_10mg	20.8 %	5.2 %	46.1 %
GOx@Fe-BTC_6minM_25mg	15.4 %	10.4 %	47.9 %
GOx@Fe-BTC_6minM_50mg	17.5 %	5.4 %	44.8 %
Fe-BTC_30minM	30.1 %	1.6 %	38.5 %
GOx@Fe-BTC_30minM_10mg	21.3 %	4.3 %	43.9 %
GOx@Fe-BTC_30minM_25mg	19.7 %	8.8 %	46.1 %
GOx@Fe-BTC_30minM_50mg	16.6 %	13.1 %	45.7 %

Table 3.2. Weight losses extracted from the TG curves of all Fe-BTC and GOx@Fe-BTC samples.

Nitrogen physisorption

N_2 adsorption/desorption isotherms and pore size distributions for Fe-BTC and GOx@Fe-BTC samples are reported in Figure 3.6. Such samples present a I-type isotherm, which is typical of microporous material (Figure 3.6 a, c).[8] Data obtained for GOx@Fe-BTC_6minM_25mg and GOx@Fe-BTC_6minM_50mg are not shown since such samples did not significatively adsorb. We hypothesised that all pores of such samples result filled by the enzyme. Compared to Fe-BTC samples, GOx@Fe-BTC composites showed a reduced SSA and micropore volume (Table

3.3). A decrease in SSA and micropore volume of the material is attributed to the immobilisation of GOx which blocks a portion of the pores. Moreover, the decrease of both micropore volume and SSA was significatively higher by increasing the amount of GOx. As shown in Figure 3.6 b, d, a decrease of the intensity of the first peak and a shift to higher pore dimensions in the pore size distribution curves was also observed with increasing GOx amounts. These results indicated that GOx has been embedded into Fe-BTC.

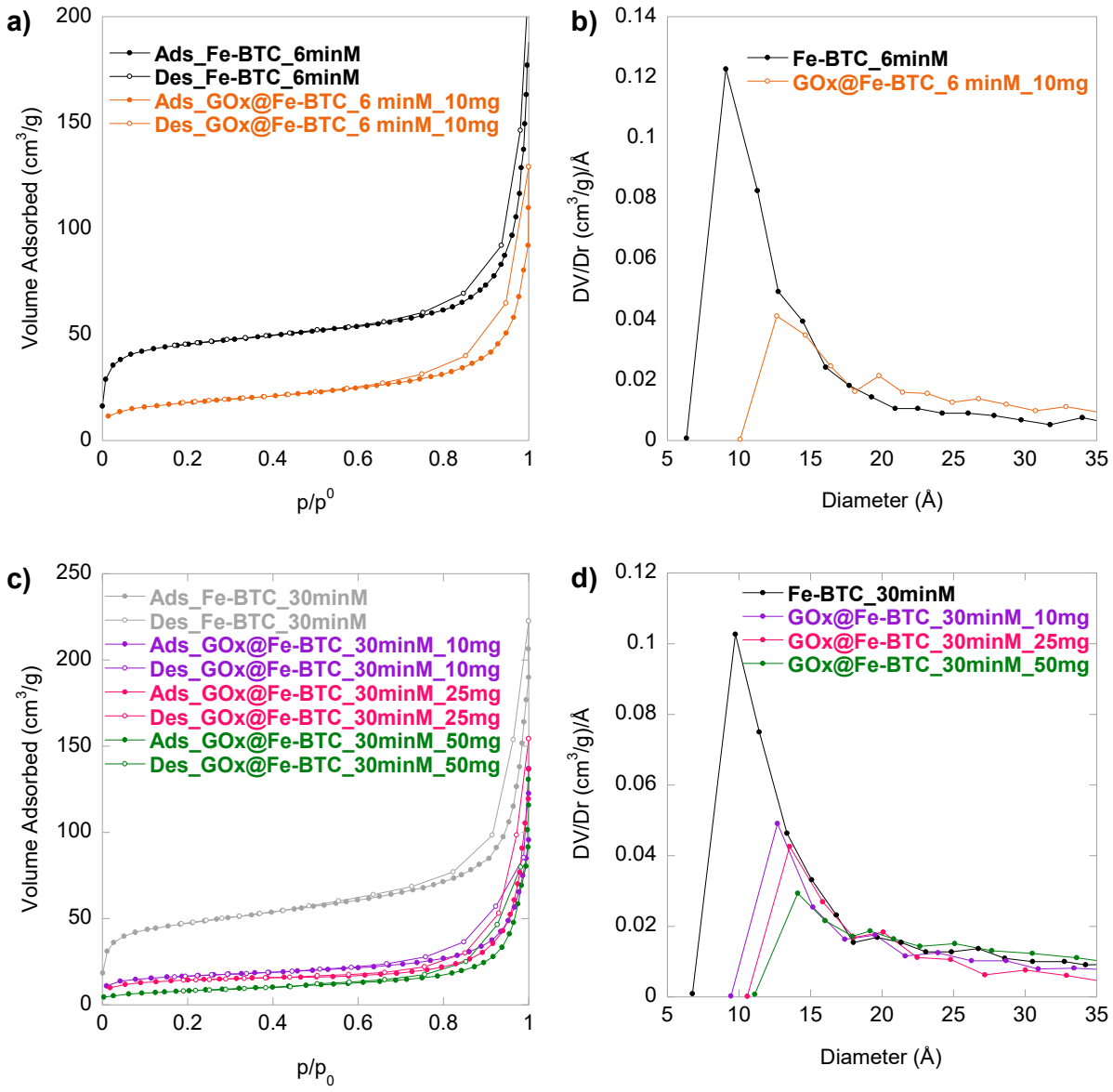

Figure 3.6. N_2 adsorption/desorption isotherms obtained at -196 °C (a, c) and pore size distributions (b, d) of Fe-BTC and GOx@Fe-BTC samples.

Sample	SSA m^2/g	Micropore volume (cm^3/g)	Mesopore volume (cm^3/g)	Macropore volume (cm^3/g)
Fe-BTC_6minM	204	0.069	0.062	0.030
GOx@Fe-BTC_6minM_10mg	73	0.026	0.048	0.019
GOx@Fe-BTC_6minM_25mg	n.a.	n.a.	n.a.	n.a.
GOx@Fe-BTC_6minM_50mg	n.a.	n.a.	n.a.	n.a.
Fe-BTC_30minM	194	0.071	0.078	0.040
GOx@Fe-BTC_30minM_10mg	73	0.025	0.042	0.022
GOx@Fe-BTC_30minM_25mg	63	0.022	0.044	0.032
GOx@Fe-BTC_30minM_50mg	4	0.012	0.040	0.027

Table 3.3. Specific Surface Area (SSA) and macro-, meso- and micropore volume of Fe-BTC and GOx@Fe-BTC samples. %RSD SSA = 2; %RSD pore volume = 1. n.a.: not available (i.e., the sample did not adsorb).

3.2.2. Catalytic activity and stability

Catalytic activity of all GOx@Fe-BTC samples was evaluated. On the one hand, as shown in Figure 3.7, relative activity of GOx@Fe-BTC_6minM samples reached its maximum for GOx@Fe-BTC_6minM_25mg. On the other hand, relative activity of GOx@Fe-BTC_30minM samples increased with increasing GOx amounts, even though the highest relative activity result has been recorded for GOx@Fe-BTC_6minM_25mg.

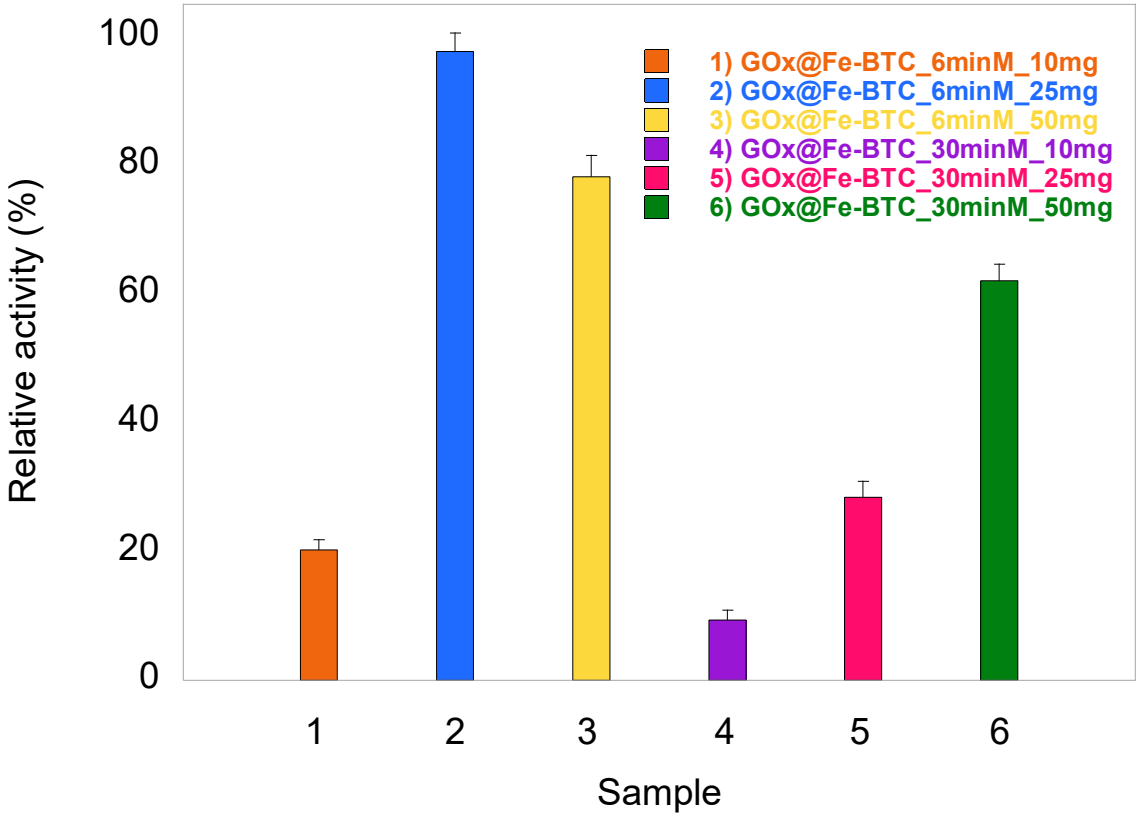

Figure 3.7. Relative activity of GOx@Fe-BTC hybrid composite materials. Activity normalised at Abs_{652nm} = 0.508. Error bars represent the standard deviations of three independent experiments.

Regarding leaching out from the support, none of the samples showed enzyme leaching when washing the material after the synthesis. Conversely, GOx@Fe-BTC_6minM_25mg (Figure 3.8 b) and GOx@Fe-BTC_6minM_50mg (Figure 3.8 c) showed a significative leaching after incubation in acetate buffer (10 mM; pH 4) for 24 hours.

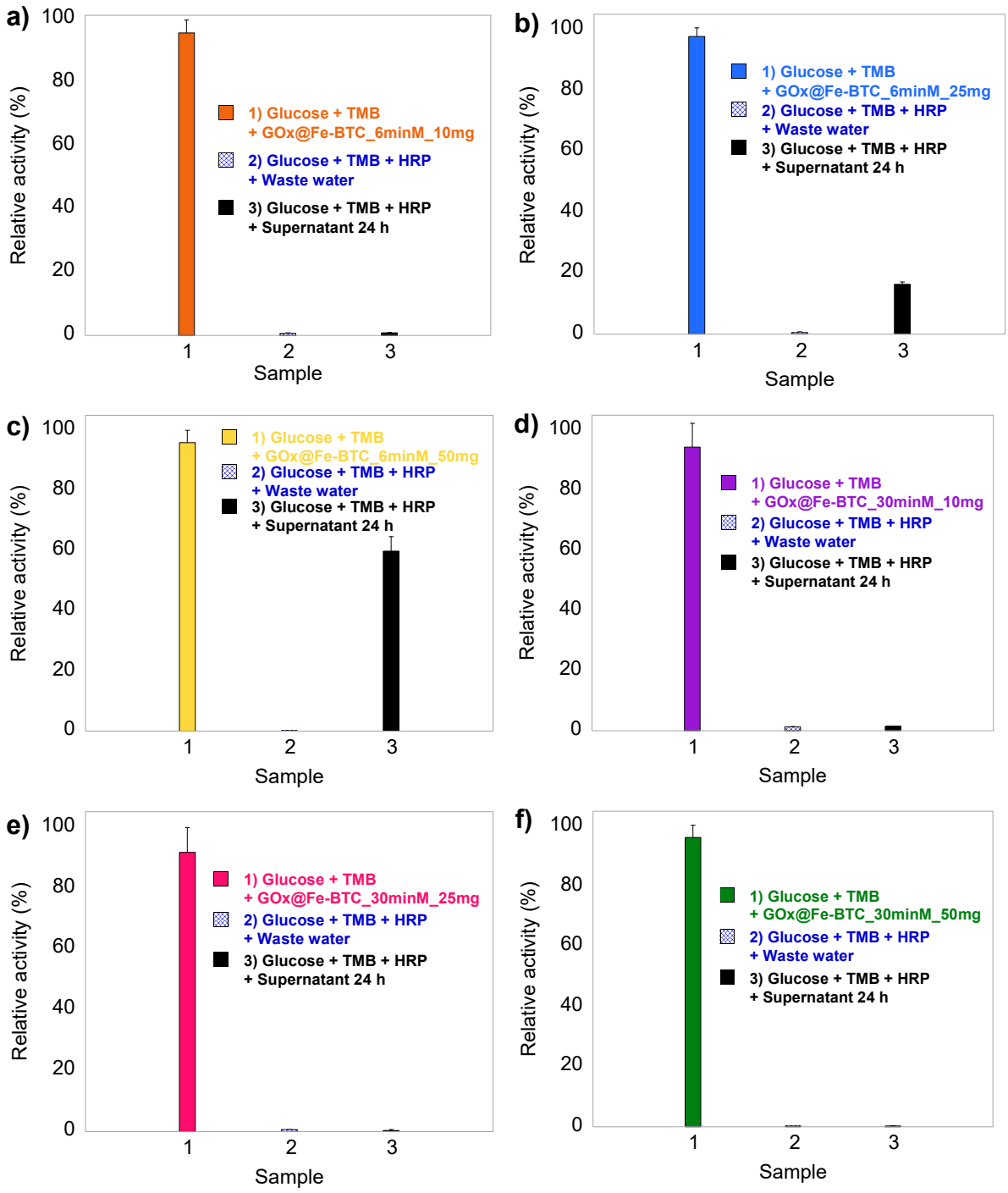

Figure 3.8. Leaching tests performed on GOx@Fe-BTC samples. Error bars represent the standard deviations of three independent experiments.

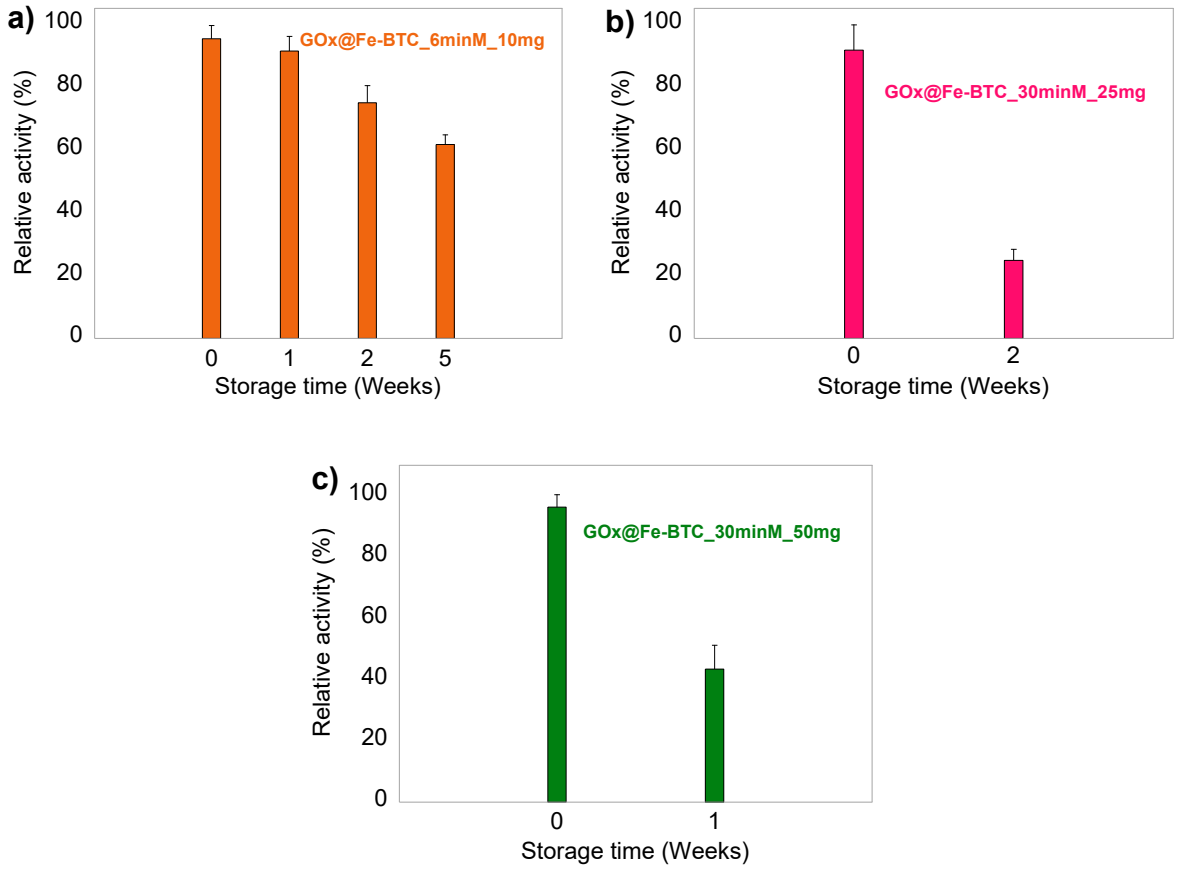

Figure 3.9. Catalytic stability of GOx@Fe-BTC samples. Error bars represent the standard deviations of three independent experiments.

Figure 3.9. showed catalytic stability monitored for GOx@Fe-BTC_6minM_10mg, GOx@Fe-BTC_30minM_25mg and GOx@Fe-BTC_30minM_50mg. Catalytic stability of GOx@Fe-BTC_6minM_25mg, GOx@Fe-BTC_6minM_50mg were not investigated due to the remarkable leaching out from the Fe-BTC support. Furthermore, catalytic stability of GOx@Fe-BTC_30minM_10mg was not monitored because of the low relative activity shown by this sample. The best result in terms of catalytic stability was obtained for GOx@Fe-BTC_6minM_10mg, which retained up to 60 % of its activity for 5 weeks, unlike GOx@Fe-BTC_30minM_50mg and GOx@Fe-BTC_30minM_25mg, whose activity significatively decreased after 1 and 2 weeks, respectively. Compared to results reported in the literature where the catalytic activity of the hybrid material dramatically decreased after one week,[9,10] GOx@Fe-BTC_6minM_10mg sample has proven to possess an exceptional catalytic stability performance, becoming appealing for long-term storage and utilisation . Further investigations have been performed on this sample.

3.2.3. Temperature, storage conditions, and biocatalyst concentration dependence on GOx@Fe-BTC catalytic activity

Similar to free GOx, the catalytic activity of GOx@Fe-BTC biocatalyst is closely dependent on experimental conditions. The effect of temperature, storage conditions, and biocatalyst concentrations on the relative activity of GOx@Fe-BTC (6 min grinding time, 10 mg GOx) was investigated.

As shown in Figure 3.10, immobilised (Figure 3.10 a) and free GOx (Figure 3.10 b) showed a similar temperature profile with the maximal relative activity at 35 °C and a significant activity loss above 45 °C. Therefore, enzyme immobilisation did not alter the temperature dependence of catalytic activity of GOx.

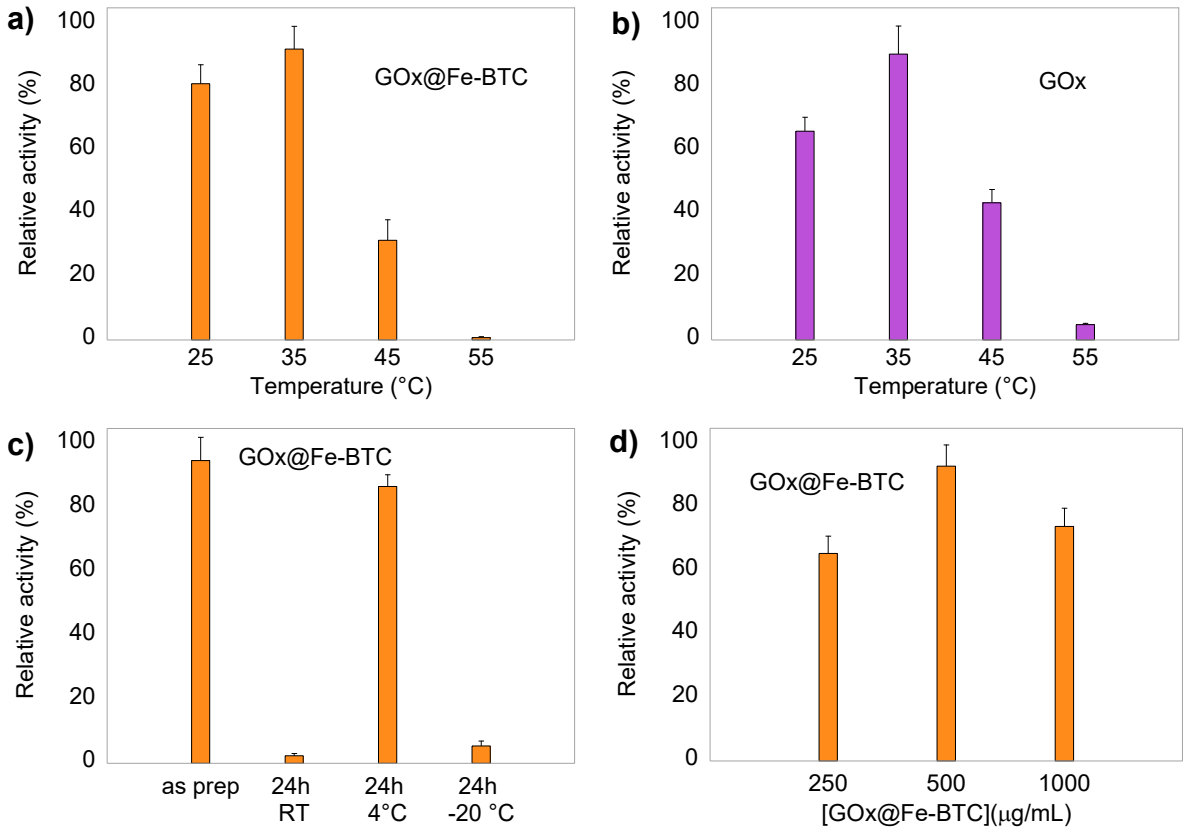

Figure 3.10. Effect of temperature (a), storage conditions (c), and biocatalyst concentration (d) on GOx@Fe-BTC catalytic activity. Temperature profile of GOx (b). Error bars represent the standard deviations of three independent experiments.

The effect of different storage conditions was also investigated. As depicted in Figure 3.10 c, catalytic activity of GOx@Fe-BTC hybrid composite is almost fully retained storing the sample at 4 °C, unlike storage at room temperature or -20 °C which have been observed to cause a

significant activity loss within only 24 hours. The activity dependence of the concentration of the biocatalyst in the test samples was also evaluated. As shown in Figure 3.10 d, relative activity reached the maximum when GOx@Fe-BTC concentration is 500 μg/mL. A decrease of relative activity was observed while increasing the catalyst concentration. As already discussed in Section 2.2, the higher the catalyst concentration, the higher is the surface of biocatalyst available to adsorb oxTMB and remove it from solution. Therefore, a lower concentration of oxTMB in solution is detected. According to the experimental results above, storage at 4 °C represented the optimal conditions to retain biocatalyst activity. Moreover, optimum reaction temperature, and GOx@Fe-BTC concentration, were 35 °C, and 500 μg/mL, respectively.

Therefore, an exceptional GOx@Fe-BTC biocatalyst has been synthesised via mechanochemical approach without using any solvents, at room temperature, in just 6 minutes, using little amount of enzyme. These results represent an unprecedented breaking point compared to conventional synthesis methods in solution. The use of any solvents has been demonstrated to be completely unnecessary for the synthesis of this material. Such a solvent-free method could further emerge the potential of Fe-BTC MOFs as immobilisation supports. Indeed, the long-term catalytic stability of the material, together with the rapid, facile, eco- and bio-compatible synthesis route are desirable for industrial scale-up, owing to minimizing the environmental footprint of the process while providing the same efficiency of conventional routes. The absence of solvents, which could gain access into the active sites affecting the local environment of biomolecules, ensures an outstanding protection from chemical, and biological degradation while retaining bioactivity. This solvent-free approach can afford maintaining biomolecules' functionality while protectively coating them by robust and porous supports. This represents one of the main goals in the field of *ex vivo* applications of biomolecules, which are often hindered by an intrinsic activity loss during the immobilisation process. Stability of biomolecules depends on biological, chemical, and physical factors. Indeed, a careful evaluation of the immobilisation conditions (concentrations, temperature, pH) has been carried out prior to one-pot synthesis of GOx@Fe-BTC composites.[11] In this regard, the encapsulation of GOx molecules have been achieved in just one-step by simply adding the enzyme together with the support's precursors in the solid state. This approach can be potentially adapted to an infinite variety of guest molecules and MOFs, making the fabrication of biomolecule@MOF composites a remarkably easy, green, and cost-efficient procedure.

3.3. References

[1] Yan, Z.; Niu, Q.; Mou, M.; Wu, Y.; Liu, X.; Liao, S. A Novel Colorimetric Method Based on Copper Nanoclusters with Intrinsic Peroxidase-like for Detecting Xanthine in Serum Samples. *J. Nanoparticle Res.* **2017**, *19* (7). https://doi.org/10.1007/s11051-017-3904-9.

[2] Pangkumhang, B.; Jutaporn, P.; Sorachoti, K.; Khamdahsag, P.; Tanboonchuy, V. Applicability of Iron (III) Trimesic (Fe-BTC) to Enhance Lignin Separation from Pulp and Paper Wastewater. *Sains Malays.* **2019**, *48* (1), 199–208. https://doi.org/10.17576/jsm-2019-4801-23.

[3] Leclerc, H.; Vimont, A.; Lavalley, J. C.; Daturi, M.; Wiersum, A. D.; Llwellyn, P. L.; Horcajada, P.; Férey, G.; Serre, C. Infrared Study of the Influence of Reducible Iron(Iii) Metal Sites on the Adsorption of CO, CO2, Propane, Propene and Propyne in the Mesoporous Metal-Organic Framework MIL-100. *Phys. Chem. Chem. Phys.* **2011**, *13* (24), 11748–11756. https://doi.org/10.1039/c1cp20502a.

[4] Patra, S.; Hidalgo Crespo, T.; Permyakova, A.; Sicard, C.; Serre, C.; Chaussé, A.; Steunou, N.; Legrand, L. Design of Metal Organic Framework-Enzyme Based Bioelectrodes as a Novel and Highly Sensitive Biosensing Platform. *J. Mater. Chem. B* **2015**, *3* (46), 8983–8992. https://doi.org/10.1039/c5tb01412c.

[5] Lestari, W. W.; Hartono, J.; Adreane, M.; Nugrahaningtyas, K. D.; Purnawan, C.; Rahardjo, S. B. Electro-Synthetic Optimization of Host Material Based on MIL-100(Fe). *Molekul* **2016**, *11* (1), 61. https://doi.org/10.20884/1.jm.2016.11.1.195.

[6] Moradi, S. E.; Dadfarnia, S.; Haji Shabani, A. M.; Emami, S. Removal of Congo Red from Aqueous Solution by Its Sorption onto the Metal Organic Framework MIL-100(Fe): Equilibrium, Kinetic and Thermodynamic Studies. *Desalin. Water Treat.* **2015**, *56* (3), 709–721. https://doi.org/10.1080/19443994.2014.947328.

[7] Lv, H.; Zhao, H.; Cao, T.; Qian, L.; Wang, Y.; Zhao, G. Efficient Degradation of High Concentration Azo-Dye Wastewater by Heterogeneous Fenton Process with Iron-Based Metal-Organic Framework. *J. Mol. Catal. A Chem.* **2015**, *400*, 81–89. https://doi.org/10.1016/j.molcata.2015.02.007.

[8] F. Rouquerol; J. Rouquerol; K. Sing. *Adsorption by Powders and Porous Solids*; Elsevier, 1999.

[9] Yee, Y. C.; Hashim, R.; Mohd Yahya, A. R.; Bustami, Y. Colorimetric Analysis of Glucose Oxidase-magnetic Cellulose Nanocrystals (CNCS) for Glucose Detection. *Sensors (Switzerland)* **2019**, *19* (11), 1–12. https://doi.org/10.3390/s19112511.

[10] Tocco, D.; Carucci, C.; Todde, D.; Shortall, K.; Otero, F.; Sanjust, E.; Magner, E.; Salis, A. Enzyme Immobilization on Metal Organic Frameworks: Laccase from Aspergillus Sp. Is Better Adapted to ZIF-Zni Rather than Fe-BTC. *Colloids Surfaces B Biointerfaces* **2021**, *208*, 112147. https://doi.org/10.1016/j.colsurfb.2021.112147.

[11] Mannias, G.; Scano, A.; Pilloni, M.; Magner, E.; Ennas, G. Tailoring MOFs to Biomedical Applications: A Chimera or a Concrete Reality? The Case Study of Fe-BTC by Bio-Friendly Mechanosynthesis. *Comments Inorg. Chem.* **2022**, *00* (00), 1–21. https://doi.org/10.1080/02603594.2022.2153837.

Chapter 4:

Sonochemical synthesis, characterisation, and intrinsic peroxidase-like activity of Fe-BTC

4. Sonochemical synthesis, characterisation, and intrinsic peroxidase-like activity of Fe-BTC

4.1. Experimental section

4.1.1. Reagents and materials

Iron(III) nitrate nonahydrate ($Fe(NO_3)_3 \cdot 9H_2O$, 98%), tetramethyl ammonium hydroxide pentahydrate ($TMAOH \cdot 5H_2O$, 97%), 1,3,5-benzenetricarboxylic acid (H_3BTC, 95%), 3,3′,5,5′-tetramethylbenzidine (TMB, ≥99%), hydrogen peroxide solution (H_2O_2, 30% (w/w) in H_2O), Ethanol (EtOH, ≥99.8%), glacial acetic acid (AcOH, ≥ 99%), and sodium acetate trihydrate ($NaAc \cdot 3H_2O$) were purchased by Sigma-Aldrich and used as received without further purification.

4.1.2. Synthesis

In a typical synthesis two solutions are prepared. Solution 1 was prepared by dissolving 0.3225 g of $Fe(NO_3)_3 \cdot 9H_2O$ in 15 mL of deionised water. Solution 2 was obtained by dissolving 0.1178 g of H_3BTC and proper amounts of $TMAOH \cdot 5H_2O$ in 15 mL of deionised Then, solutions 1 and 2 were mixed, instantaneously yielding an orange-coloured sol. The quantities of $TMAOH \cdot 5H_2O$ were calculated in order to give a different pH in the resulting mixed solution: 0.4078, 0.4531 or 0.4984 g to obtain pH 3, 4 or 5, respectively. Concentrations in the resulting solution were: H_3BTC (3.9 mg/mL), $Fe(NO_3)_3 \cdot 9H_2O$, (10.8 mg/mL), and $TMAOH \cdot 5H_2O$ (13.6, 15.1 or 16.6 mg/mL). The suspension was kept in a cooling bath and immediately processed by 20 cycles of 10 s ultrasound irradiation and 60 s rest at room temperature (ultrasound frequency: 23 kHz; amplitude: 15 μm). Synthesis was carried out on a Soniprep 150 sonicator (Figure 4.1) using a titanium probe (tip diameter: 9.5 mm).

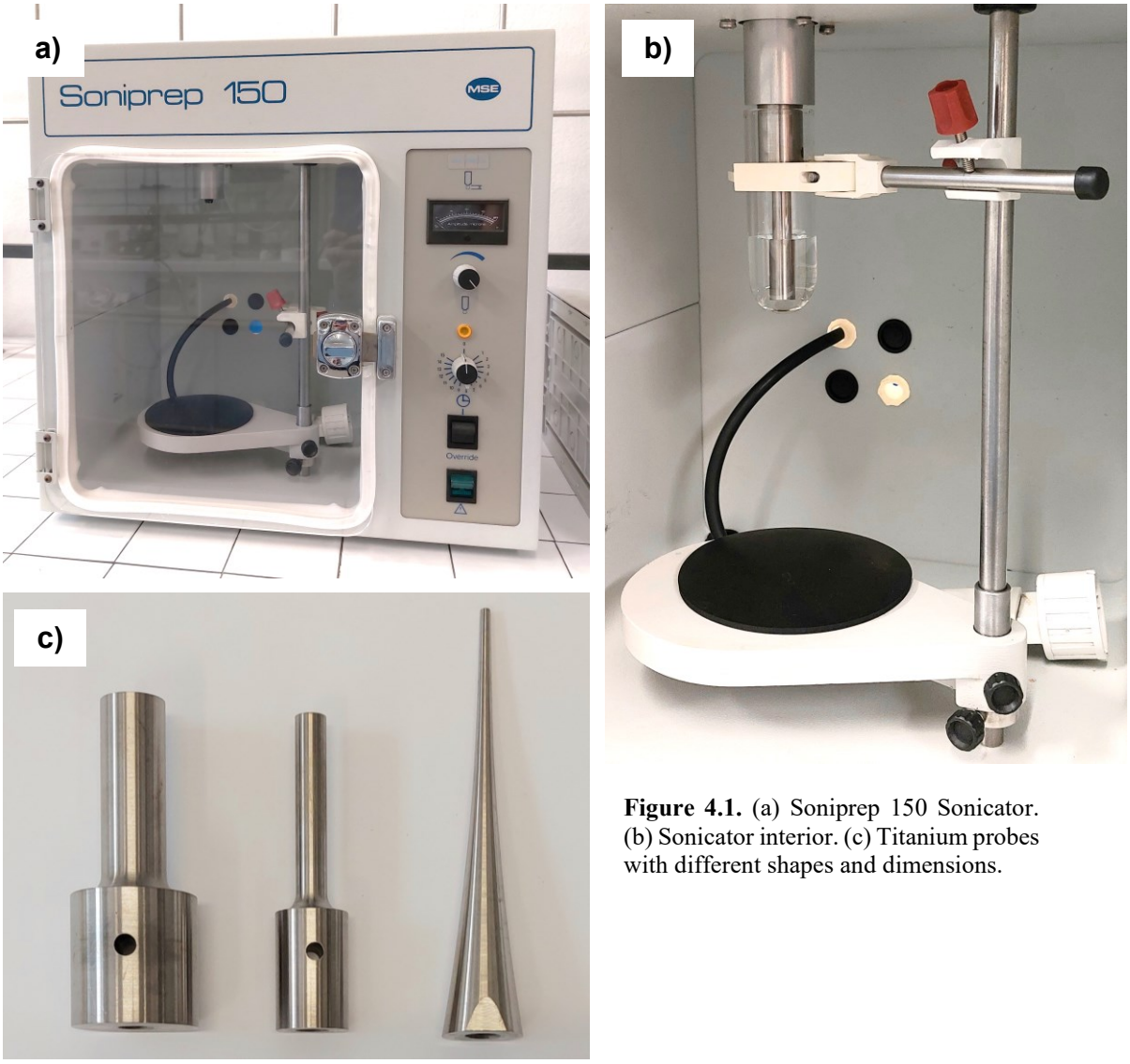

Figure 4.1. (a) Soniprep 150 Sonicator. (b) Sonicator interior. (c) Titanium probes with different shapes and dimensions.

The gel product was recovered by centrifugation (2500 rpm, 10 min), and washed twice with deionised water. The sample was finally air-dried at RT under ambient pressure.

To identify the optimal reaction conditions, synthesis was also carried out using an ethanolic solution (50% v/v) for the preparation of solutions 1 and 2. Higher concentrations of reactants have been also evaluated: H_3BTC (7.8 mg/mL), $Fe(NO_3)_3 \cdot 9H_2O$, (21.6 mg/mL), and $TMAOH \cdot 5H_2O$ (30.2 mg/mL).

A schematic representation of a sonochemical synthesis of Fe-BTC in aqueous solution is given in Figure 4.2.

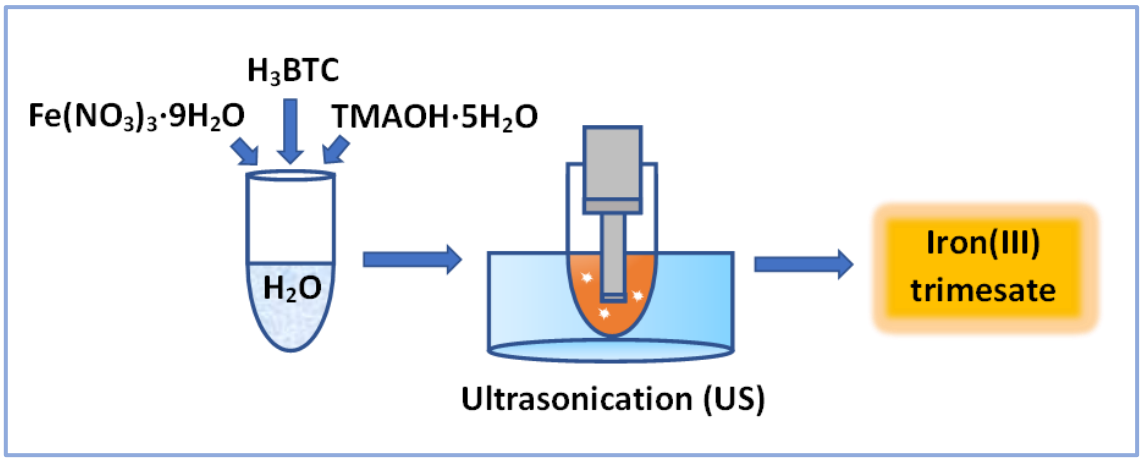

Figure 4.2. Schematic illustration of a sonochemical synthesis of Fe-BTC.

4.1.3. Characterisation

Fourier-transform infrared (FT-IR) spectra were recorded using a Bruker Tensor 27 spectrophotometer within the 400-4000 cm^{-1} scanning range. X-ray powder diffraction (XRPD) patterns were collected on a Bruker D8 Advance Diffractometer using Cu-Kα radiation (λ = 1.54056 Å, I = 30 mA, V = 40 kV) in a scanning range between 7° and 80° 2-theta (step size = 0.05° 2-theta). Due to the high iron fluorescence radiation emission stimulated by the Kα copper radiation, to obtain a satisfactory signal-to-noise ratio in the XRPD pattern an appropriate acquisition time was selected. Differential scanning calorimetry analysis (DSC) and thermogravimetric analysis (TGA) were carried out on a Perkin-Elmer STA 6000 simultaneous thermal analyser in a temperature range between 25 and 850 °C (heating rate = 10 °C/min) under O_2 flow (40 mL/min). N_2 physisorption was performed on a Sorptomatic 1990 CE apparatus (Fisons Instruments) at -196 °C. Prior to measurement, all the samples were outgassed at 150 °C under vacuum for 17 h. Pore size distribution was estimated by using Horvath-Kavazoe (HK) equation to the adsorption branches of the N_2 isotherms. Specific Surface Area (SSA) was determined from adsorption data by applying Dubinin-Radushkevich (DR) method.

4.1.4. Evaluation of the peroxidase-mimic activity of Fe-BTC

To evaluate the intrinsic peroxidase-like activity of Fe-BTC, four test samples were examined, containing: (1) Fe-BTC (250 μg/mL), TMB (0.4 mM) and H_2O_2 (0.5 mM) in acetate buffer (10

mM, pH = 4); (2) TMB (0.4 mM) and H_2O_2 (0.5 mM) in acetate buffer (10 mM, pH = 4); (3) Fe-BTC (250 µg/mL), and TMB (0.4 mM) in acetate buffer (10 mM, pH = 4); (4) TMB (0.4 mM) in acetate buffer (10 mM, pH = 4). The solution mixtures were incubated at 35 °C under magnetic stirring (150 rpm) for 1 hour. Then, the test samples were centrifugated at 5000 rpm for 10 minutes and supernatants were collected. Absorbance of supernatants was then recorded at 652 nm on a Cary 5000 UV-Vis-NIR spectrophotometer (Agilent Technologies).

4.2. Results and Discussion

4.2.1. Formation of a xerogel

Unlike mechanochemical synthesis (discussed in Chapter 2), sonochemical synthesis of Fe-BTC led to the formation of a gel material, rather than a powder. After air-drying, the gel underwent a progressive shrinking process, cracking into small fractions of a transparent solid xerogel (Figure 4.3). Gel formation is ascribable to the fast nucleation kinetics prompted by ultrasounds. US hinders a further grow of nanocrystals that could aggregate through non-covalent interactions forming a gel.[1] Gel state hold great promise for MOFs applications, since it provides lower mass transfer resistance and higher gas adsorption capability compared to powders.[2]

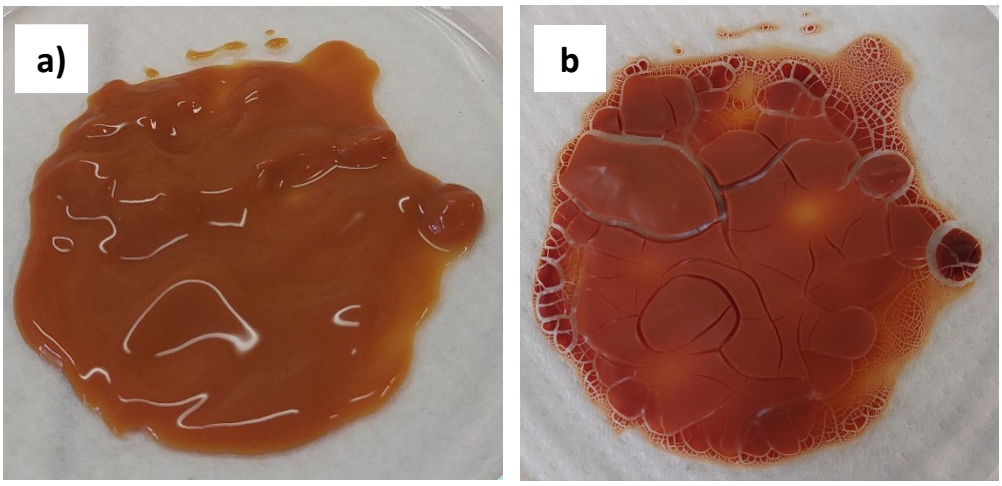

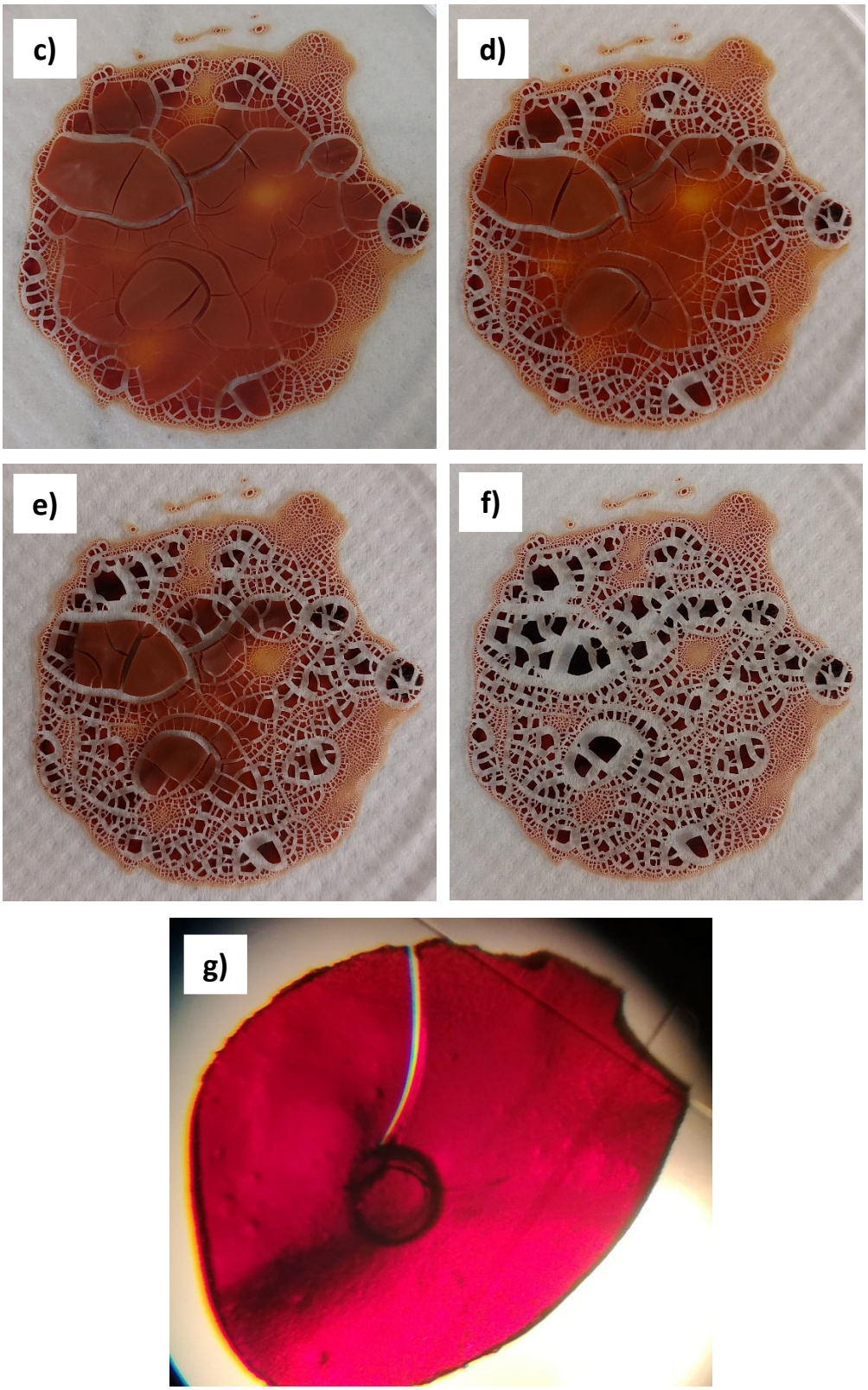

Figure 4.3. Direct photography throughout the air-drying process of a Fe-BTC material obtained via ultrasonication: freshly synthesised wet gel obtained after US irradiation (a), and after air-drying for 24 (b), 27 (c), 28 (d) and 30 hours (e); dried xerogel after 48 hour-drying (f). Light microscope image of a section of the xerogel (g).

4.2.2. Effect of pH

All samples were characterised by N_2 physisorption, TGA, DSC, XRPD, and FT-IR in order to investigate the effect of pH on textural properties, thermal stability, and microstructure of the material. To distinguish among the different working pH conditions, Fe-BTC samples were labelled as US_pH3, US_pH4 and US_pH5 (US stands for ultrasonicated).

X-ray Powder Diffraction

Figure 4.4 shows XRPD patterns of the samples US_pH3, US_pH4 and US_pH5 synthesised via sonochemical approach. All samples show a similar diffraction pattern in terms of position of diffraction peaks, consistently with the XRPD patterns obtained for the mechanochemically-prepared Fe-BTC (see Chapter 2), and results reported in the literature for Fe-BTC materials prepared via conventional methods.[3] An intense diffraction peak centred at 10.65° 2-theta with a visible shoulder at ca. 14.30° 2-theta was observed for all samples. The following peaks at ca. 18.76, 23.83, 28.09, 33.36, 42.49° 2-theta are less intense and broader than the first one. The presence of broad diffraction peaks is in agreement with the disordered structure of Fe-BTC material in comparison with crystalline MIL-100(Fe).[4] Despite the different working pH conditions, samples microstructure did not show relevant differences by XRPD.

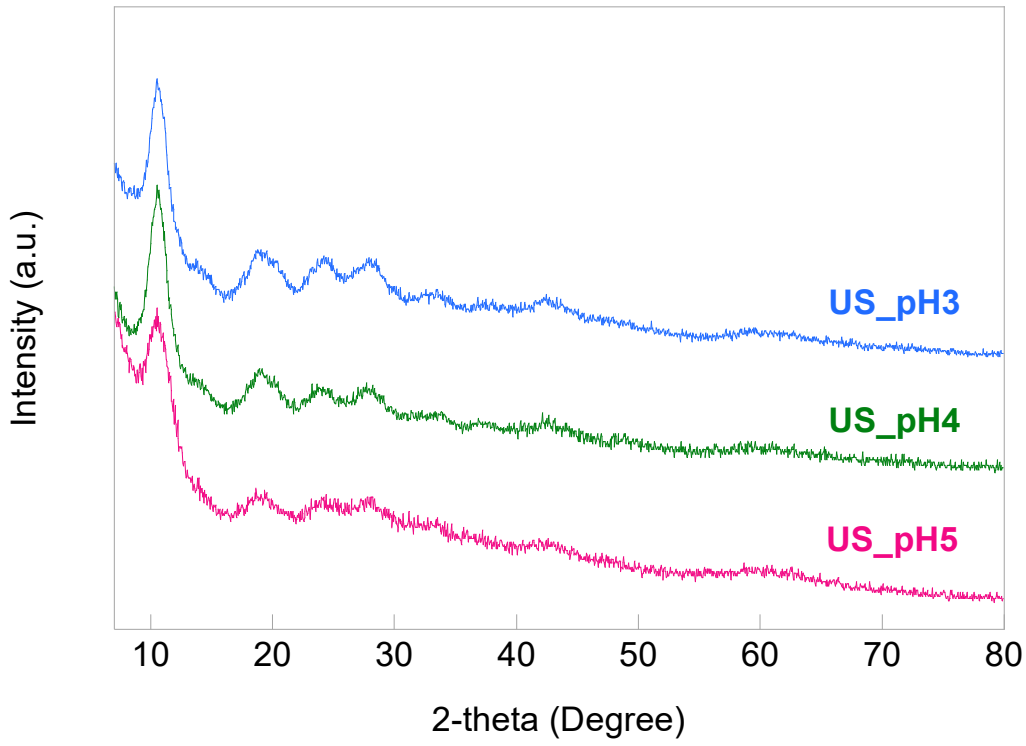

Figure. 4.4 XRPD patterns of US_pH3, US_pH4 and US_pH5 recorded from 7 to 80° 2-theta.

Fourier-Transform Infrared Spectroscopy

FT-IR spectra obtained for US_pH3, US_pH4 and US_pH5 in the 4000-400 cm^{-1} range are reported in Figure 4.5. The broad band in the 3600-3100 cm^{-1} region is attributed to the stretching vibrations of hydroxyl groups and water molecules coordinated to iron octahedra and adsorbed water molecules.[5] The weak band at 3080 cm^{-1} is ascribable to the aromatic C–H stretching vibrations. A weak carbonyl band at 1703 cm^{-1} is visible in all samples. The band at 1625 cm^{-1} is due to the C=O stretching of carboxylate groups, while the bands at ca. 1564 and 1371 cm^{-1} are ascribable to the asymmetric and symmetric stretching of the O–C–O group, respectively. The bands at 759 and 706 cm^{-1} are attributed to the C–H bending vibrations of aromatic rings, whereas the band at 463 cm^{-1} is ascribable to the stretching of Fe-O bonds.[6,7] It is noteworthy that the spectra of the samples synthesised via sonochemical approach at different pH are similar as well as to the FT-IR spectra obtained for the samples prepared via mechanochemical method (see Chapter 2), and results reported in the literature for Fe-BTC MOFs.[8] Therefore, even though the different working pH conditions, all samples showed no significative microstructural differences by FT-IR.

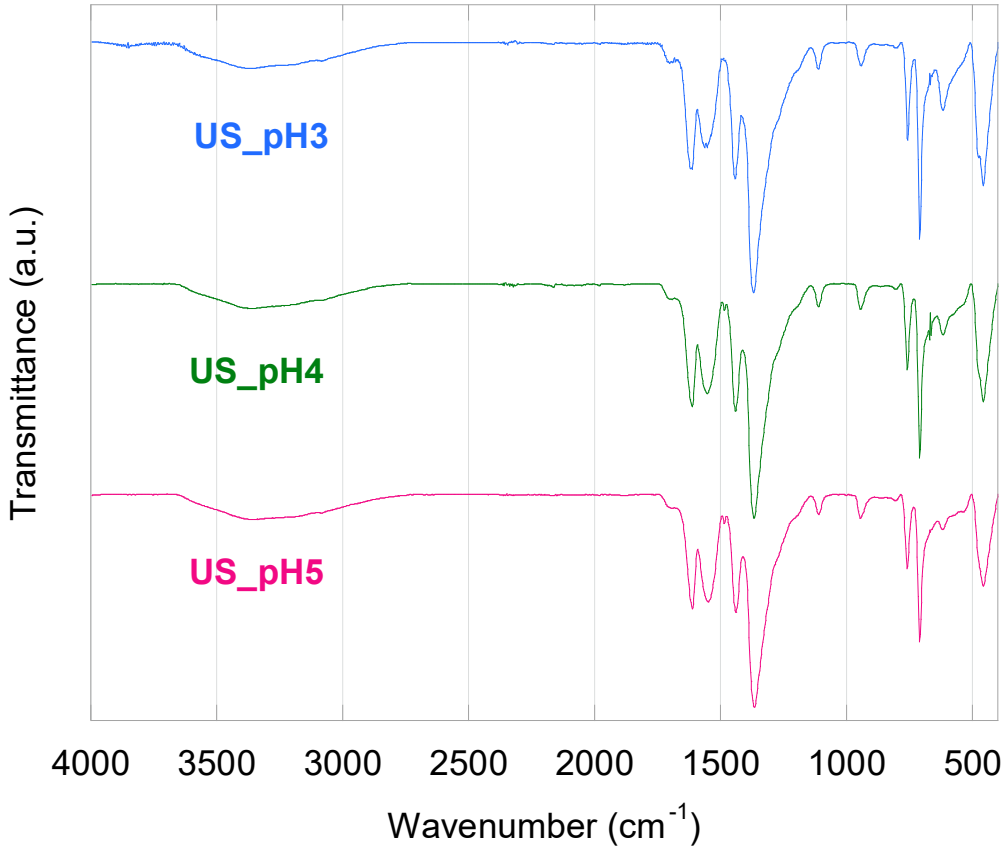

Figure 4.5. FT-IR spectra of US_pH3, US_pH4 and US_pH5 from 400 to 4000 cm^{-1}.

Thermal Analysis

Thermal behaviour of the ultrasonicated samples was investigated under oxygen flow. Thermogravimetric (TG) curves, the corresponding derivative curves (dTG) and the DSC curves obtained for US_pH3, US_pH4 and US_pH5 are shown in Figure 4.6. Similar to mechanochemically-prepared Fe-BTC (see Chapter 2), TG curves of samples (Figure 4.6a) showed three weight losses in the 25 – 850 °C range. The first weight loss occurred up to 150 °C and derived from the loss of adsorbed water molecules. The second weight loss took place between 150 and 260 °C and it was attributed to the departure of water molecules coordinated to the iron trimers. The third and last weight loss in the 260 – 450 °C range was attributed to the decomposition of the framework into hematite by combustion, as also confirmed by the presence of an intense exothermic peak at ca. 350 °C in the DSC curves of the samples (Figure 4.6c).

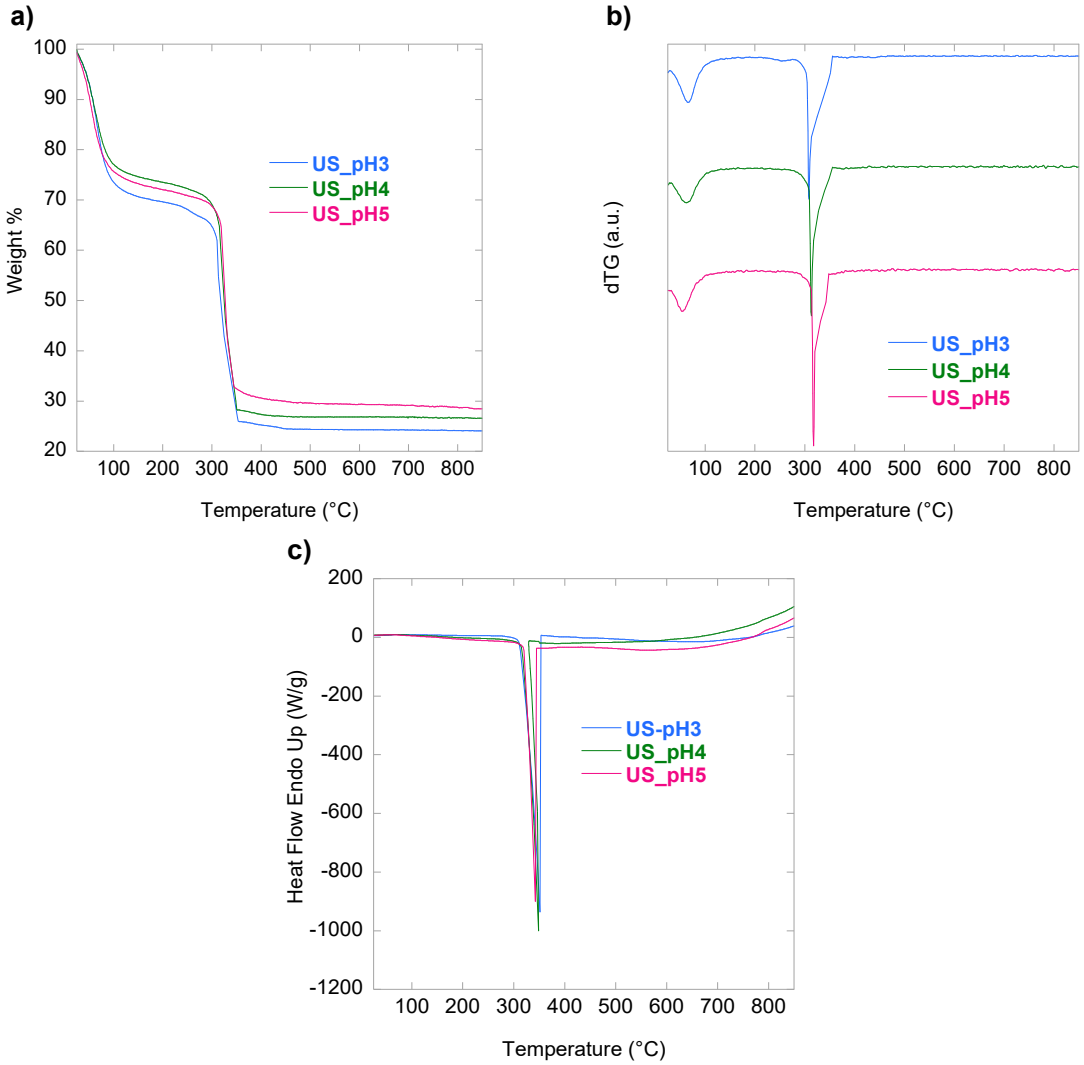

Figure 4.6. TG (a), dTG (b) and DSC (c) curves of US_pH3, US_pH4 and US_pH5 samples, obtained between 25 and 850 °C (10 °C/min) under O_2 flow (40 ml/min).

Nitrogen physisorption

N_2 adsorption/desorption isotherms and pore size distributions for US_pH3, US_pH4 and US_pH5 are shown in Figure 4.7. All samples present a I-type isotherm, which is typical of microporous material,[9] and a plateau at ca. $p/p^0 = 0.12$. The presence of a peak centred at around 6 Å in pore size distribution curves (Figure 4.7b) of both US_pH3 and US_pH4 testifies that the average dimension of a large fraction of pores is around 6 Å for these two samples. A small population of pores of higher dimensions (around 12 Å) is also observable, in accordance with the presence of two types of cages in MIL-100(Fe). 6Å-diameter pores are absent in US_pH5 which only shows a broad and less intense peak in the 10-15 Å region.

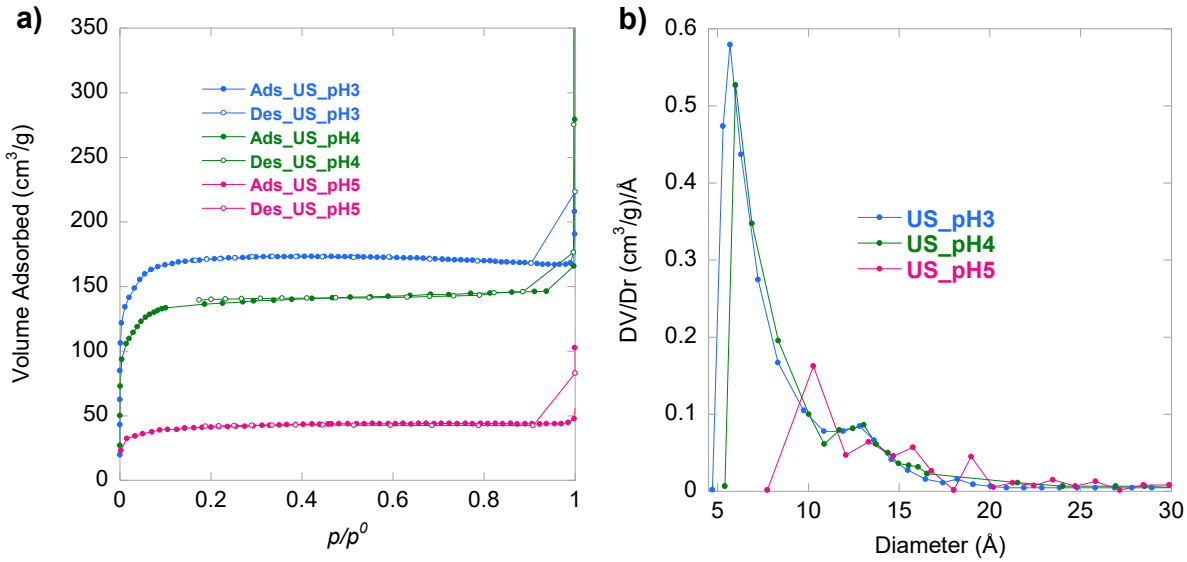

Figure 4.7. N_2 adsorption/desorption isotherms obtained at -196 °C (a) and pore size distributions (b) of US_pH3, US_pH4 and US_pH5.

The US_pH3 sample showed the best results in terms of micropore volume (0.263 cm^3/g) and SSA (742 m^2/g). As well as previously discussed for samples obtained via mechanochemical approach (see Chapter 2), a decrease of textural properties with increasing pH was observed (Table 4.1), consistently with the framework formation mechanism proposed by Seo et al.[10] (previously reported in section 1.2.6.3). Therefore, textural properties of this material are noticeably affected by pH, and they can be tuned by simply varying the amount of base used in the synthesis, whether via mechanochemical or sonochemical approach.

Sample	SSA (m^2/g)	Micropore volume (cm^3/g)	Mesopore volume (cm^3/g)	Macropore volume (cm^3/g)
US_pH3	742	0.263	0.005	0.000
US_pH4	589	0.210	0.017	0.001
US_pH5	181	0.063	0.006	0.000

Table 4.1. Specific Surface Area (SSA) and macro-, meso- and micropore volume of US_pH3, US_pH4 and US_pH5. %RSD SSA = 2; %RSD pore volume = 1.

Even though the best results in terms of micropore volume and SSA have been attained at pH 3, further investigation has been conducted on synthesis at pH 4 in sight of *in situ* immobilisation of GOx. Indeed, GOx shows a broad activity range (pH 4-7)[11] and iron(III) trimesate materials have proven to possess intrinsic peroxidase-like activity in a pH range between 2.5 and 5.[12] Therefore, pH 4 synthesis conditions are likely to represent the optimal balance between retention of GOx and Fe-BTC enzymatic and enzymatic-mimic activity, respectively, and satisfactory textural properties, physicochemical integrity of Fe-BTC.

4.2.3. Effect of concentration

Different concentrations of reactants were examined to establish the best synthesis conditions, and the influence on the properties of the material was investigated. Synthesis were performed at pH 4 and corresponding samples were labelled as US_low.conc and US_high.conc to distinguish among the different synthesis conditions (listed in Table 4.2.)

Sample	H_3BTC (mg/mL)	$Fe(NO_3)_3 \cdot 9H_2O$ (mg/mL)	$TMAOH \cdot 5H_2O$ (mg/mL)
US_low.conc	3.9	10.8	15.1
US_high.conc	7.8	21.6	30.2

Table 4.2. Reactant concentrations examined for the sonochemical synthesis of Fe-BTC.

As reported in Figure 4.8, samples show a similar XRPD pattern in terms of relative intensity and position of diffraction peaks. Therefore, reactant concentrations did not affect the sample's microstructure.

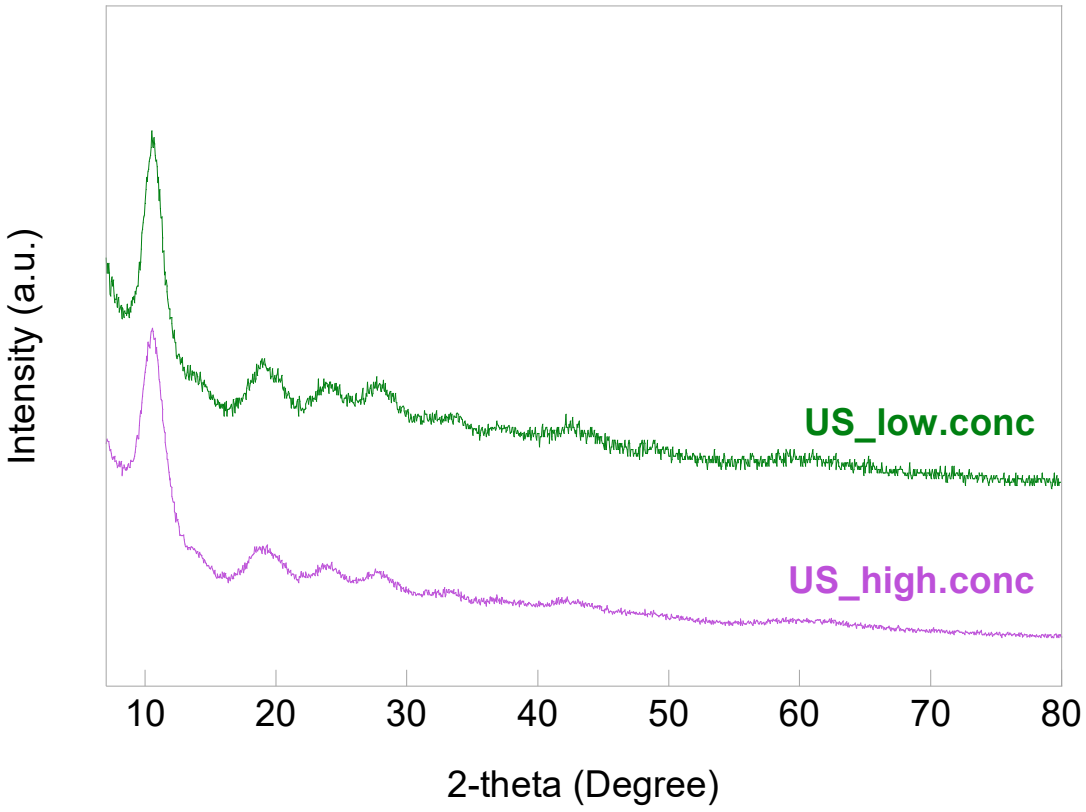

Figure. 4.8. XRPD patterns of US_low.conc and US_high.conc recorded from 7 to 80° 2-theta.

Regarding textural properties, US_high.conc showed lower SSA and micropore volume compared to the sample obtained using lower concentrations of reactants (Table 4.3).

Sample	SSA (m^2/g)	Micropore volume (cm^3/g)	Mesopore volume (cm^3/g)	Macropore volume (cm^3/g)
US_low.conc	589	0.210	0.017	0.001
US_high.conc	126	0.041	0.008	0.002

Table 4.3. Specific Surface Area (SSA) and macro-, meso- and micropore volume of US_low.conc, and US_high.conc. %RSD SSA = 2; %RSD pore volume = 1.

Furthermore, pore size distribution curves obtained for both samples differ in terms of intensity and peak positions (Figure 4.9 b). US_low.conc exhibits an intense peak at around 6 Å, and a less intense peak between 10.5 and 15 Å. Conversely, the first peak in the pore size distribution curves of US_high.conc is less intense and centred at higher diameter values (ca. 8.8 Å) compared to the samples obtained using lower concentrations of reactants.

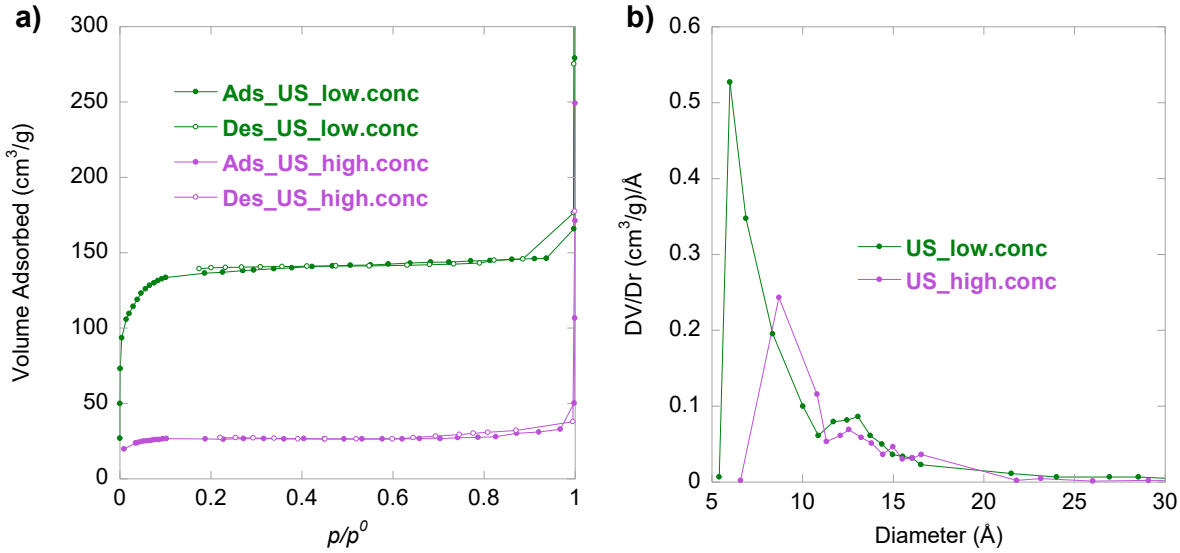

Figure 4.9. N_2 adsorption/desorption isotherms obtained at -196 °C (a) and pore size distributions (b) of US_low.conc, and US_high.conc.

Therefore, concentrations of reactants employed for the synthesis of US_high.conc led to lower textural properties. Indeed, after mixing the solutions of reactants the precipitation of a dense brownish orange solid was observed only for US_high.conc. This could hinder proper formation, growth, and collapse of bubbles in the liquid and, thus, the formation of a considerable permanent porosity of the sample.

4.2.4. Effect of solvents

Effect of the solvent used for sonochemical synthesis of Fe-BTC MOF on the properties of the material was also evaluated. In particular, synthesis was performed using deionised water or ethanol 50% v/v as solvents, and corresponding samples were labelled US_H_2O and US_$EtOH_{50\%v/v}$, respectively.

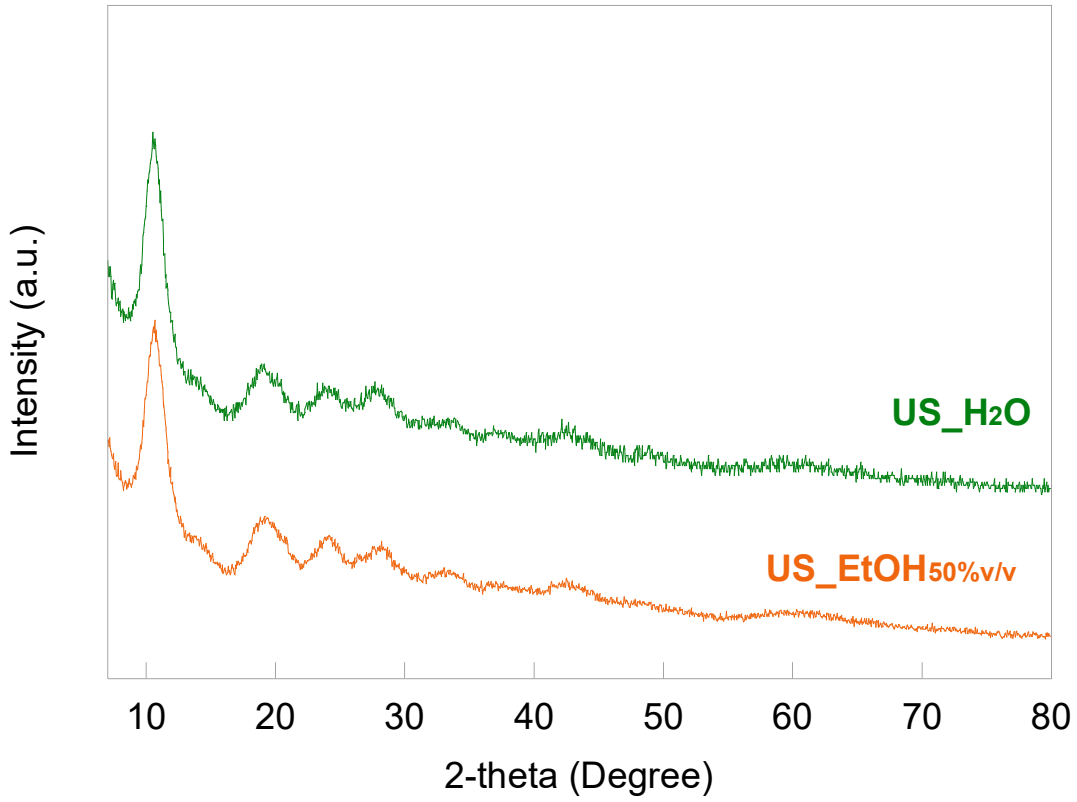

Figure. 4.10. XRPD patterns of US_H_2O and US_$EtOH_{50\%v/v}$ recorded from 7 to 80° 2-theta.

Figure 4.10 reports diffraction patterns obtained for US_H_2O and US_$EtOH_{50\%v/v}$, revealing no significant differences among samples in terms of relative intensity and position of diffraction peaks. Therefore, samples showed similar microstructure regardless of the use of water or ethanol 50% v/v as solvents.

However, SSA and micropore volume remarkably decreased when using ethanol 50% v/v rather than H_2O, as reported in Table 4.4.

Sample	SSA (m^2/g)	Micropore volume (cm^3/g)	Mesopore volume (cm^3/g)	Macropore volume (cm^3/g)
US_H_2O	589	0.210	0.017	0.001
US_$EtOH_{50\%v/v}$	173	0.052	0.004	0.002

Table 4.4. Specific Surface Area (SSA) and macro-, meso- and micropore volume of US_H_2O and US_$EtOH_{50\%v/v}$. %RSD SSA = 2; %RSD pore volume = 1.

Moreover, a shift of the first peak in the pore size distribution curves from 6 to 7.6 Å was observed (Figure 4.11 b).

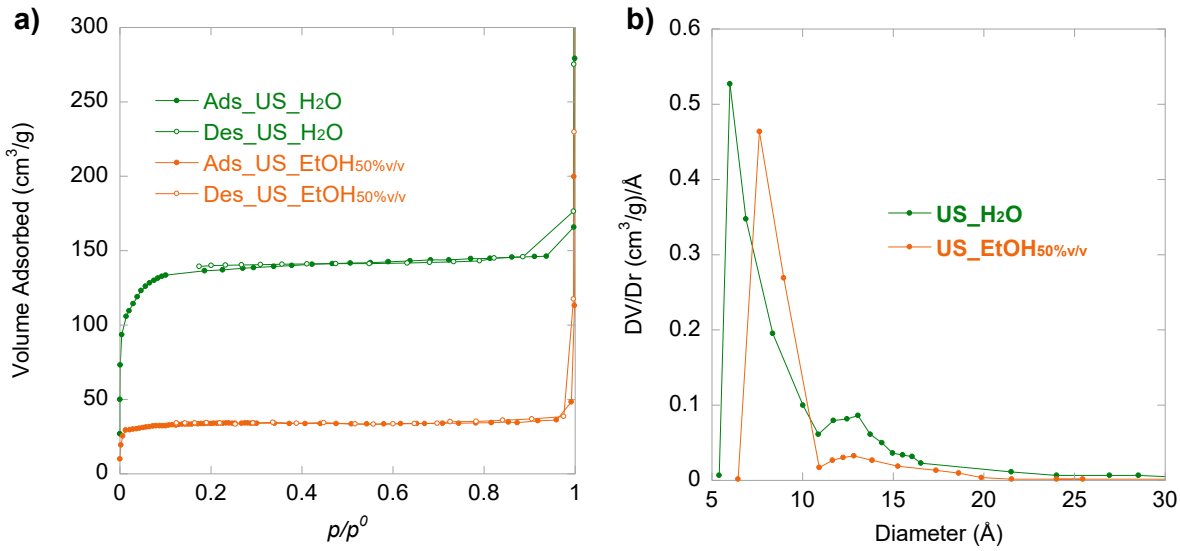

Figure 4.11. N_2 adsorption/desorption isotherms obtained at -196 °C (a) and pore size distributions (b) of US_H_2O and US_$EtOH_{50\%v/v}$.

The decrease of textural properties when using ethanol 50% v/v as solvent for the sonochemical synthesis of Fe-BTC can be explained considering the increasing solubility of trimesic acid in ethanol−water binary solvents.[13] The higher solubility of trimesic acid in ethanol 50% v/v gave rise to accelerated deprotonation rate of H_3BTC. Consequently, higher condensation rate was reached during the synthesis of US_$EtOH_{50\%v/v}$ compared to US_H_2O, hindering the obtainment of a significant permanent porosity of the sample, according to the framework formation mechanism (see section 1.2.6.3).[10,14]

4.2.5. Intrinsic peroxidase-mimic activity

The intrinsic peroxidase-mimic activity of the Fe-BTC material synthesised by ultrasonication was evaluated by investigating the catalytic oxidation capacity of the material over a chromogenic peroxidase substrate (TMB) in the presence of H_2O_2. In the absence of both Fe-BTC and H_2O_2, the characteristic absorbance peak of oxidised TMB at 652 nm was not detected. Conversely, a weak absorbance peak at 652 nm was visible for the reaction system consisting of TMB in the presence of Fe-BTC but in the absence of H_2O_2. This result confirmed a weak capability of the MOF to oxidise TMB in the absence of H_2O_2. A slightly higher absorbance at 652 nm was observed for TMB in the only presence of H_2O_2. A considerable increase in the absorbance at 652 nm was observed for the reaction system containing TMB in the presence of both Fe-BTC and H_2O_2. This attested the significant intrinsic peroxidase-like activity of Fe-BTC, being able to catalyse the oxidation of peroxidase substrate in the presence of hydrogen peroxide.

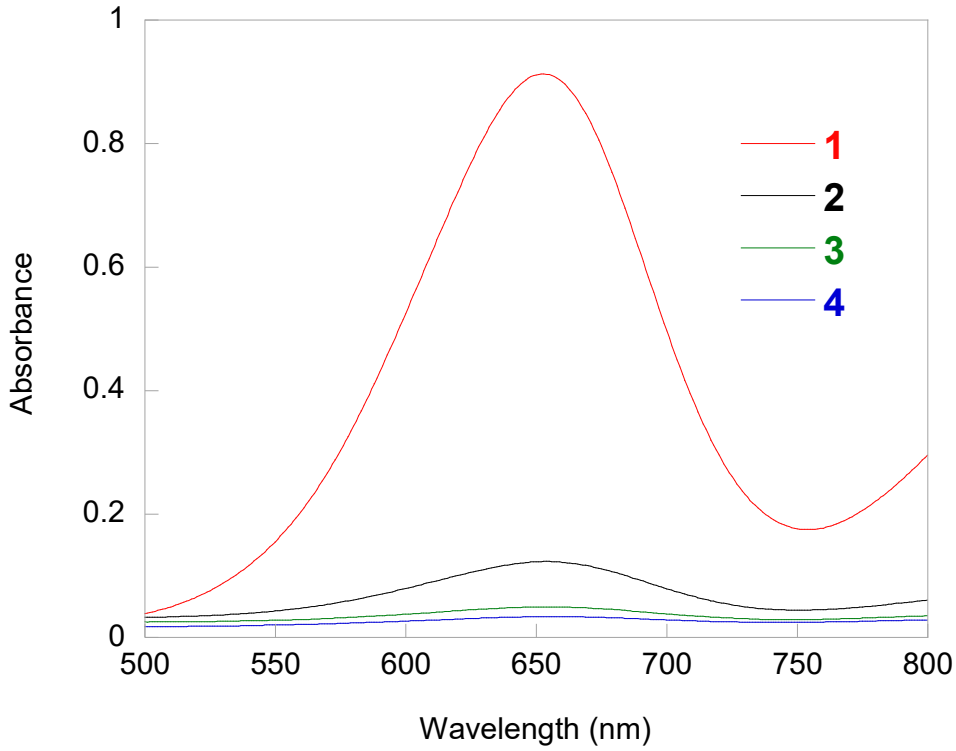

Figure 4.12. Absorption spectra of different reaction systems: TMB+H_2O_2+Fe-BTC (1, red), TMB+H_2O_2 (2, black), TMB+Fe-BTC (3, green), TMB (4, blue) in acetate buffer (10 mM, pH 4), at 35 °C after 1 hour incubation. The concentrations were 250 µg/mL for Fe-BTC, 0.4 mM for TMB and 0.5 mM for H_2O_2.

4.3. References

[1] Ennas, G.; Gedanken, A.; Mannias, G.; Kumar, V. B.; Scano, A.; Porat, Z.; Pilloni, M. Formation of Iron (III) Trimesate Xerogel by Ultrasonic Irradiation. *Eur. J. Inorg. Chem.* **2022**, No. Iii. https://doi.org/10.1002/ejic.202101082.

[2] Hou, J.; Sapnik, A. F.; Bennett, T. D. Metal-Organic Framework Gels and Monoliths. *Chem. Sci.* **2020**, *11* (2), 310–323. https://doi.org/10.1039/c9sc04961d.

[3] Sanchez-Sanchez, M.; De Asua, I.; Ruano, D.; Diaz, K. Direct Synthesis, Structural Features, and Enhanced Catalytic Activity of the Basolite F300-like Semiamorphous Fe-BTC Framework. *Cryst. Growth Des.* **2015**, *15* (9), 4498–4506. https://doi.org/10.1021/acs.cgd.5b00755.

[4] Sapnik, A. F.; Bechis, I.; Collins, S. M.; Johnstone, D. N.; Divitini, G.; Smith, A. J.; Chater, P. A.; Addicoat, M. A.; Johnson, T.; Keen, D. A.; Jelfs, K. E.; Bennett, T. D. Mixed Hierarchical Local Structure in a Disordered Metal–Organic Framework. *Nat. Commun.* **2021**, *12*, 2062. https://doi.org/10.1038/s41467-021-22218-9.

[5] Leclerc, H.; Vimont, A.; Lavalley, J. C.; Daturi, M.; Wiersum, A. D.; Llwellyn, P. L.; Horcajada, P.; Férey, G.; Serre, C. Infrared Study of the Influence of Reducible Iron(Iii) Metal Sites on the Adsorption of CO, CO2, Propane, Propene and Propyne in the Mesoporous Metal-Organic Framework MIL-100. *Phys. Chem. Chem. Phys.* **2011**, *13* (24), 11748–11756. https://doi.org/10.1039/c1cp20502a.

[6] Lestari, W. W.; Hartono, J.; Adreane, M.; Nugrahaningtyas, K. D.; Purnawan, C.; Rahardjo, S. B. Electro-Synthetic Optimization of Host Material Based on MIL-100(Fe). *Molekul* **2016**, *11* (1), 61. https://doi.org/10.20884/1.jm.2016.11.1.195.

[7] Moradi, S. E.; Dadfarnia, S.; Haji Shabani, A. M.; Emami, S. Removal of Congo Red from Aqueous Solution by Its Sorption onto the Metal Organic Framework MIL-100(Fe): Equilibrium, Kinetic and Thermodynamic Studies. *Desalin. Water Treat.* **2015**, *56* (3), 709–721. https://doi.org/10.1080/19443994.2014.947328.

[8] Pangkumhang, B.; Jutaporn, P.; Sorachoti, K.; Khamdahsag, P.; Tanboonchuy, V. Applicability of Iron (III) Trimesic (Fe-BTC) to Enhance Lignin Separation from Pulp and Paper Wastewater. *Sains Malays.* **2019**, *48* (1), 199–208. https://doi.org/10.17576/jsm-2019-4801-23.

[9] F. Rouquerol; J. Rouquerol; K. Sing. *Adsorption by Powders and Porous Solids*; Elsevier, 1999.

[10] Seo, Y. K.; Yoon, J. W.; Lee, J. S.; Lee, U. H.; Hwang, Y. K.; Jun, C. H.; Horcajada, P.; Serre, C.; Chang, J. S. Large Scale Fluorine-Free Synthesis of Hierarchically Porous Iron(III) Trimesate MIL-100(Fe) with a Zeolite MTN Topology. *Micropor. Mesopor. Mater.* **2012**, *157*, 137–145. https://doi.org/10.1016/j.micromeso.2012.02.027.

[11] Pazur, J. H.; Kleppe, K. The Oxidation of Glucose and Related Compounds by Glucose Oxidase from Aspergillus Niger. *Biochemistry* **1964**, *3* (4), 578–583. https://doi.org/10.1021/bi00892a018.

[12] Zhang, J. W.; Zhang, H. T.; Du, Z. Y.; Wang, X.; Yu, S. H.; Jiang, H. L. Water-Stable Metal–Organic Frameworks with Intrinsic Peroxidase-like Catalytic Activity as a Colorimetric Biosensing Platform. *Chem. Commun.* **2014**, *50* (9), 1092–1094. https://doi.org/10.1039/c3cc48398c.

[13] Zhang, D.; Xu, Q. Solubility of 1,3,5-Benzenetricarboxylic Acid in Different Solvents. *J. Chem. Eng. Data* **2016**, *61* (2), 1003–1006. https://doi.org/10.1021/acs.jced.5b00870.

[14] Du, M.; Xu, G.; Zhang, J.; Li, T.; Guan, Y.; Guo, C. Effect of H2O/DMF Mixed Solvents on Formation of MIL-100(Fe) and Dye Adsorption. *J. Solid State Chem.* **2022**, *312* (May), 123248. https://doi.org/10.1016/j.jssc.2022.123248.

Chapter 5:

Sonochemical synthesis, characterisation, and catalytic activity of GOx@Fe-BTC hybrid composite

5. Sonochemical synthesis, characterisation, and catalytic activity of GOx@Fe-BTC hybrid composite

5.1. Experimental section

5.1.1. Reagents and materials

Iron(III) nitrate nonahydrate ($Fe(NO_3)_3 \cdot 9H_2O$, 98%), tetramethyl ammonium hydroxide pentahydrate ($TMAOH \cdot 5H_2O$, 97%), 1,3,5-benzenetricarboxylic acid (H_3BTC, 95%), 3,3′,5,5′-tetramethylbenzidine (TMB, ≥99%), hydrogen peroxide solution (H_2O_2, 30% (w/w) in H_2O), Ethanol (EtOH, ≥99.8%), glacial acetic acid (AcOH, ≥ 99%), and sodium acetate trihydrate ($NaAc \cdot 3H_2O$) were purchased by Sigma-Aldrich and used as received without further purification.

5.1.2. Synthesis

In a typical synthesis two solutions are prepared. Solution 1 was prepared by dissolving 0.3225 g of $Fe(NO_3)_3 \cdot 9H_2O$ in 15 mL of deionised water. Solution 2 was obtained by dissolving 0.1178 g of H_3BTC and 0.4531 g of $TMAOH \cdot 5H_2O$ in 15 mL of deionised water. Solutions 1 and 2 were mixed, instantaneously yielding an orange-coloured sol. Then, an appropriate amount of glucose oxidase (2.5, 6.3 and 12.5 mg) was added. pH of the resulting reaction mixture was ca. 4.0, and reactants concentrations were: H_3BTC (3.9 mg/mL), $Fe(NO_3)_3 \cdot 9H_2O$, (10.8 mg/mL), $TMAOH \cdot 5H_2O$ (15.1 mg/mL), and GOx (0.08, 0.2 or 0.4 mg/mL). This reaction mixture was kept in a cooling bath and immediately processed by 20 cycles of 10 s ultrasound irradiation and 60 s rest at room temperature (ultrasound frequency: 23 kHz; amplitude: 15 μm). Synthesis was carried out on a Soniprep 150 sonicator using a titanium probe (tip diameter: 9.5 mm). The gel product was recovered by centrifugation (2500 rpm, 10 min), and washed twice with deionised water. Sample was finally collected and stored at 4°C. A schematic representation of a sonochemical synthesis of GOx@Fe-BTC in aqueous solution is given in Figure 5.1.

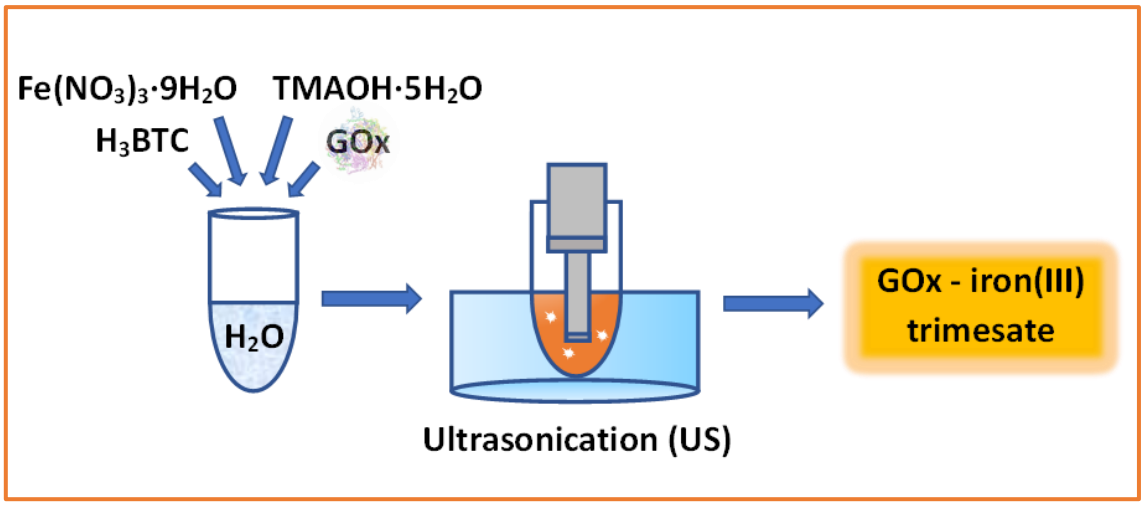

Figure 5.1. Schematic representation of a sonochemical synthesis of GOx-iron(III)trimesate hybrid composite.

5.1.3. Characterisation

Fourier-transform infrared (FT-IR) spectra were recorded using a Bruker Tensor 27 spectrophotometer within the 400-4000 cm^{-1} scanning range. X-ray powder diffraction (XRPD) patterns were collected on a Bruker D8 Advance Diffractometer using Cu-Kα radiation (λ = 1.54056 Å, I = 30 mA, V = 40 kV) in a scanning range between 7° and 80° 2-theta (step size = 0.05° 2-theta). Due to the high iron fluorescence radiation emission stimulated by the Kα copper radiation, to obtain a satisfactory signal-to-noise ratio in the XRPD pattern an appropriate acquisition time was selected. Thermogravimetric analysis (TGA) was carried out on a Perkin-Elmer STA 6000 simultaneous thermal analyser in a temperature range between 25 and 850 °C (heating rate = 10 °C/min) under O_2 flow (40 mL/min). N_2 physisorption was performed on a Sorptomatic 1990 CE apparatus (Fisons Instruments) at -196 °C. Prior to measurement, all the samples were outgassed at room temperature under vacuum for 24 hours. Pore size distribution was estimated by using Horvath-Kavazoe (HK) equation to the adsorption branches of the N_2 isotherms. Specific Surface Area (SSA) was determined from adsorption data by applying Dubinin-Radushkevich (DR) method.

5.1.4. Catalytic activity of GOx@Fe-BTC

Biocatalytic activity of GOx@Fe-BTC hybrid biocomposite was evaluated. Experiments were performed by adding GOx@Fe-BTC (500 μg/mL), TMB (0.4 mM) and glucose (0.5 mM) in acetate buffer (pH 4, 10 mM). The solution mixtures were incubated at 35°C under magnetic stirring (150 rpm) for 1 hour. Then, the test samples were centrifugated at 5000 rpm for 10 minutes and supernatants were collected. Absorbance of the supernatants was then recorded at 652 nm on a Cary 5000 UV-Vis-NIR spectrophotometer (Agilent Technologies). All measurements were performed in triplicate and the average value reported. The relative activity was calculated using the following formula:[1]

$$Relative\ activity\ (\%) = \frac{A}{A_{max}} \times 100\%$$

Where A_{max} is the maximum absorbance recorded, and A is the absorbance measured at same conditions.

5.1.5. Leaching test

Enzyme leaching-out from the support was investigated. In order to ascertain the degree of leaching after the immobilisation process, catalytic activity of wastewater collected after the synthesis of GOx@Fe-BTC was measured. Wastewater was incubated at 35°C under magnetic stirring (150 rpm) for 1 hour with TMB (0.4 mM), HRP (0.1 μg/mL), and glucose (0.5 mM) in acetate buffer (pH 4, 10 mM). Then, the test sample was centrifugated at 5000 rpm for 10 minutes and supernatants were collected. Absorbance of the supernatant was then recorded at 652 nm on a Cary 5000 UV-Vis-NIR spectrophotometer (Agilent Technologies). GOx leakage from the support was also evaluated by incubating GOx@Fe-BTC in acetate buffer (pH 4.0, 10 mM) for 24 hours. After centrifugation (5000 rpm for 10 minutes), enzymatic activity of supernatant was tested as described above. All measurements were performed in triplicate and the average value reported.

5.1.6. pH dependence on GOx@Fe-BTC catalytic activity

pH profile of Fe-BTC peroxidase-mimic activity was examined over the pH range 3 – 5 (acetate buffer, 10 mM). Experiments were performed by adding Fe-BTC (500 μg/mL) or GOx and HRP (0.2 and 0.1 μg/mL, respectively), TMB (0.4 mM) and glucose (0.5 mM) in the appropriate buffer. The solution mixtures were incubated at 35°C under magnetic stirring (150 rpm) for 1 hour. Then, the test samples were centrifugated at 5000 rpm for 10 minutes and supernatants were collected. Absorbance of the supernatants was then recorded at 652 nm on a Cary 5000 UV-Vis-NIR spectrophotometer (Agilent Technologies). All measurements were performed in triplicate and the average value reported.

5.1.7. Catalytic stability

Stability tests were performed by testing the catalytic activity of GOx@Fe-BTC hybrid biocomposite after storage at 4°C for 1, 2, 3, 4 and 5 weeks. Experiments were carried out by adding GOx@Fe-BTC (500 μg/mL), TMB (0.4 mM) and glucose (0.5 mM) in acetate buffer (10 mM, pH = 4). The solution mixtures were incubated at 35°C under magnetic stirring (150 rpm) for 1 hour. Then, the test samples were centrifugated at 5000 rpm for 10 minutes and supernatants were collected. Absorbance of the supernatants was then recorded at 652 nm Absorbance of the supernatants was then recorded at 652 nm on a Cary 5000 UV-Vis-NIR spectrophotometer (Agilent Technologies). All measurements were performed in triplicate and the average value reported.

5.1.8. Colorimetric biosensing of glucose

A dose-response curve for glucose detection (A_{652nm} vs glucose conc.) using GOx@Fe-BTC under the optimum conditions was obtained. Experiments were carried out by adding GOx@Fe-BTC (500 μg/mL), TMB (0.4 mM) and different concentrations of glucose (0 – 4000 μM) in acetate buffer (10 mM, pH = 4). The solution mixtures were incubated at 35°C under magnetic stirring (150 rpm) for 1 hour. Then, the test samples were centrifugated at 5000 rpm for 10 minutes and supernatants were collected. Absorbance of supernatants was recorded at 652 nm on a Cary 5000 UV-Vis-NIR spectrophotometer (Agilent Technologies).

5.1.9. Steady-state kinetic assay

Kinetic parameters of GOx@Fe-BTC and free glucose oxidase were evaluated by varying the concentration of glucose. Experiments were carried out at room temperature in acetate buffer (10 mM; pH = 4) using GOx@Fe-BTC (1000 μg/mL) or GOx and HRP (0.5 and 0.25 μg/mL, respectively), TMB (0.4 mM for GOx@Fe-BTC or 0.2 mM for GOx) and varying concentrations of glucose (0.25 – 30 mM). The change in absorbance at 652 nm was monitored on a Cary 5000 UV-Vis-NIR spectrophotometer (Agilent Technologies) for 180 sec. According to Michaelis−Menten equation:[2]

$$V_0 = \frac{V_{max} \cdot [S]}{K_m + [S]}$$

Where [S] is the substrate (glucose) concentration and V_0 is the initial velocity. Moreover,

$$V_0 = \frac{\Delta A}{\Delta t \cdot \epsilon}$$

Where ΔA is the change in absorbance, Δt is the time variation and ε is the molar extinction coefficient (oxTMB molar extinction coefficient, $\varepsilon_{652nm} = 3.9 \times 10^4\ M^{-1}\ cm^{-1}$).[3]
The Michaelis–Menten constant (K_m) and the maximum reaction rate (V_{max}) can be calculated by using the double reciprocal of Michaelis−Menten equation:

$$\frac{1}{V_0} = \frac{K_m}{V_{max}} \frac{1}{[S]} + \frac{1}{V_{max}}$$

The plot $1/V_0$ vs. $1/[S]$ (known as Lineweaver–Burk or double reciprocal plot) is linear. V_{max} is obtained from the intercept and K_m is calculated from the slope.[2]

5.2. Results and Discussion

GOx@Fe-BTC hybrid composite materials have been synthesised via sonochemical approach adding different enzyme amounts, as resumed in Table 5.1.

Sample	pH	US irradiation time (sec)	GOx added (mg)
Fe-BTC_US	4	200	0
GOx@Fe-BTC_US_2.5mg	4	200	2.5
GOx@Fe-BTC_US_6.3mg	4	200	6.3
GOx@Fe-BTC_US_12.5mg	4	200	12.5

Table 5.1. Samples prepared via sonochemical approach and corresponding synthesis conditions.

5.2.1. Physicochemical characterisation

All Fe-BTC and GOx@Fe-BTC samples were characterised by X-ray powder diffraction. Fourier-Transform infrared spectroscopy, thermal analysis, and nitrogen physisorption.

X-ray Powder Diffraction

Microstructure of samples has been investigated by XRPD and FT-IR. XRPD patterns obtained for Fe-BTC and GOx@Fe-BTC samples are shown in Figure 5.2. Despite the different amount of enzyme, diffraction patterns of GOx@Fe-BTC_US_2.5mg, GOx@Fe-BTC_US_6.3mg, and GOx@Fe-BTC_US_12.5mg samples do not differ significantly from the one obtained for Fe-BTC_US. All patterns are similar in terms of position of diffraction peaks (ca. 10.65, 18.76, 23.83, 28.09, 33.36, and 42.49° 2-theta), proving the obtainment of a Fe-BTC material. Therefore, similar to the mechanochemically-prepared samples (see Chapter 3), immobilisation of GOx during sonochemical synthesis did not affect MOF's microstructure.

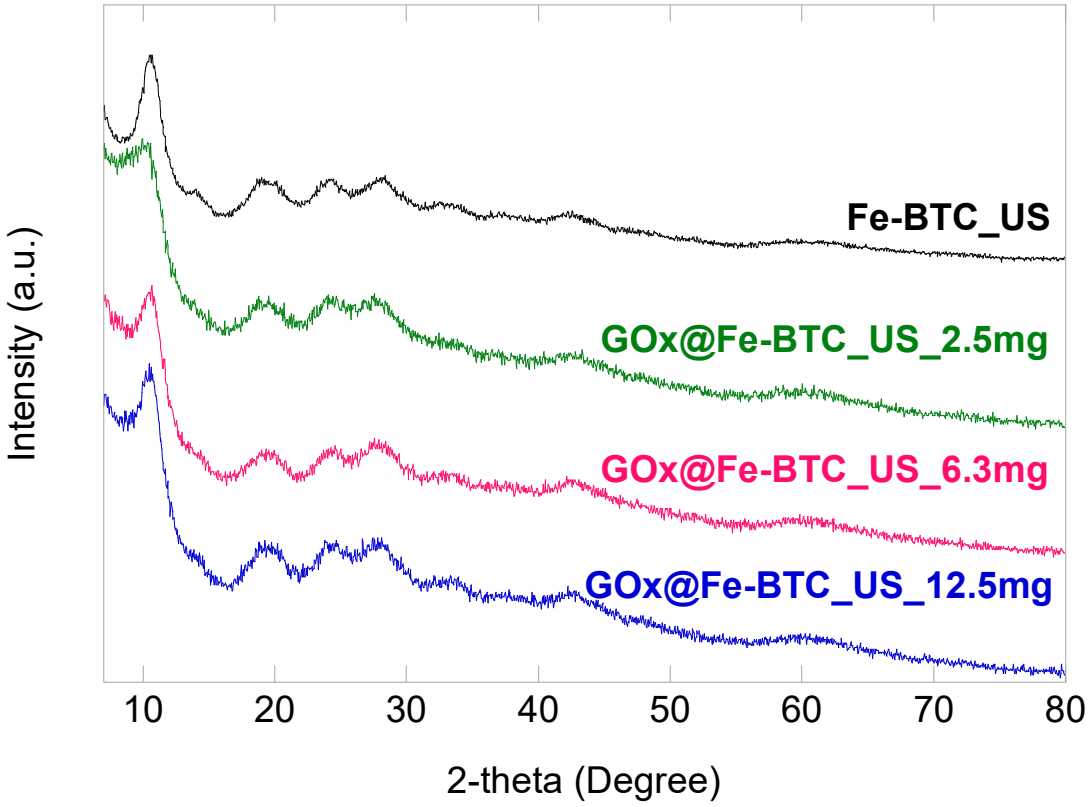

Figure 5.2. XRPD patterns of Fe-BTC and GOx@Fe-BTC samples from 7 to 80° 2-theta.

Fourier-Transform Infrared Spectroscopy

Microstructure of sonochemical-prepared Fe-BTC and GOx@Fe-BTC samples was also investigated by FT-IR. FT-IR spectra of all samples (Figure 5.3) are similar as well as to the FT-IR spectra obtained for mechanochemical-prepared samples (see Chapter 3), and results reported in the literature for Fe-BTC material.[4] The broad band in 3600-3100 cm^{-1} region can be attributed to the stretching vibrations of hydroxyl groups and water molecules coordinated to iron octahedra and adsorbed water molecules.[5] The relative intensity of this band is higher for Fe-BTC_US compared to GOx@Fe-BTC samples. The presence of a lower extent of adsorbed water on GOx@Fe-BTC samples could be attributed to the presence of GOx into Fe-BTC, since the pores of the MOF resulted filled by the enzymes. The band at 1625 cm^{-1} is assigned to the C=O stretching of carboxylate groups and the band at 1564 cm^{-1}, arising from the asymmetric stretching of O–C–O groups, likely mask the bands characteristic of enzyme molecules (i.e., C=O stretching vibrations of peptide bonds, and a combination of C–N stretching and N–H in-plane bending vibrations of the peptide groups, respectively).[6] The band at 1371 cm^{-1} is attributed to the symmetric stretching vibration of the O–C–O group. The bands

at 759 and 706 cm^{-1} are attributes to the C–H bending vibrations of aromatic rings, while the band at 463 cm^{-1} is ascribable to the stretching of Fe-O bonds.[7–9]

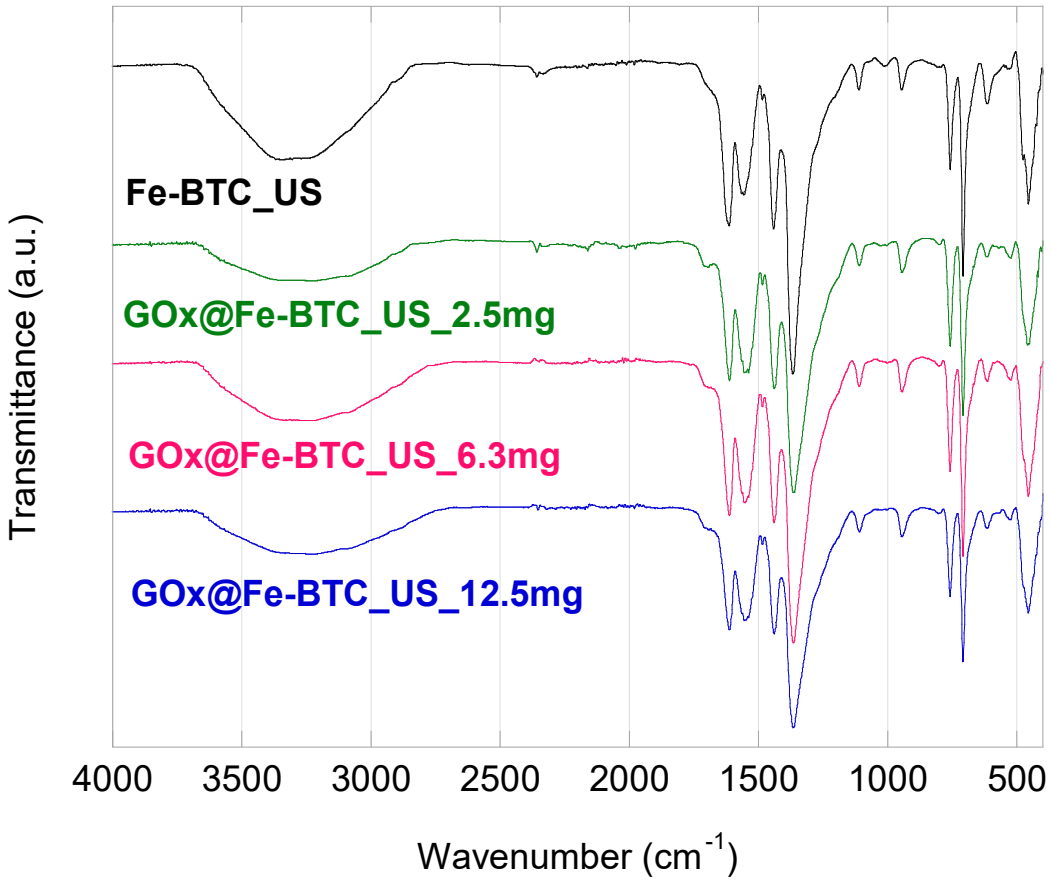

Figure 5.3. FT-IR spectra of Fe-BTC and GOx@Fe-BTC samples from 400 to 4000 cm^{-1}.

Despite the different amount of enzyme added, all samples showed no relevant microstructural differences by FT-IR and XRPD. Therefore, enzyme immobilisation did not affect the obtainment of the MOF structure.

Thermal Analysis

Thermal behaviour of the samples was examined under oxygen flow. Figure 5.4 showed TG, and dTG curves of Fe-BTC and GOx@Fe-BTC samples prepared via sonochemical approach. All samples showed three weight losses characteristic of Fe-BTC material: a first weight loss up to 150 °C due to the departure of adsorbed water molecules; a second weight loss between 150 and 260 °C arising from the loss of water molecules coordinated to iron trimers; a third and last weight loss over the 260 – 450 °C range attributed to the decomposition of the framework. The weight loss of Fe-BTC_US at 25 – 150 °C is significantly higher than that observed for

GOx@Fe-BTC_US samples. This could be attributed to the immobilisation of the enzyme into the pores of Fe-BTC. Indeed, due to the presence of GOx, a lower amount of water molecules is adsorbed within the pores. This is in agreement with the higher extent of adsorbed water observed also by FT-IR spectroscopy. Moreover, the weight loss in between 150 and 260 °C increased by increasing the amount of enzyme added (Table 5.2). This is because of the degradation of GOx (Figure 5.4 c), further confirming its immobilisation into the MOF.

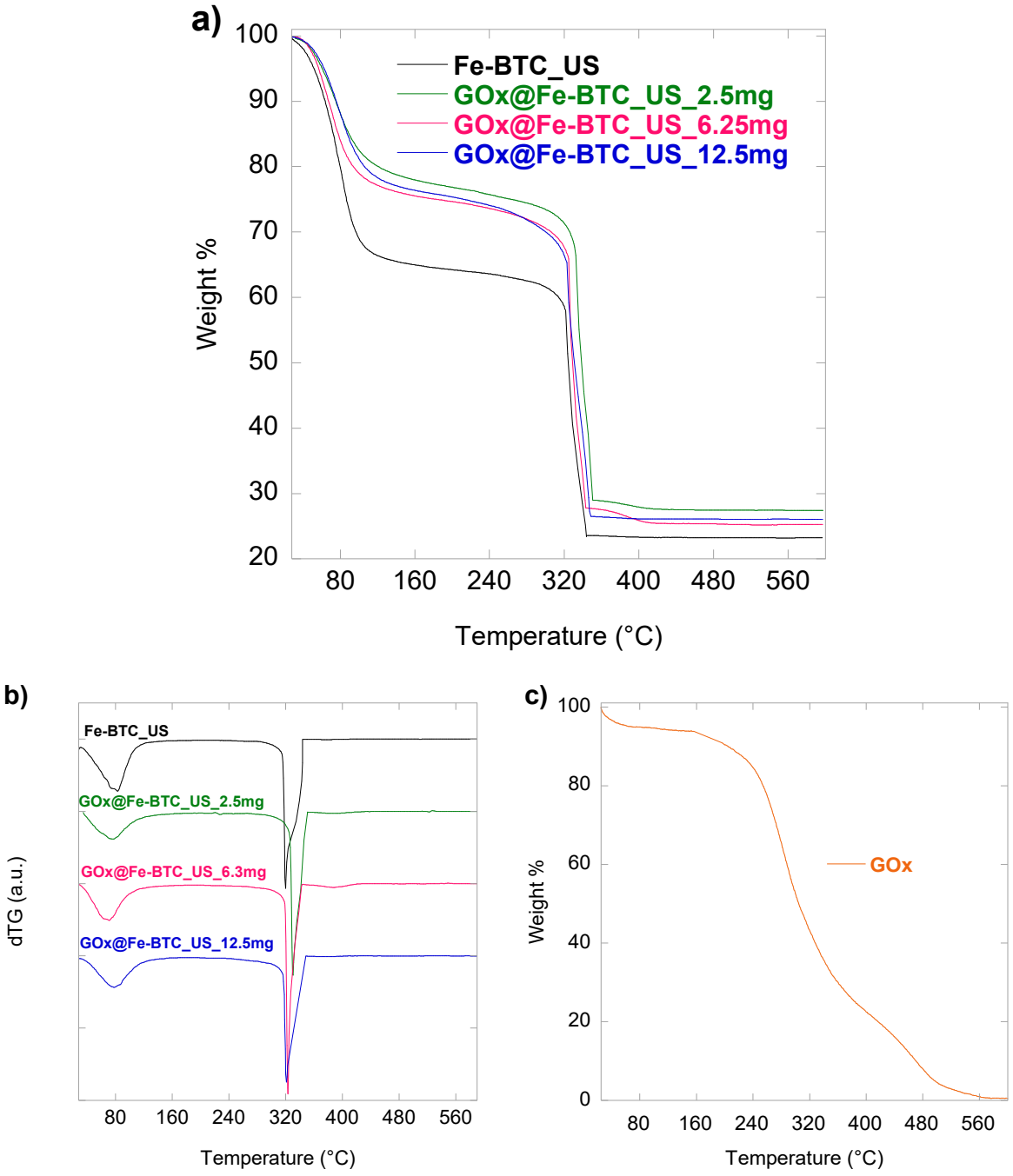

Figure 5.4. TG (a), and dTG (b) of Fe-BTC and GOx@Fe-BTC samples obtained via sonochemical approach, and TG curve of GOx, between 25 and 600°C (10°C min^{-1}) under O_2 flow (40 ml min^{-1}).

Sample	1st weight loss (25-150 °C)	2nd weight loss (150-260 °C)	3rd weight loss (260-450 °C)
Fe-BTC_US	35.6 %	2.2 %	39.1 %
GOx@Fe-BTC_US_2.5mg	22.2 %	5.5 %	44.8 %
GOx@Fe-BTC_US_6.25mg	23.9 %	6.4 %	44.4 %
GOx@Fe-BTC_US_12.5mg	22.8 %	7.8 %	43.3 %

Table 5.2. Weight losses extracted from the TG curves of all Fe-BTC and GOx@Fe-BTC samples.

Nitrogen physisorption

N_2 adsorption/desorption isotherms and pore size distributions for Fe-BTC_US are reported in Figure 5.5. This sample presents a I-type isotherm, which is typical of microporous material (Figure 5.5 a).[10] Data obtained for GOx@Fe-BTC_US_2.5mg, GOx@Fe-BTC_US_6.3mg, and GOx@Fe-BTC_US_12.5mg samples are not shown since such samples did not significatively adsorb. We hypnotised that all porosity of such samples resulted to be filled/blocked by the enzyme, indicating that GOx has been immobilised into Fe-BTC MOF.

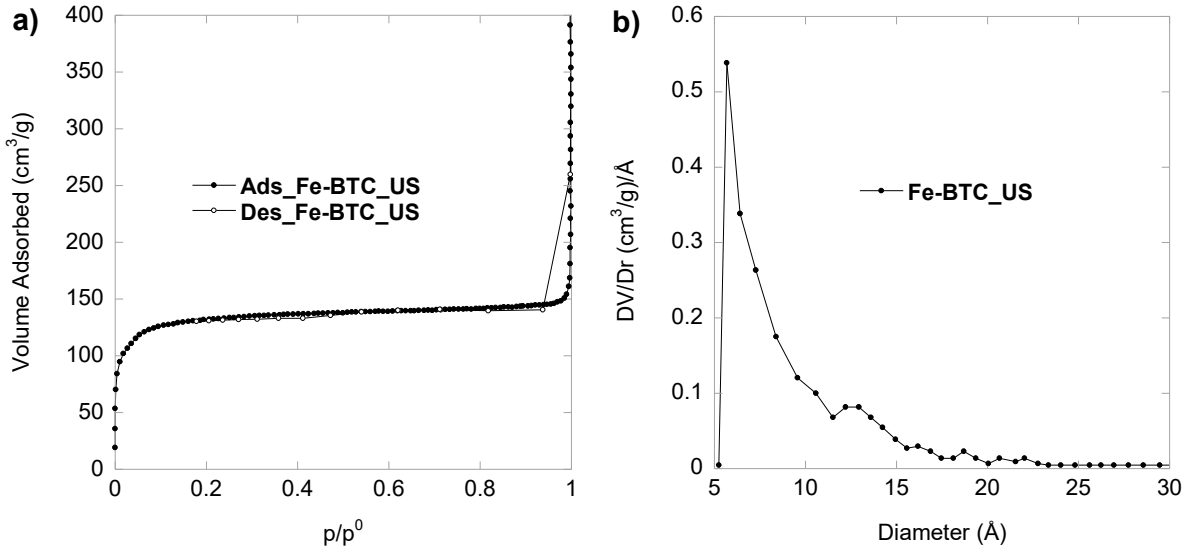

Figure 5.5. N_2 adsorption/desorption isotherms obtained at -196°C (a) and pore size distributions (b) of Fe-BTC and GOx@Fe-BTC samples.

Sample	SSA (m^2/g)	Micropore volume (cm^3/g)	Mesopore volume (cm^3/g)	Macropore volume (cm^3/g)
Fe-BTC_US	565	0.201	0.023	0.004
GOx@Fe-BTC_US_2.5mg	n.a.	n.a.	n.a.	n.a.
GOx@Fe-BTC_US_6.3mg	n.a.	n.a.	n.a.	n.a.
GOx@Fe-BTC_US_12.5mg	n.a.	n.a.	n.a.	n.a.

Table 5.2. Specific Surface Area (SSA) and macro-, meso- and micropore volume of Fe-BTC and GOx@Fe-BTC samples. %RSD SSA = 2; %RSD pore volume = 1. n.a.: not available (i.e., the sample did not adsorb).

5.2.2. Catalytic activity and stability

Catalytic activity of all GOx@Fe-BTC samples was evaluated. As shown in Figure 5.6, relative activity of GOx@Fe-BTC_US samples increased with increasing GOx amounts.

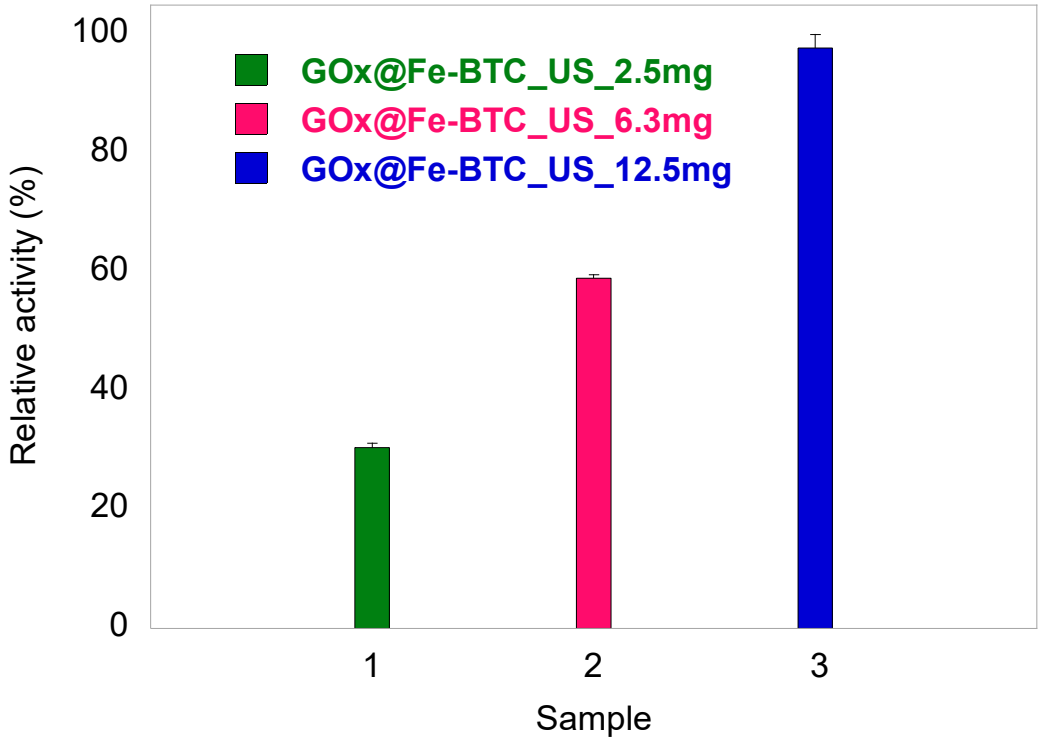

Figure 5.6. Relative activity of GOx@Fe-BTC hybrid composite materials. Activity normalised at Abs_{652nm} = 0.888. Error bars represent the standard deviations of three independent experiments.

As shown in Figure 5.7. a, c, e, none of the samples showed enzyme leaching out from the support neither when washing the material after the synthesis, nor after incubation in acetate buffer (10 mM; pH 4) for 24 hours.

Figure 5.7. b, d, f showed catalytic stability monitored for GOx@Fe-BTC_US_2.5mg, GOx@Fe-BTC_US_6.3mg, and GOx@Fe-BTC_US_12.5mg samples. The best result in terms of catalytic stability was obtained for GOx@Fe-BTC_US_12.5mg, which retained up to 70 % of its activity for 4 weeks. Conversely, GOx@Fe-BTC_US_2.5mg lost almost 30 % of its activity after 4 weeks, and GOx@Fe-BTC_US_6.3mg 40 % of activity after only 1 week. Compared to results reported in the literature, where the catalytic activity of the hybrid material dramatically decrease after one week,[11,12] GOx@Fe-BTC_US_12.5mg sample has proven to possess an exceptional catalytic stability performance, becoming appealing for long-term storage and utilisation. Further investigations have been performed on this sample.

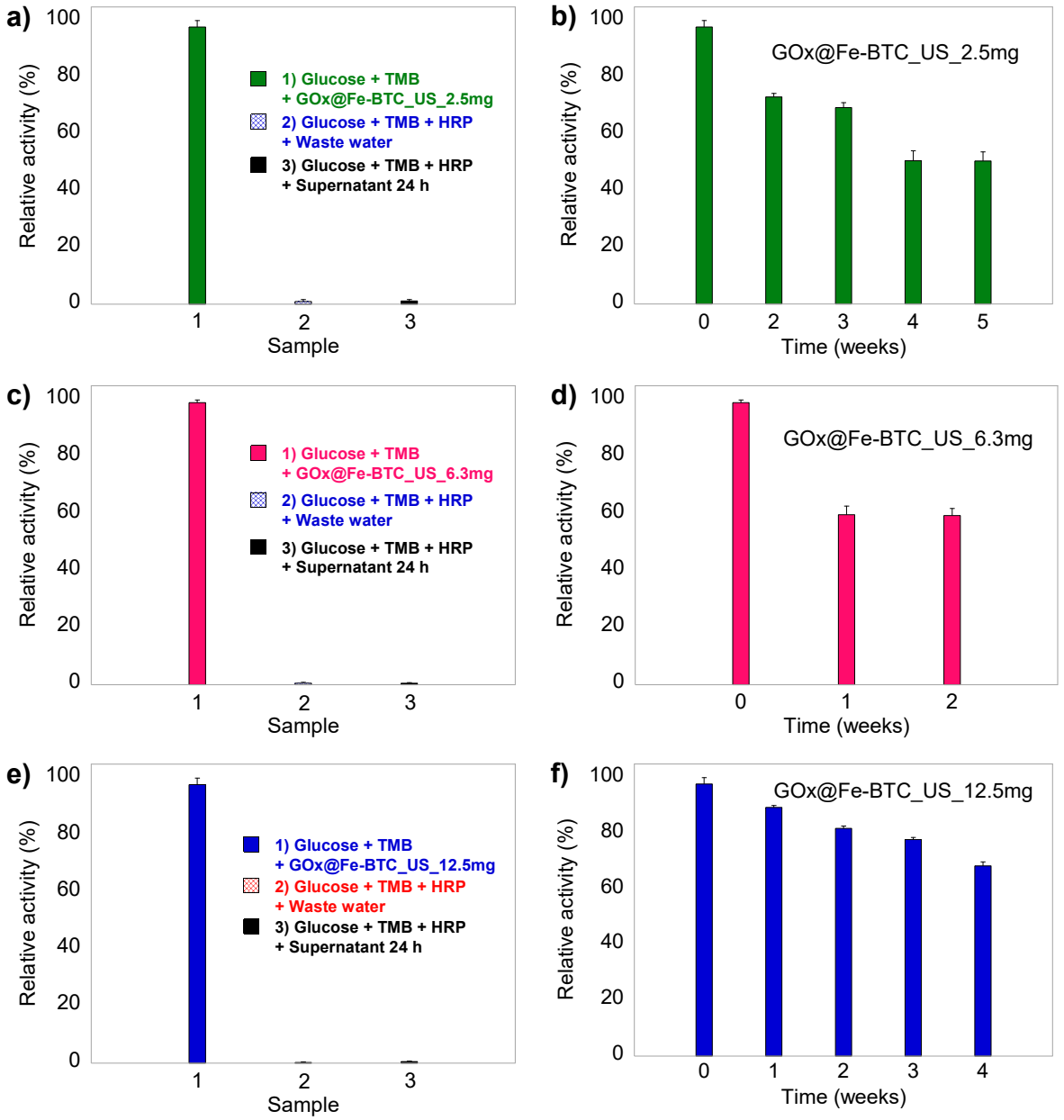

Figure 5.7. Leaching tests (a, c, e) performed on GOx@Fe-BTC samples. Catalytic stability (b, d, f) of GOx@Fe-BTC samples. Error bars represent the standard deviations of three independent experiments.

5.2.3. pH dependence on GOx@Fe-BTC catalytic activity

Similar to free GOx, the catalytic activity of GOx@Fe-BTC biocatalyst is closely dependent on experimental conditions. The effect of pH on the relative activity of GOx@Fe-BTC_US_12.5mg was investigated.

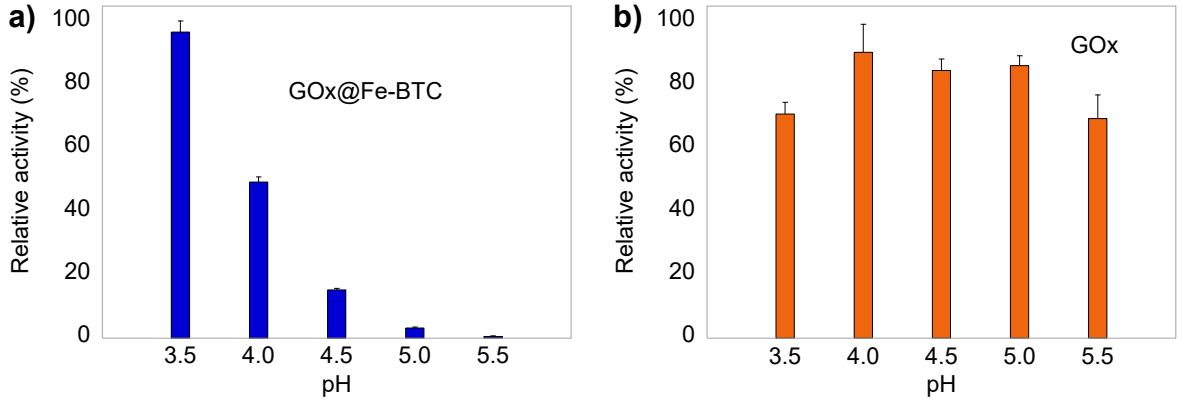

Figure 5.8. Effect of pH (a) on GOx@Fe-BTC catalytic activity. pH profile of GOx (b). Error bars represent the standard deviations of three independent experiments.

As shown in Figure 5.8 a, the activity of GOx@Fe-BTC gradually decreased from pH 3.5 to 5.5. pH profile of immobilised GOx (Figure 5.8 a) differed from that observed for GOx, whose relative activity increased from pH 3.5 to 4, and slightly decreased from 4.0 to 5.5 (Figure 5.8 b).

5.2.4. Steady-state kinetic assay

To further investigate the catalytic activity of the GOx@Fe-BTC_US_12.5mg sample, steady-state kinetic experiments were performed. Typical Michaelis-Menten curves were obtained for both GOx@Fe-BTC (Figure 5.9 a) and GOx (Figure 5.9 c). Kinetic parameters K_m and V_{max}, summarised in Table 5.3, were obtained from Lineweaver–Burk double-reciprocal plots (Figure 5.9 b, d). As shown in Table 5.3, the K_m value calculated for GOx@Fe-BTC is ca. 17 times lower than the value obtained for GOx, revealing a much better affinity for immobilised GOx to glucose compared to free GOx. The V_{max} value for GOx@Fe-BTC is lower compared to GOx, suggesting a relatively slower reaction rate for immobilised GOx than free GOx.

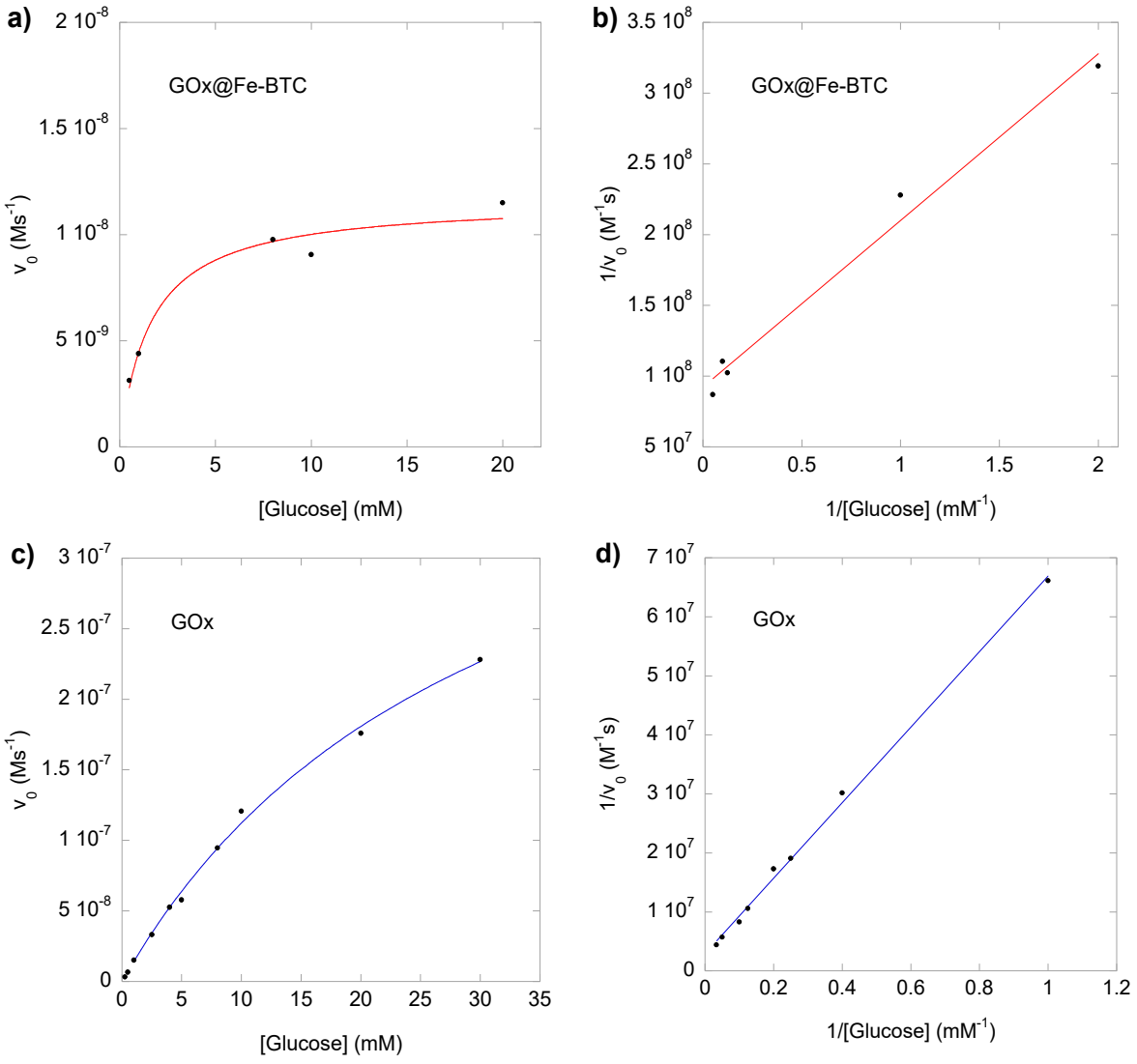

Figure 5.9. Steady-state kinetic analysis using the Michaelis–Menten model for GOx@Fe-BTC (a) and GOx (c) and the Lineweaver–Burk double-reciprocal plots for GOx@Fe-BTC (b) and GOx (d).

Catalyst	Substrate	E (M)	K_m (mM)	V_{max} (M/s)
GOx@Fe-BTC	Glucose	$1.14 \cdot 10^{-3}$	1.28	$1.09 \cdot 10^{-8}$
GOx	Glucose	$3.13 \cdot 10^{-9}$	21.88	$3.42 \cdot 10^{-7}$

Table 5.3. Comparison of the kinetic parameters of GOx@Fe-BTC and GOx. [E] is the biocatalyst concentration, K_m is the Michaelis constant, V_{max} is the maximum reaction rate.

Given such a remarkable affinity towards glucose, sonochemically-prepared GOx@Fe-BTC hybrid composite could be efficiently used as a colorimetric assay platform to detect glucose concentrations.

5.2.5. Colorimetric biosensing of glucose

A colorimetric biosensing of glucose was performed using GOx@Fe-BTC_US_12.5mg as biocatalyst. Figure 5.10 showed the dose-response curve obtained in a [Glucose] range between 0 and 4000 µM. The absorbance at 652 nm progressively increased with the increase of glucose concentration. A good linear response of the absorbance at 652 nm was found in the 0 – 500 µM [Glucose] range with a correlation coefficient of 0.99847.

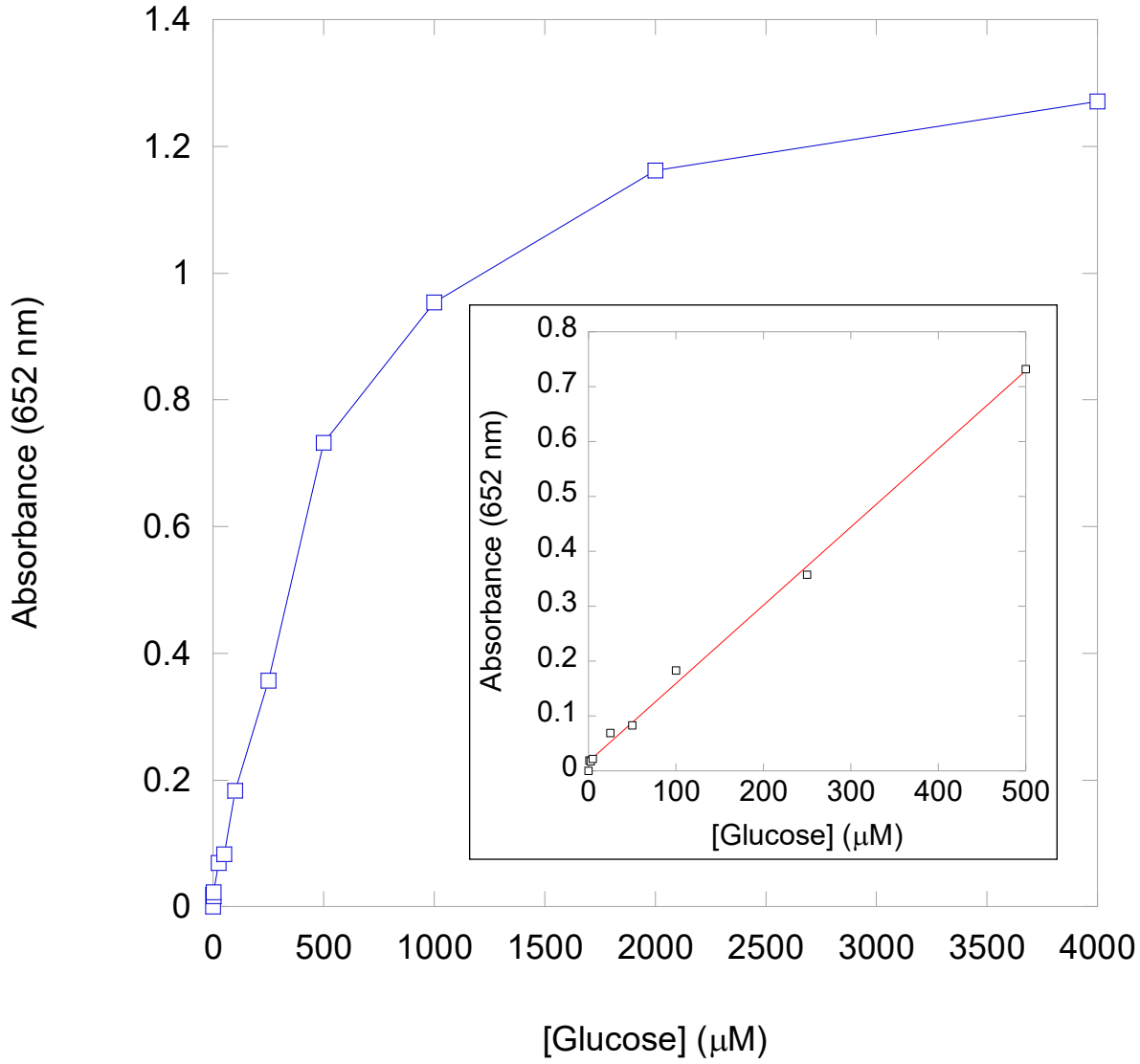

Figure 5.10. Dose–response curve for glucose detection in the 0 – 4000 µM range. Inset: linear calibration plot between the absorbance at 652 nm and glucose concentration. Experiments were carried out using GOx@Fe-BTC (500 µg/mL), TMB (0.4 mM) and different concentration of glucose (0 – 4000 µM) in acetate buffer (10 mM, pH = 4). The solution mixtures were incubated at 35°C under magnetic stirring (150 rpm) for 1 hour.

Table 5.4 shows a comparison of different hybrid composite materials used as a colorimetric platform for glucose detection. Compared to several other reported biocatalysts, GOx@Fe-BTC

material prepared via sonochemical approach showed a wider linear range MIL-100(Fe), especially when comparing with a GOx@Fe-BTC material prepared via conventional method by Zhao and collaborators.[13] Despite a slightly wider linear range obtained by Chang et al.,[14] it has been revealed a good sensitivity of the colorimetric detection assay developed in the present thesis work.

Catalyst	Substrate	Linear range (μM) Glucose	Ref.
GOx@hemin@ZIF-8	Glucose	0 – 250	[15]
GOx/NiPd@ZIF-8	Glucose	10 – 300	[16]
GOx/Fe_3O_4@ZIF-8	Glucose	5 – 250	[17]
GOx/Fe_3O_4/graphene oxide nanocomposite	Glucose	0.5 – 600	[14]
GOx@Fe-BTC	Glucose	5 – 100	[13]
GOx@Fe-BTC	Glucose	0 – 500	This work

Table 5.4. Comparison of various hybrid composite-based colorimetric assays used for glucose detection.

Therefore, an exceptional GOx@Fe-BTC biocatalyst has been synthesised via sonochemical approach, under green, rapid, and biocompatible conditions Synthesis is performed at room temperature, in just 200 seconds, and working in aqueous solution under mild pH. Small amounts of enzyme are needed and simply added during the synthesis in order to favour an *in situ* immobilisation of the biomolecule within the MOF. Embedding of enzymes into MOF is revealed by the absence of leaching out from the support and by the lack of absorption of the samples during nitrogen physisorption experiments. Moreover, it has been demonstrated that GOx immobilisation does not alter the microstructure of the MOF. Therefore, immobilisation has been achieved in just one step simply adding GOx together with the precursors of the support in the solid state. Additional post-synthetical immobilisation steps are avoided. Indeed, the rapid, facile, eco- and bio-compatible synthesis through alternative sonochemical method, together with the long-term catalytic stability of the material, the remarkable affinity towards glucose and the good sensitivity showed by the colorimetric detection assay, make GOx@Fe-BTC hybrid composite material suitable for industrial scale-up, showing a relatively low environmental footprint compared to traditional pathways.

5.3. References

[1] Yan, Z.; Niu, Q.; Mou, M.; Wu, Y.; Liu, X.; Liao, S. A Novel Colorimetric Method Based on Copper Nanoclusters with Intrinsic Peroxidase-like for Detecting Xanthine in Serum Samples. *J. Nanoparticle Res.* **2017**, *19* (7). https://doi.org/10.1007/s11051-017-3904-9.

[2] Nelson, D. L.; Cox, M. M. *Lehninger Principles of Biochemistry*, 7th ed.; WH Freeman, 2017.

[3] Metelitsa, D. I.; Naumchik, I. V.; Karaseva, E. I.; Polozov, G. I.; Shadyro, O. I. Inhibition of Peroxidase Oxidation of Aromatic Amines by Substituted Phenols. *Prikl. Biokhim. Mikrobiol.* **2003**, *39* (4), 401–412.

[4] Pangkumhang, B.; Jutaporn, P.; Sorachoti, K.; Khamdahsag, P.; Tanboonchuy, V. Applicability of Iron (III) Trimesic (Fe-BTC) to Enhance Lignin Separation from Pulp and Paper Wastewater. *Sains Malays.* **2019**, *48* (1), 199–208. https://doi.org/10.17576/jsm-2019-4801-23.

[5] Leclerc, H.; Vimont, A.; Lavalley, J. C.; Daturi, M.; Wiersum, A. D.; Llwellyn, P. L.; Horcajada, P.; Férey, G.; Serre, C. Infrared Study of the Influence of Reducible Iron(Iii) Metal Sites on the Adsorption of CO, CO2, Propane, Propene and Propyne in the Mesoporous Metal-Organic Framework MIL-100. *Phys. Chem. Chem. Phys.* **2011**, *13* (24), 11748–11756. https://doi.org/10.1039/c1cp20502a.

[6] Patra, S.; Hidalgo Crespo, T.; Permyakova, A.; Sicard, C.; Serre, C.; Chaussé, A.; Steunou, N.; Legrand, L. Design of Metal Organic Framework-Enzyme Based Bioelectrodes as a Novel and Highly Sensitive Biosensing Platform. *J. Mater. Chem. B* **2015**, *3* (46), 8983–8992. https://doi.org/10.1039/c5tb01412c.

[7] Lestari, W. W.; Hartono, J.; Adreane, M.; Nugrahaningtyas, K. D.; Purnawan, C.; Rahardjo, S. B. Electro-Synthetic Optimization of Host Material Based on MIL-100(Fe). *Molekul* **2016**, *11* (1), 61. https://doi.org/10.20884/1.jm.2016.11.1.195.

[8] Moradi, S. E.; Dadfarnia, S.; Haji Shabani, A. M.; Emami, S. Removal of Congo Red from Aqueous Solution by Its Sorption onto the Metal Organic Framework MIL-100(Fe): Equilibrium, Kinetic and Thermodynamic Studies. *Desalin. Water Treat.* **2015**, *56* (3), 709–721. https://doi.org/10.1080/19443994.2014.947328.

[9] Lv, H.; Zhao, H.; Cao, T.; Qian, L.; Wang, Y.; Zhao, G. Efficient Degradation of High Concentration Azo-Dye Wastewater by Heterogeneous Fenton Process with Iron-Based Metal-Organic Framework. *J. Mol. Catal. A Chem.* **2015**, *400*, 81–89. https://doi.org/10.1016/j.molcata.2015.02.007.

[10] F. Rouquerol; J. Rouquerol; K. Sing. *Adsorption by Powders and Porous Solids*; Elsevier, 1999.

[11] Yee, Y. C.; Hashim, R.; Mohd Yahya, A. R.; Bustami, Y. Colorimetric Analysis of Glucose Oxidase-magnetic Cellulose Nanocrystals (CNCS) for Glucose Detection. *Sensors (Switzerland)* **2019**, *19* (11), 1–12. https://doi.org/10.3390/s19112511.

[12] Tocco, D.; Carucci, C.; Todde, D.; Shortall, K.; Otero, F.; Sanjust, E.; Magner, E.; Salis, A. Enzyme Immobilization on Metal Organic Frameworks: Laccase from Aspergillus Sp. Is Better Adapted to ZIF-Zni Rather than Fe-BTC. *Colloids Surfaces B Biointerfaces* **2021**, *208*, 112147. https://doi.org/10.1016/j.colsurfb.2021.112147.

[13] Zhao, Z.; Pang, J.; Liu, W.; Lin, T.; Ye, F.; Zhao, S. A Bifunctional Metal Organic Framework of Type Fe(III)-BTC for Cascade (Enzymatic and Enzyme-Mimicking) Colorimetric Determination of Glucose. *Microchim. Acta* **2019**, *186* (5). https://doi.org/10.1007/s00604-019-3416-7.

[14] Chang, Q.; Tang, H. Optical Determination of Glucose and Hydrogen Peroxide Using a Nanocomposite Prepared from Glucose Oxidase and Magnetite Nanoparticles Immobilized on Graphene Oxide. *Microchim. Acta* **2014**, *181* (5–6), 527–534. https://doi.org/10.1007/s00604-013-1145-x.

[15] Cheng, H.; Zhang, L.; He, J.; Guo, W.; Zhou, Z.; Zhang, X.; Nie, S.; Wei, H. Integrated Nanozymes with Nanoscale Proximity for in Vivo Neurochemical Monitoring in Living Brains. *Anal. Chem.* **2016**, *88* (10), 5489–5497. https://doi.org/10.1021/acs.analchem.6b00975.

[16] Wang, Q.; Zhang, X.; Huang, L.; Zhang, Z.; Dong, S. GOx@ZIF-8(NiPd) Nanoflower: An Artificial Enzyme System for Tandem Catalysis. *Angew. Chemie - Int. Ed.* **2017**, *56* (50), 16082–16085. https://doi.org/10.1002/anie.201710418.

[17] Hou, C.; Wang, Y.; Ding, Q.; Jiang, L.; Li, M.; Zhu, W.; Pan, D.; Zhu, H.; Liu, M. Facile Synthesis of Enzyme-Embedded Magnetic Metal-Organic Frameworks as a Reusable Mimic Multi-Enzyme System: Mimetic Peroxidase Properties and Colorimetric Sensor. *Nanoscale* **2015**, *7* (44), 18770–18779. https://doi.org/10.1039/c5nr04994f.

6. Conclusions

Innovative, rapid, and facile one-pot synthesis of GOx@Fe-BTC under green, biocompatible conditions has been successfully achieved via alternative mechanochemical and sonochemical routes. On the one hand, mechanochemical synthesis was conducted without using any solvents, in just 6 minutes grinding, under room temperature and mild pH conditions. This innovative solvent-free synthesis protocol demonstrated that the obtainment of the framework could be achieved in the absence of any solvents but only using the mechanical energy imparted into the system through ball milling. This represents an unprecedented breaking point compared to conventional batch-based methods and could help further emerging the unexpressed potential of iron(III) trimesate MOFs as immobilisation supports, especially on the industrial level. Indeed, a solventless pathway is appealing to industrial scale-up, reducing the environmental footprint of the process. Moving towards new strategies that involve less steps and reduce, or completely avoid, the use of solvents, is demanding but still essential for sustainability. On the other hand, sonochemical synthesis was carried out in just 200 seconds, using only deionised water as solvents, under mild pH and room temperature conditions. Besides the extremely rapid synthesis reactions, the fast nucleation kinetics prompted by ultrasounds also favoured the obtainment of a gel product. Gel state provides good gas adsorption capabilities and reduced mass transfer resistance compared to powders, paving the way for a variety of applications of this MOF. Both mechanochemical and sonochemical synthesis have proven to be easily tunable to bio-friendly conditions. In particular, they have been *ad hoc* tailored to the optimal stability/activity conditions reported for GOx, looking towards a full retainment of enzyme molecules' functionality while protectively coating them by porous and robust supports. The encapsulation of GOx has been achieved in one-step by simply adding the guest together with the support's precursors. This represents a benchmark for *ex vivo* applications of biomolecules, whose use is often limited by an intrinsic loss of activity due to the immobilisation process. Indeed, biomolecule stability is affected by physical, biological, and chemical factors, requiring careful evaluation of the immobilisation conditions (pH, temperature, concentrations). Microstructure and thermal stability of the material have proven not to be affected by pH. Conversely, textural properties can be modulated by simply varying the amount of base. Such a pH-dependent fine tuning of MOF porosity allows setting the accessibility and diffusion of the substrates to the active sites by changing synthetic parameters. This has been demonstrated to be crucial to develop highly performing biosensors, biocatalysts and drug delivery systems

with enhanced activity and selectivity. Indeed, GOx@Fe-BTC hybrid composites have been exploited as a platform for the colorimetric sensing of glucose, combining the catalytic activity of immobilised GOx, with the intrinsic peroxidase-like activity shown by the Fe-BTC support. This detection assay showed wide linear range and good sensitivity. Moreover, GOx@Fe-BTC biocatalyst showed higher affinity towards glucose compared to free GOx. The enzyme-mimic behaviour of Fe-BTC MOF has been also successfully applied for the detection of hydrogen peroxide in solution, showing a great performance in terms of linear range and better affinity towards the substrate compared to HRP. Preliminary studies also demonstrated interesting potentialities of Fe-BTC material as valsartan carrier for drug-delivery purposes. Therefore, this Ph.D. research demonstrated that the preparation of enzyme-MOFs hybrid composites can be easily achieved in rapid reaction times, under green and biocompatible conditions using alternative mechanochemical and sonochemical methods. This is of main interest, especially in recent years, in which finding alternative and greener options urges to be addressed in every field of human life. The possibility to *ad hoc* modulate the mildness of the reaction mixture, according to the stability of the guest and the desirable porosity of the support, provides an outstanding protection from biological, and chemical degradation with maintenance of bioactivity. Both approaches can be potentially adapted to an infinite variety of MOFs and guest molecules, making the *in situ* fabrication of biomolecule-MOF-based composites a remarkably easier, cheaper, and greener procedure compared to batch-based methods.

List of Abbreviations

Ac	Acetate
AcOH	Acetic acid
FT-IR	Fourier transform infrared spectroscopy
BET	Brunauer–Emmett–Teller
BTC	1,3,5-benzenetricarboxylate, trimesate
CP	Coordination polymer
CUS	Coordinatively unsaturated site
DSC	Differential scanning calorimetry
EtOH	Ethanol
FAD	Flavin adenine dinucleotide
Fe-BTC	Disordered iron(III) trimesate
GOx	Glucose oxidase
H_3BTC	Benzene-1,3,5-tricarboxylic acid, trimesic acid
HRP	Horseradish peroxidase
IUPAC	International Union of Pure and Applied Chemistry
LAG	Liquid-assisted grinding
MC	Mechanochemistry
MIL	Material Institute of Lavoisier
MOF	Metal-organic framework
MTN	Mobil – thirty-nine
NG	Neat grinding
oxTMB	Oxidised TMB
PBS	Phosphate buffered saline

RSD	Relative standard deviation
RT	Room temperature
SBU	Secondary building unit
SEM	Scanning electron microscopy
SSA	Specific surface area
TGA	Thermogravimetric analysis
TMAOH	Tetramethylammonium hydroxide
TMB	3,3',5,5'-tetramethylbenzidine
US	Ultrasounds
UV-vis	Ultraviolet-visible
XRPD	X-ray powder diffraction
ZIF	Zeolitic imidazolate framework

Acknowledgments

In the first place, my sincere gratitude goes to my supervisor Prof. Guido Ennas for his precious support and helpful advice during these three years.

Also, I wish to thank Dr. Alessandra Scano, for her immense encouragement and inspiration, Dr. Martina Pilloni, and Dr. Federico Casti, for their precious collaboration.

Further to this, I would like to express my thanks to Dr. Daniela Meloni and Franca Sini for their enormous help and support.

My sincere gratitude goes to Dr. Sarah Hudson, who has been my supervisor during the six months I spent in Bernal Institute, University of Limerick (Ireland).

I would like to thank all my family and friends for their encouragement and immense patience.

I wish to thank CeSAR (Centro Servizi d'Ateneo per la Ricerca) of the University of Cagliari (Italy) for the SEM and XRPD experiments performed with a FEI Quanta 200 Microscope and a Bruker D8 Advance Diffractometer, respectively.

I would also like to gratefully acknowledge Sardinian Regional Government for the financial support of my Ph.D. scholarship (P.O.R. Sardegna F.S.E. Operational Programme of the Autonomous Region of Sardinia, European Social Fund 2014-2020 – Asse III “Istruzione e Formazione” – Obiettivo Tematico 10 “Investire nell’istruzione, nella formazione e nella formazione professionale per le competenze e l’apprendimento permanente” per le aree di specializzazione D.G.R. n. 43/12 del 01/09/2015: ICT, Reti intelligenti per la gestione efficiente dell’energia, Biomedicina, Turismo e beni culturali e ambientali).